The Role of Upper-Ocean Mixing in Large-Scale Ocean and Climate Dynamics

A Dissertation
Presented to the Faculty of the Graduate School
of
Yale University
in Candidacy for the Degree of

Doctor of Philosophy

by
Georgy Eduardovich Manucharyan

Dissertation Director: Alexey Fedorov

December 2014

I dedicate this thesis to my parents, Irina and Eduard Manucharyan, who kindly encouraged me to pursue an academic career.

Acknowledgements

I would like to acknowledge my advisor Alexey Fedorov for his support and many productive discussions throughout my graduate studies. My committee members George Veronis, John Wettlaufer, Ronald Smith and Mary-Louise Timmermans for their insightful comments on my research. Special thanks to George Veronis and John Wettlaufer for igniting my interest in the fields of geophysical fluid dynamics, applied mathematics, and laboratory experiments. Florian Sévellec for discussions on dynamical system approaches to climate model simulations and data analysis. Christopher Brierley for his insights into the climate dynamics problems of the past geological epochs, and Natalie Burls for discussions on ENSO dynamics. Jin-Qiang Zhong for his invaluable help in setting up laboratory experiments. Woosok Moon and Andrew Wells for endless conversations on various scientific topics. My brother Vladimir Manucharyan for our discussions on the relevance of fluid dynamics theories to problems in quantum mechanics.

Declaration

No part of this Thesis has previously been submitted for a degree at this or any other university. The work described in this Thesis is entirely that of the author, except where reference is made to previously published or unpublished work.

Georgy E Manucharyan

Yale University

Department of Geology & Geophysics

March 2014

Abstract

The Role of Upper-Ocean Mixing in Large-Scale
Ocean and Climate Dynamics

Georgy Eduardovich Manucharyan

2014

The objective of this research is to understand the effects of small scale processes on large scale dynamics in fluid flows and to assess its implications for climate. An example of small scale processes that are central to this study are tropical cyclones (TC), which are intense localized atmospheric vortices actively interacting with the ocean during their life cycle. Despite the great strength of an individual cyclone and its serious economical impacts on coastal population, the cumulative effects of such rare events on large scale oceanic circulation and climate remain largely unexplored.

The study begins with an investigation of small-scale turbulent entrainment processes driven by shear instabilities of the wind-generated ocean currents that arise in the growing oceanic mixed layer during the passage of a TC. The mixed layer growth depends on the turbulent entrainment coefficient which despite its common use in geophysical applications remains poorly constrained by observations. Two sets of laboratory experiments performed here identified the dependence of the entrainment coefficient on the key flow characteristics. The first experiment revealed that the entrainment across a sharp density interface in shear driven flows scales as the Richardson number (a non-dimensional ratio of stratification to shear) to the power of $-3/2$. While the second experiment, exploring the dynamics of rotating density currents, implied that the entrainment is inversely proportional to

the background rotation rate of the reference frame.

Enhanced upper ocean mixing leaves a trace of a deepened mixed layer along the path of a TC and a corresponding oceanic current. However, these currents are subject to baroclinic instability that generates a series of mesoscale eddies which affect the oceanic restratification. Here, the instabilities of upper ocean fronts were analyzed with the aim of a high resolution primitive equation model of fluid flow. Theory-based analysis of the data showed that most unstable modes are self-propagating dipoles that detach and have a probability to escape the influence of the meandering front. Shallow fronts that separate mixed layers of approximately equal depth were found to have the highest probability of dipole escape. The general conclusions of the study found immediate application in the Arctic Ocean dynamics explaining persistent observations of eddies far from their formation sites.

The long-term implications for the ocean circulation are explored in a context of two processes: upper ocean mixing and the vorticity forcing from the cyclonic core of the TC. Upper ocean mixing by TCs results in cold sea surface temperature anomalies and an increased atmospheric heat flux into the ocean. Cumulative effects result in an oceanic circulation that transports heat polewards and equatorwards. It is shown here, that the intensity of oceanic circulation depends of the frequency and strength of mixing events with highly intermittent mixing being less efficient compared to steady mixing. The influx of heat towards the equator creates climate conditions that resemble the past geological epochs including the Pliocene. These conditions are distinguished by their weak zonal temperature gradients at the equator, a phenomenon that modern climate models are unable to reproduce. Here, the strength of upper ocean mixing was used as a tool to explore sensitivity of the equatorial dynamics in a wide range of climates. It is shown that despite dramatic changes in mean state there are corresponding changes in the driving mechanisms that explain a persistent interannual variability dominated by the El Niño - Southern Oscillation.

The cyclonic winds in the core of a TC leave a scar of negative potential vorticity anomaly along its track, that manifests itself in the lifted thermocline. These anomalies eventually split into series of eddies that move towards the western boundary while interacting with other eddies and currents. Such a convoluted dynamics is explored in a high resolution multiple-layer shallow-water model, which was devised here from scratch and explicitly resolves small scale TC forcing within a realistically large size of the ocean basin. If was found that vorticity forcing from TCs could spin up a large scale ocean circulation in the form of either a single gyre in the linear regime (weak TC) or a double gyre in a nonlinear regime (strong TC). The study demonstrates that fluid flows have a strong memory of past forcing events and that a series of localized small scale perturbations could aggregate to form large scale features.

Keywords: tropical cyclones, turbulent entrainment, frontal instabilities, large-scale ocean circulation, El Niño - Southern Oscillation.

Contents

List of Figures

Chapter 1

Introduction

The PhD research presented here involves a range of theoretical and experimental problems in fluid dynamics with a focus on geophysical and climate problems. The underlying theme is related to oceanic response to different types of forcing including the strongly localized wind stress forcing from tropical cyclones. The immediate oceanic response to forcing and the small scale turbulent processes associated with it are investigated in Chapters 2 through 4, whereas Chapters 5 through 7 are devoted to the exploration of the large scale circulation and climate dynamics response arising from the accumulation of small scale events. Presented below is a general motivation behind the projects developed here, with a more detailed and technical introduction written in the beginning of each of the subsequent chapters.

1.1 Thesis outline

This study begins with a problem of understanding the oceanic response to strong winds from tropical cyclones (also known as hurricanes in the Atlantic Ocean, and typhoons in the Pacific Ocean). Tropical cyclones are relatively rare localized atmospheric vortices with winds of extreme strength that actively interact with the ocean. Momentum transfer from the atmospheric winds into ocean generates strong surface ocean currents along the hurricane track [Bender et al., 1993]. These currents are concentrated in the oceanic mixed layer (a surface layer of weakly stratified waters bounded by a strong density jump at the base). The dynamics at the base of the mixed layer is dominated by the shear instabilities that entrain colder waters from depth of a thermally stratified ocean to its surface [Price, 1981]. This mixing providing major irreversible changes in oceanic stratification that are manifested at the surface in a form of a cold wake [D'Asaro et al., 2007]. In turn, hurricanes, that feed on latent heat fluxes from warm ocean waters, substantially weaken in response to colder surface waters [Schade and Emanuel, 1999]. Thus, oceanic mixed-layer dynamics plays an important role in prediction of hurricane intensity.

The growth of the turbulent mixed layer into a stratified interior of the fluid is a challenging problem as it involves the energy transport between different scales of motion in the presence of growing instabilities. The mixed-layer development is investigated in Chapter 2 using a set of laboratory experiments with the aim to simulate oceanic response under forcing by surface stress. The dynamics is explained from the perspective of scaling laws based on flow energetics in Section 2.2. Turbulent fluxes of deeper denser waters across the base of the mixed layer are parameterized to be proportional to the mixed layer velocity [e.g. Ellison and Turner, 1959]. Such a parameterization is widely used in many geophysical applications including the general circulation models of oceanic and atmospheric flows. However direct measurements of turbulent entrainment fluxes are complicated in natural environments and the magnitude of the entrainment coefficient remains largely unconstrained. The analysis of experimental data helped to put the constraints on the entrainment coefficient by establishing its dependence on the interface Richardson number of the flow. Furthermore, an experiment revealed the emergence of fine-scale structures (secondary mixed layers) which affect the turbulent buoyancy fluxes in a complex way that cannot be described through simple entrainment rate parameterization. Such structures have been previously observed in stratified flows with no mean shear, and were thought to appear as an instability associated with non-monotonic dependency of the buoyancy flux on the buoyancy gradient [Balmforth et al., 1998; Phillips, 1972]. Here, a phenomenological turbulent buoyancy transport model was devised for flows with mean shear with the aim of interpreting the existence and long term evolution of secondary mixed layers observed in the experiments (Section 2.3).

For appropriately large-scale geophysical flows the dynamics is further complicated by the presence of the Earth's rotation that puts additional constraints on the efficiency of turbulent entrainment [Griffiths, 1986]. In Chapter 3 the dependence of the entrainment coefficient on the background rotation rate of the fluid is investigated within a framework of rotating density currents. These flows, ubiquitous in oceanic and atmospheric dynamics, are fluid masses submerged into relatively stationary ambient fluids of different density, with their motion driven by the buoyancy force. The dynamics of such currents is significantly affected by the turbulent entrainment processes which lead to an exchange of density and momentum with the environment. It is expected that Coriolis forces arising due to rotation of the reference frame would deflect the trajectories of density currents. However, effects of rotation on the small-scale shear turbulence at the edges of density currents are more subtle.

In the absence of rotation, the turbulence is allowed to develop in all three dimensions, whereas in the presence of rotation there is a tendency of turbulent eddies to have their vorticity aligned with the rotation axis of the reference frame. With higher rotation rates such a constraint becomes more prominent and tends to suppress the small-scale entrainment processes [Fleury et al., 1991] which, in turn, affect the trajectory of the bulk of the density current. In Section 3.2 a mathematical model for these currents is systematically derived and analytical solutions are obtained. And in Section

3.4 a set of laboratory experiments is described that confirms key predictions of the analytical model. This makes it possible to use the experimental data to quantify the suppression of effective entrainment rate due to the presence of rotation (Section 3.5).

While Chapters 2 and 3 are aimed at investigating shear-driven turbulent processes that are of direct relevance to immediate oceanic response to tropical cyclones, further chapters address oceanic adjustment at time and spatial scales much greater than those of the forcing. As was described earlier, the passage of a tropical cyclone leaves a region of increased mixed-layer depth along its path. Since the usual horizontal scale of the forcing is typically of the order of the oceanic baroclinic deformation radius, the abrupt difference in the mixed-layer depth and associated horizontal density gradients generate geostrophic circulation in the upper ocean. Such a circulation is established within a few periods of inertial oscillations, but is subject to baroclinic instabilities that act on longer time scales. The eddies generated by the instability release the potential energy stored in the ocean and affect its stratification and consequently the atmospheric heat fluxes. Surface ocean fronts are very common in oceanographic observations and thus their dynamics is explored here as a general theoretical problem (Chapter 4).

High resolution fluid dynamic simulations revealed that for such fronts the fastest growing mode of instability is in the form of self-propagating dipoles [Hogg and Stommel, 1985] that could transport heat and salt across the front (Section 4.3). However, most of them are formed with unequal strength and thus have strongly curved trajectories that lead to their eventual recirculation back to the front. An idealized quasi-geostrophic model for such dipoles is derived and used to identify the essential parameters controlling their maximum separation distance from the front (Section 4.4). The dipoles are then detected in a range of different frontal configurations and their statistical properties allowed to classify the fronts in terms of generation probability of far propagating dipoles. Furthermore, the dipoles, being able to transport properties across the front, are tightly linked to the frontal slumping speed which is an important dynamical feature of freely evolving fronts (Section 4.6). This study, posed as a general frontal instability problem, found one of its applications in explaining the Arctic Ocean dynamics where the surface ocean front is producing eddies that are eventually observed far away from their origins.

The ocean has a strong response to tropical cyclones on time and spatial scales of the order of the forcing scale, but can such localized events cumulatively affect the long term climate? To address this question, I separate the two different effects of tropical cyclones on the ocean dynamics: first, the increased upper ocean mixing described earlier and second, the vorticity input into the currents due to cyclonic winds in the core of the tropical cyclone. The vorticity forcing deposits energy into quasi-geostrophic ocean currents in the form of cyclonic potential vorticity anomalies along the track. These are manifested as the upwelling of the thermocline due to forced divergence of upper ocean currents and a scar of the negative potential vorticity anomalies forms along tropical cyclone track. The oceanic circulation associated with it is baroclinically unstable and eventually breaks down into a series of mesoscale eddies. These eddies drift westward due to the planetary beta effect, interact with currents and other eddies and are subjected to dispersion and dissipation. The long term mean currents that arise from such a convoluted dynamics are investigated in Chapter 5. The break down of cyclonic scar into eddies are simulated in a primitive equation model while the long-term mean circulation is examined in a shallow-water ocean model where tropical cyclones are prescribed as vortices moving in random directions.

Qualitatively different cumulative effects arise from intermittent upper-ocean mixing by tropical cyclones. Since cold waters that were entrained into the surface layer are warmed by the atmosphere there is a net input of heat into the upper ocean [Sriver and Huber, 2007]. These warming effects are investigated in the framework of an advection-diffusion equation with a time dependent diffusivity. Such a model represents oceanic dynamics associated with the heat advection by the wind-driven gyres. The model helps to establish a connection between the frequency of the mixing events and the amount of heat being fluxed through the surface boundary (Chapter 6). From a climate-dynamics point of view, the energetics requires the influx of additional heat to be balanced by its transport away from the regions of tropical-cyclone activity. An important consequence of this is that part of the heat is advected by the mean circulation towards equatorial oceans and decreases its zonal temperature gradient – a key element of tropical dynamics [Fedorov et al., 2010].

In present-day climate, the eastern equatorial Pacific is cooled down by the strong upwelling of deeper waters to the surface forming a cold tongue, while the western side is composed of warm waters with almost no upwelling. This asymmetry results in about 5 ℃ east-west difference in sea surface temperature and is linked to the whole climate system [Gu and Philander, 1997]. Climates with almost vanishing zonal gradients (*e.g.* that of the Pliocene epoch, $\sim$3 million years ago) provide conditions seemingly contradictory with our understanding of climate [Fedorov et al., 2006], such that the state of the art climate models are completely unable to reproduce it. Introducing upper ocean mixing allows one to achieve such climates within a general circulation model and provides an opportunity to investigate the tropical dynamics within it.

Perhaps the most important feature of the tropical dynamics is the El Niño - Southern Oscillation (ENSO) which is a pronounced mode of climate variability that affects weather patterns worldwide [Philander, 1990]. Growing evidence suggests that ENSO was active over vast geological epochs, including the Pliocene epoch, despite its profound changes in tropical climate [Scroxton et al., 2011]. The mechanisms for sustained ENSO in such climates are poorly understood. Here, a comprehensive climate model was used to explore the sensitivity of the strength of ENSO events to the mean sea surface temperature gradient in the equatorial Pacific (Chapter 7). The magnitude of ocean-atmosphere feedbacks that control the stability of the natural mode of ENSO are assessed by systematically reducing the underlying fluid dynamic equations down to a model of a damped oscillator (Section 7.4). The mechanisms for sustained ENSO activity in reduced zonal gradient climates are further discussed. This study fills the gap in our theoretical understanding of ENSO dynamics in climates with weak east-west temperature gradients.

1.2 Methodological approaches

Throughout this research an attempt is made to simplify the complicated climate dynamics problems down to their fundamental mechanisms and connect them to basic ideas of fluid dynamics. To obtain a better quantitative insight into the problem various mathematical models are used, ranging from the most complex general circulation climate models (Sections 6.2 and 7.2) to intermediate quasi-geostrophic (Section 4.4) and shallow-water models (Section 5.4), and to models as simple as a physical oscillator (e.g. Section 7.4). There are however, both positive aspects and drawbacks related to the use of each of these methods.

While climate models take into account all the factors they possible could to simulate our climate, there is a large computational cost associated with them and the analysis of such convoluted models is often limited which prohibits gaining valuable insight into the problem. The idealized models, on the other hand, give possibilities of analytical treatment of the problem and theory development (e.g Sections 2.3, 3.3). However, their construction requires great intuition as one could easily miss out on necessary physics. Laboratory experiments (Sections 2.2 and 3.4)are another great tool in exploring the fluid dynamics and climate problems, which allow to simulate physical phenomena in a controlled environment without the need for high resolution numerical models. One drawback here is that obtaining a necessary network of observations (e.g. three dimensional fields of density and velocity) is very difficult, which limits the capabilities of data analysis. Observational data sets (e.g. Section 5.2) are invaluable as they provide a test for any developed theory. The field of climate science, however, often sufferers from the shortness of observational records and their low spatial resolution.

Where possible the accent of the research here is put onto theory development guided by numerical modeling, laboratory experiments, and/or observational data.

1.3 Publications

The research presented in this thesis is conducted entirely during my graduate studies at Yale University. Parts of it have been published, are under review, or in preparation for submission in the form of the following articles:

- Manucharyan G.E. (2010), Dynamics of the Mixed Layers in Stratified Shear Flows, WHOI GFD Summer School, Annual Proceedings Volume 2010, pp 240-259;
- Manucharyan, G. E., C. M. Brierley, and A. V. Fedorov (2011), Climate impacts of intermittent upper ocean mixing induced by tropical cyclones, *Journal of Geophysical Research*, 116, C11038;
- Manucharyan G.E. & M.-L. Timmermans (2013), Generation and separation of mesoscale eddies from surface ocean fronts, *Journal of Physical Oceanography*, 43, 25452562;
- Manucharyan G.E., W. Moon, F. Sevellec, A.J. Wells, J.-Q. Zhong, & J.S. Wettlaufer (2013), Steady rotating density currents on a slope, *Journal of Fluid Mechanics* (in press);
- Manucharyan G.E. & A.V. Fedorov, Persistent ENSO in climates with reduced equatorial SST gradient, *Journal of Climate* (under review);

- Manucharyan G.E. & A.V. Fedorov, Tropical cyclones vorticity input to the ocean currents, in preparation for *Journal of Physical Oceanography*;
- Manucharyan G.E. & C.P. Caulfield, Mixed layer growth in stratified sheared flows, in preparation for *Journal of Fluid Mechanics*.

Chapter 2

Dynamics of the Mixed Layers in Stratified Sheared Flows

The material contained in this chapter has been published in the Annual Proceedings Volume of the WHOI GFD Summer School under the title "Dynamics of the Mixed Layers in Stratified Sheared Flows" [Manucharyan, 2010].

2.1 Introduction

A vast variety of geophysical flows occurs in density stratified fluids in the presence of sheared mean velocity profiles. Under such conditions it's been observed that vigorous turbulence leads to generation of mixed layers within the fluid, e.g. the regions of homogeneous density separated from each other by strong density gradients (interfaces). These layers could be of large vertical scales as well as of fine scales. Example of such flows are the destratification of the upper layer of the ocean under the action of the surface wind stress and the formation of multiple mixed layers which are observed within the seasonal thermocline in the ocean as well as in fresh lakes Simpson and Woods [1970]. Such structures in a turbulent flows are thought to play a crucial role in determining the turbulent fluxes of momentum, buoyancy and other tracers which in turn affect the further dynamics of the flow. In spite of their ubiquity, the problem of turbulent transport remains one the most difficult ones in geophysics.

Previous studies investigated mechanisms acting in stratified turbulent flows - a review of those can be found in Fernando [1991]. The formation of small scale mixed layers in stratified fluids driven by external mechanical sources of turbulence were investigated by theoretically by Balmforth et al. [1998], and experimentally by Park et al. [1994]. In the present study the dynamics of layers is explored within a turbulent fluid in a presence of a sheared mean flow. A set of experiments was performed in which a linearly stratified fluid is driven by the stress applied by a rotating horizontal disk at the surface. This setting leads to the formation of the surface mixed layer extending from the disk into the interior of the fluid. Its evolution with time and its dependence on the stratification and the rotation of the disk are obtained. Furthermore, small scale mixed layers were observed below the surface mixed layer. They have a complicated dynamics with multiple regimes, which we attempted to characterize. The description of the experiment and the behavior of the observed mixed layers is presented in section (2.2). Further, a phenomenological model is developed that explains the mechanism under which the secondary mixed layers are formed. It parametrized the action of the two mechanisms: shear generation of the turbulence due to Kelvin-Helmholtz type of instabilities, and the mean-flow generated turbulence though the vortex scraping mechanism. The resulting gradient-type mixing model predicts the formation of the instabilities in a particular parameter regime that leads to mixed layers formation. The instabilities are related to those described by Phillips [1972] and Posmentier [1977]. The model description, its analysis and numerical simulations are presented in section (2.3). The summary of the work is in section 2.4.

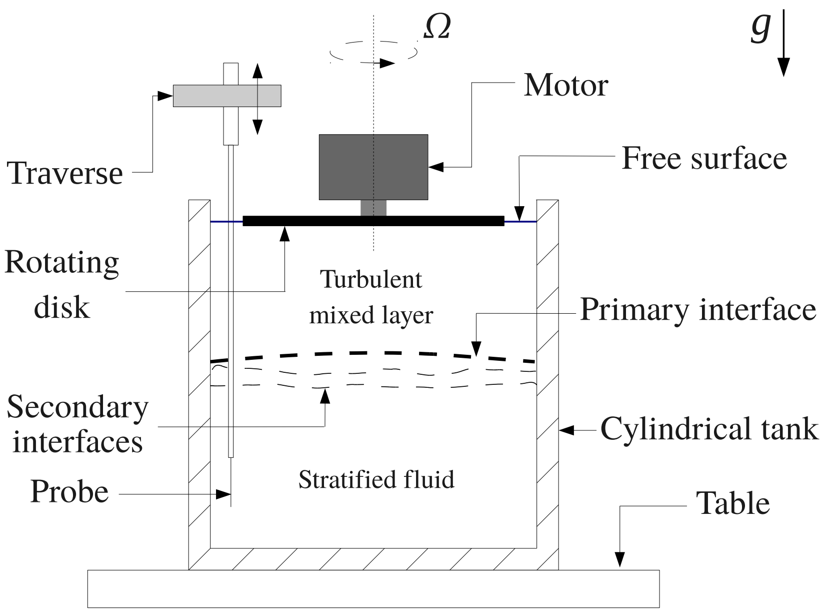

Figure 2.1: Experimental set-up: cylindrical tank filled with linearly stratified fluid, rotating disk at the surface of the fluid, conductivity probe that takes a measurements every 2 minutes.

2.2 Experiments

A series of experiments was made where a stratified fluid was forced by a rotating horizontal disk at the surface in order to investigate the dynamics of the formed mixed layers under various cases of stratification and the disk rotating speeds. The experimental setting is similar to that used by Davies et al. [1995], who investigated the flow generated during the spin-up process and the established secondary circulation.

2.2.1 Experiment arrangement

The experimental set-up is shown in Figure 2.1. A cylindric tank of 30 cm height and 30 cm diameter was filled with a salt-stratified water. Only linear stratifications were considered, which were obtained with a standard double bucket technique Oster and Yamamoto [1963]. The range of density variations within the fluid was from 2% to 20%. A horizontal disk with diameter of 24 cm is located at the surface of the fluid, with its axis of rotation aligned with the axis of the cylinder. The rotation speed of the disk is controlled by the motor (attached above the disk) that gives a range of 0.5 – 10 rad/s. Measurements of vertical density profiles were obtained using a conductivity probe taking 100 measurements per 1 cm of fluid, moving vertically with a speed of 3 mm/s. Measurements were taken only when the probe was moving down to avoid fluxes of water along the probe that would contaminate the data. The probe Reynolds number is of the order of 100 (this is an upper bound, which is reached at the edge of a disk); thus, measurements are not considerably affected by the presence of the probe on the scales considered in the current study - $O(cm)$. The profiled depth of the fluid was 20 cm, whereas the total height is $27cm$. Density was calculated based on conductivity with a calibration using a 3rd order polynomial as a mapping function. To reduce temperature effects on conductivity the fluid was allowed to reach room temperature (20^oC) before the start of the experiment. Thus, the control parameters that define the outcome of the experiment were the stratification of the fluid (expressed as a Brunt–Väisälä frequency, N) and the rotating speed of the disk, Ω.

There are multiple non-dimensional parameters involved in these experiments. The most relevant one is the Richardson number, which will be defined here as $Ri = \frac{N^2}{\Omega^2}$. This definition should not be confused with the local Richardson number $\frac{N^2}{{U_z}^2}$ which varies with time and the location in the fluid. The explored range of $Ri \in (0.15 - 2.3)$. Another parameter would be the disk edge Reynolds number: $Re = \frac{UL}{\nu} \sim 10^5$, where U is the azimuthal

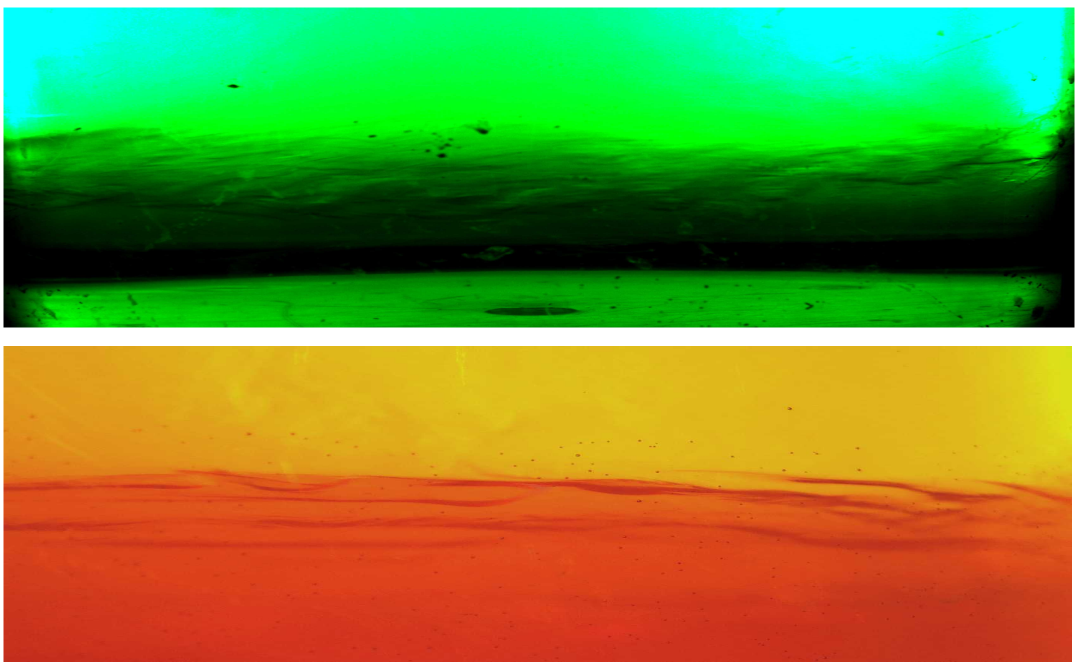

Figure 2.2: Images of the typical interfaces between the well mixed layer and a linearly stratified layer below it.

velocity at the edge of the disk, L is the radius of the disk, and ν is the kinematic viscosity of water. A flow with such high values of Reynolds number could be considered turbulent and independent of the exact value of Re. The Schmidt number for the salt-stratified water is $\sigma = \frac{\nu}{\kappa} \sim 700$, where κ is the salt diffusivity. The tank aspect ratio as well as the ratio of the disk radius to the height of the water column is ~ 1. All geometrical parameters as well as the Schmidt number were fixed throughout all experiments. Thus, the only non-dimensional parameter that describes the different outcomes of the experiments is the Richardson number.

2.2.2 Observations of density profiles

After the tank is filled with the stratified fluid the disk is set in motion. As was mentioned previously, the disk Reynolds number is big enough that the flow adjacent to it becomes turbulent. Such flows are very effective in diffusing buoyancy and momentum. Thus, a mixed layer forms below the disk, with almost homogeneous density and velocity distributions. The growth of such a layer however is suppressed by the stable stratification of the fluid. As the mixed layer deepens the gravitational potential energy of the fluid increases because mixing process effectively lifts the center of the mass of a water column by mixing dense waters upwards against the gravitational field. Furthermore, mixing in a stratified fluid leads to formation of a density jump at the base of the mixed layer. The density jump suppresses turbulence and effectively separates the turbulent flow in the upper mixed layer from the almost quiescent layer underneath. Within the mixed layer there is a mean azimuthal flow due to the coherent rotation of the disk. This flow is also suppressed when it reaches strong stratification at the base of the layer creating a strong shear and providing other mechanisms of the generation of turbulence which will be discussed further.

Figure 2.2 shows images of two interfaces. The top one near $z = 0.8$ appears at early stages in the development of the mixed layer and is charac-

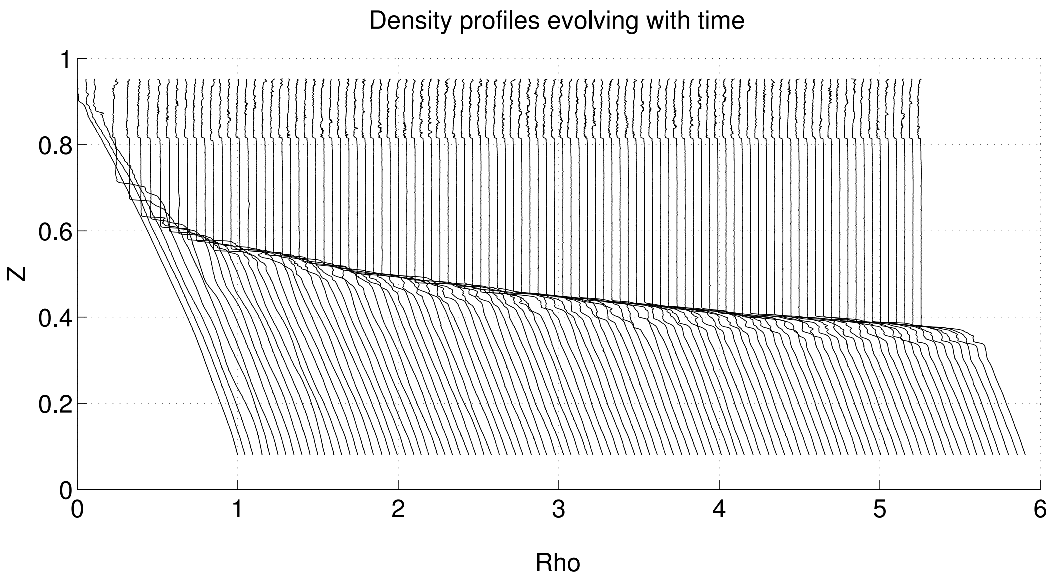

Figure 2.3: Density profiles plotted for different times after the start of the experiment. Profiles are shifted along the X-coordinate by $0.03 g/cm^3$ from each other.

terized by a weak density jump across it, energetic eddies and large thickness (a few cm). The one shown at the bottom, forms during later stages and has low energy eddies of smaller sizes (less then a cm) and much stronger density jump across it. The signature of these interfaces is clearly present in the vertical density profiles, the time evolution of which is shown on Figure 2.3. Initially, linearly stratified fluid is mixed down from the top and forms a mixed layer as well as the density jump at the base of it, both of which are growing in magnitude. The interface separating the mixed layer from the almost undisturbed bottom layer changes its characteristics as well. The profile taken at $t = 0.2h$ (hours) shows the presence of unstable stratification, which resulted from the overturning of energetic eddies at the base of the mixed layer. The density interface for this profile corresponds to a type shown on Figure 2.2 (top). At the profile taken at $t = 6h$ it is hard to see the density structures resulted from overturning of eddies because turbulence is highly suppressed there and eddies are of smaller scale; this interface corresponds the one on Figure 2.2(bottom).

The presence of the density jump and a velocity shear across it points to a possibility of generation of the Kelvin-Helmholtz type of instabilities at the interface that leads to its further erosion. However, these types of instabilities would be present if the local Richardson number $(N^2/{U_z}^2)$ is sufficiently small. Eventually the flow would reach conditions stable to K-H disturbances as the velocity of the mixed layer would gradually slow down, whilst the density jump across the interface would increase. At this point, the erosion of the interface would continue due to the mean flow acting frictionally on turbulent eddies at the interface (vortex scraping). Thus, whether it's the mean flow or its shear, there is a mechanism that would generate mixing at the stable interface and lead to its further deepening.

Exp#	N	Ω	Ri	α	A
9	0.5	1.13	0.2	0.2	0.42
13	0.5	1.34	0.14	0.18	0.5
14	0.52	0.72	0.52	0.2	0.32
15	1.37	1.7	0.65	0.23	0.27
17	1.3	0.95	1.87	0.246	0.19
18	1.1	1.5	0.54	0.22	0.29
19	1.12	1.7	0.43	0.2	0.36
20	1.18	1.13	1.09	0.25	0.21
21	1.3	1.34	0.95	0.24	0.23
22	0.98	0.95	1.05	0.24	0.24
23	0.84	2.08	0.16	0.21	0.46
24	0.78	0.72	1.18	0.24	0.23
25	1.46	1.13	1.67	0.25	0.18
26	1.7	1.7	1	0.225	0.22
27	1.7	1.13	2.25	0.225	0.24
28	1.72	3.14	0.3	0.18	0.41
29	1.6	1.94	0.67	0.22	0.29
30	1.42	1.13	1.57	0.23	0.22
31	1.5	1.18	1.6	0.24	0.22
32	0.94	1.5	0.4	0.23	0.29

Table 2.1: The table shows the experiment settings: initial stratification of the fluid (N), the disk angular velocity Ω. The last two columns show the coefficients of the power law fit for evolution of the mixed layer depth $\hat{h} = A\hat{t}^{\alpha}$.

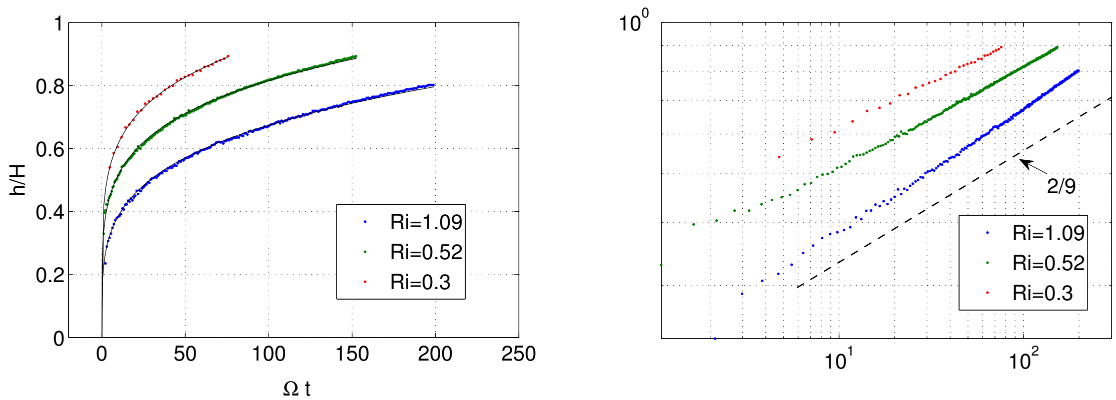

Figure 2.4: A non-dimensional depth of the primary mixed layer is plotted as a function of non-dimensional time (left) and on a log-log plot (right). The dashed line shows a 2/9 power law on a log-log plot

2.2.3 Development of the primary mixed layer

As was described earlier, a mixed layer forms at the disk and expands into the fluid reaching the thickness of the order of the tank size. It will be referred to as the primary mixed layer. In certain cases, there are other layers that form below it (secondary mixed layers) which are of smaller scales and have much weaker interfaces. These will be discussed in the next section.

For many geophysical applications it is important to know the growth of the primary mixed layer with time as it controls the distribution of tracers as well as the dynamics of the flow . To present the observations, the mixed layer depth h is non-dimensionalized by the depth of the fluid ($\hat{h} = h/H_w$), and time t by the period of rotation of the disk ($\hat{t} = \Omega t$). Figure 2.4(left) shows the time evolution of the primary mixed layer for typical experiments: the layer grows rapidly at first, then the growth slows down due to the increasing density jump at the base of the layer. Figure 2.4(right) shows the thickness of the layer as a function of time on a log-log plot with a corresponding linear fit (coefficient of determination $R^2 = 0.89$). This fit suggests a power law $\hat{h} = A\hat{t}^{\alpha}$, where A and α presumably are functions of the Richardson number - the control parameter of the experiment. Indeed, Figure 2.5 shows that there is a particular dependence of the fit coefficients on the Richardson number. The power α stays relatively constant at a value of 0.22 with some trend towards smaller values at lower Richardson numbers. The coefficient A of the fit seems to scale with the Richardson number as $A \sim Ri^{-0.33}$ as shown in Figure 2.5(right). Thus, the experimental data shows that the non-dimensional mixed layer depth scales as $\hat{h} \sim Ri^{-0.33}\ \hat{t}^{0.22}$.

To understand the obtained dependence of the mixed layer depth evolution, consider the energy balance of the system. The source for the generation of the mean flow as well as the mixing of the stratified fluid is the power produced by frictional stress due to motion of the disk. It scales as $P \sim \tau U \sim U^3$, where $\tau \sim U^2$ is the frictional stress and U is the characteristic azimuthal velocity of the mixed layer near the disk. Further, a linearly stratified fluid that was mixed to a depth h would have its gravitational potential energy increased by $\Delta GPE = \int_{-h}^{0}(\rho - \rho_0) gz dz \sim N^2 h^3$, where ρ_0 is the initial linear density profile and ρ is the value obtained by adiabatic mixing the initial profile within the layer of thickness h. At last, the kinetic energy of the mixed layer would scale as $KE \sim U^2 h$ and the dissipation D is assumed to be proportional to the energy production ($D = \gamma P$). Thus, the energy balance is described by the following equation:

$$\frac{d}{dt}(KE + PE) = P - D \Rightarrow \frac{d}{dt}(U^2 h + N^2 h^3) \sim U^3$$

At this point, an assumption is made that the flow reaches a state where the kinetic energy of the mixed layer approaches a constant value and the energy input redistributes between potential energy and dissipation. If $KE = const$ then $U \sim h^{-1/2}$ and the energy balance model becomes $h^2 h_t \sim h^{-3/2} \Rightarrow h \sim t^{2/9}$. The obtained power law for the growth of the mixed layer is consistent with observations since they indicate a power of 0.22 (Figure 2.5). The dependence of the fitted coefficient $A \sim Ri^{-1/3}$ suggests that the assumed constant value of the kinetic energy is a function of Ri as well. This relation,

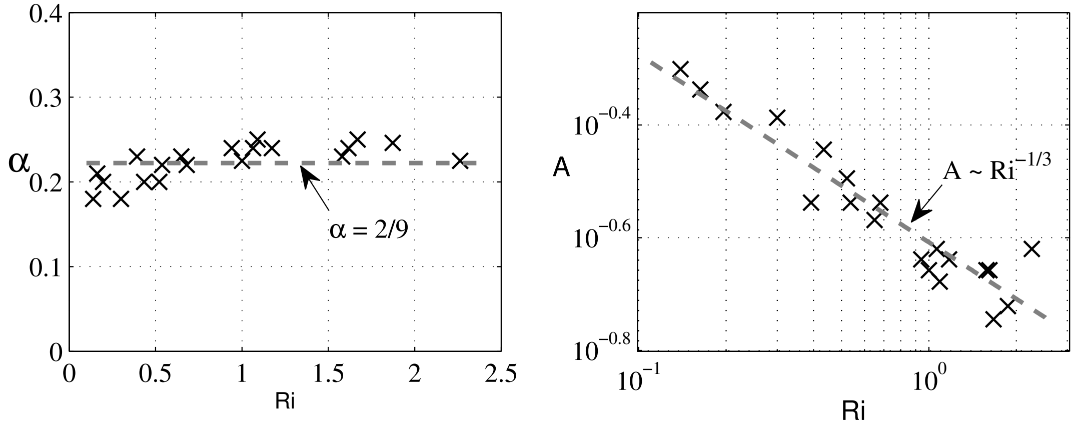

Figure 2.5: Coefficients of the power fit for the depth of the mixed layer are plotted as functions of Ri. On the left is the coefficient $\alpha = \alpha(Ri)$; coefficient $A = A(Ri)$ plotted on a log-log scale (right).

could not be determined based on the simple energy balance model. The assumptions made in constructing an energy balance could be verified with measurements of the velocity of the fluid using, for example, PIV techniques. In the current experiment these measurements were not produced, but for further progress they are of vital importance.

2.2.4 Entrainment coefficient

One of the relations that are of fundamental importance in geophysical flows is the dependence of the entrainment coefficient on the interfacial Richardson number defined here as:

$$Ri = g\frac{\Delta\rho}{\rho_0}\delta/U^2 \tag{2.1}$$

where δ is the interface thickness (found to be constant in time for all experiments) and $\Delta\rho$ is the density jump across the primary mixed layer.

The interfacial Richardson number increases with time as the density jump across the mixed layer base increases whilst the velocity jump decreases. Higher interfacial Richardson numbers are indicative of suppressed turbulence regime. The turbulence, however is not completely gone and there is still some entrainment occurring at very high Ri numbers. Note, that interfacial Richardson number should not be confused with the initial Richardson number used earlier which is a constant for an experiment as it is based on the initial stratification and rotation rate of the disk.

There has been a vast amount of experimental work to measure this dependence directly as well as indirectly, with various results obtained in different set-ups but most of them suggesting a power law relation. In our experiments the scaling of entrainment arises naturally after making the assumption of a constant kinetic energy. Defining the entrainment coefficient as $E = \dot{h}/U$ we require that it should be a function of the local Richardson number and it should be a universal law valid for all of the experiments (i.e. independent of time and N/Ω).

We begin by identifying the appropriate scaling for the time evolution of the interfacial Richardson number $Ri \sim N^2\delta h^2 \sim t^{4/9}$, as well as for the entrainment coefficient $E \sim h^{1/2}\dot{h} \sim t^{-6/9}$, where we made use of the empirical fact that $h \sim t^{2/9}$ and the assumption of a constant kinetic energy $U \sim h^{-1/2}$. Now it is clear that the scaling law for entrainment should be in this form:

$$E \sim Ri^{-\frac{3}{2}}. \tag{2.2}$$

The result agrees with a number of studies; however, there have been various results obtained for different experiments with power laws ranging approximately from -1 to -2.

Given the obtained scaling we can identify how the kinetic energy should scale with Ω and N. For our calculations we take $KE = hU^2 = f(N, \Omega)$. Now we keep track of all the constants involving N and Ω. Recall that,

$$Ri = \frac{N^2h^2}{2f} \quad and \quad E = h^{1/2}\dot{h}/f^{1/2} \tag{2.3}$$

and then use the expression for h:

$$h/H = a(N/\Omega)^{-2/3}(\Omega t)^{2/9} \tag{2.4}$$

$$\begin{aligned} Ri^{-3/2} \quad &\sim [\delta N^2(aH(N/\Omega)^{-2/3}\Omega^{2/9})^2]^{-3/2} f^{3/2} && (2.5)\\ E \quad &\sim (aH(N/\Omega)^{-2/3}\Omega^{2/9})^{3/2} f^{-1/2} && (2.6) \end{aligned}$$

the two should be equal to within a constant multiplicative factor:

$$f(N,\Omega) \sim \Omega^2 H^{9/4}\delta^{3/4}, \tag{2.7}$$

quite a curios result that the kinetic energy reaches a constant which is independent of the initial stratification of the fluid. This is a testable prediction of our theory and it would be great it someone would check if it is valid.

One other implication of this derivation is that we now are able to plot the interfacial Ri number for all of the experiments, defined up to an unknown multiplicative constant (universal for our experiments):

$$Ri \sim \frac{N^2}{\Omega^2}(\frac{\delta}{H})^{\frac{1}{4}}(\frac{h}{H})^2 \tag{2.8}$$

2.2.5 Dynamics of a secondary mixed layer

We also observe secondary mixed layers which are ubiquitous in our high Ri number experiments. These could be easily seen in density profiles which show a typical pattern: below a strong primary interface separating a well mixed turbulent boundary layer from an almost stationary linearly stratified layer there is a small mixed layer and a secondary interface at the bottom of it(Fig. 2.3). The interfaces are best viewed by plotting the buoyancy frequency which has a strong peak at the location of the interface and substantially reduced values in the mixed-layer regions. To better view their temporal evolution we plot the buoyancy frequency N in the moving ref-

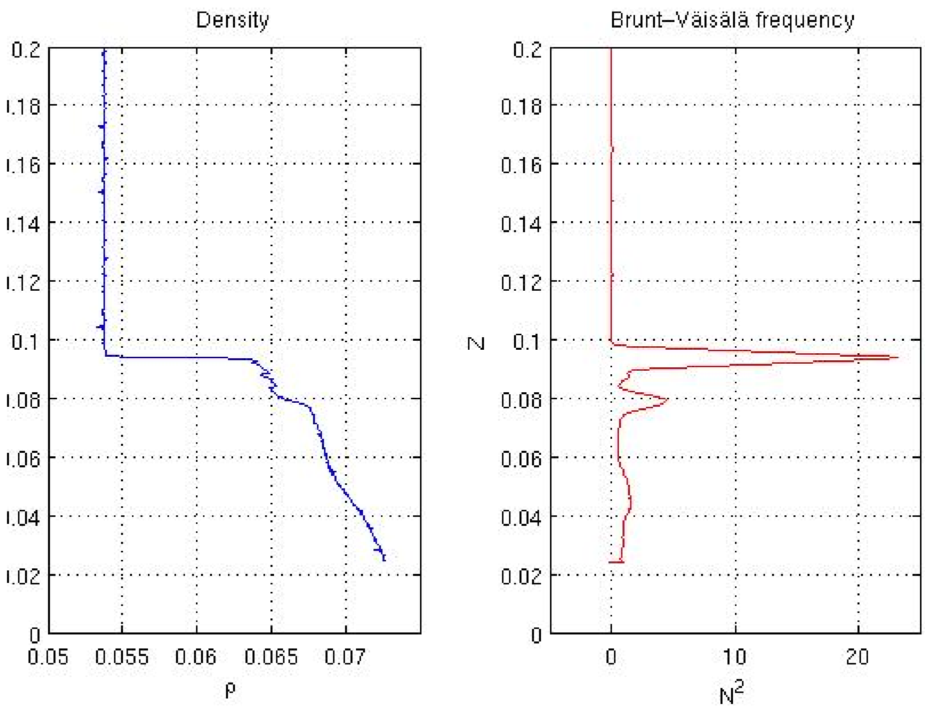

Figure 2.6: A typical density profile containing a primary mixed layer as well as a secondary one (left).Brunt–Väisälä frequency showing peaks at the bases of mixed layers.

erence frame following the location of the primary interface such that its coordinate stays constant at $z = 0$ (Fig. 2.7). These secondary interfaces are much weaker then the primary one (note the logarithmic scale of N on Fig. 2.7) and are persistent with time scales ranging from about minutes to multiple hours. When the interface Ri number is small ($Ri < 0.3$), the primary interface deepens fast accompanied with a highly turbulent layer which tends to destroy the existing secondary layers making their life time considerably shorter (less then 2 minutes, which is not resolved by our observations). For higher Ri numbers ($0.3 < Ri < 1$) we see clear formation of the staircases with consequent slow time scale drift either towards or away from the primary interface with consequent merger or decay (Fig. 2.7a,b); for even higher Ri numbers ($Ri > 1$) we observed the locked states where the secondary staircases do not drift or decay for multiple hours and move along with the primary interface till the end of the experiments (Fig. 2.7c).

We attribute the existence of the secondary mixed layers to the Phillips type instability that arises in stratified turbulent flows. A simplified view of the instability was described within a set-up of a linearly stratified turbulent fluid where the arising non uniformity in turbulent eddy energy led to a dependence of the vertical buoyancy fluxes on a local Richardson number ($Ri = U_z/b_z$). Assuming there exists such a law $f_b = F(Ri)$ relating the equilibrium buoyancy flux f_b to the local Ri number and applicable throughout the experiment, then the shape of this curve would dictate the stability of such flow. If $F(Ri)$ is a non-monotonic function, then the regions where the buoyancy flux decreases with increasing Ri number would be unstable as small perturbations in buoyancy gradient would grow. The shape of this hypothetical curve is related to the production and transfer and dissipation of the turbulent energy - processes which are not well understood or parametrized. Instead, this description represents a useful phenomenological view on these processes. How does this instability relate to the observed secondary interfaces?

In our experiments the observed turbulence is significantly reduced at the primary interface, however it is still present in about 1-2 cm below the interface. Horizontal velocities are also known to penetrate through the stratification jump (Fig. 2.2). Furthermore, the eddy kinetic energy concentrated in the primary mixed layer leaks through the base of it providing a source of energy to affect the stratification below the primary interface. The density profiles in this interfacial region represent a transition from a strong buoyancy gradient at the primary interface to a linear stratification (constant N^2) below it. These conditions allows for a generation of Phillips-type instabilities provided that the non-monotonic shape of the buoyancy flux curve is appropriate.

The dynamics of the secondary mixed layers is extremely complicated. Understanding it to a level of making predictions requires a precise theoretical model bucked up by extensive observations of not only density but also velocity fields, turbulent buoyancy and momentum fluxes. However, due to time and equipment constraints these elaborate measurements could not be performed. Thus, the theoretical part of this research will be focused on explaining the formation of secondary layers in an idealized phenomenological framework.

2.3 Phenomenological model

Secondary mixed layers arise in a stratified fluid that is subjected to the action of a turbulent flow with a mean shear. The turbulent nature of the flow is the key to understanding the phenomenon. The proposed mechanism is as follows. The sheared mean flow driven by the rotating disk is a source of turbulent motion which is inhomogeneously distributed within a stratified fluid depending on its stratification. The buoyancy itself is affected by turbulent fluxes. Thus, the formation of the layers could be related to the instability of the turbulent flux-buoyancy relation as was first proposed by Phillips [1972]

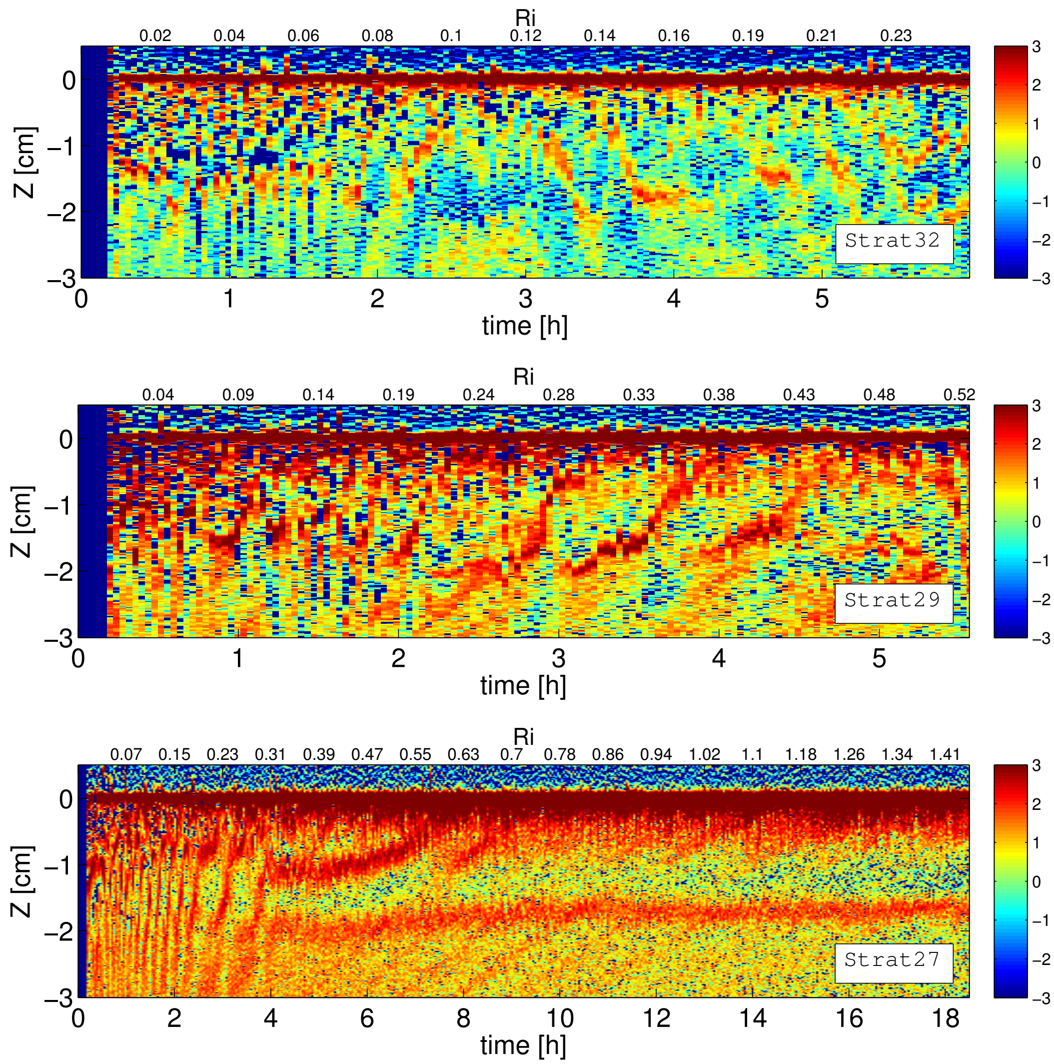

Figure 2.7: Time evolution of the buoyancy frequency for the region below the primary interface (located at z=0) in experiments with Ri numbers 0.39, 0.68, and 2.26 (from top to bottom correspondingly). Logarithmic scale is used for the color bar. Note the development of secondary interfaces and their persistence for long time scales.

and Posmentier [1977]. Suppose, the evolution of buoyancy b is controlled by the divergence of the downward turbulent buoyancy flux F:

$$\frac{\partial b}{\partial t} = \frac{\partial F}{\partial z}$$

and this flux is a function of the buoyancy gradient $F = F(b_z)$. The equation has obvious steady state solutions with constant flux; however, such solutions were unstable if the flux would be a decreasing function of buoyancy gradient *i.e.* $\frac{\partial F}{\partial b_z} < 0$. Figure 2.8 shows the mechanisms of the instability. A linear steady state buoyancy profile (dashed line) has a value of buoyancy gradient that corresponds to a negative vertical derivative of the buoyancy flux. After introducing a small perturbation (black line) there will appear anomalous buoyancy fluxes (blue arrows). In regions where the perturbations have higher buoyancy gradient the anomalous flux is negative and it is positive in regions of lower gradients. As could be seen from the evolution equation the current distribution of the buoyancy fluxes would lead to a growth of the initial perturbation, meaning that the base state is unstable. This instability would lead to buoyancy profiles consisting of a series of mixed layers separated by strong interfaces (staircases). In the case of $\frac{\partial F}{\partial b_z} > 0$ the created fluxes would lead to the decay of the buoyancy anomaly - this state is stable.

This model considers the buoyancy equation only and assumes a particular shape of the flux-gradient curve. However, the exact form of this curve would depend on particular mixing mechanisms that create the turbulent buoyancy fluxes. In the following section a gradient-type mixing model will be devised to describe the development of buoyancy profiles under the action of the mean flow-generated turbulence. The formation of the layers in the model would be related to the mechanism described above by calculating the exact form of the flux-gradient relation. The model would consist of evolution equations written for buoyancy as well as for turbulent kinetic energy that is drained from the mean flow. The aim is to describe the secondary mixed layers only, so it is assumed that the primary layer has been formulated and

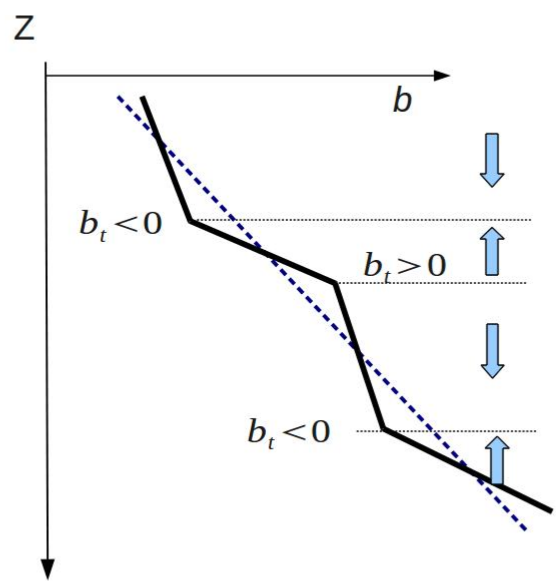

Figure 2.8: Schematic representation of the instability mechanism that leads to layer formation. Dashed line represents the initial buoyancy profile, black line is the slightly perturbed profile, anomalous buoyancy fluxes denoted by blue arrows.

the mean velocity profile is established.

2.3.1 Model formulation

The approach taken in constructing a mixing model is similar to that implemented by Balmforth et al. [1998] and Barenblatt et al. [1993]. The model parameterizes turbulent vertical transports as gradient transports using eddy diffusivity and viscosity. Thus, the conservation laws for horizontally averaged buoyancy b and turbulent kinetic energy e are as follows

$$\frac{\partial b}{\partial t} = \frac{\partial}{\partial z}(\kappa\frac{\partial b}{\partial z}) \tag{2.9}$$
$$\frac{\partial e}{\partial t} = \frac{\partial}{\partial z}(\kappa\frac{\partial e}{\partial z}) + S, \tag{2.10}$$

where S is a source term for the energy and κ is the turbulent diffusivity. The source term represents production and destruction of the turbulent energy and in this formulation consists of four terms:

$$S = -\kappa b_z - \alpha\frac{e^2}{\kappa} + \frac{1}{1+Ri}\kappa {U_z}^2 + \frac{Ri}{1+Ri}U^2 e^{1/2} l^{-1} \tag{2.11}$$

As mentioned previously, the mixing of buoyancy leads to an increase in the gravitational potential energy of the system. Thus, the role of the first term $(-\kappa b_z)$ is to convert the eddy kinetic energy into potential energy preventing the artificial accumulation of the total energy $E = \int_0^H (e - bz)dz$. The second term $-\alpha\frac{e^2}{\kappa}$ is the dissipation, which is on dimensional grounds proportional to the energy e and to the inverse of the eddy turnover time $\tau \sim \kappa/e$; α is a small parameter which controls the intensity of the dissipation and effectively defines the number of turnover periods over which an eddy would dissipate. The last two terms are the production terms due to the action of a mean flow. From visual observations of the experiments there seem to be two mechanisms in action. At low local Richardson numbers ($Ri = N^2/{U_z}^2$), where the destabilizing effect of the shear is dominating the stabilizing effect of the stratification, the turbulence is generated due to Kelvin-Helmholtz type instabilities. These instabilities, however, are suppressed at high Ri. Hence, the representation of the energy production is of the form $\frac{1}{1+Ri}\kappa {U_z}^2$. At high Ri the turbulence is generated by the mean flow acting on turbulent eddies (vortex scraping) by inducing a frictional stress. The amount of power introduced by such a mechanism is proportional to $U^2 e^{1/2} l^{-1}$, where U^2 is scaling for the stress exerted by the mean flow, $e^{1/2}$ is a characteristic velocity of an eddy and l is its length scale. Factors $\frac{Ri}{1+Ri}$ and $\frac{1}{1+Ri}$ are chosen to ensure that the two mechanisms would act in their corresponding regime of Richardson numbers.

Eddy diffusivity, as well as viscosity, is[1] proportional to $le^{1/2}$. To close the system the characteristic eddy size l needs to be defined. Since the model aims to describe mixing in the stratified fluid there are several length scales involved. In the limit of strong stratification the size of eddies would be proportional to the Ozmidov's length scale $(e/b_z)^{1/2}$. This restriction comes from the fact that eddies overturn density layers leading to increase in potential energy. Thus, for a given energy of an eddy and the ambient stratification there would be a restriction on its size. In the limit of weak stratification, the characteristic length scale for an eddy $l = d$ should be related to the geometrical parameters *i.e.* the size of the tank[2]. Thus, to interpolate the two length scales in the limits of strong and weak stratifications expression for the eddy length scale l is chosen to be

$$\frac{1}{l^2} = \frac{1}{d^2} + \gamma \frac{1}{e/b_z} \tag{2.12}$$

where γ is a parameter that determines the length scale in the limit of strong

[1]For simplicity eddy viscosity and diffusivity are taken to be the same, however this assumption could be relaxed

[2] A restriction of the length scale in the weakly stratified case avoids singularities in the model.

stratification. It should be pointed out that the model is written in terms of locally defined dynamical variables, meaning that all the scales are controlled by local dynamics and do not depend on global profiles of the variables. However, this doesn't always take place in reality. For example, the model used for the eddy length scale states that in the case of locally weak stratification the length should be equal to d - some geometrical restriction. However, vertical profiles of stratification containing mixed layers bounded by strong stratification would impose an equivalent 'geometrical' constraint on an eddy size in the location within the mixed layer - the eddy size could not be greater than the thickness of a mixed layer with strong interfaces. Thus, the parameter d should be considered as an effective one that takes into account geometrical constrains as well as the global buoyancy profile. In the current model, for simplicity it is assumed to be constant.

The resulting model is effectively a set of coupled nonlinear diffusion equations, which require boundary and initial conditions to be completed. As boundary conditions, the fluxes of energy and buoyancy are set to be zero at the top and the bottom boundaries of the domain e.i. $e_z = 0, b_z = 0$ at $z = 0, H$. The initial conditions will be discussed in a section 2.3.3. Thus, the complete equation set of the mixing model is the following:

$$b_t = (\kappa b_z)_z \tag{2.13}$$

$$e_t = (\kappa e_z)_z - \kappa b_z - \alpha \frac{e^2}{\kappa} + \frac{1}{1+Ri}\kappa {U_z}^2 + \frac{Ri}{1+Ri} U^2 e^{1/2} l^{-1} \tag{2.14}$$

$$\kappa = l e^{1/2} \tag{2.15}$$

$$\frac{1}{l^2} = \frac{1}{d^2} + \gamma \frac{1}{e/b_z} \tag{2.16}$$

$$Ri = \frac{b_z}{{U_z}^2} \tag{2.17}$$

where α, γ, d are fixed parameters; characteristic velocity U and velocity shear U_z represent the forcing for this system and are assumed to be constant.

In principle, the above equations could be combined to give an evolution equation for the turbulent diffusivity κ - the variable that determines the evolution of the buoyancy profile.

Since the purpose of the model is to describe the formation of mixed layers it is convenient to use the buoyancy gradient ($g = b_z$) instead of buoyancy as a dynamical variable. The mixed layers have a distinct signature in the buoyancy-gradient profile: low values within the mixed layer and sharp peaks at the interfaces. Further, it is useful to use a non-dimensional equation set with the following definition of dimensionless quantities:

$$\hat{t} = \frac{Ut}{\gamma d}, \quad \hat{z} = \frac{z}{\gamma^{1/2} d}, \quad \hat{e} = \frac{e}{U^2} \quad \hat{g} = g\frac{\gamma d^2}{U^2}, \quad \hat{l} = \frac{l}{d}, \quad Q = (\frac{U}{U_z d})^2 \tag{2.18}$$

In dimensionless form the equations are

$$\begin{aligned}
g_t &= (\kappa g)_{zz} && (2.19)\\
e_t &= (\kappa e_z)_z - \kappa g - \alpha\gamma\frac{e^2}{\kappa} + \frac{\gamma\kappa + Qg^{3/2}}{1 + g/\gamma} && (2.20)\\
\kappa &= \frac{e}{(e+g)^{1/2}} && (2.21)\\
b.c. &: \; e_z = 0, g = 0 \; at \; z = 0, H && (2.22)
\end{aligned}$$

where the parameter Q describes the relative importance of the mean flow and the mean shear in the energy production term; the local Richardson number is proportional to the buoyancy gradient only ($Ri = g/\gamma$).

2.3.2 Steady states and their stability

Consider the model steady states that have a constant energy and buoyancy gradient $(e_0, g_0) = const$. These violate the boundary conditions, nonetheless away from the influence of the boundaries it is useful to consider their

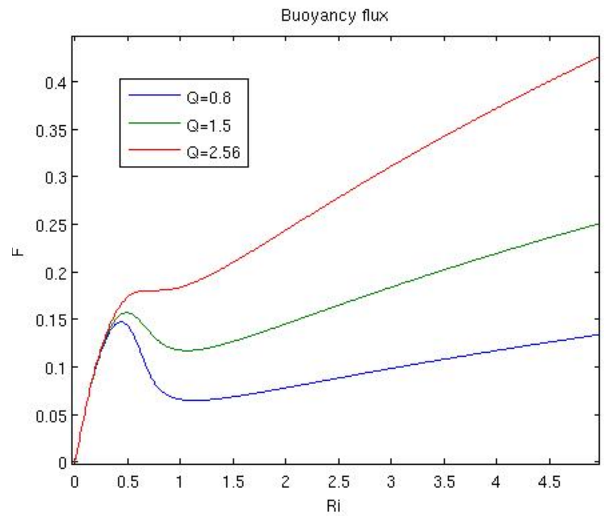

Figure 2.9: Steady-state buoyancy flux plotted as a function of the Richardson number for the three representative values of the forcing parameter Q.

stability. Such steady states should have no production of turbulent kinetic energy ($S = 0$) in order for dynamic variables not to change with time:

$$-\kappa_0 g_0 - \alpha\gamma \frac{e_0^2}{\kappa_0} + \frac{\gamma\kappa_0 + Q g_0^{3/2}}{1 + g_0/\gamma} = 0 \tag{2.23}$$

$$\kappa_0 = \frac{e_0}{(e_0 + g_0)^{1/2}} \tag{2.24}$$

This sets a constrain, which effectively defines energy and buoyancy flux as a function of buoyancy gradient (or Richardson number) for the considered steady-state solutions:

$$e_0 = E(g_0) \tag{2.25}$$

$$\kappa_0 g_0 = F(g_0) \tag{2.26}$$

As was discussed earlier, instabilities develop if the initial profile has the Richardson number which is within the range of the negative slope of the buoyancy flux. Figure 2.9 shows the steady state buoyancy flux as a function of Richardson number ($Ri = g/\gamma$). The numerical values of parameters are chosen as $\alpha = 0.1, \gamma = 0.2$. The representative mean flow parameter $Q = 0.8, 1.5, 2.56$. Curves with values of $Q < 2.56$ show a non-monotonic behavior, having a region where the derivative of the flux is negative. At low values of Ri, the instabilities are not possible due to extremely high turbulent energy created by shear instabilities that are not suppressed by the stratification. At high Richardson numbers the buoyancy flux is controlled by the turbulence produced by the mean flow which is proportional to $g^{1/2}$, hence the increase of the buoyancy flux with the increase in stratification. However, the shear production term is $\sim e/g^{3/2}$, which means that there is strong penalty in energy production for an increase in stratification - hence the turbulent flux due to shear production should decrease with the stratification at high Richardson numbers. Thus, the effect of the mean shear tends to destabilize the system and create mixed layers, whereas the mean flow turbulence has a stabilizing effect. Hence, in the intermediate range of Ri numbers the slope is negative due to shear production term; however, this region is of finite size due to the action of the mean flow turbulence at higher values of Ri. This means that the instability could not grow unbounded in time: at some point the effect of the mean flow turbulence would suppress the growth. Thus, the existence and development of instabilities depend crucially on the relative importance of the mean flow to shear production terms which is determined by the value of the parameter Q. If the forcing Q is greater than 2.56 the flux-gradient curve monotonically increases with the value of Richardson number - the stabilizing effect of the mean flow is dominant. For such forcing all the buoyancy profiles would be stable.

The described instabilities can now be identified from the formulated model equations and their growth rates can be quantified. Linearizing the equations around the basic state (e_0, g_0) and assuming exponentially growing solutions for perturbations $(\hat{e}, \hat{g}) \sim exp(\lambda t - ikz)$ leads to a linear stability problem:

$$\lambda \begin{pmatrix} \hat{g} \\ \hat{e} \end{pmatrix} = \begin{pmatrix} -k^2 f_g & -k^2 f_e \\ S_g & -k^2\kappa + S_e \end{pmatrix} \begin{pmatrix} \hat{g} \\ \hat{e} \end{pmatrix}$$

where $f = \kappa g$ is the buoyancy flux, S is the source term in the energy equation and all the partial derivatives are calculated at the point (e_0, g_0). Thus, for a given value of parameter Q and an initial value of the Richardson number a growth rate λ can be calculated as a function of the wavenumber k. Figure 2.10 shows growth rates calculated for $Q = 1.5$ and for values of base state $Ri = 0.3, 0.7, 1.3$. The growth rate is positive for $Ri = 0.7$ which is located at the negatively sloped part of the flux curve (Figure 2.9). The growth rate is negative for the values of Richardson numbers of 0.3 and 1.3 that belong to the monotonically increasing part of the slope - these are stable solutions. An important property of the written model is that in the case of the unstable steady states the growth rate of the perturbations has a high wavenumber cutoff[1] which means that small scale perturbations do not grow with time - instead, they decay. This property allows direct numerical simulations of the development of the instabilities and their evolution leading to the formation of the mixed layers.

2.3.3 Numerical simulations

Numerical simulations of the mixing model were performed using a second order vertical discretization scheme and a first order time forwarding with an adaptive time stepping. The computational domain is $z = [0, 1200]$ having 600 uniformly distributed grid points. Initial conditions for the numerical

[1]The high wavenumber cutoff is due to the diffusion of the turbulent kinetic energy

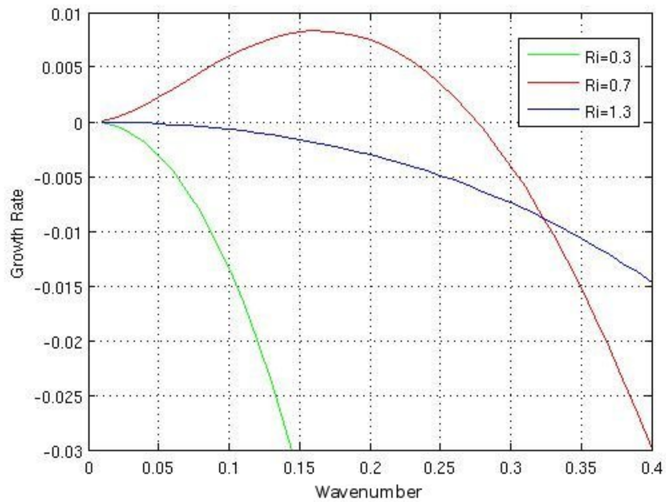

Figure 2.10: Growth rate plotted as a function of the wavenumber for different values of the base state Richardson numbers and for a fixed parameter $Q = 1.5$ (as predicted by the linear stability analysis).

simulation are chosen to be $Ri = 0.8$ for the buoyancy profile[1], $e = 0.01$ for the turbulent kinetic energy and the forcing parameter $Q = 1$. Based on a linear stability analysis such a configuration should be unstable. Indeed, the numerical simulations confirm it. Figure 2.11 shows snapshots of the modeled Ri at different times - it is clearly seen that the instabilities are developing in the form of sharp peaks in buoyancy gradient profiles. First, the instabilities develop close to boundaries because there are larger perturbations from the steady state there. Then, they appear in the interior and eventually fill the whole domain except for small regions adjacent to boundaries which are affected by zero flux boundary conditions.

Figure 2.12 shows a snapshot of the buoyancy gradient g, turbulent kinetic energy e and a corresponding buoyancy flux f. The buoyancy flux seems to be

[1] To satisfy initial conditions at the boundaries the distribution of Ri was chosen such that it is constant within the interior of the domain and continuously approaches zero at the boundaries.

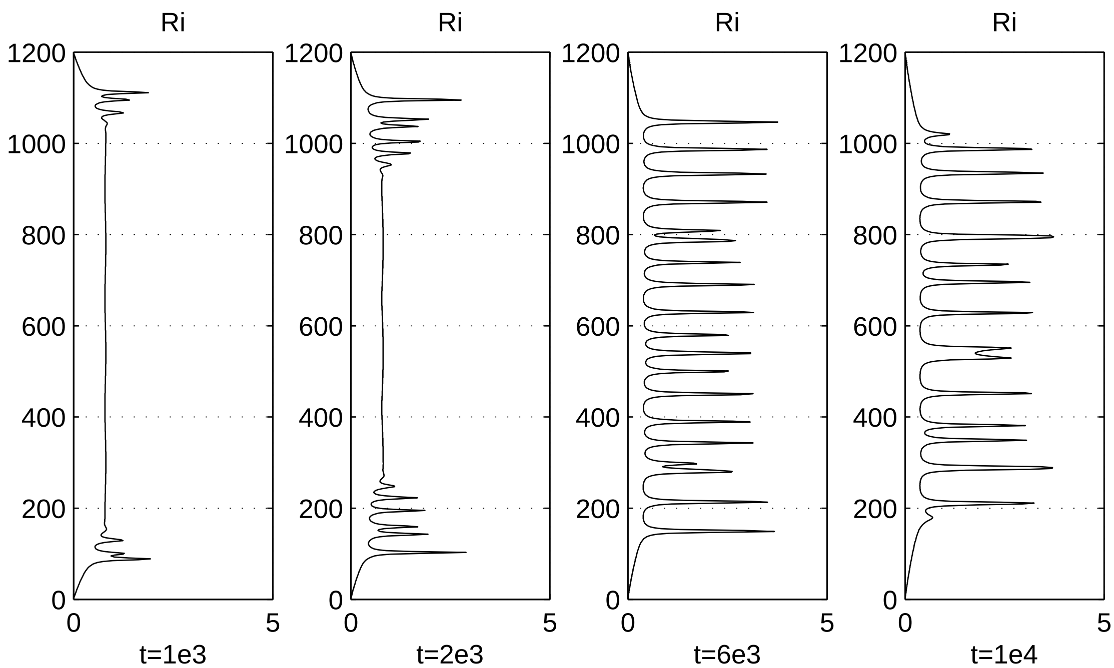

Figure 2.11: Numerically simulated evolution of the instabilities manifested in the vertical profiles of the Richardson number. Low Ri numbers correspond to mixed layers (weak stratification) and the location of sharp peaks correspond to interfaces between the layers (high stratification).

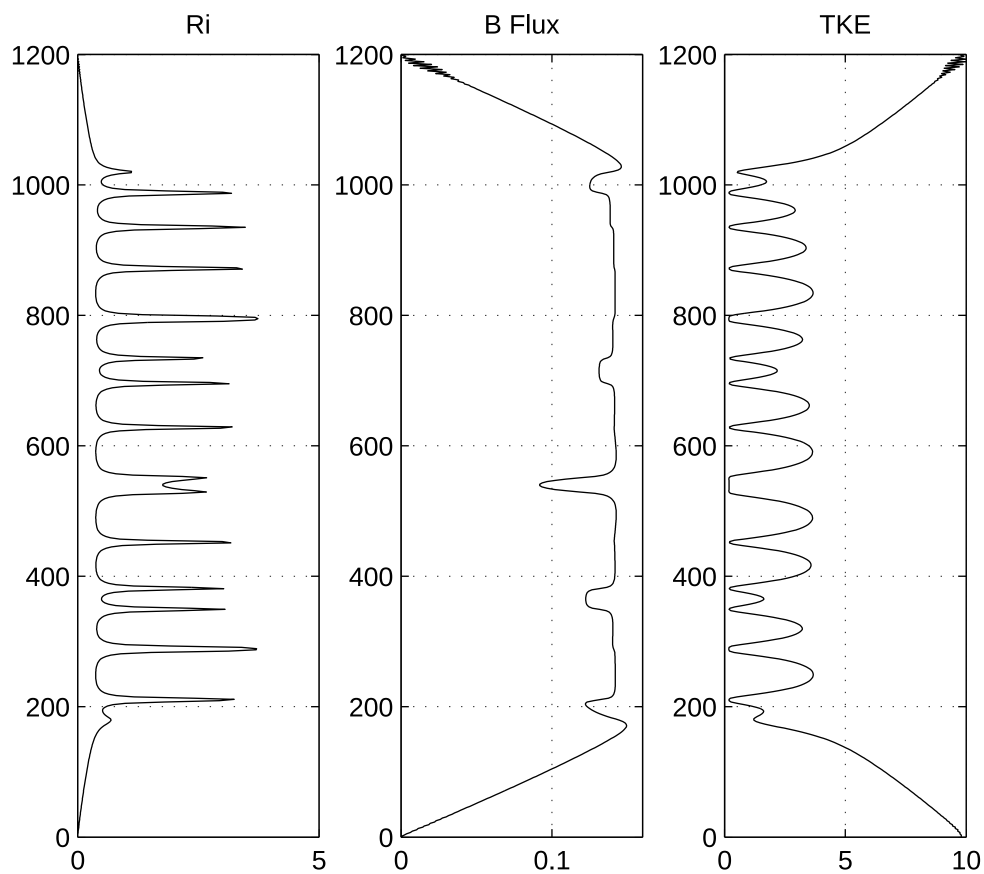

Figure 2.12: A snapshot of model variables at $t = 1e4$: Richardson number (or buoyancy gradient) (left), buoyancy flux (middle) and turbulent kinetic energy (right) plotted as a functions of depth.

relatively constant in the interior region, but with isolated regions of low flux. The energy distribution is higher in the regions of weak stratification and has minimums inside highly stratified interfaces. The instabilities develop having a wavelength corresponding to the one that has a maximum growth rate predicted by linear stability analysis. However, it has been observed that after the initial development stage the structure tends to coarsen with time by merging or decaying mechanisms. The individual peaks are quasi-steady solutions of the equations and evolve by weakly interacting with each other. The result of the interaction could be considered as a secondary instability that leads to the coarsening through erosion or collision of the adjacent interfaces Radko [2007]. The time scales for the two instabilities would depend on the base.

Figure 2.13 shows the time evolution of the buoyancy gradient and the buoyancy flux throughout the whole simulation. The initial development stage lasts till the time $t \approx 4000$ and is characterized by the formation of the peaks in buoyancy gradient. The overall structure, however, tends to coarsen. The peaks either merge with each other creating higher and broader peaks, or they decay in amplitude and disappear amplifying the adjacent peaks (Figure 2.13, top). The flux on the other hand, started from an initial condition that has a weak constant value within the interior and after the instabilities have developed its value also remained constant, but at a higher value (Figure 2.13, bottom). Note that the merging and decaying events are accompanied by a transient decrease in buoyancy flux. This is clearly seen at Figure 2.12, where, for example, the double peaks at $z \approx 550$ or $z \approx 750$ are about to merge and the corresponding values of the buoyancy flux are decreased. The edge regions which are characterized by weak stratification and buoyancy flux are continuously growing free of instabilities. The end result of such a simulation is the full homogenization of the buoyancy, since the system is forced by the mean flow which is a continuous source of turbulent mixing.

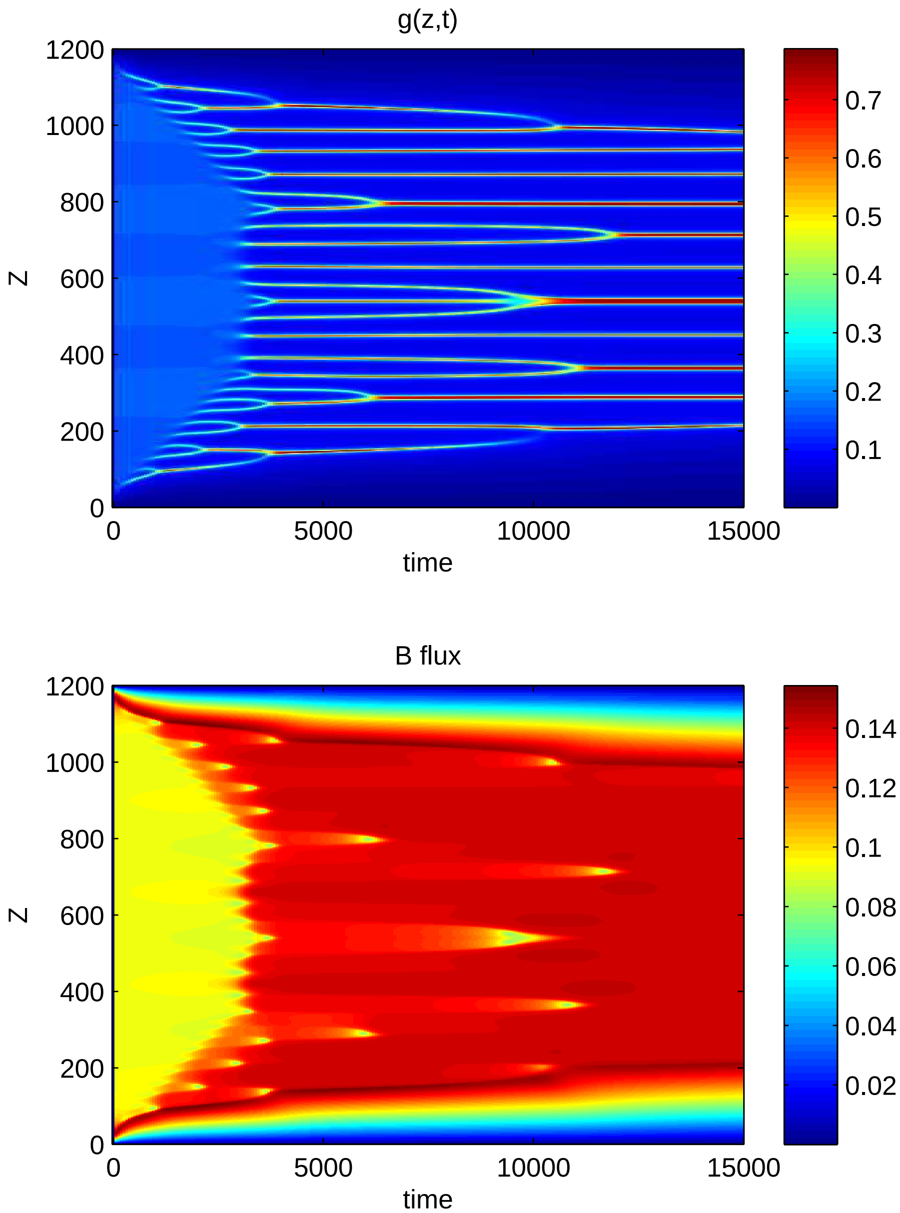

Figure 2.13: Time evolution of the modeled vertical profiles of the Richardson number (top) and the buoyancy flux (bottom). Note, that the development of interfaces leads to increased buoyancy flux and the mergers of interfaces correspond to the its transient reduction.

The numerical simulation, showed that a series of mixed layers could form in a region subjected to the action of the mean flow turbulence. However, the simulation was performed in an idealized setting so that it could confirm the results of the linear analysis of the stability of the model. The model shows the mechanism of layer formation only conceptually. In reality, there are many more factors that contribute to the evolution of the layers. First of all, the mixing model uses constant characteristic shear and the mean flow as a mechanisms for the generation of turbulence. However, the mean flow is affected by changes in stratification and should be accounted for in the model if the instabilities develop at a similar time scale as the variations in mean flow. Furthermore, in the experiments there is a nonuniform buoyancy gradient profile, as it has a dominant peak at the base of the primary mixed layer. The existence of this layer affects the evolution of the adjacent secondary mixed layers. Nonetheless, the model shows the important features of the evolution of the secondary mixed layers: spontaneous generation of the layers, the merging of the layers and their decay - all of which have been observed in the experiments. Even though the proposed model simulates behavior similar to the observations, the assumption of the model should be verified experimentally - this would require elaborate measurements of the mean flow as well as that of the turbulent buoyancy and momentum fluxes.

2.4 Discussion

A series of experiments were performed on a linearly stratified fluid subjected to the surface frictional stress induced by a rotating disk. The control parameters for the experiments were the magnitude of the stratification (N^2) and the rotating speed of the disk (Ω) resulting in a single non-dimensional parameter $Ri = N^2/\Omega^2$. Two types of mixed layers have been observed - the primary layer extending from the surface into the interior of the fluid, and the secondary mixed layer of much smaller scale that forms underneath it. The growth of the primary layer with time seems to obey a power law $\hat{h} \sim Ri^{-1/3}\hat{t}^{2/9}$. This result is consistent with the energy balance model that assumes a constant kinetic energy withing the layer.

The secondary mixed layers show a complicated behavior, having several regimes depending on time and the Richardson number of the experiment. A physical mechanism for the formation of the secondary mixed layers has not been clearly identified from the observations due to the lack of observational data, namely of the turbulent fluxes and the mean flow. Nonetheless, the hypothesis has been put forward that relates the formation of these layers to an instability of the flux-gradient type that could arise in stratified turbulent flows. A one dimensional mixing model has been devised and the instabilities were investigated theoretically as well as through numerical simulations. The resulting mixed layers form only in a particular regime that puts constraints on the magnitude of the mean flow with respect the its shear and the Richardson number for the profile. Furthermore, the dynamics predicts the destruction of the mixed layers through merging and decay - the processes observed in experiments.

Based on the mixing model, the results of the experiments could be interpreted as follows. Supported by the disk generated turbulence, the primary mixed layer grows creating a large density gradient at its base. At the same time, the mean flow is established within the primary layer. The flow is suppressed as it reaches high stratification and thus the shear is created at the base of the mixed layer. This sets a particular value of the model parameter Q, which reflects the relative importance of the mean flow to the mean shear. The magnitude of the flow as well as of its shear changes with time as the mixed layer grows, meaning that Q is a function of time as well as space. The formation of the secondary mixed layers below the primary is observed when the necessary conditions for the instabilities are met: the parameter Q is smaller then the critical value, and the local Richardson numbers belong to the unstable part of the flux-gradient curve. Such a constrain identifies a confined region in a fluid where the instabilities could occur. The instabilities within this region lead to the development of the layers; however, the magnitude of the instabilities is suppressed by the stabilizing effect of the mean flow turbulence. That explains why secondary mixed layers are not completely destratified. After the spontaneous development of the layers, comes the stage of slow evolution when the layers either merge with the primary interface or decay by erosion - consistent with the behavior of the observed layers. The change in the regime is the shift from the dominating collision instability to the erosion instability which is associated with the change in the basic state.

Chapter 3

Turbulent Entrainment in Rotating Density Currents

The material contained in this chapter has been published in the *Journal of Fluid Mechanics* under the title "Steady turbulent density currents on a slope in a rotating fluid" [Manucharyan et al., 2014].

3.1 Introduction

In fluids with horizontal density differences in a gravitational field disturbances will propagate to release the stored potential energy of their initial configuration. Such flows, variously referred to as density, gravity or buoyancy currents, are ubiquitous in geophysical, astrophysical, and engineering settings [e.g., Huppert et al., 2006; McKee and Ostriker, 2007; Monaghan, 2007; Simpson, 1999] and a principal goal in their study revolves around predicting their rate of propagation given the initial geometry and density difference. Mixing plays an important role in turbulent currents, with the flow dynamics strongly influenced by exchanges of mass and momentum with the ambient fluid. Such is the case in many turbulent atmospheric and oceanic flows, including dense overflows in the ocean [e.g. Price and O'Neil Baringer, 1994; Smith, 1975] or landfalling cold fronts in the atmosphere [e.g. Garratt et al., 1989], but these share much of the same basic physical mechanisms at play during star formation and within turbulent accretion discs [e.g. Lignieres et al., 1996; Rieutord and Zahn, 1995; Youdin and Shu, 2002]. As a particular example, dense overflows in ocean basins represent important components of the circulation, but the relevant mixing processes occur on length scales that are unresolved in climate models [e.g., Ivanov et al., 2004; Price and O'Neil Baringer, 1994]. Hence, dynamically informed parameterisations are required to characterise buoyancy-driven currents. For flow down a slope from a persistent source of buoyancy flux, the initial transient propagation of the head of the current is driven by downslope differences in hydrostatic pressure across the density-front [e.g. Shapiro and Zatsepin, 1997; Wobus et al., 2011], whilst the downslope component of the gravitational body force becomes more significant in the subsequent phase of quasi-steady propagation. It is the latter, steady phase of propagation upon which we focus here.

When the length and time scales are appropriate, the problem is complicated by the presence of the Earth's rotation that puts additional constraints on the dynamics of currents and on the efficiency of turbulent entrainment [Griffiths, 1986]. An important consequence of rotation is that large scale density currents running down the continental shelves get deflected by the Coriolis forces and eventually tend to propagate along the isobaths [Griffiths, 1986], which are contours of constant depth. The flow along an isobath is considered to be in geostrophic balance with the Coriolis force balancing the pressure gradient force. However, it has been argued that frictional forces associated with bottom Ekman layers play a key role in breaking geostrophic balance and allowing a component of the current to cascade downwards [see Shapiro and Hill, 1997, for example]. Wirth [2009] pointed out that such density currents consist of a main thick current (or vein) and a thin frictional layer below it. For flows with negligible inertia and no entrainment, Wirth [2009] showed that the dynamics of the vein is mainly geostrophic, but is modified by the presence of an Ekman layer. The Ekman layer leads to drainage of fluid from the vein into the frictional layer where it falls downslope and eventually mixes with the surrounding waters. As a result the main current slowly drifts downslope and its trajectory can be used to estimate the frictional drag [Wirth, 2011]. In this study we focus on the dynamics of the vein and, in particular, on how mixing processes affect its trajectory before reaching any geostrophically balanced state.

Mixing of ambient fluid into a dense current is often characterised in terms of an entrainment ratio $E = w_e/U$, the ratio of a mean inflow w_e normal to the interface and the mean velocity of the current U, itself depending on the instantaneous density and hence mixing. This entrainment hypothesis, introduced in the modelling of turbulent plumes [Morton et al., 1956], underlies many models of turbulent buoyancy-driven currents [see Turner, 1986, for a survey]. Such mixing can play a critical role not only in the trajectory and dynamics of a particular dense current, but also in the maintenance of stratification in the interior of an ocean basin via the "filling-box" mechanism of Baines and Turner [1969]. For example, Hughes and Griffiths [2006] and Wåhlin and Cenedese [2006] suggested that weak yet persistent entrainment into dense overflows could play a leading-order role in controlling the structure of the thermocline in the ocean interior. In the Arctic, a halocline separates warm, deep waters from the colder, fresher surface ocean and provides a barrier to vertical heat transfer that could melt the overlying sea ice cover [Carmack, 2000; Timmermans et al., 2009]. The analysis and laboratory experiments of Wells and Wettlaufer [2007] suggested that mixing rates can control whether dense currents penetrate the halocline and ventilate the deep ocean, or else intrude into the halocline and maintain the stratification via the "filling-box" mechanism. Hence, mixing in dense currents provides an important contribution to the evolution of ocean stratification, and, via the potential for feedback on sea ice melting, to the state of the climate system as a whole.

The entrainment ratio E has been parameterised on the basis of a range of laboratory data and field observations [see Turner, 1986; Wells et al., 2010, for reviews]. For currents of thickness h, reduced gravity g', and viscosity ν, flowing on a slope of angle α to the horizontal, the data show that entrainment increases with both the Reynolds number $\mathrm{Re} = Uh/\nu$, which characterizes the vigour of turbulence, and the Froude[1] number $\mathrm{Fr} = U/\sqrt{g'h\cos\alpha}$ which characterises the tendency for shear driven mixing to overcome the stabilising effect of stratification. Here U represents the relevant velocity scale along the slope, and for flows in pure geostrophic balance would correspond to the Nof velocity $U_{\mathrm{geo}} \sim g'\tan\alpha/f$, where f is the Coriolis parameter [Nof, 1983; Wells, 2007]. The dependence of E on Fr and Re across a compilation of both rotating and non-rotating experiments and field measurements has been characterised by the empirical parameterization of Cenedese and Adduce [2010]. Alternatively, Wells et al. [2010] constructed a theory using a flux coefficient, which measures the ratio of buoyancy flux compared to viscous dissipation. This results in a scaling $E = A(\mathrm{Re}, \alpha)\mathrm{Fr}^n$ where the prefactor $A(\mathrm{Re}, \alpha)$ depends on Reynolds number and slope angle. The exponent n captures a variety of scalings, with $n \to 0$ for $\mathrm{Fr} \gg 1$, $n \sim 2$ for $\mathrm{Fr} \sim 1$, and $n \gg 1$ for $\mathrm{Fr} \ll 1$, which is consistent with the trend in the observations. However, there is some scatter of the data about the mean trend, and in particular, observations indicate a substantial increase in mixing for larger Reynolds numbers [Cenedese and Adduce, 2010; Princevac et al., 2005; Wells et al., 2010]. This scatter could be due to intrinsic dynamical variability of turbulent entrainment about a mean value, to the technical challenges of measuring entrainment, or to differences in entrainment depending on the dynamical source of turbulence.

The previously-described measurements of the entrainment parameter, E, rely on a variety of methods. In the absence of rotation, measurements of full velocity profiles allow E to be determined directly from mass conservation

[1]Note that some studies use the Richardson number $\mathrm{Ri} = \mathrm{Fr}^{-2}$.

for both the flow of dense salty water on a laboratory scale slope [Ellison and Turner, 1959], and in field observations of katabatic winds [Princevac et al., 2005]. An alternative approach constrains theoretical predictions using readily measured experimental features, such as the evolution of the background stratification in a filling box [Wells and Wettlaufer, 2005]. This allows a value of E to be inferred that is dynamically consistent with theory, and accounts for downslope evolution of the flow without requiring detailed measurements of velocity profiles. Entrainment into dense rotating currents in the ocean has been estimated from changes in the mass flux between two or more points on the path of the current [see Cenedese and Adduce, 2010, for a summary]. Laboratory studies of rotating currents have estimated entrainment from the increase in volume of the current between the source and the base of the tank [Cenedese and Adduce, 2008; Cenedese et al., 2004; Wells, 2007]. In order to determine a value for E, a characteristic velocity scale is identified and assumed constant along the length of the flow. For example, Wells [2007] identified a velocity scale from the initial mass flux, whilst Cenedese et al. [2004] and Cenedese and Adduce [2008] use the propagation speed of the initial unsteady density front that is driven by downslope variations of hydrostatic pressure and precedes the subsequent steady flow driven by the downslope component of gravity. For these measurements in rotating systems it is plausible that variations of the downslope velocity between measurement points may contribute to the scatter of the measured E values around the parameterizations of Wells et al. [2010] and Cenedese and Adduce [2010]. Motivated by this background, we developed a theoretical model for steady flow of a turbulent rotating density current down a conical sloping surface. The approach accounts for downslope development of the flow and provides a framework for systematic studies of entrainment dynamics in well-characterised laboratory experiments.

In the following section we develop the formulation of the problem of a shelf-slope system in which a density current is delivered onto the surface of a cone, considering both axisymmetric flow and isolated currents of finite angular extent. The essence of the problem can be thought of as a steady rotating version of the model of Morton et al. [1956] but with bottom friction associated with the fact that our "plume" is a current on a slope [Ellison and Turner, 1959]. In §3.3 we determine numerical solutions for a representative laboratory setup, along with analytic solutions for a dense current from an initial buoyancy source where the initial fluxes of mass and momentum are small and dynamically negligible, along with a first-order asymptotic correction to account for the initial mass and momentum fluxes. The attractor solution qualititatively reproduces the asymptotic behaviour of the numerical solutions away from the source, and allows us to characterise the parametric dependence of the flow on entrainment. The linearised asymptotic correction is necessary to account for the initial conditions and provide a good quantitative approximation to the numerical solutions across the full length of the flow. A set of experiments is described in §3.4 demonstrating how the theory captures the correct flow structure and allows us to estimate how the turbulent entrainment varies with rotation rate. The work is summarized in §3.6, where we describe ongoing experimental research and implications for future studies.

3.2 Formulation of the plume model

The model considers fluid of density $\tilde{\rho}$ introduced onto the surface of a solid cone of slope angle α to the horizontal, immersed in a background fluid of uniform density ρ_0, as illustrated in figure 3.1. The system rotates with angular velocity Ω parallel to both gravity g and the vertical. With flow confined below the apex of the cone, we use an orthogonal coordinate system relative to the conical surface, with s representing distance downslope parallel to the conical surface, η the distance normal to the cone, and θ the azimuthal angle. The local velocity components in each direction are $\mathbf{u} = (u_s, u_\eta, u_\theta)$.

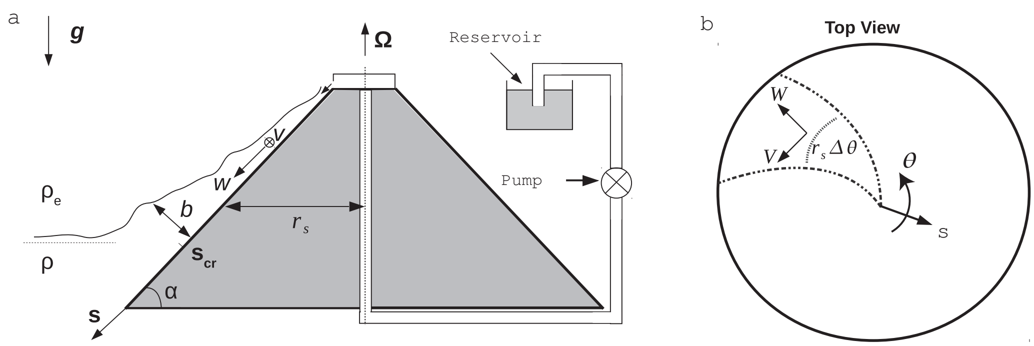

Figure 3.1: Schematic view of the density current on a cone in a rotating fluid, as described further in the main text. (a) View from side, indicating system geometry, notation, and experimental set up. (b) View from above for a current with effective angular extent $\Delta\theta$.

3.2.1 Plume model for a density current on a cone

The governing equations for the density current flow in a rotating reference frame are derived from first principles in Appendix B.1, following the approach of Morton et al. [1956] and Ellison and Turner [1959] to derive plume equations for the down-slope fluxes. For flow of angular extent $\Delta\theta$ over the surface of the cone as illustrated in figure 3.1b, conservation of mass, azimuthal and vertical momentum, and buoyancy are given by

$$\frac{d}{ds}\left(\Delta\theta r_s b w\right) = \Delta\theta r_s v_e, \tag{3.1}$$

$$\frac{d}{ds}\left(\Delta\theta r_s b w^2\right) = \Delta\theta r_s b g \sin\alpha \frac{\rho-\rho_0}{\rho_0} - \Delta\theta r_s b f v + \ldots$$

$$+\Delta\theta b v^2 \cos\alpha - \frac{\tau_s}{\rho_0}\Delta\theta r_s, \tag{3.2}$$

$$\frac{d}{ds}\left(\Delta\theta r_s b w v\right) = \Delta\theta r_s b f w - \Delta\theta b v w \cos\alpha - \frac{\tau_\theta}{\rho_0}\Delta\theta r_s, \text{ and} \tag{3.3}$$

$$\frac{d}{ds}\left(\Delta\theta r_s b w \frac{\rho-\rho_0}{\rho_0}\right) = 0, \tag{3.4}$$

where the effective plume width b, mean plume velocity (w, v) and mean density ρ are defined in terms of the fluxes

$$\int_0^{2\pi}\int_0^{\infty} ru_s d\eta d\theta \equiv br_s w\Delta\theta, \tag{3.5}$$

$$\int_0^{2\pi}\int_0^{\infty} ru_s^2 d\eta d\theta \equiv br_s w^2\Delta\theta, \tag{3.6}$$

$$\int_0^{2\pi}\int_0^{\infty} ru_\theta u_s d\eta d\theta \equiv br_s vw\Delta\theta, \qquad \text{and} \tag{3.7}$$

$$\int_0^{2\pi}\int_0^{\infty} ru_s\frac{\tilde{\rho}-\rho_0}{\rho_0} d\eta d\theta \equiv bwr_s\frac{\rho-\rho_0}{\rho_0}\Delta\theta, \tag{3.8}$$

where $r_s = s\cos\alpha$ is the local radius of the cone, $f = 2\Omega\cos\alpha$ is the Coriolis parameter, $r = s\cos\alpha + \eta\sin\alpha$, and we have assumed self-similar profiles for u_s, u_θ and $\tilde{\rho} - \rho_0$ when determining the buoyancy-force term and Coriolis-force term as discussed in Appendix B.1. For axisymmetric flow the angular extent is $\Delta\theta = 2\pi$, whilst for flows of finite angular extent $\Delta\theta$ must be specified separately as discussed in §3.2.2. To close the model, we must specify the entrainment velocity v_e and the shear stress at the base $\tau = (\tau_s, \tau_\theta)$. We extend the entrainment criterion of Morton et al. [1956] to account for two velocity components by assuming that the entrainment velocity is proportional to the mean speed of the current on the slope,

$$v_e = E\sqrt{v^2 + w^2}, \tag{3.9}$$

where E is the entrainment coefficient. For large Reynolds number flow, the turbulent drag is dominated by eddy momentum fluxes, with the eddy velocity determined from the mean flow speed. Hence we set

$$\frac{\tau}{\rho_0} = K\sqrt{v^2 + w^2}(w, v), \tag{3.10}$$

where K is the friction coefficient [Taylor, 1920]. In §3.6 we discuss the impact of an alternative drag parameterisation that approximates Ekman veering. For axisymmetric flow with $\Delta\theta = 2\pi$ the resulting equations (3.1)–(3.10) yield a closed system of four ordinary differential equations, which are solved with initial conditions for prescribed values of b, w, v, and ρ at a particular distance s_I close to the top of the cone. In addition to analytical solutions, the system was integrated numerically using forward-Euler time-stepping, with convergence confirmed as the discretisation step $\Delta s \to 0$.

3.2.2 Density currents from isolated sources of confined angular extent

The equations (3.1)–(3.10) are also a valid description of the flow of a single stream of fluid as illustrated in figure 3.1b, once the angular extent $\Delta\theta$ has been specified. In Appendix B.1 we show that whenever the variation of angular extent $\Delta\theta$ is sufficiently small (according to (B.17)), then a single stream flow can be described by a subsection of constant angle, $\Delta\theta$, of the corresponding axisymmetric flow. Hence, when changes in $\Delta\theta$ are small, the trajectory of the centre line of a single-stream flow is given by a path line of the axisymmetric solution. Changes in $\Delta\theta$ can be driven either by the force resulting from lateral gradients in hydrostatic pressure at the edge of the current, or by the widening of the current via turbulent entrainment along the current sides. To estimate the influence of changing $\Delta\theta$ in the model, we computed the relative magnitude of an associated term in the momentum equation – $d(\ln\Delta\theta)/d(\ln r)$ (see Appendix B.1 and criterion B.17). For a sample experimental current path without rotation the resulting change in $\Delta\theta$ has only a moderate effect on the dynamics, with the average value $\overline{d(\ln\Delta\theta)/d(\ln r)} = 24\%$, and so in the absence of any validated theoretical model for changes in $\Delta\theta$, we develop analytic solutions for constant $\Delta\theta$. Note that this approximation implicitly prevents rapid widening of the current in a hydraulic jump [Pratt et al., 2007], and the assumption may need to be relaxed in alternative flow configurations.

3.3 Model solutions

The development of the axisymmetric flow described by (3.1)–(3.10) depends on the initial fluxes of mass, momentum and buoyancy, in addition to the entrainment parameter E and friction parameter K. Whilst the theory can describe a wide range of steady turbulent flows on conical slopes, ranging from pure momentum jets to buoyancy-driven wall plumes, in this paper we focus on initial conditions relevant to a buoyancy-driven overflow that is primarily controlled by the input buoyancy flux, with small initial fluxes of mass and momentum. We begin by illustrating the behaviour of a numerical solution of (3.1)–(3.10) in an example experimental setting, before deriving analytical solutions and a first-order asymptotic correction for a special case that reveals the essential features of the dynamics.

3.3.1 General solution properties

The thick black curves in figure 3.2 illustrate a numerical solution of the plume model (3.1)–(3.10) that is representative of a laboratory setting, with initial fluxes of buoyancy, mass and momentum released some distance $s = s_I$ below the apex of the cone. The solution involves a critical point occurring at a particular depth $s = s_{cr}$. In the vicinity of this critical point the downslope component of velocity approaches zero (see Fig. 3.2) as the flow approaches a state of purely azimuthal flow. In the framework of our steady-state axisymmetric plume model there are no physical solutions beyond the critical point, and fluid is not allowed to penetrate below it. Hence the persistent flux of fluid results in a divergence of the modelled plume width. This results in a breakdown of the boundary-layer approximation employed by the theory, which assumes that the current is thin compared to the along-slope extent, with additional physical processes becoming important in a small neighbour-

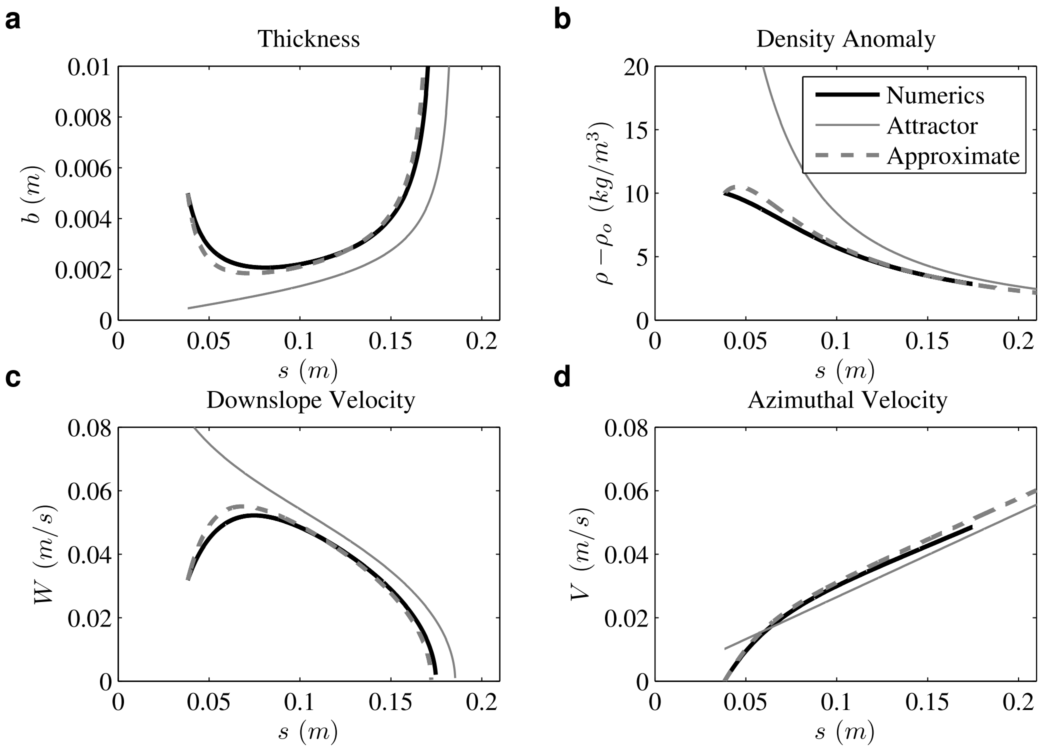

Figure 3.2: Flow development with distance s from the apex of the cone. Thick black solid curves show the numerical solution of the full equation set (3.1)–(3.10) whilst thin gray curves show the asymptotic attractor solution (3.20)–(3.22), and dashed curves show the approximate solution including higher order corrections (3.24) and (3.29)–(3.31). The downslope flow ceases at a critical point s_{cr} where $w \to 0$, $b \to \infty$, and the boundary layer approximation breaks down. The parameters used are representative of a laboratory experimental set up, with $g = 9.8\,\mathrm{m\,s^{-2}}$, $\rho_o = 1000\,\mathrm{kg\,m^{-3}}$, $\Omega = 0.6\,\mathrm{rad\,s^{-1}}$, $\alpha = 36°$, and for illustration we set $E = 0.1 \sin\alpha$ [Wells and Wettlaufer, 2005] and $K = 2 \times 10^{-3}$ consistent with the order of magnitude determined by Taylor [1920]. The prescribed initial conditions at $s = 0.038$m are $\rho = 1010\,\mathrm{kg\,m^{-3}}$, $b = 0.5 \times 10^{-2}$ m, $w = 3.2 \times 10^{-2}\,\mathrm{m\,s^{-1}}$, and $v = 0\,\mathrm{m\,s^{-1}}$.

hood of the critical point. We thus expect that in laboratory experiments there will still be downslope leakage of dense fluid beyond the critical point. However, one should be able to observe an abrupt change in the behaviour of the flow as it approaches the critical level. At this juncture it is appropriate to note an analogy with critical levels for intrusion of plumes into stratified ambients [Morton et al., 1956]. In the plume model of Morton et al. [1956] the flow is arrested at a critical point due to the stratification reducing the relative buoyancy force, with the inertia of the plume causing it to slightly overshoot the level of neutral buoyancy before the plume is decelerated. For rotating density currents the outward flow is arrested at a critical point by rotation, with the Coriolis forces counteracting the downslope buoyancy forces and stopping the downslope flow after the current overshoots a level where Coriolis and buoyancy forces are in geostrophic balance.

The path line of a tracer particle released into the axisymmetric flow has no downslope component at the critical point s_{cr}. As illustrated by the thick black curves in figure 3.3a, the trajectory[1] $s = s(\theta)$ terminates at the critical point (where $w = 0$) after traversing a finite angle around the cone, rather than $\theta(s) \to \infty$, because the azimuthal velocity v remains bounded on approach to the critical point. Clearly, the trajectories depend on the entrainment ratio E, which we explore further in §3.3.4.

3.3.2 The attractor solution

To shed light on the generality of the dynamics illustrated by the numerical solutions, we now derive an analytic solution of the full model (3.1)–(3.10) for initial conditions with a constant initial buoyancy flux, and negligible initial fluxes of mass and momentum. We later demonstrate that this solution is an attractor for the flow dynamics with arbitrary initial fluxes. From (3.4)

[1]Note that this trajectory also corresponds to the centre-line of a single stream flow of constant angular extent.

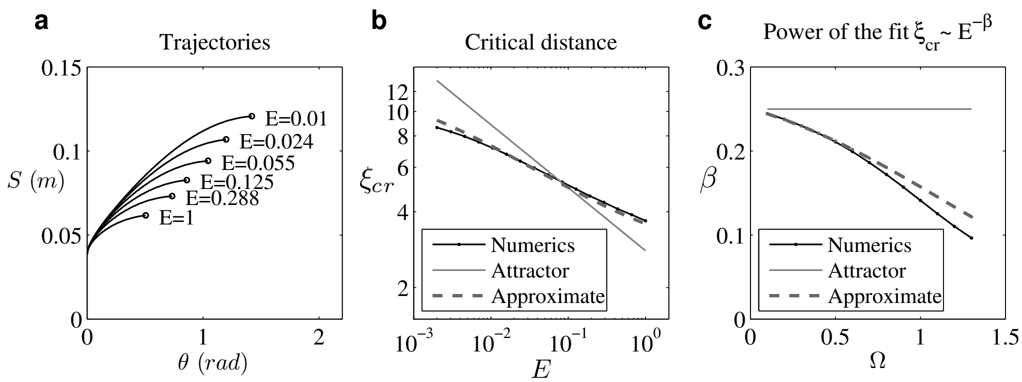

Figure 3.3: a) Fluid parcel trajectories $s(\theta)$ (solid curves) from numerical solutions for a range of entrainment coefficients E, $\Omega = 1\,\mathrm{rad\,s^{-1}}$ and all remaining parameters as in figure 3.2. Circles denote the critical point achieved at the end of the trajectories. b) Sensitivity of the non-dimensional critical point $\xi_{cr} = s_{cr} f^{3/4} Q_B^{-1/4}$ to the entrainment coefficient E, plotted for $\Omega = 1\,\mathrm{rad\,s^{-1}}$. Numerical solutions (thick black solid curve) are compared to the analytical scaling (3.32) for the attractor (thin gray curve) and the approximate solution (dashed curve) with higher order corrections (3.24) and (3.29)–(3.31). Note the logarithmic scales. c) Approximate power-law exponent β plotted as a function of $\Omega\,(\mathrm{rad\,s^{-1}})$, where β is estimated from a power law fit $\xi_{cr} = AE^{-\beta}$ to the curves in panel (b) and similar curves with different rotation rates, to approximate the sensitivity of the critical distance to entrainment. The numerical solution converges toward the attractor at small Ω.

we immediately observe that the downslope buoyancy flux Q_B is conserved,

$$\Delta\theta r_s bw \frac{\rho - \rho_0}{\rho_0} g \sin\alpha = \Delta\theta \cos\alpha \, Q_B, \tag{3.11}$$

with its value determined from the initial conditions. One could think of Q_B as the normalised integral mass flux of salt (or other density tracer) passing through a particular depth, which in the steady state has to be independent of depth to prevent accumulation of salt. It is natural to non-dimensionalise variables using Q_B and f, and so we introduce a dimensionless coordinate $\xi = sf^{3/4}Q_B^{-1/4}$ and define the new variables

$$P = \frac{sbwf^{5/4}}{Q_B^{3/4}}, \quad W = \frac{sbw^2 f}{Q_B}, \quad V = \frac{sbwvf}{Q_B}, \tag{3.12}$$

which represent dimensionless fluxes of mass, downslope momentum and azimuthal momentum respectively, scaled by $\Delta\theta\cos\alpha$. Neglecting changes in $\Delta\theta$, the system (3.1)–(3.3) can be written as

$$\dot{P} = E\sqrt{W^2 + V^2}\frac{\xi}{P}, \tag{3.13}$$

$$\dot{W} = \frac{P}{W} - \frac{VP}{W} + \frac{V^2}{W\xi} - K\sqrt{W^2 + V^2}\frac{W\xi}{P^2}, \quad \text{and} \tag{3.14}$$

$$\dot{V} = P - \frac{V}{\xi} - K\sqrt{W^2 + V^2}\frac{V\xi}{P^2}, \tag{3.15}$$

where $\dot{[\,]} \equiv d/d\xi$. Note that the only remaining parameters in (3.13)–(3.15) are the entrainment coefficient E and drag coefficient K.

It is useful to sum W times (3.14) and V times (3.15) and recast this system in terms of the variable $F = V^2 + W^2$,

$$\dot{P} = E\sqrt{F}\frac{\xi}{P}, \tag{3.16}$$

$$\dot{F} = 2P - 2K\frac{F^{3/2}\xi}{P^2}, \qquad \text{and} \tag{3.17}$$

$$\dot{V} = P - \frac{V}{\xi} - K\sqrt{F}\frac{V\xi}{P^2}. \tag{3.18}$$

For the special case of an initial point source of buoyancy at the apex of the cone, with no fluxes of mass or momentum, the initial conditions are

$$V = W = P = 0 \qquad \text{at} \quad \xi = 0, \tag{3.19}$$

so that $F(0) = 0$. Seeking power-law similarity solutions in ξ for P, F and V we obtain

$$P = \frac{3}{2^{2/3}5^{2/3}}\frac{E^{2/3}}{\left(1+\frac{5}{4}\frac{K}{E}\right)^{1/3}}\xi^{5/3}, \tag{3.20}$$

$$F = \frac{9}{2^{8/3}5^{2/3}}\frac{E^{2/3}}{\left(1+\frac{5}{4}\frac{K}{E}\right)^{4/3}}\xi^{8/3}, \qquad \text{and} \tag{3.21}$$

$$V = \frac{9}{2^{2/3}5^{2/3}11}\frac{E^{2/3}}{\left(1+\frac{5}{4}\frac{K}{E}\right)^{1/3}\left(1+\frac{5}{11}\frac{K}{E}\right)}\xi^{8/3}, \tag{3.22}$$

which straightforwardly yield $b(s)$, $v(s)$, $w(s)$, and $\rho(s)$ using algebraic manipulation. In Appendix B.2 we show that this solution is a unique attractor for the system of ordinary differential equations (3.16)–(3.18) for arbitrary initial conditions. That is, for sufficiently large s, the solutions (3.20)–(3.22) will approximate the leading order asymptotic behaviour[1] of any solution of (3.16)–(3.18).

In addition to the qualitative flow structure already discussed, two inter-

[1]Note that we expect this attractor solution to provide a useful approximation when $s_I \ll s < s_{cr}$, which requires the critical level s_{cr} to be sufficiently far downstream from the initial level s_I.

esting features revealed by the leading order attractor solution are as follows. First, the resulting dimensional azimuthal velocity is $v \sim 3fs/(11+5K/E)$, which increases linearly with depth, has no explicit dependence on the buoyancy force and, for small frictional coefficients, depends only weakly on the entrainment rate. Second, the downslope mass flux

$$\Delta\theta r_s bw \sim \Delta\theta\cos\alpha\frac{3}{2^{2/3}5^{2/3}}\frac{E^{2/3}}{\left(1+\frac{5}{4}\frac{K}{E}\right)^{1/3}}Q_B^{1/3}s^{5/3}, \tag{3.23}$$

is independent of the rotation rate f (except via any implicit dependence of the entrainment parameter E on rotation).

Figure 3.2 compares the analytic attractor solution (thin grey curves) to numerical solutions with small, but non-zero initial fluxes of mass and momentum (thick black curves) relevant to an example experimental configuration. The attractor solution captures the qualitative behaviour of the numerical solutions, after an initial transient due to the experimental initial conditions not lying on the attractor. However, to achieve an improved quantitative comparison for initial conditions relevant to our experiments, it is useful to consider the next-order corrections to the asymptotic attractor solution (3.20)–(3.22) in order to account for the non-zero initial fluxes of mass and momentum in experimental settings.

3.3.3 Linearised correction to the attractor solution

Inspection of numerical solutions, such as those in figure 3.2, shows that for large rotation rates Ω the disagreement of the attractor solution with the numerical solution is large because the critical point $s = s_{cr}$ is reached before the solution is adjusted to the attractor. However, for $\Omega \to 0$ or $Q_B \to \infty$ (3.12) shows that the initial conditions P_0, V_0, F_0 approach zero at $\xi = \xi_I \to 0$, thus recovering the initial conditions for the attractor solution. Hence, the attractor also acts as an asymptotic solution for small rotation rates or large buoyancy fluxes. We make use of this fact and calculate an approximate solution in the whole range of ξ using a generalized asymptotic expansion of the true solution around the attractor:

$$P = P_a + \hat{P}, \quad F = F_a + \hat{F}, \quad V = V_a + \hat{V}. \tag{3.24}$$

Taking $\hat{P} \ll P_a$, $\hat{F} \ll F_a$, $\hat{V} \ll V_a$ and linearizing (3.16)–(3.18) around the attractor solution we find

$$\frac{\partial \hat{P}}{\partial \xi} = \frac{10}{9\xi^2}\hat{F} - \frac{5}{3\xi}\hat{P}, \tag{3.25}$$

$$\frac{\partial \hat{F}}{\partial \xi} = 2\hat{P}, \qquad \text{and} \tag{3.26}$$

$$\frac{\partial(\xi\hat{V})}{\partial \xi} = \xi\hat{P}, \tag{3.27}$$

where we have set $K = 0$ for mathematical simplicity which corresponds to neglecting drag. For a typical value of $K = 10^{-3}$, this approximation results in only small quantitative differences from the full numerical solution, as illustrated in figure 3.2. Eliminating $\hat{P}$ from (3.25)–(3.26) leads to an Euler equation for $\hat{F}$,

$$\xi^2\ddot{\hat{F}} + \frac{5}{3}\xi\dot{\hat{F}} - \frac{20}{9}\hat{F} = 0. \tag{3.28}$$

with solution

$$\hat{F} = A_1\xi^{\alpha_1} + A_2\xi^{\alpha_2}, \tag{3.29}$$

$$\hat{P} = \frac{A_1\alpha_1}{2}\xi^{\alpha_1} + \frac{A_2\alpha_2}{2}\xi^{\alpha_2}, \qquad \text{and} \tag{3.30}$$

$$\hat{V} = \frac{1}{2}\frac{A_1\alpha_1}{\alpha_1+1}\xi^{\alpha_1} + \frac{1}{2}\frac{A_2\alpha_2}{\alpha_2+1}\xi^{\alpha_2} + A_3\xi^{-1}, \tag{3.31}$$

where $\alpha_{1,2} = -1/3 \pm \sqrt{7/3}$ and the coefficients $A_{1,2,3}$ are determined from the initial conditions. We note here, that if the initial conditions are far from the attractor, constants $A_{1,2,3}$ would be $O(1)$ and thus the linearisation of the solution around the attractor would not be formally justified. Nonetheless, this method allows us to construct a solution that satisfies the initial conditions exactly and still preserves the same attractor solution as $\xi \to \infty$ since the perturbations grow slower then the attractor ($\alpha_{1,2} < 5/3$). Whilst a further correction could be made or the impact of small, but non-zero, K could be considered, this first-order correction provides sufficient accuracy over the experimentally motivated range of parameters we consider in this paper. This is illustrated in figure 3.2 by the good comparison between this approximate solution (dashed curves) and the full numerical solution (thick black curve) (see also Fig. 3.3).

3.3.4 Sensitivity to entrainment

Figure 3.3*b* illustrates the dependence of the non-dimensional value of the critical point $\xi_{cr} = s_{cr} f^{3/4} Q_B^{-1/4}$ on the entrainment rate E. It is clear that as turbulent entrainment increases the distance to the critical point $s = s_{cr}$ decreases, which can be understood as a result of two effects. Increased entrainment of ambient fluid via turbulent mixing results in a decreased mean density of the mixture, and hence a weakened buoyancy force. Furthermore, the ambient fluid has no momentum, and so increased entrainment reduces the downslope momentum of the mixture. These effects combine to reduce the distance flowed downslope.

For cases where $s_{cr} \gg s_I$ we can estimate s_{cr} from the asymptotic solution (3.20)–(3.22). The critical depth s_{cr} is obtained when $W = 0$ which corresponds to $V^2 = F$, and yields

$$s_{cr} = \left(\frac{6655}{108}\right)^{1/4} \frac{\left(1 + \frac{5}{11}\frac{K}{E}\right)^{3/4}}{\left(1 + \frac{5}{4}\frac{K}{E}\right)^{1/4}} \left(\frac{Q_B}{E f^3}\right)^{1/4}. \tag{3.32}$$

The friction parameter is typically small, with K of order 10^{-3} [Taylor, 1920], and for $K/E \ll 1$ (3.32) yields the leading order scaling $s_{cr} \propto E^{-1/4}$. Note that the dependence on buoyancy flux Q_B and entrainment rate E is rather weak, but there is a stronger dependence on the Coriolis parameter f.

As illustrated by the thin grey curve in figure 3.3*b*, the scaling (3.32) from the asymptotic solution captures the leading order magnitude of the numerical solutions (thick black curve) for moderate values of E of order 0.1, but does not capture the scaling behaviour with E. This disagreement arises because the numerical solutions are still influenced by the values of the initial condition and have not yet closely approached the attractor before s_{cr} is reached. Accounting for non-zero initial fluxes of mass and momentum using the first order asymptotic correction, the approximate solution (dashed curve) produces much closer agreement with the numerical solution as seen in Figs. 3.2 and 3.3. Figure 3.3*c* illustrates the sensitivity of ξ_{cr} to entrainment for different rotation rates, by plotting the exponent β of a power law fit $\xi_{cr} = AE^{-\beta}$ to data for different rotation rates Ω. For large Ω the numerical solution (thick black curve) produces a power-law exponent β which differs markedly from the value $\beta = 0.25$ for the attractor solution (thin gray curve) expected from (3.32). The agreement improves markedly and the numerical scaling exponent approaches the attractor exponent as $\Omega \to 0$, consistent with the rationale described in §3.3.3. The approximate solution (dashed curve), accounting for the full initial conditions via a linearised correction, produces much better agreement with the scaling exponent β observed in the numerical solutions. Hence, whilst the full solution of (3.1)–(3.10) approaches the asymptotic attractor solution (3.20)–(3.22) for large s, we conclude that the approximate linearised correction (3.24) and (3.29)–(3.31) may be required in experimental settings with large rotation rates where the initial fluxes of mass and momentum play a non-trivial role.

We demonstrated that the modelled flow dynamics is sensitive to the entrainment parameter E, suggesting that an indirect measure of entrainment can be achieved in suitable experiments by observing flow quantities such as s_{cr}. This motivates a series of laboratory experiments to examine the theory discussed in this section and to investigate the effects of rotation on the effective entrainment rate.

3.4 Experimental comparison

3.4.1 Experimental arrangement

A set of laboratory experiments were conducted to investigate the dynamics of a single stream turbulent flow of small angular extent. Consistent with the situation shown in figure 3.1 we consider flow on a truncated cone with slope angle $\alpha = 36°$ to the horizontal, maximum radius of 18.4 cm and minimum radius of $r_I = 3.1\,\mathrm{cm}$ so that $s_I = r_I/\cos\alpha = 3.8\,\mathrm{cm}$.

The cone was mounted at the centre and 4 cm above the base of a large tank of $100\,\mathrm{cm} \times 100\,\mathrm{cm}$ square cross section, allowing a large overflow region to minimise the influence of any "filling box" effects in the far field fluid over the course of an experiment. The tank was filled to a depth of 8 cm above the top of the truncated cone, to minimise the influence of an effective two-layer geostrophic flow induced by the input of dense fluid. Sutherland et al. [2004] showed that this effect is significant for shallower flows.

The tank was spun up into an approximate state of solid-body rotation with an angular velocity $0.4\,\mathrm{rad\,s^{-1}} \leq \Omega \leq 1.3\,\mathrm{rad\,s^{-1}}$ which was varied between experiments. This range of angular velocities was chosen for practical reasons, with the lower limit ensuring that the lower edge of the current does not approach the edge of the cone as the current reaches the critical level s_{cr}, whilst the upper limit was chosen for safety reasons. A dense $\mathrm{NaCl} - \mathrm{H_2O}$ solution was dyed with potassium permanganate, with total density excess $\Delta\rho = \rho_i - \rho_e$ measured using an oscillating type densitometer (Anton Paar DMA 3.5N). The dense fluid was introduced at the top of the cone via the following flow injection mechanism. A pump supplied dense water at flow rates $0.0185\,\mathrm{cm^3s^{-1}} < Q < 0.0305\,\mathrm{cm^3s^{-1}}$ to an enclosed cylindrical "pill-box" shaped reservoir of 3.1 cm radius and 1 cm depth. The pill box reservoir was filled with glass beads and the piping was filled with sponge material so that flow through it acted to suppress small flow oscillations introduced by the pump. Dense fluid exited the pill box reservoir via a cylindrical hole drilled adjacent and parallel to the cone surface. The small hole diameter $d = 0.5\,\mathrm{cm}$ produces a sufficient initial velocity for the dense current to be initiated in a turbulent state with visible eddying motion. Earlier attempts with an axisymmetric flow release resulted in only unsteady laminar flow without significant eddy-driven mixing, because the flow rates of the available pump could not achieve a sufficiently high Reynolds number when spread over an axisymmetric source. Table 3.1 summarises the experimental parameters. Note that in determining the buoyancy flux Q_B given by (3.11) and appropriate to the theory, we estimate the angular extent $\Delta\theta$ of the current as described below.

3.4.2 Structure of the current

Plan view images were recorded at a frame rate of 24Hz for the approximate 500 s duration of an experiment using a digital camera mounted above the tank in the rotating frame and DigiFlow software (Dalziel Research Partners, Cambridge). Distribution of the grayscale intensity in the plan-view images also provides information concerning the density distribution in the current. The grayscale intensity increases with increased concentration of dye and fluid density. After a 45 s transient period during which the flow develops, the subsequent $11,000$ images were analysed using a custom written MATLAB code. For further analysis the images were time averaged over 10 inertial periods, where the inertial period is $1/(2\Omega)$, to smooth out the effects of small scale eddies and to avoid shadow effects from the background lighting, thus obtaining time series of the large scale variability of the density current. The initial angular extent of the current was estimated from the time-averaged grayscale colour intensity, by fitting a gaussian profile $A \exp\left[-(\theta - \theta_0)^2/\sigma_\theta^2\right]$ to the data averaged over $3.6\,\mathrm{cm} < r < 4.1\,\mathrm{cm}$, a short distance beyond the

Exp #	Ω $(\mathrm{rad\,s^{-1}})$	$\Delta\rho/\rho_e$	Q_B $(\times 10^{-7}\mathrm{m^4 s^{-3}})$	s_{cr} $(\times 10^{-2}\mathrm{m})$	E
1	0.4000	0.0155	2.9857	14.2022	0.1237
2	0.5000	0.0154	1.9933	11.5521	0.1110
3	0.5020	0.0124	1.5588	10.9935	0.0998
4	0.5750	0.0129	1.6219	11.9110	0.0435
5	0.5760	0.0129	2.5308	11.2503	0.0923
6	0.5970	0.0124	1.5531	11.0566	0.0499
7	0.6330	0.0124	1.4824	9.3200	0.0992
8	0.6480	0.0124	1.5837	9.7397	0.0742
9	0.6640	0.0124	1.5161	9.6984	0.0690
10	0.7050	0.0154	2.1543	9.8181	0.0836
11	0.7480	0.0124	1.4703	9.5860	0.0463
12	0.7900	0.0154	2.0020	9.1946	0.0737
13	0.8420	0.0137	1.6768	8.6796	0.0552
14	0.9060	0.0124	1.4863	8.8555	0.0331
15	1.0080	0.0124	1.4466	7.8438	0.0471
16	1.0670	0.0124	1.5565	7.4783	0.0578
17	1.1520	0.0124	1.5023	8.1990	0.0186
18	1.2960	0.0124	1.5161	7.7706	0.0162

Table 3.1: List of experimental conditions and derived quantities. The rotation rate Ω, initially normalised density difference $\Delta\rho/\rho_e$ and initial dimensional buoyancy flux $Q_B\Delta\theta$ supplied by the pump are imposed for each experiment, and the initial angular extent $\Delta\theta = 0.5\,\mathrm{rad}$ is diagnosed from the data as described in the main text. The final two columns show the estimated critical distance s_{cr} at which the downslope propagation of the core of the current stops, and the corresponding entrainment coefficient E inferred as a value that produces best agreement between the observed s_{cr} and a numerical solution, described further in the main text.

initial contact of the current with the cone. We estimate the angular extent using $\Delta\theta = M\sigma_\theta$, with $M = 4$ chosen corresponding to the central 95% of a gaussian distribution. There is some arbitrariness in the choice of $\Delta\theta$, but we note that different values of M simply result in a uniform linear rescaling of all values of Q_B. Hence, whilst this rescaling may uniformly effect the absolute values of the entrainment parameter, E, inferred below, the rescaling does not influence the relative changes of E with Ω. We expect non-negligible errors associated with the nonlinearity of the mapping function between the pixel intensity and the density and thickness of the current as well as due to refraction effects. Thus, rather than estimating a value of $\Delta\theta$ for each experiment individually subject to large statistical fluctuations, we choose to use a constant value of $\Delta\theta = 0.50\,\mathrm{rad}$ which is an ensemble mean value over all the experiments (with ensemble standard deviation $\sigma(\Delta\theta) = 0.13\,\mathrm{rad}$).

Figure 3.4 shows an example of both the instantaneous and time-averaged structure of the current, with the scale indicating changes in dye colour intensity extracted from the black and white images. For the rotation rates reported here the dense current propagates both down the cone surface and azimuthally until a state of azimuthal flow is approached at $s = s_{cr}$. The core of the current approaches the critical level $s = s_{cr}$ (where the theory breaks down) after traversing an angle of order $\theta \sim 60^\circ$ and there is strong downslope leakage in a thin unsteady laminar layer featuring roll waves, but lacking notable entraining eddy structures. This leakage leads to the current dispersing over the lower section of the cone surface. There is also weak downslope leakage in an Ekman layer along the length of the current, but image analysis allows us to extract the maximum dye colour intensity to track the turbulent entraining core of the current. We note here that the time-averaged current cannot transport buoyancy downslope across the critical level (because $w = 0$ there). The entire buoyancy flux supplied by the source is transported across the critical level by the subsequent transient leakage.

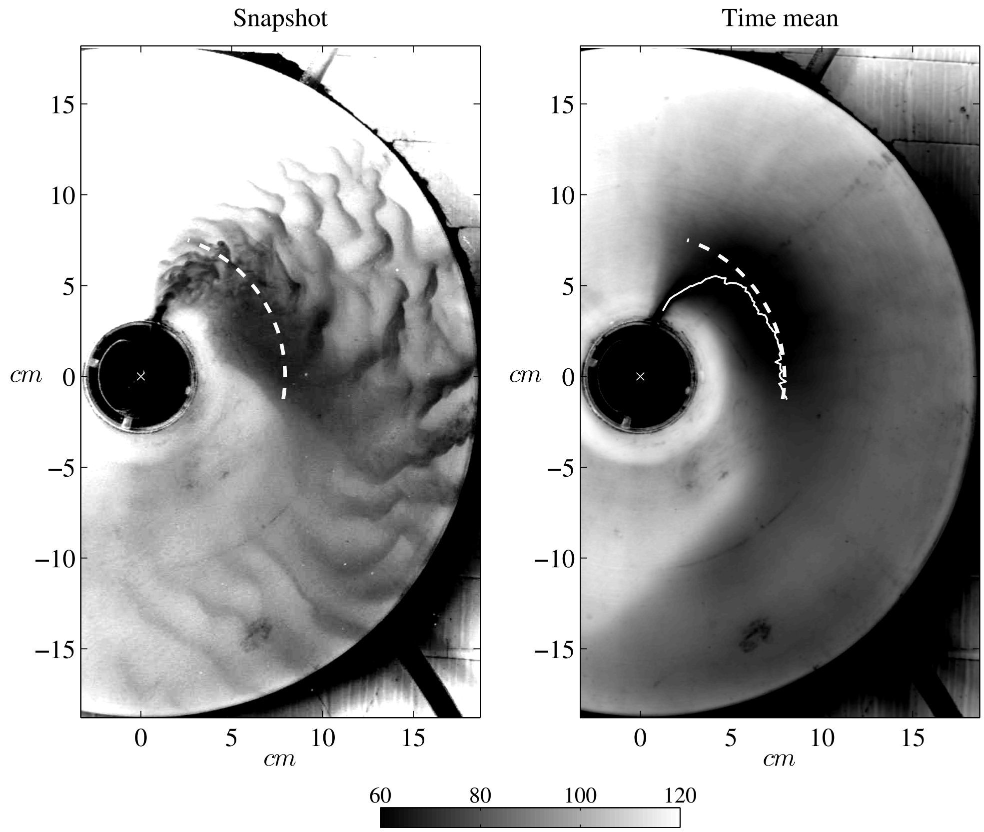

Figure 3.4: (a) A top view snap shot of the single stream density current for the experiment #10 listed in Table 3.1 and (b) a corresponding image temporally averaged over 10 inertial periods. The scale shows the gray scale pixel intensity in the digital images, with regions of higher concentration of the dyed fluid in the descending dense current having darker intensity. Overlaid are the centreline trajectory (white solid curve) and a critical level indicated by a circular white dashed arc with a radius R_{cr}; white crosses denote the axis of rotation.

3.4.3 Effective trajectories and critical depth

In order to quantitatively analyse the flow, the following automated image processing algorithm was used to extract the path of the current and its temporal variability. Since the theoretical model describes the trajectory of a Reynolds-averaged flow, we split the original data into a sequence of images that are time-averaged over 10 inertial periods. For each time-averaged image (numbered with $j = 1, \ldots, J$), we estimate a flow centreline path $R_j(\theta)$ by finding the maximum grayscale colour intensity on each ray θ = constant with 1 degree increments, using polar coordinates centered on the tip of the cone. A 9-point "lowess" smoothing filter [Cleveland, 1981] is then applied along the θ dimension to remove outliers from each of the trajectories $R_j(\theta)$. An example time-averaged trajectory $R(\theta) = \left[\sum_j R_j(\theta)\right]/J$ is shown by the white solid curve in figure 3.4b, whilst figure 3.5 illustrates the variability of all individual subsample trajectories (thin gray curves) compared to the time-averaged trajectory (thick black curve). In figure 3.5, the standard deviation increases significantly approaching the region of smallest $dR/d\theta$ for $60^\circ \lesssim \theta \lesssim 90^\circ$, consistent with the breakdown of the theoretical model and leakage from the core of the current as the critical level is approached. As an objective and reproducible estimate of the distance at which the breakdown occurs, we first define an index $I_W(\theta) = dR/d\theta \;\; [\mathrm{STD}(R)]^{-1}$, which is the slope of the trajectory normalized by the standard deviation $\mathrm{STD}(R)$ due to temporal variability at each value of θ. The index has large values at the beginning of a trajectory and obtains its first local minimum when the slope starts to diminish significantly and the variability of the current increases. We thus define the critical radius R_{cr} (and hence the critical downslope distance $s_{cr} = R_{cr}/\cos\alpha$) by fitting a horizontal line between the point of the first minimum in I_W and the remaining path up to an angle θ_{end}, after which the current is significantly diluted and the path detection algorithm fails. The low-frequency temporal variability of the trajectories leads to uncertainties in determining s_{cr}, which we estimate using the standard deviation based on

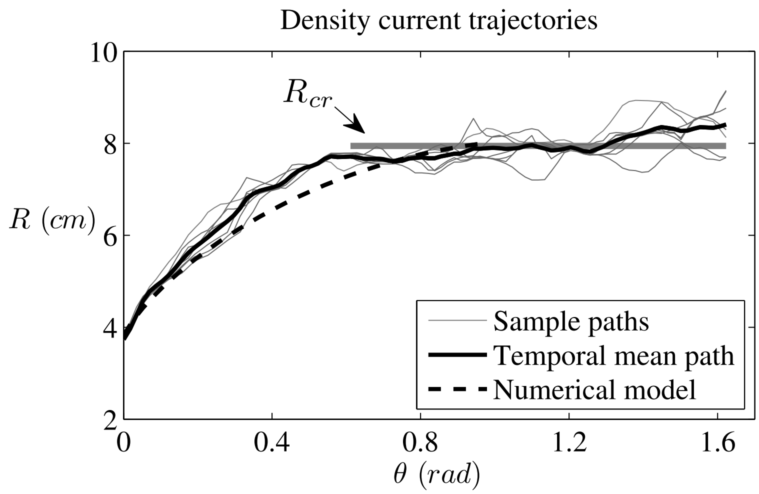

Figure 3.5: Reconstructed time-averaged trajectory given in polar form $R(\theta)$ (black solid curve) for experiment #10 listed in table 3.1, with sample trajectories indicating time variability (gray solid curves). The level of R_{cr} is plotted starting from the value of θ where the I_W-index takes it's first minimum (horizontal gray line). A numerical solution (dashed black curve) is obtained using the experimental initial conditions and the best fit entrainment coefficient corresponding to the observed R_{cr}.

the difference between the mean path and the approximated horizontal line (Fig. 3.5).

3.4.4 Critical point and entrainment estimates

Figure 3.6a illustrates the dimensionless critical point $\xi_{cr} = s_{cr} f^{3/4} Q_B^{-1/4}$ for each experiment as a function of the rescaled dimensionless rotation rate $\hat{\Omega} = f s_I^{4/3} Q_B^{-1/3}$. Despite the initial buoyancy flux varying between different experiments as listed in table 3.1, the general trend clearly shows that ξ_{cr} increases linearly as the rotation rate increases. We attribute this increase to the dependence of the entrainment coefficient on the rotation rate. As an attempt to quantify this, we investigate the consequences of assuming that

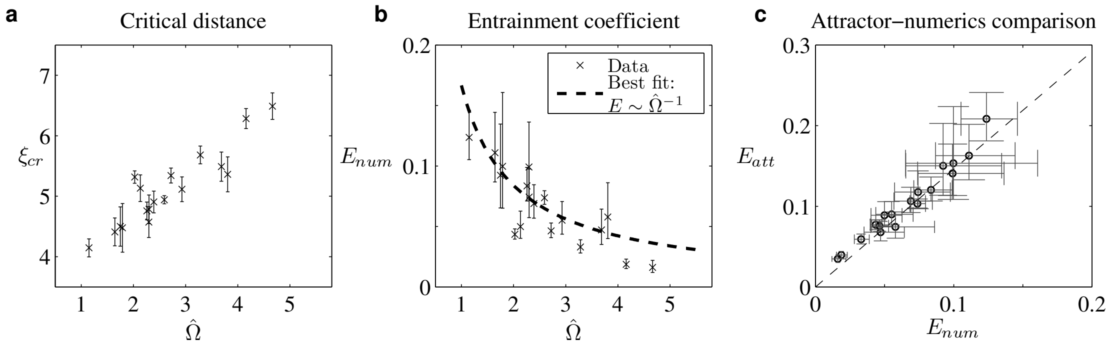

Figure 3.6: Variation with dimensionless rotation rate $\hat{\Omega} = f s_I^{4/3} Q_B^{-1/3}$ of (a) nondimensional critical distance ξ_{cr}, and (b) entrainment parameter E_{num} estimated so that a numerical integration of the full plume equations matches the observed value ξ_{cr}. Error bars for ξ_{cr} are estimated from one standard deviation of the observed variability of ξ_{cr} over time, and these are used to estimate error bars for E. The best fit scaling law for $E \propto \hat{\Omega}^{-1.0}$ is plotted as a dashed curve. (c) Comparison of E_{att} estimated from (3.32) to E_{num}, where the dashed line shows a linear fit $E_{\text{att}} = 1.46 E_{\text{num}}$.

the entrainment coefficient E is independent of s, so that a single value of E applies to each experiment. We firstly calculate an entrainment coefficient consistent with the numerical solution of the plume equations, using an optimisation routine that adjusts E to minimise the difference between the numerically obtained s_{cr} and the value based on experiments. The initial conditions for the numerical solutions are derived using the measured values described in table 3.1, combined with an estimated initial velocity scale $w_0 \approx Q_m/\pi d^2$ where Q_m is the measured initial mass flux and $d = 0.5\,\text{cm}$ is the diameter of the source nozzle. The velocity scale w_0 factors only into the estimate of the small initial momentum flux. In figure 3.6*b* we plot the value of E so determined as a function of the dimensionless rotation rate $\hat{\Omega} = f s_I^{4/3} Q_B^{-1/3}$. Whilst the data show inherent scatter they are consistent with the trend $E \propto 1/f$ indicated by the dashed curve. A power law fit yields 95% confidence bounds for the scaling exponent as $E \propto \hat{\Omega}^{-0.99 \pm 0.35}$ with an

R-squared value of 0.69. The entrainment values for experiments with low rotation rates are less well-constrained due to large temporal variability of the currents. We indicate this variability with error bars calculated using the standard deviation of the spread in s_{cr} from the individual trajectories $R_j(\theta)$. Note that the attractor scaling (3.32) gives $E \propto s_{cr}^{-4}$, and so we heuristically expect that the spread in E will be much larger than the spread in s_{cr}.

3.5 The dependence of entrainment on dimensionless groups

To investigate the robustness of this result we also considered an alternative estimate of entrainment, by inverting the attractor scaling (3.32) and using the observed s_{cr} to determine a value $E = E_{\text{att}}$. Figure 3.6c compares E_{att} to the estimate based on a full numerical integration E_{num}. The data can be approximated by a linear relationship $E_{\text{att}} = 1.46E_{\text{num}}$, showing that the attractor solution captures the trend of the variation of E between experiments, but tends to overestimate its value relative to the full numerical solution. A power-law fit to this second estimate yields $E_{\text{att}} \propto \hat{\Omega}^{-1.05\pm0.24}$ which is also consistent with the trend $E \propto 1/f$ identified above. This suggests that the variation of E with f appears to be robust and independent of the choice of $M = 4$ in the estimate $\Delta\theta = M\sigma_\theta$; a different choice of M results in a uniform rescaling of Q_B in (3.32) and hence only modifies the proportionality constant in the trend $E_{\text{att}} \propto \hat{\Omega}^{-1.05\pm0.24}$ without changing the exponent.

The scaling dependence with the Coriolis parameter f and choice of dimensionless rotation rate is explored in further detail in figure 3.7. The Buckingham-Pi theorem requires that the entrainment parameter E depends only on non-dimensional quantities. The physical quantities characterising the attractor state are f, Q_B, and the downslope co-ordinate s. Although in principle E could depend on the non-dimensional co-ordinate ξ, one cannot construct a constant non-dimensional group to characterise the significance

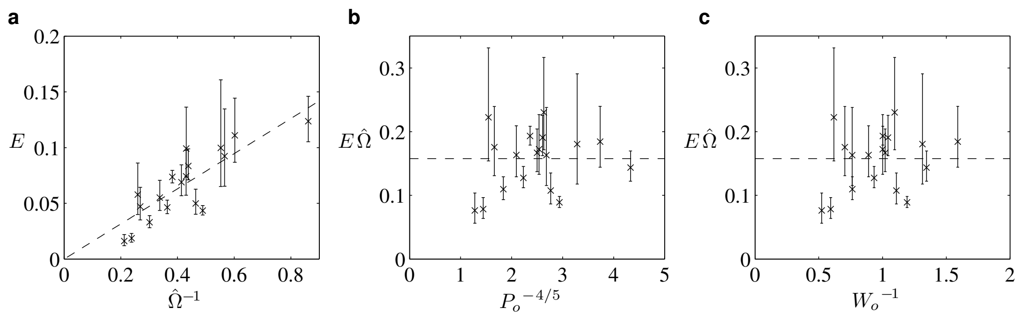

Figure 3.7: Investigation of scaling of the entrainment rate E with the dimensionless groups $\hat{\Omega} = f s_I^{4/3} Q_B^{-1/3}$, P_0 and W_0 defined by (3.12), that depend on the rotation rate f. (a) Variation of scaled entrainment rate E with $\hat{\Omega}^{-1}$ (cross symbols with error bars as in figure 3.6) is consistent with a fitted linear trend $E = 0.21\,\hat{\Omega}^{-1}$ shown by a dashed line. (b) Variation of the renormalised quantity $E\hat{\Omega}$ with $P_0^{-4/5} \propto 1/f$ (cross symbols with error bars), and (c) variation of $E\hat{\Omega}$ with $W_0^{-1} \propto 1/f$ (cross symbols with error bars), indicate that the $E = 0.21\,\hat{\Omega}^{-1}$ trend (dashed line) captures the leading scaling with f, with no further systematic variation with the initial conditions P_0 or W_0.

of rotation for each experiment without invoking the initial conditions. The experimental initial conditions introduce the initial length scale s_I, along with additional fluxes of mass and downslope momentum, with the initial flux of azimuthal momentum being negligible. This leads to three independent dimensionless groups that depend on f, which can be characterised by *(a)* $\hat{\Omega} = \xi_I^{4/3} = f s_I^{4/3} Q_B^{-1/3}$, *(b)* P_0 defined using (3.12), and *(c)* W_0 defined using (3.12) (note that $V_0 \equiv 0$ is redundant). Figure 3.7*a* shows that the variation of E_{num} with $1/\hat{\Omega}$ is consistent with a linear trend, in support of the scaling $E \propto 1/f$. To investigate whether this trend captures the dominant variation with f, the renormalised quantity $E\hat{\Omega}$ is plotted versus $P_0^{-4/5}$ in figure 3.7*b*, and versus W_0^{-1} in figure 3.7*c*, where $P_0^{-4/5} \propto 1/f$ and $W_0^{-1} \propto 1/f$. The reduced quantity $E\hat{\Omega}$ shows no clear systematic dependence on $P_0^{-4/5}$ or W_0^{-1}, indicating that the scaling $E \propto 1/\hat{\Omega}$ captures the dominant variation with rotation rate. The results behave similarly for E_{att} (not shown) consistent with the broadly linear trend for $E_{\mathrm{att}} \propto E_{\mathrm{num}}$.

A scaling $E \propto 1/f$ was also observed in the experiments of Wells [2007] for axisymmetric flow on a rotating cone, which the author interpreted in terms of a scaling $E \propto \mathrm{Fr}_{\mathrm{geo}}$ where $\mathrm{Fr}_{\mathrm{geo}} = \sqrt{g'/h}\tan\alpha/f$ was calculated using the geostrophic Nof velocity $U_{geo} = g'\tan\alpha/f$ and the initial thickness h of the current. However, our theoretical model reveals the challenges associated with identifying a relevant Froude number for the entire trajectory of the flow, which evolves away from a state characterised by the initial thickness towards an attractor state that depends only on Q_B, f, α and s. There is no azimuthal velocity at the source, and hence the initial local Froude number $\mathrm{Fr}_i = w_0/\sqrt{b_0 g_0' \cos\alpha}$ is characterised by the initial velocity w_0, current thickness b_0 and reduced gravity g_0' ,which are all independent of f. If the entrainment ratio E is constant, the flow then evolves towards the local

Froude number in the attractor state,

$$\mathrm{Fr}_{\mathrm{att}} \equiv \frac{\sqrt{v^2+w^2}}{\sqrt{bg'\cos\alpha}} = \sqrt{\frac{5\tan\alpha}{4E+5K}} \left[1-\left(\frac{s}{s_{cr}}\right)^{8/3}\right]^{1/4}, \tag{3.33}$$

which varies along the flow. Thus the local Froude number differs from $\mathrm{Fr}_{\mathrm{geo}}$ as the flow develops, and the direct relevance of $\mathrm{Fr}_{\mathrm{geo}}$ to the entire flow is difficult to rationalize.

The predicted variation of Froude number along the flow also highlights the potential limitation of using a single constant value of the entrainment coefficient E along the entire length of the flow, as is commonly assumed when inferring entrainment values from experimental data. An alternative hypothesis is that the entrainment coefficient instead is a function of the local Froude number. To investigate this hypothesis, the theoretical solutions must be modified to allow the entrainment coefficient to vary along the flow, with E given by an as-yet-undetermined function of Froude number. A full investigation of the validity of these assumptions lies beyond the scope of the present study. However, an experimental design that allows estimates of entrainment accounting for local changes in Froude number along the current represents a compelling challenge for future work. The present theoretical framework offers a potentially valuable tool to contribute to such a goal.

3.6 Discussions

We have developed a theoretical framework for steady turbulent density currents flowing down a conical slope in a rotating system, from both an axisymmetric source of dense fluid and a single stream flow from a source of confined angular extent. As a demonstration of the utility of this modelling framework, we have presented solutions for flow with a constant entrainment coefficient and demonstrate that the flow evolves towards a critical level where there is no downslope flow. The inertia of the current causes it to overshoot a level of geostrophic balance between buoyancy and Coriolis forces, with the downslope propagation of the current subsequently arrested when the upslope component of the Coriolis force exceeds downslope buoyancy forces. In contrast to earlier studies of flows with negligible inertia [for a summary, see Griffiths, 1986; Shapiro and Hill, 1997; Wirth, 2009], our model of a turbulent entraining buoyancy-driven flow suggests the state of azimuthal flow is attained even in the presence of basal friction. However, we expect our model to be adequate in simulating only the approach of the density current to its critical level, and not any subsequent propagation in a state of geostrophic balance as was considered by Shapiro and Hill [1997] and Wirth [2009]. The steady model approximations break down at the critical level, as the plume thickness becomes large and violates the boundary layer approximation. Because of this we expected to observe a subsequent leakage of dense fluid down the slope. In fact, since the current does not transfer buoyancy downwards at the critical level, and in a statistical steady state the buoyancy flux should be constant at every depth level, the entire salt flux that enters at the source is transferred to the bottom of the tank through the transient leakage. Quantifying the transient leakage dynamics remains a difficult problem as it involves the parameterization of a transient turbulent Ekman layer subject to an overlying inertial flow, which remains an open question. For example, Wobus et al. [2011] showed that the viscous Ekman layer drainage in transient gravity currents is not well characterised by the drag law (3.10). To test the robustness of the existence of a critical level in our model, we obtained further solutions using a different parameterization of the frictional Ekman drag motivated by the results in appendix B of Wilchinsky et al. [2007], who observed that drag is oriented at approximately $10°$ to the current trajectory. Our alternative drag law replaces (3.10) with a drag that varies linearly with the plume speed but rotated by a constant angle relative to the flow. We found that the critical level still exists when frictional forces have a component perpendicular to the flow and the value s_{cr} depends on the friction coefficient K as well as on the angle to the current. Nevertheless, while the appropriate parameterizations of drag are still in question, the robust structure of the mean current and the distance at which it reaches the critical level allow us to infer fundamental properties of the turbulent fluxes that control the flow.

We derived analytical solutions for the special case of initial conditions with a constant buoyancy flux but negligible initial fluxes of mass and momentum delivered at the apex of the cone. This special solution serves as an attractor for general initial conditions, with the flow asymptotically approaching it as the current develops downslope. The attractor yields the prediction (3.32) for the dependence of the critical level on system parameters, which scales as $s_{cr} \propto (Q_B/Ef^3)^{1/4}$ in the limit of weak friction with $K/E \ll 1$. However, for experimental configurations with large rotation rates the true solution does not closely approach the attractor before it reaches a critical level, below which the solution to the plume equations does not exist. In this case, we constructed an approximate solution by using an asymptotic expansion around the attractor. This correction to the solution satisfies the initial conditions and proved to be a reasonable approximation across a range of appropriate parameters. We note here, that a similar analysis of equations modified to represent planar slope dynamics could be performed straightforwardly and leads to qualitatively similar solutions (see Appendix B.3).

Guided by our theoretical understanding of the plume dynamics, we conducted a set of laboratory experiments for the case of a single stream flow of confined angular extent. The experimental system exhibits behaviour consistent with the existence of a critical point. We explored experimentally the sensitivity of the critical point s_{cr} to the rotation rate of the reference frame. Furthermore, guided by our plume model solutions we inferred the entrainment rate under the assumption that E is constant for each experiment. The data suggest that for rotationally-dominated flow, the entrainment has the form $E \propto 1/f$, implying a suppression of turbulent mixing with increasing background rotation.

Such a dependence on rotation has previously been interpreted in terms of entrainment proportional to a geostrophic Froude number $Fr_{\rm geo} = \sqrt{g'/h}\tan\alpha/f$ [Wells, 2007], which would be consistent with the slower geostrophic flow at higher rotation rates leading to reduced shear and thus reduced mixing. However, if we assume a spatially uniform value of the entrainment ratio E, the theoretical model considered here shows that the flow develops from initial conditions where the input Froude number is independent of f, toward an attractor with a more complicated dependence on f. Hence, the local Froude number differs from the geostrophic Froude number $\mathrm{Fr}_{\rm geo}$, suggesting that the explanation for the observed reduction in entrainment with increased rotation rate is more complicated than previously anticipated.

The model developed here provides a theoretical structure that can be applied to future studies, allowing entrainment to be more precisely quantified in a well-defined experimental and theoretical setting. In particular, whereas previous experiments [Cenedese and Adduce, 2008; Cenedese et al., 2004; Wells, 2007] have sought to characterise entrainment as a function of Froude number, our theoretical solutions for constant entrainment demonstrate that the local Froude number evolves along the length of the flow. Whilst previous estimates of entrainment in rotating laboratory experiments have determined the mean entrainment for flows with given experimental conditions, our results suggest that the variation of Froude number along the flow may complicate attempts to infer a functional relationship $E(\mathrm{Fr})$ using a constant Froude number based on the initial conditions and/or purely geostrophic flow. Subject to suitable specification of an entrainment function E, our theory is applicable to a wide range of turbulent flows from jets to purely buoyancy driven currents.

Chapter 4

Separation of Mesoscale Eddies from Surface Ocean Fronts

The material contained in this chapter has been published in the *Journal of Physical Oceanography* under the title “Generation and separation of mesoscale eddies from surface ocean fronts” [Manucharyan and Timmermans, 2013].

4.1 Introduction

Instabilities associated with strong upper-ocean fronts can produce eddies that lead to significant vertical and lateral property exchanges. Many observational and numerical studies have examined these frontal dynamics, associated eddy formation, and cross-front exchanges [e.g. Boccaletti et al., 2007; Herbette et al., 2004; Lee et al., 2006; Spall, 1995; Spall and Chapman, 1998; Thomas, 2008; Thomas et al., 2008]. Spall [1995] formulated a mechanism for eddy formation at meandering upper-ocean fronts, with low potential vorticity (PV) water on the dense side of the front. When the front accelerates downstream, a compensating agestrophic cross-front flow results. The ageostrophic flow will be convergent on the dense side of the front, and, by conservation of mass, a deep cross-front flow will arise from the dense side to the light side in the subsurface layer below the front. Parcels subducted from a deep surface layer will be characterized by anomalously low PV and anticyclonic circulation to compensate for compression. This process typically forms a dipole, with anticyclonic vorticity driven by compression and cyclonic vorticity driven by stretching in the upper layer as fluid is carried away from the front [e.g. Spall, 1995]. Such dipoles have the ability to self-propagate and can transport anomalous water properties away from the front. Hogg and Stommel [1985] termed a pair of upper and lower-layer eddies of opposite sign a *heton* because of the self-propagating pair's ability to transport heat. Spall and Chapman [1998] formulated a theoretical relationship between the magnitude of eddy density flux across a surface front and the frontal parameters, under the assumption that the transport is produced by baroclinic eddy pairs [see also Pedlosky, 1985]. They argue that this flux is proportional to the self propagation speed of the dipole; their numerical model results confirm that cross-front exchanges are mainly via self-propagating eddy pairs. Hetons are also known to play an important role in transferring heat away from localized convection regions [Legg and Marshall, 1993; Legg et al., 1996] and have been observed to form at oceanic boundary currents [Ahlnäs et al., 1987; Carton, 2010, 2001; Chérubin et al., 2007; de Ruijter et al., 2004; Morel and McWilliams, 2001] and generated in laboratory experiments in stratified flows [e.g. Flierl et al., 1983; Stern and Whitehead, 1990; Van Heijst and Clercx, 2009; Van Heijst and Flor, 1989; Voropayev et al., 1991] and 2D soap films [e.g. Couder and Basdevant, 1986].

The analysis here is partially motivated by an observational study of mesoscale eddies in the Arctic Ocean that are believed to be generated by the instability of an upper-ocean front [Timmermans et al., 2008]. Timmermans et al. [2008] analyzed ocean temperature and salinity measurements beneath sea-ice cover to identify a large number of energetic anticyclonic eddies located immediately below the mixed-layer (in the upper Arctic halocline) in

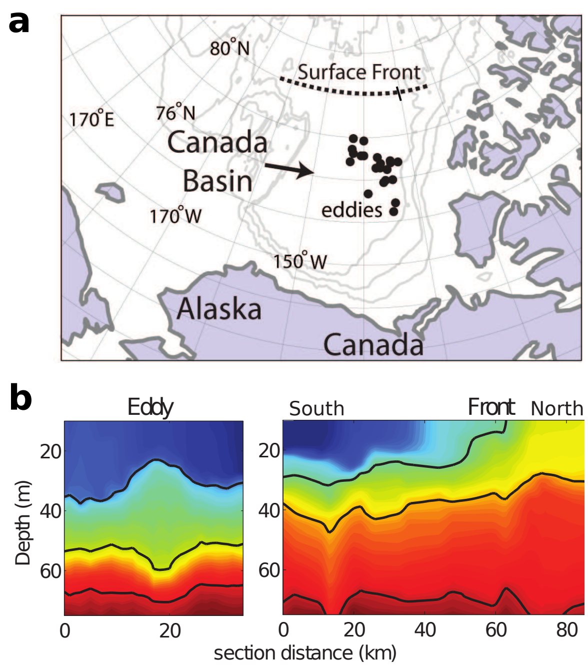

Figure 4.1: (a) Map of the Arctic Ocean's Canada Basin, showing the location of a surface front, and dots denoting the location of the sub-mixed-layer eddies studied by Timmermans et al. [2008]; the eddies are exclusively anticyclones and are believed to originate at the front. Note that the uneven distribution of eddies in the southern Canada Basin reflects the distribution of water-column profiles. (b) Cross sections of potential density (anomaly from 1000 referenced to the surface) through a typical eddy and perpendicular to the surface front (modified from Timmermans et al. [2008]; data are from Ice-Tethered Profilers [www.whoi.edu/itp, Krishfield et al. [2008]; Toole et al. [2011]]).

the Arctic Ocean's Canada Basin (Fig. 4.1a). The anticyclones have typical diameters of about 10 km (Fig. 4.1b), and strong azimuthal velocities, up to around 30 cm/s. The anomalous water mass signature of the Arctic eddies suggests that they are generated at a surface density front observed around $\sim 80^0$N and extending approximately in the zonal direction (Fig. 4.1a). The density front separates two distinct water masses: a relatively lower density (fresh) and shallow mixed layer to the south, and a relatively higher density (salty) and deep mixed layer to the north[1] (Fig. 4.1b). Timmermans et al. [2008] argue that the mechanism leading to the generation of the anticyclones is consistent with the mechanism outlined by Spall [1995].

The sub-mixed layer eddies studied by Timmermans et al. [2008] are observed at great distances away from the front where they are purported to originate – up to 500 km (Fig. 4.1a). The mechanisms that are responsible for such a separation are not understood as observations in this region are limited. Here, we propose that the eddies move away from the front as self-propagating dipoles, and examine the conditions under which this is possible. Through high resolution numerical simulations and idealized analytical models, we examine eddy formation at unstable upper ocean fronts, and most importantly, the conditions under which eddies could propagate away from the originating front.

The paper is outlined as follows. In the next section we describe the numerical model employed to simulate frontal instability and eddy formation, and consider initial frontal configurations appropriate for the Arctic case. In section 4.3, we describe frontal instabilities, slumping and eddy formation, demonstrating the possibility that self-propagating dipoles can propagate away from a slumping front. In section 4.4, we explore the dynamics of dipole self-propagation and derive an analytical expression for the maximum distance a dipole could travel away from its formation site. The

[1]Note that the surface Arctic Ocean beneath sea ice is mostly at the freezing temperature, so the cooler mixed layer is to the north.

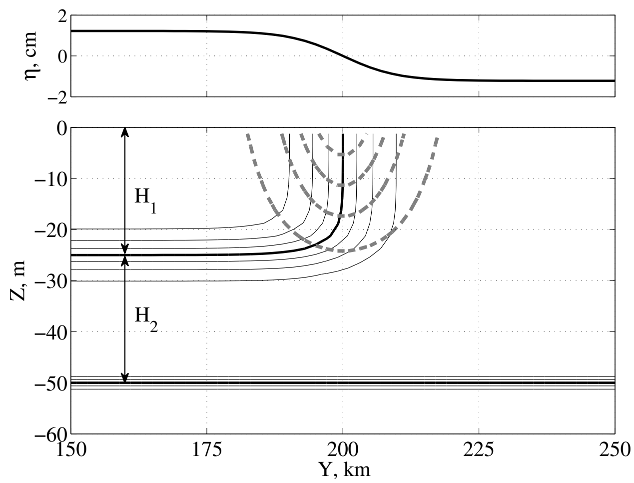

Figure 4.2: Schematic illustrating an initial frontal configuration, approximately corresponding to the Arctic front (Fig. 4.1). (Top) the elevation of the free surface η across the front. (Bottom) black contours showing isopycnals spaced by 0.125 kg/m^3; the two thick black contours are isopycnals $\rho_1 = 23.5$ kg/m^3 and $\rho_2 = 24.25$ kg/m^3 (anomalies from 1000) and the dashed contours denote the along-front velocity with 2 cm/s contour spacing and a maximum contour of 7 cm/s.

radius of a self-propagating dipole trajectory depends critically on the ratio ϵ of translation velocities of each vortex in the dipole. Section 4.5 examines the probability of generation of nearly balanced dipoles (i.e. $\epsilon \approx 1$) which can self-advect far from the front. In section 4.6, guided by the idealized model predictions, we examine the relationship between initial frontal parameters and the properties of dipoles generated. Results are summarized and discussed in section 4.7.

4.2 Numerical model set-up

The instability of an idealized surface front is simulated numerically with the MIT general circulation model [Adcroft et al., 2008]. This is a primitive equation ocean model, which we use in its hydrostatic formulation. An f-

plane approximation is used for all but one experiment; the β-effect (due to the curvature of the earth) is negligible at the high latitudes of interest. The model domain is a rectangular prism with dimensions 300 km by 400 km in the horizontal, and 400 m in the vertical. Horizontal resolution of the model is 0.5 km and it has 28 levels in the vertical, with resolution varying from 2.5 m at the surface to 200 m at the bottom. The high resolution is required to resolve mesoscale dynamics with typical values for the deformation radius of the first baroclinic mode throughout our experiments ranging from about 3 to 10 km. Horizontal boundary conditions are periodic in the along-front direction (x-direction), with free slip and no buoyancy flux at the north and south boundaries of the domain. A free-slip condition is applied at the bottom, with no wind or buoyancy forcing at the surface. The simulations presented here model the relaxation of a surface density front from its initial state.

Horizontal viscosity and horizontal tracer diffusivity are set equal to 2 m^2/s, vertical diffusivity to 10^{-5} m^2/s, and a biharmonic viscosity to 10^5 m^4/s – the minimum values required for numerical stability of the model at a given resolution. We have tested a range of vertical and horizontal resolutions as well as various diffusivities to conclude that the chosen values are sufficient to resolve the relevant processes involved in frontal instability and eddy formation.

4.2.1 Initial conditions

The following idealized cross-frontal (y-direction) structure is specified (see Fig. 4.2):

$$\rho - \rho_0 = \frac{\Delta\rho_y}{4}[\tanh(\frac{-z+H_1}{\delta h})+1][\tanh(\frac{y-L/2}{L_f})-1]+ \\ + \Delta\rho_z \mathcal{H}(z-H_1-H_2) \quad (4.1)$$

[see Thomas, 2008]. Here, L_f is the frontal width, $\Delta\rho_y$ is density difference across the upper layer (layer 1 of thickness H_1, Fig. 4.2) and $\Delta\rho_z$ is density difference across the underlying layer (layer 2 of thickness H_2 on the light side of the front), $\rho_0 = 1023$ kg/m^3 is a reference density, $\delta h = 5$ m is the thickness of the pycnocline separating the layers, L is the domain size in the cross-frontal direction, and $\mathcal{H}$ is the Heaviside step function. The initial frontal structure is uniform in the x-direction.

The initial elevation of the free surface η and velocity profiles (U, V) are calculated using the thermal wind balance, and assuming a level of no motion at the bottom of the domain:

$$\eta(y) = \frac{1}{\rho(y,0)} \int_{-H}^{0} [\rho(y,z) - \frac{1}{2}(\rho(0,z) + \rho(L,z))] dz, \tag{4.2}$$

$$U(y,z) = \frac{g}{f} \int_{-H}^{z} \frac{1}{\rho} \frac{\partial \rho}{\partial y} dz, \quad V(y,z) = 0, \tag{4.3}$$

where f is the Coriolis parameter and $H = 400$ m is the total depth of the domain. Small-amplitude random perturbations (white noise) are superimposed on the initial density distribution to initiate frontal instability. For each set of initial conditions we perform at least 6 simulations with different perturbation field realizations to improve the reliability of eddy statistics. This is an alternative to having a wider model domain in the along-front direction; with typical frontal meanders having about 10 km length scales, 6 experiments allows for the simulation of hundreds of frontal meanders. Numerical calculations are performed for 70 model days (1 day $\approx$ 2 inertial periods), which is sufficient for the instabilities to substantially run down the front.

The key parameters prescribing the front are $H_{1,2}$, L_f and $\Delta\rho_y$ ($\Delta\rho_z$ is less important). The relevant non-dimensional parameters are

$$Ro = \frac{g_1' H_1}{f^2 L_f^2}, \quad Bu = \frac{g_1'(H_1 + H_2)}{f^2 L_f^2}, \tag{4.4}$$

where the Rossby number Ro (related to the baroclinic component of the flow) characterizes the relative importance of Coriolis to inertial terms in the momentum equation, and the Burger number ($Bu = R_d^2/L_f^2$) characterizes the width of the front compared to the baroclinic deformation radius $R_d = \sqrt{g_1'(H_1 + H_2)}/f$ (with reduced gravity $g_1' = g\Delta\rho_y/\rho_0$). The remaining dimensionless parameter is the frontal aspect ratio $(H_1 + H_2)/L_f$.

For the Arctic front (Fig. 4.1b), $g_1' \approx 0.01$, $H_1 \approx 30$ m, $H_2 \approx 20$ m, $f = 1.4 \times 10^{-4}$ s^{-1} and $L_f \approx 10$ km, giving $Ro \approx 0.15$, $Bu \approx 0.25$ and $R_d \approx 5$ km (experiment #3, Table 4.1). In section 4.6, we investigate whether and how the properties of generated dipoles depend on the initial frontal configuration by simulating the evolution for a range of initial conditions as outlined in Table 4.1.

4.2.2 Methods

We approximate the 3-dimensional output of the numerical model as three two-dimensional layers[1]. The layers are separated by isopycnals: 23.5 and 24.25 kg/m^3 (Fig. 4.2), except for experiments #14 and 15, Table 4.1. For a given layer, we calculate its thickness h and the vertically averaged velocity field $(\overline{U}, \overline{V})$ in the layer. This is similar to splitting the fluid motion into contributions from the first and second baroclinic modes. In numerical experiments the vertical stratification is diffusing with time, thus slightly altering the vertical structure of the baroclinic modes, however its general shape is preserved making the splitting into layers a useful simplification.

We use these 2D velocities, along with layer thicknesses, to compute a diagnostic for the flow dynamics – the potential vorticity Q:

$$Q = \frac{\zeta + f}{h}, \quad \zeta = \frac{\partial \overline{V}}{\partial x} - \frac{\partial \overline{U}}{\partial y}, \tag{4.5}$$

[1]Note that the thickness of the bottom layer is relatively large and for simplicity of the analysis, we later consider it to be motionless (i.e., assuming 2.5-layer dynamics).

#	H_1 m	H_2 m	g'_1 m/s^2	L_f km	U_g cm/s	Ro	Bu
1	20	30	0.01	10	7.0	0.10	0.25
2	25	30	0.01	10	8.8	0.12	0.25
3	30	20	0.01	10	10.5	0.15	0.25
4β	30	20	0.01	10	10.5	0.15	0.25
5	35	15	0.01	10	12.3	0.17	0.25
6	40	10	0.01	10	14.0	0.20	0.25
7	35	65	0.01	10	12.3	0.17	0.50
8	35	165	0.01	10	12.3	0.17	1.00
9	20	5	0.01	10	7.0	0.1	0.13
10	80	20	0.01	10	28.0	0.4	0.50
11	30	20	0.01	5	21.0	0.6	1.00
12	30	20	0.01	20	5.3	0.04	0.06
13	30	20	0.01	40	2.6	0.01	0.02
14	30	20	0.04	10	42.0	0.15	1.00
15	30	20	0.0025	10	2.6	0.15	0.06

Table 4.1: Frontal configurations investigated in the numerical experiments. Parameters are defined in the text. Experiment $\#4\beta$ used $\beta = 10^{-11}$ s^{-1}m^{-1}.

where ζ is the relative vorticity and h is the layer thickness. The analytical model of eddies presented in section 4 uses the linear quasi-geostrophic equations, and the linearized version of the PV anomaly with respect to the background is computed as

$$Q' = \frac{\zeta}{\bar{h}} - \frac{fh'}{\bar{h}^2}, \tag{4.6}$$

where $\bar{h}$ represents the mean layer thickness of the surrounding fluid, and h' is the perturbation from that mean.

On short time scales, dissipative processes such as momentum and tracer diffusivity have a negligible effect on the first order dynamics, and the subducted parcels preserve their initial PV thus making this quantity a suitable water mass tracer [see e.g. Spall, 1995]. On time scales of order months vertical diffusivity acts to dissipate the PV anomalies associated with eddies.

4.3 Frontal instabilities and dipole formation

4.3.1 Slumping

We begin with a description of the evolution of the front as the model progresses (Fig. 4.3). Instabilities and eddies release potential energy and slump the front. After ~20 inertial periods (IP) from the beginning of the simulation instabilities with the shortest resolved wavelengths are observed; these grow to form eddies which are generated on top of slower growing mesoscale instabilities having length scales of a few tens of kilometers [see e.g. Boccaletti et al., 2007; Fox-Kemper et al., 2008; Lapeyre et al., 2006; Sakai, 1989; Stone, 1966]. At about 50 IP the mesoscale instabilities are fully developed while the smaller scales are mostly absent (Fig. 4.3). An inverse cascade of energy to larger scales [Rhines, 1979; Smith and Vallis, 2001] is clearly present in the simulations (Fig. 4.4a), with the length scales of the dominant perturbations increasing linearly with time (Fig. 4.4b). The increase in length scale of the

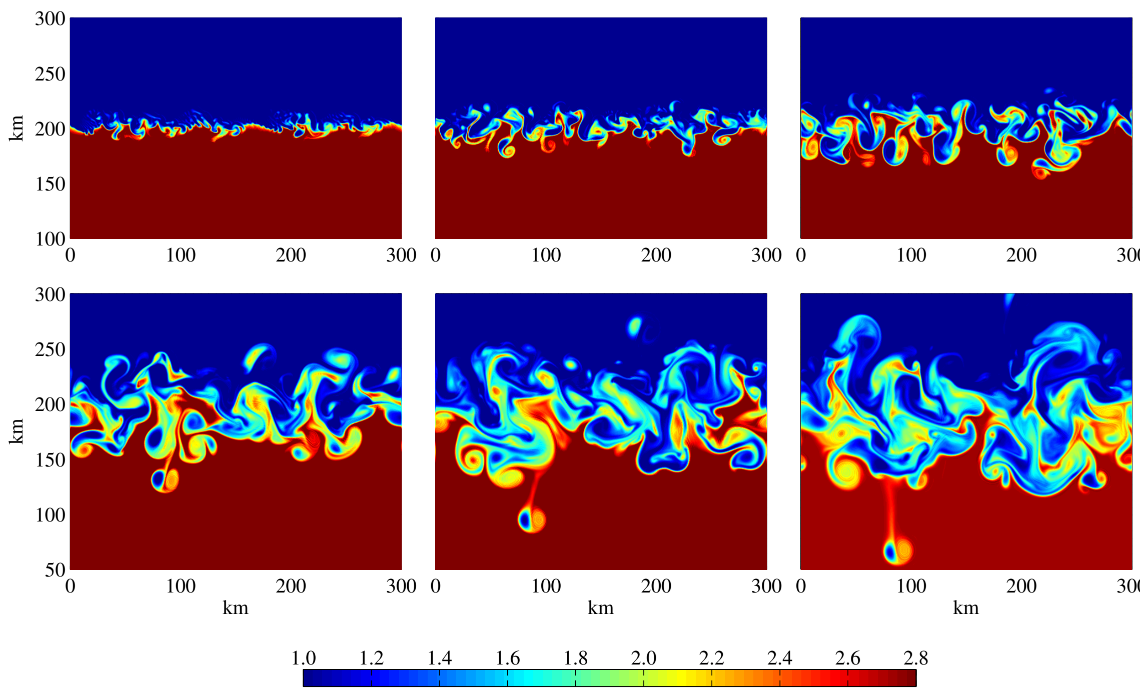

Figure 4.3: Plan view of the model domain showing the formation of frontal instabilities as a simulation (with initial conditions corresponding to experiment #5, Table 4.1) progresses (snapshots are taken on model days: 12, 16, 23, 35, 47, and 58 [1 day ≈ 2 IP]). Colors indicate PV (Eq. 4.5) in layer 2, normalized by the value on the deep side of the front ($f/(H_1 + H_2)$). Note the formation of dipoles in the early stages, and later separation of a dipole from the front.

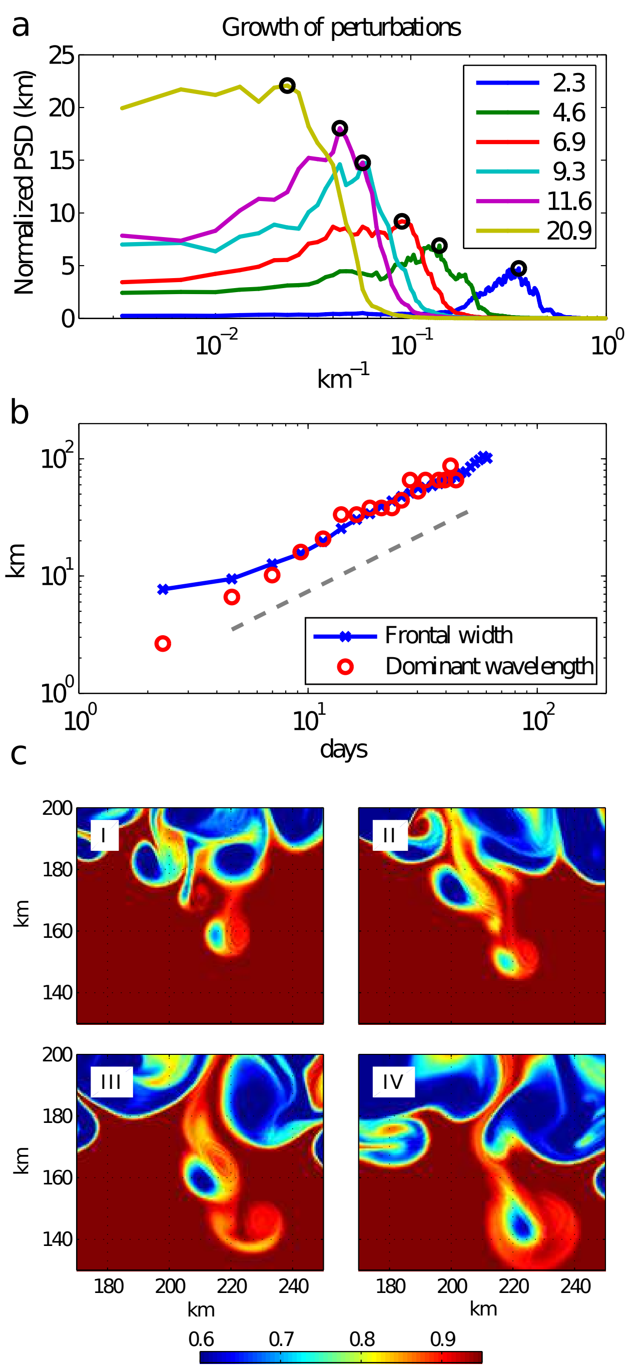

Figure 4.4: a) Time evolution of the normalized power spectral density (PSD) of free-surface height anomaly along the front (legend shows time in days); circles denote the dominant wavenumber. b) Frontal width (blue) and the dominant perturbation scale (red) vs. time. c) Time sequence of PV anomaly in layer 2 demonstrating the growth of separated eddies through mergers; panels I-IV correspond to days 30, 35, 44, 51 for the experiment shown in Fig. 4.3.

dominant perturbations is a result of two processes: merger of eddies of the same vorticity sign (Fig. 4.4c) and the fact that longer wavelength meanders have slower growthrates [e.g. Eady, 1949]. Several studies have addressed the details of dipole-dipole interaction [e.g. Reinaud et al., 2009; Sokolovskiy and Verron, 2000; Voropayev et al., 1991], with dipole instabilities also known to lead to splitting of a single dipole [Reinaud et al., 2009].

The evolution of the frontal slumping region (Fig. 4.4b) is estimated by calculating the width in the cross-front direction of an interval over which the eddy kinetic energy is at least 60% of its maximum value (corresponding to 2 standard deviations of a Gaussian fit). Initially, the frontal width is larger than the scale of dominant perturbations, corresponding to multiple eddies forming within the frontal region (Fig. 4.4b). After about 10 days, the frontal width is of the same size as the scale of dominant eddies and the two grow at the same rate. The width increases with time almost linearly, which corresponds to growth of the energetic area by merger of vortex dipoles [see Carton, 2001, and references therein]. The slumping speed poses a significant constraint on the probability of eddy detachment from the front as slow moving eddies are likely to be re-incorporated into the front. This is addressed in section 4.6.

4.3.2 Dipole formation

The simulations show dipoles to be common features, which are easily identified as PV anomalies of opposite sign located in different layers and shifted horizontally from each other (Figs. 4.5 and 4.6). In the early stages of growth of a frontal meander, layer 1 meanders at a distinctly smaller scale than layer 2; the ratio of scales is approximately proportional to the ratio of the first to second baroclinic deformation radii (see Appendix A.1). The layer 1 meander is offset to the right (east) side of the layer 2 meander, in the direction of the vertical shear of the mean front. The layer 1 meander grows faster than that in layer 2 and forms a cyclone by pinching off from

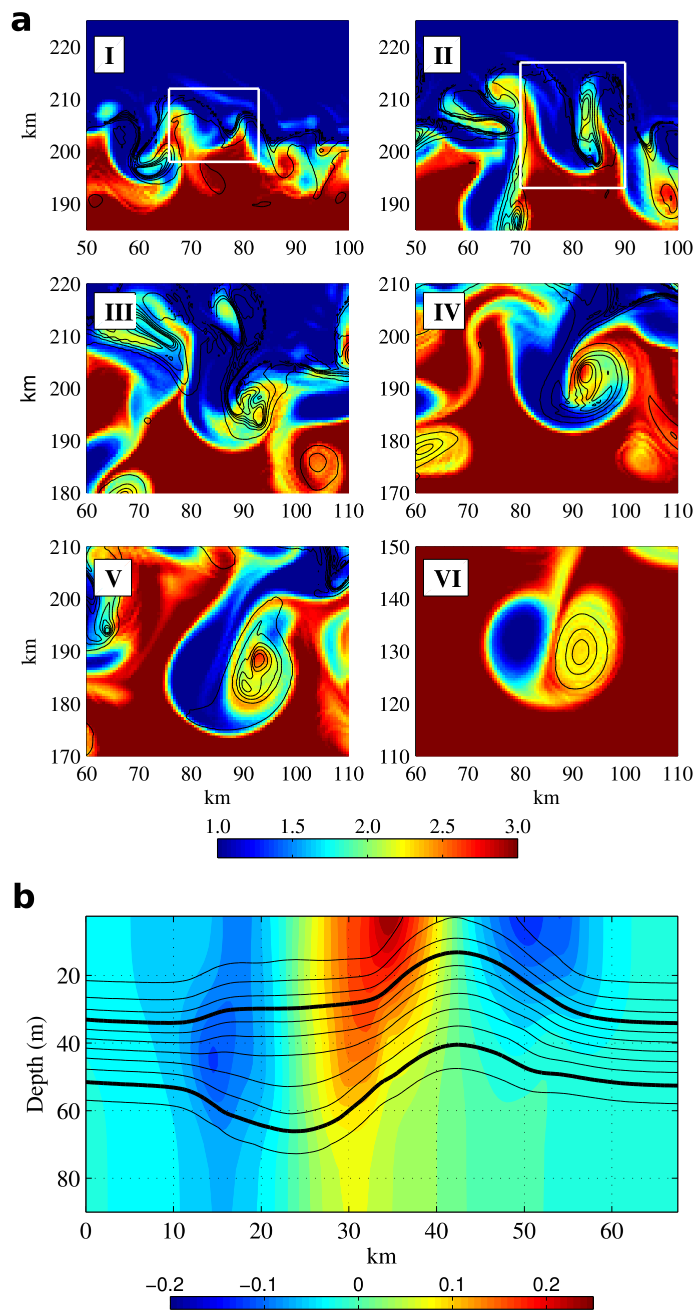

Figure 4.5: (a) Potential vorticity field in layer 1 (black contours) and layer 2 (colors) showing the time evolution of frontal meanders leading to production of a typical dipole; frames I-VI are model days 12, 14, 16, 18, 21, and 35 (Fig. 4.3). (b) Vertical section through the center of a typical dipole that clearly escaped the influence of its originating front (Fig. 4.3, model day 47). Colors indicate speed (m/s) perpendicular to the section, and contours are isopycnals (with spacing 0.125 kg/m^3). Note the effects of vertical mixing as compared to the initial configuration.

the strongly elongated high PV anomaly water mass. At the same time, the layer 2 meander grows and as it penetrates the shallow side of the front it develops anticyclonic vorticity. At this stage the cyclone in layer 1 has developed a cyclonic flow field in layer 2 that advects the anticyclone away from the front (this process of self advection of dipole pairs is known as the *hetonic mechanism*, [see e.g. Gryanik, 1983; Gryanik et al., 2006; Hogg and Stommel, 1985]). Note that the upper layer cyclone must be offset horizontally from the lower layer anticyclone in the direction of the mean flow, otherwise the hetonic mechanism would damp the perturbation. Ultimately, the layer 2 meander becomes sufficiently elongated that the anticyclone also pinches off. After separation from the front the PV anomalies that constitute each eddy adjust to the flow field associated with these anomalies through nonlinear advection to eventually form a pair of coherent stable vortices. Fig. 4.6 illustrates how the cyclone (positive PV anomaly in layer 1) originates within the frontal outcropping region (having very high PV) while the anticyclone (negative PV anomaly in layer 2) originates on the deep (low PV) side of the front. There is a signature of a weaker anticyclone located directly below the cyclone. The anticyclonic PV anomaly is created due to diffusive spin down of the relative vorticity in the second layer generated from a cyclone in a first layer. The magnitude of this effect can be reduced by decreasing horizontal viscosity, although at the expense of increasing the model resolution.

The majority of dipoles observed in the numerical experiments do not evade the influences of the slumping front and inverse cascade. Most dipoles generated by the instability recirculate back to the front due to their curved trajectories and the increasing frontal width. There are cases, however, where a dipole is observed to escape the frontal influence (e.g. final panel, Fig. 4.3). The observed self-propagation speed of the detached dipole in Fig. 4.3 is ~ 4 cm/s (corresponding to about 100 km in a month). Attention is focused here on eddies advected from the side of the front with the deep mixed layer to the shallower side as these are the eddies relevant to the Arctic Ocean. While

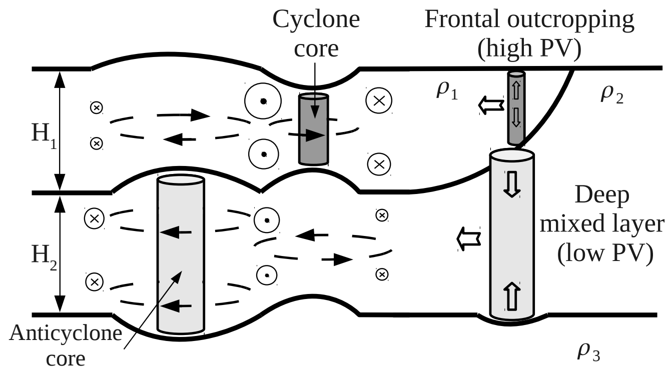

Figure 4.6: Schematic of dipole formation indicating the water mass origins of the cyclone and anticyclone.

numerical simulations show eddies forming on the deeper side of the front, these are surface intensified features and hence would be dissipated rapidly by mixing processes either of frictional origin due to winds and the motion of sea ice, or due to convection arising from surface buoyancy fluxes. The sub-mixed layer anticyclones on the shallow side of the front are likely to be preserved for longer times as they are insulated from surface processes by the strong stratification at the base of the mixed layer. We hypothesize here that dipole self-propagation is the key to understanding the shallow anticyclones observed in the Arctic Ocean. In the following sections, we examine what dipole characteristics favor their escape from the frontal region, and whether there are particular frontal configurations that lead to enhanced production of separated dipoles.

4.4 Dipole trajectories

Dipoles are composed of the two dominant PV anomalies (cyclonic in layer 1 and anticyclonic in layer 2), shifted horizontally by a distance Δ of about one eddy radius (e.g. Fig. 4.5). This induces a self propagation which can be understood in terms of interactions between the two vortices – the core of

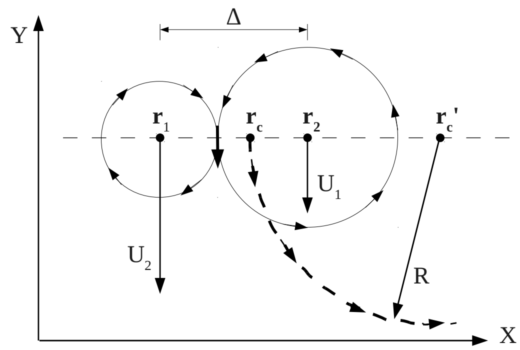

Figure 4.7: (a) Schematic indicating the parameters of the dipole; symbols shown are as defined and used in the text.

the first vortex is advected by the velocity field induced by the second vortex and vice-versa [e.g. Saffman, 1992]. While much progress has been made in understanding the dynamics of dipoles [see Carton, 2001, and references therein], here we develop a specific formalism that allows us to interpret and analyze modeled frontal instabilities in the context of dipole trajectories.

4.4.1 Kinematics

To calculate dipole trajectories, consider the constant translation velocities of each vortex in the dipole U_i (for $i = 1, 2$), defined positively for a cyclone-anticyclone pair as in Fig. 4.7. The propagation velocities are directed perpendicular to the line connecting the centers of the vortices and thus the separation distance between the vortices Δ does not change in time. The kinematic equations describing the time evolution of center positions $\mathbf{r}_i = (x_i, y_i)$ of the vortices are as follows:

$$\dot{\mathbf{r}}_1 = \frac{U_1}{\Delta}\,\mathbf{k} \times (\mathbf{r}_2 - \mathbf{r}_1) \tag{4.7}$$

$$\dot{\mathbf{r}}_2 = \frac{U_2}{\Delta}\,\mathbf{k} \times (\mathbf{r}_2 - \mathbf{r}_1). \tag{4.8}$$

Combining these equations yields an oscillator equation for the separation distance between vortices,

$$(\ddot{\mathbf{r}_2 - \mathbf{r}_1}) + \omega^2(\mathbf{r}_2 - \mathbf{r}_1) = 0, \tag{4.9}$$

where frequency $\omega = (U_2 - U_1)/\Delta$. Thus, in a reference frame moving with one vortex the other vortex rotates around it and vice versa; in the special case of balanced vortices (i.e. $U_1 = U_2$) they move parallel to each other.

It is useful to define the coordinate of a self propagating dipole (same sign for U_1 and U_2) as

$$\mathbf{r}_c = \frac{U_2\mathbf{r}_1 + U_1\mathbf{r}_2}{U_1 + U_2}, \tag{4.10}$$

where $\mathbf{r}_c$ lies between the two eddies and is an analogue of the center of vorticity for two dimensional point dipoles. Its derivative with respect to time defines a dipole translation speed $U_d = 2U_1U_2/(U_1 + U_2)$. Obtaining a solution for $\mathbf{r}_{1,2}$ for an example dipole with cyclone and anticyclone initially at $(0, 0)$ and $(\Delta, 0)$ respectively, we find that the dipole center propagates on a circular path with coordinates

$$\mathbf{r}_c - \mathbf{r}'_c = 2\Delta\frac{U_1U_2}{U_2^2 - U_1^2}\left[\begin{array}{c} -\cos\ \omega t \\ -\sin\ \omega t \end{array}\right], \tag{4.11}$$

where $\mathbf{r}'_c$ is the center of a circle (Fig. 4.7). Therefore, the radius of a dipole trajectory R depends critically on the ratio of vortex propagation velocities ϵ:

$$R = \frac{2\Delta}{|\epsilon - \frac{1}{\epsilon}|}, \quad \epsilon = \frac{U_2}{U_1}. \tag{4.12}$$

The derivation is valid not only for U_1 and U_2 constant in time, but also for cases where their ratio ϵ is constant in time, since the time dependency can be incorporated into a rescaled time variable. In this case the dipole would move along a circular trajectory with a time-dependent velocity. This proves to be a useful result as we observe that the dipole vortices decay in time (due to diffusion and entrainment) at a similar rate such that ϵ remains relatively constant.

The radius of the trajectory varies strongly in the region of $\epsilon \approx 1$ where the dipole trajectory is essentially a straight line in our finite domain (e.g. Fig. 4.3, final panel). However, for values of $\epsilon > 1.6$ (or $\epsilon < 0.6$) the radius becomes less than twice the separation distance Δ. In this case, the dipole has a strongly curved trajectory, and takes little time to propagate back to its originating front and be engulfed. The circular trajectories of dipoles are clearly observed in our numerical simulations, and these paths lead to the majority of initially detached dipoles being re-absorbed by the front. Thus, the value of ϵ poses a strong constraint on the probability for dipole escape far from the front (i.e., $R >> \Delta$).

Because it is not possible to split the velocity field obtained from the numerical model into advecting contributions from each of the two eddies in a dipole, we proceed by developing an idealized dynamical model of the dipole flow field based on PV anomalies of each of the two eddies. Our aim is to identify factors controlling the ratio of self-propagating velocities ϵ.

4.4.2 Dynamics

It is intuitive that for a given dipole its ratio ϵ should be determined by the relative strength of the cyclone and anticyclone as well as the stratification parameters of the ambient fluid. We thus proceed to derive this relationship using a quasi-geostrophic set of equations [Pedlosky, 1982; Vallis, 2006], which is sufficient to represent the essential dynamical features of dipoles [see e.g. Carton, 2001; Flierl, 1987; Flierl et al., 1980; Polvani, 1991; Swaters, 1995]. Here, we assume 2.5-layer dynamics (i.e., 2 active layers, and a bottom stationary layer) with eddies in a dipole represented as delta functions of PV anomalies with magnitudes $S_{1,2}$ (the point vortex assumption is relaxed later). We further simplify by considering the linear quasi-geostrophic equations with the rigid lid approximation:

$$\nabla^2\psi_1 + F_1(\psi_2 - \psi_1) = S_1\delta(\mathbf{r}_1), \tag{4.13}$$

$$\nabla^2\psi_2 + F_2(\psi_1 - \psi_2) - F_3\psi_2 = S_2\delta(\mathbf{r}_2), \tag{4.14}$$

where $\psi_{1,2}$ are the stream functions for layer 1 and layer 2 respectively, and $\mathbf{r}_1 - \mathbf{r}_2 = \mathbf{\Delta}$. The stratification parameters are:

$$F_1 = \frac{f^2}{g_1' H_1}, \quad F_2 = \frac{f^2}{g_1' H_2}, \quad F_3 = \frac{f^2}{g_2' H_2}, \tag{4.15}$$

where g_1' and g_2' denote reduced gravity corresponding to the density difference across the base of layer 1 and layer 2 respectively. It is useful to split the solution to this equation into two contributions: the circulation $u_2(r)$ that arises in layer 2 due to the vortex in layer 1 that advects the core of the vortex in layer 2, and similarly the circulation $u_1(r)$ (see Appendix A.1). These velocities are found to be

$$u_2(r) = -S_1F_2\frac{K_1(r/\lambda_1)/\lambda_1 - K_1(r/\lambda_2)/\lambda_2}{\lambda_2^{-2} - \lambda_1^{-2}} \tag{4.16}$$

$$u_1(r) = \ S_2F_1\frac{K_1(r/\lambda_1)/\lambda_1 - K_1(r/\lambda_2)/\lambda_2}{\lambda_2^{-2} - \lambda_1^{-2}}. \tag{4.17}$$

where K_1 is the first order modified Bessel function of the second kind, and $\lambda_{1,2}$ are the first and second baroclinic deformation radii (defined in the Appendix A.1). Bessel functions appear in the solutions, because the equation for the baroclinic mode involves a Laplace operator in cylindrical coordinates. In a special case of $F_3 = 0$ the equation becomes equivalent to a 2-layered system and would have a barotropic mode with a logarithmic stream function profile ($1/r$ velocity decay). In the case of point vortices, the functional dependence of the propagating velocities is the same. Note that for point vortices $U_i = u_i(r = \Delta)$. This allows for a simple relation for their ratio

$$\epsilon = \frac{S_1}{S_2}\frac{H_1}{H_2}. \tag{4.18}$$

Thus, for a dipole to propagate far from the front (ϵ close to unity), its cyclone and anticyclone components should be balanced in strength expressed in terms of their PV anomalies scaled by the mean layer thicknesses.

The relation (4.18) is obtained for point vortices and provides useful insights, however numerical simulations show that PV anomalies of each eddy in a dipole are better represented with a Gaussian profile (Fig. 4.8a). Radially symmetric Gaussian PV anomalies allow for simplifications and the use of Hankel transformations to obtain stream function profiles (Eq. A.24, Appendix A.2). The analytical model uses the radii and magnitudes of the PV anomalies and a separation distance Δ to obtain the velocity profiles for each dipole. Simulations indicate four PV anomalies (two in each layer) associated with a single dipole, although the dominating effects on the velocity field are due to the cyclone in layer 1 and the anticyclone in layer 2 (Figs. 4.5b, 4.6 and 4.8a). This approximate linear solution agrees reasonably well with the velocity fields of dipoles in the numerical model, with the biggest discrepancies in the regions of overlap between the two vortices in the dipole (Fig. 4.8). This disagreement likely arises from comparing the 2.5-layer theory to motions in a continuously stratified fluid. This is analogous to assuming that all the motion occurs in the first and second baroclinic modes, which neglects contributions from higher modes. Further, we were able to make use of a fully linearized model by splitting the full velocity field into two contributions, one from the cyclone and the other from the anticyclone. This approximation is likely to have the largest errors in the overlap region, where due to strong currents the nonlinearities in the PV equations are not insignificant. Nevertheless, the analytical model results are useful in that they provide a ratio of self-propagating velocities, essential for assessing the

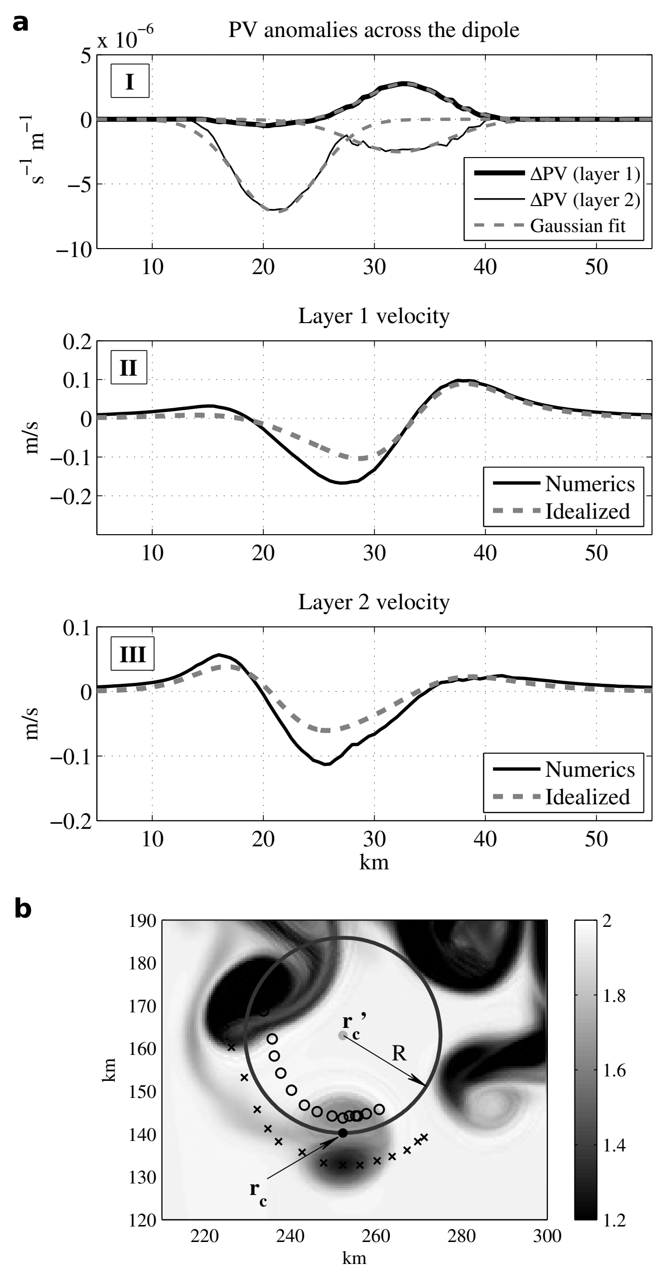

Figure 4.8: (a) (I) PV anomalies (Eq. 4.6) across a dipole in layer 1 and 2, and the corresponding Gaussian fit to individual eddies (black dashed line). Velocity profiles, in (II) layer 1 and (III) layer 2, across a dipole taken from the output of the numerical model (solid black) and calculated using an idealized Gaussian vortex model (dashed gray).(b) An example dipole trajectory (the normalized PV field in layer 2 is shown, initial conditions are experiment #2, Table 4.1) with the estimated radius derived from the idealized theoretical model prediction based on the magnitudes of the dipole PV anomalies. The crosses show the path of the anticyclone in layer 2 and the circles the cyclone in layer 1.

trajectory of a dipole.

If the sizes of cyclone and anticyclone PV anomalies are the same within the Gaussian approximation, the expression for ϵ is identical to that for point vortices (Eq. 4.18), since the solutions for self-propagating velocities in both layers have the same functional dependence (Appendix A.1). It should be noted that in the non quasi-geostrophic simulations the average size of a layer 1 cyclone is about 10-20% smaller than a layer 2 anticyclone because the presence of eddies alters the background vorticity and layer thickness leading to smaller deformation radii for cyclones.

Thus, a combination of the idealized dynamic and kinematic models gives a prediction for the potential propagation distance of a dipole assuming no interactions with the front or other eddies. A comparison of a typical model dipole trajectory to a trajectory predicted by the idealized model based on the observed dipole PV anomalies (Fig. 4.8b) indicates generally good agreement after the initial stages[1].

4.5 Probability of balanced dipoles

The essential parameters, ϵ and Δ, that determine propagation of a dipole depend upon the characteristics of the particular frontal meander from which the dipole was produced. While it is impossible to predict the dynamics of each frontal meander produced throughout the duration of a model run, progress can be made by assuming that there exists a probability density function (PDF) for the properties of dipoles shed from a front having specified initial frontal configuration.

The model runs presented in this section are initialized by parameters appropriate for the Arctic case (Fig. 4.1b, experiment #3 Table 4.1). For each model simulation, dipoles are located by making use of the fact that

[1]Note that dipole trajectories are typically limited to propagate only about a quarter of the circle that defines their propagation before merging with other eddies or frontal meanders

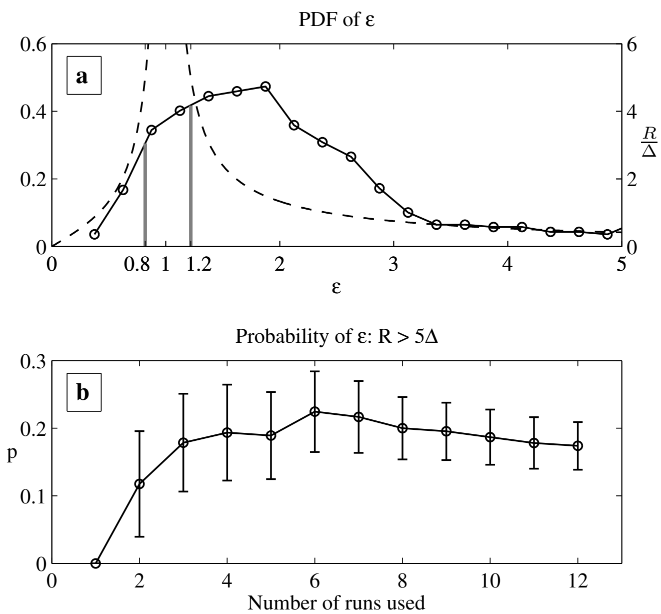

Figure 4.9: a) PDF of ϵ (solid line, left $y-$axis) and dependence of R/Δ on ϵ (Eq. 4.12, dashed line, right $y-$axis). Bin-size is 0.25. b) Convergence of the probability p of a balanced dipole vs. the number of simulations performed. A total of 115 dipoles were identified in an ensemble of 12 model runs for the frontal configuration #3 (Table 4.1).

they are composed of vortices with strong PV-anomaly maxima and minima in layers 1 and 2 respectively. These PV extrema are offset horizontally by a distance Δ which is of a similar magnitude as the characteristic size of each eddy. For the statistics we choose only coherent pinched-off dipoles with a life span of at least ~ 5 model days. After identifying prominent dipoles, we fit Gaussian profiles through their PV anomaly fields (e.g. Fig. 4.8a). In this way, for each dipole we obtain the strengths of the two vortices S_i, their horizontal length scales σ_i, and a separation distance Δ. The ratio of velocities ϵ is calculated for each dipole using the analytical solution with the Gaussian fits (see Appendix A.2). For most observed dipoles ϵ falls between 0.5 and 3, with the PDF centered at $\sim$1.5, implying that there are more eddy pairs where the cyclone dominates (Fig. 4.9a). The PDF has a long tail in the distribution at large ratios, where the cyclone is several times stronger than the anticyclone. On the small ϵ side where the anticyclone in a given dipole is stronger than the cyclone, there is a sharp cut-off at $\epsilon \approx 0.6$, implying that there is a limit to the relative strength of an anticyclone in a dipole (Fig. 4.9a).

The imbalance in strengths of eddies that compose a dipole can be understood by considering the range of possible PV anomalies for the cyclones and anticyclones. The originating front has a top layer that outcrops to the surface and the PV jump across the front can be very large (technically, infinite). This means that water parcels that are transported by meanders from the immediate frontal region to the light side of the front could have very large cyclonic PV anomalies (Fig. 4.6). On the other hand, in layer 2 there is only a finite PV gradient across the front, which bounds the PV anomaly of an anticyclone: $\Delta PV_{max} = f/(H_1 + H_2) - f/H_2$.

The probability of the production of balanced dipoles ($\epsilon \approx 1$) can be assessed by considering, for example, dipoles with $R > 5\Delta$ (or $\epsilon \in [0.82\ 1.22]$), Fig. 4.9a. We introduce $p = P(\epsilon : R > 5\Delta)$ as the probability that dipoles are balanced (with unbalanced dipoles having probability $1 - p$), and estimate p as the ratio of the number of balanced dipoles n to the total number of dipoles observed N. The standard deviation of such an estimate is equal to $\sigma_p^2 = p(1-p)/N$ (assuming N is sufficiently large for the central limit theorem to apply). The estimated probability is about 0.2 (Fig. 4.9b) which means that the majority of dipoles are unbalanced and cannot separate far from the front. The probability p has a relatively fast convergence rate; about 5 to 6 runs (giving a sample size of about 60 dipoles) are sufficient to estimate p with 20-30% error (Fig. 4.9b).

Even after a balanced dipole is produced, the probability remains that it will be absorbed by the front due to interaction with the frontal meanders and other dipoles. Dipole-dipole interactions often lead to mergers and the formation of a larger dipole, however this mechanism is not efficient enough to increase the dipole survival rate. Thus, eddy separation from the front is a rare event; throughout the range of simulated fronts and different model realizations we have observed only a handful of dipoles that were able to clearly escape the influence of the front. It is notable that escaped dipoles all have $\epsilon \approx 1$. We next proceed to examine whether there are particular frontal configurations that are favorable to the production of balanced dipoles that propagate long distances.

4.6 Sensitivity of dipole properties to key frontal parameters

4.6.1 Dependence on frontal *Rossby* numbers

Here we explore the dependence of dipole ϵ values on the initial frontal configuration from which they were produced. To begin, we vary the Ro number while keeping the Bu number fixed (experiments #1 through 6 in Table 4.1, Fig. 4.10a). This is achieved by varying H_1 from 20 m to 40 m in increments of 5 m, with $H_1 + H_2 = 50$ m and all other parameters fixed. The PDF of ϵ

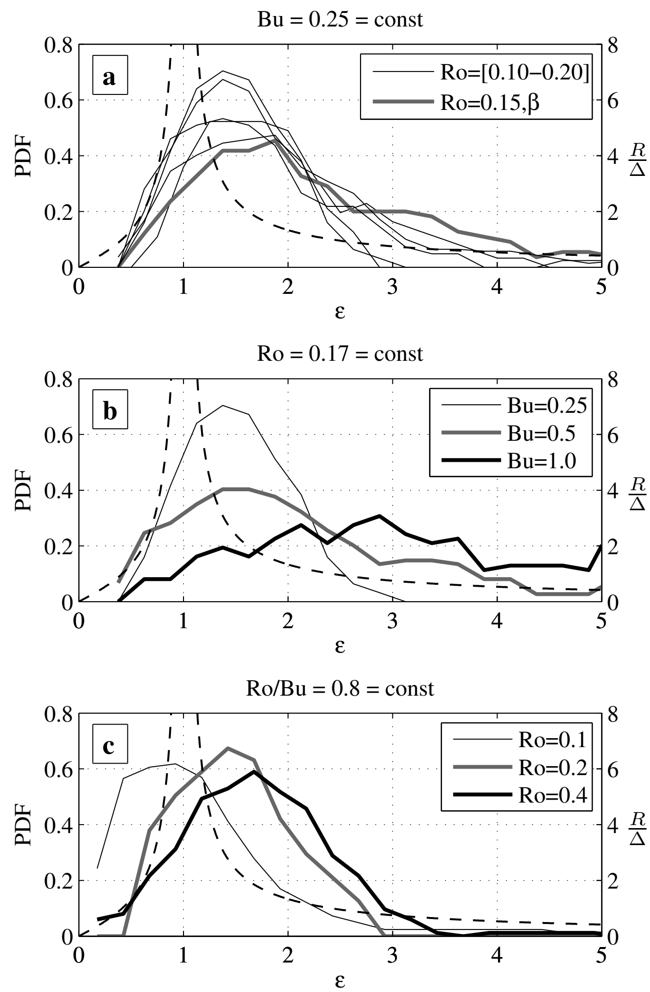

Figure 4.10: PDF of ϵ for dipoles generated from different initial frontal configurations: a) experiments #1-6, b) experiments #5, 7, 8 and c) experiments #6, 9, 10 (Table 4.1) (solid lines, left $y-$axis). The dashed lines in each (right $y-$axis) show the dependence of dipole trajectory radius on ϵ.

is qualitatively the same across these parameter ranges (Fig. 4.10a): there is a peak at about $\epsilon = 1.5$, a long tail for values of $\epsilon > 1$ and a sharp cutoff at about $\epsilon = 0.5$. The estimated probability for balanced eddy production (as in Fig. 4.9b) has no apparent dependency on the Ro number, with variations between runs being within the expected error of the estimate. One of these experiments (#4, Table 4.1) takes into account the β-effect using $\beta = 10^{-11}$ $s^{-1}m^{-1}$ (corresponding to about 60^o latitude, i.e. stronger than for the Arctic front discussed here). Here, dipoles are not significantly affected by westward β-drift [e.g. Killworth, 1983; Nof, 1981] because typical dipole propagation speeds (a few cm/s) are much faster than β-induced drift speeds (β-drift is approximately equal to the first-mode baroclinic Rossby wave phase speed $\approx \beta R_d^2 \approx 0.025$ cm/s, see Chelton et al. [2011]). However, for the frontal conditions examined here the β-effect appears to produce a slight bias towards stronger cyclones, thus decreasing the probability of balanced dipoles (Fig. 4.10a).

4.6.2 Dependence on the frontal *Burger* number

The next set of experiments explores the dependency on the Bu number while keeping the Ro number fixed, achieved by varying H_2 and keeping all other parameters fixed (experiments #5, 7 and 8, Table 4.1, Fig. 4.10b). Increasing H_2 (i.e. increasing Bu) decreases the relative PV difference across the front in layer 2, and reduces the strength of anticyclones in layer 2. The PV distribution in layer 1 remains the same, with high values in the outcropping region. As a result, for larger Bu, there are a larger number of dipoles with dominant surface cyclones; the PDF of ϵ has a fatter tail and a peak shifted towards higher values, Fig. 4.10b (i.e. the probability of generating balanced dipoles is reduced). In the first set of experiments (Fig. 4.10a), the increase in H_1 (with $H_1 + H_2$ fixed) also produced stronger anticyclones, but the ϵ ratio was not significantly affected because stronger cyclones (resulting from a faster, deeper jet) were produced in layer 1 at the same time.

Motivated by these results we explore further configurations with high Ro/Bu ratios ($Ro/Bu = H_1/(H_1 + H_2) = 0.8$, experiments #6, 9 and 10, Table 4.1) corresponding to anticyclones formed by strongly squeezing deep mixed layer waters into a thin layer as water parcels subduct across the front; such fronts generate relatively strong anticyclones. In this class of fronts we investigate ϵ statistics for shallow/weak fronts ($H_1 = 20$ m, $H_2 = 5$ m, $Ro = 0.1$) compared to deep/strong fronts ($H_1 = 80$ m, $H_2 = 20$ m, $Ro = 0.4$). A shift to lower values of the peak of the PDF of ϵ and a reduction of the high ϵ tail are observed for shallower fronts, both of which lead to a slightly increased probability p of balanced dipoles (Fig. 4.10c). For this frontal configuration, however, p remains small (similar to Fig. 4.9b).

4.6.3 Dipole propagation and frontal slumping speed

These sensitivity estimations indicate that balanced dipoles are generated across a wide range of frontal configurations, with varying but non-negligible probability. Nonetheless, not all balanced dipoles escape the influence of a slumping front; most of them do not self-propagate sufficiently fast to evade merger and recirculation processes. We thus assess the distribution of dipole drift speed U_d with respect to frontal slumping speed U_s (Fig. 4.11). The requirement for dipole escape is $U_d > U_s/2$. The peak in the distribution is around 1 for all runs; as expected, a large fraction of dipoles have drift speeds that are comparable to frontal slumping speeds because it is the dipoles themselves that influence frontal slumping. It is important to keep in mind that U_d is in the direction of U_s only in the early stages of dipole motion. Among the different frontal configurations, the distribution of U_d/U_s has a strong dependency on Bu (Ro =constant), with faster relative dipole speeds for smaller Bu, which is partially due to coupling between the layers that scales as $1/Bu$. Similar to the ϵ distribution, there is only a weak dependence on Ro (Bu =constant). For Ro/Bu =constant, small Ro fronts

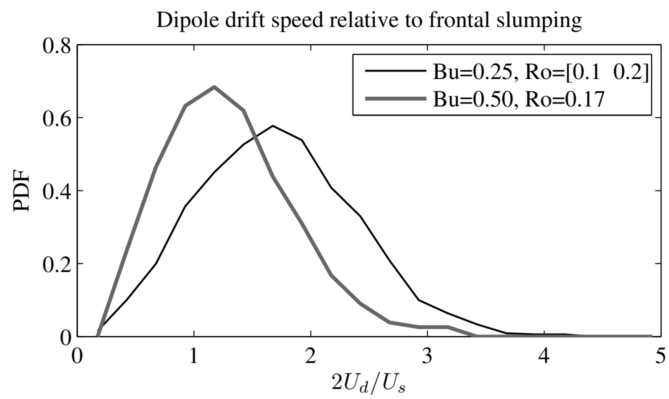

Figure 4.11: PDF of twice the ratio of dipole drift speed U_d to frontal slumping speed U_s for a range of initial frontal configurations (Table 4.1). U_s is estimated by the same procedure as for Fig. 4.4b.

tend to generate more dipoles with faster relative speeds. The initial frontal conditions that favor fast moving dipoles are in agreement with those that generate more balanced dipoles ($\epsilon \approx 1$). This is partially because the two statistics are not independent (i.e. $U_d = 2U_2/(1+\epsilon)$ implies that for fixed cyclone strengths strongly curved dipole trajectories ($\epsilon > 1$) also have smaller drift speeds).

Dipoles transport potential vorticity and buoyancy anomalies across the front and affect frontal slumping speeds in a complicated manner – there exists a wide range of kinematic trajectories that are constrained by the statistics of ϵ and U_d/U_s. Spall and Chapman [1998] estimated the frontal slumping speed to be related to the drift speed of a typical dipole, assuming that dipoles move perpendicular to the front. Curved dipole trajectories would imply decreased efficiency of frontal slumping. We next examine this effect by investigating frontal slumping speeds for a range of initial frontal configurations.

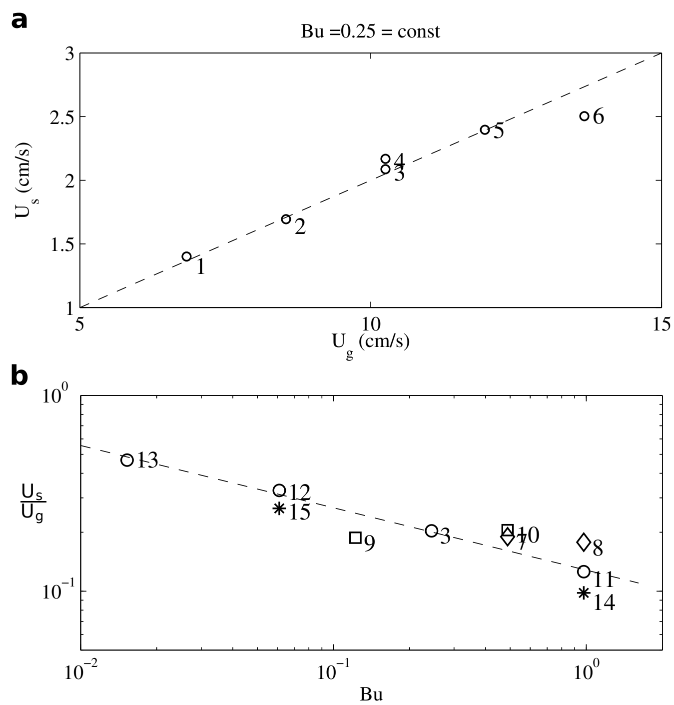

Figure 4.12: a) Frontal slumping speed as a function of initial geostrophic velocity of the front for simulations with constant Bu (experiments #1-6, with #4 having non-zero β). The dashed line corresponds to $U_s = 0.2U_f$. b) Nondimensional frontal slumping speed U_s/U_f as a function of Bu for different experiments (experiment numbers as in Table 4.1 are annotated). The dashed line represents the $Bu^{-0.4}$ scaling.

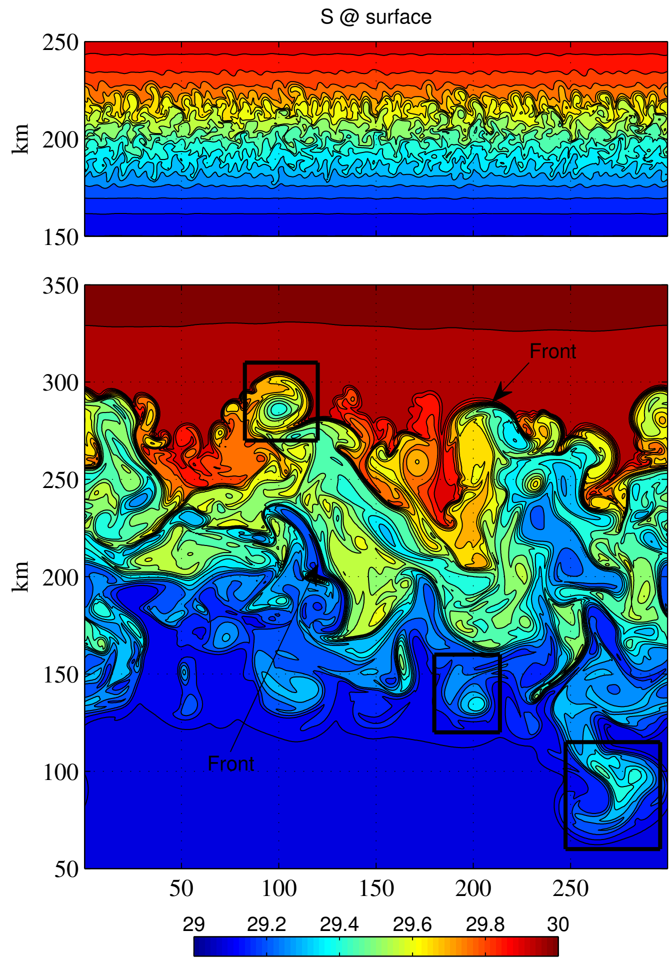

Figure 4.13: Top: Surface salinity contours for a wide front at day 30 showing the presence of multiple small scale eddies within the front (experiment #13, Table 4.1). Bottom: The surface salinity field at day 140. Note the presence of multiple fronts (arrows) separating waters of different salinities; sample dipoles are shown in black boxes.

4.6.4 Dependence on the initial frontal width

For fixed Bu number (frontal width $L_f = 10$ km, experiments #1 to 6, Table 4.1), after the initial adjustment the front slumps with almost constant speed proportional to its initial geostrophic velocity, $U_g \sim (g\Delta\rho_y H_1)(f\rho_0 L_f)$ (Fig. 4.12a). The speed of frontal slumping does not appear to be significantly affected by the β-effect. Simulations with wider initial frontal width L_f show a qualitatively different evolution (Fig. 4.13). Initially, instabilities develop everywhere within the wide front with eddies having small scales (Fig. 4.13a). These short unstable waves are of a mixed Rossby-Kelvin type and tend to alter the PV anomaly distribution before the onset of baroclinic instability [see e.g. Gula et al., 2009; Morel et al., 2006; Sakai, 1989]. At later times, wide fronts sharpen due to active frontogenesis [see e.g. Lapeyre et al., 2006; Pollard and Regier, 1992] which leads to the formation of multiple narrow fronts separating intermediate water masses that originate within the initial front (Fig. 4.13b). Strong surface fronts are evident at the outer boundaries of the frontal region (north and south edges), with several weaker fronts present in between. Dipoles are commonly observed, particularly at the strongest north and south edge fronts, however it is not possible within the formalism here to characterize dipole properties and trajectories within the wide frontal region.

The frontal width for initially thick fronts increases faster than for thin fronts and scales as $U_s/U_g \sim Bu^{-0.4}$ (Fig. 4.12b); varying the reduced gravity g'_1 (experiments #14 and 15, Table 4.1) has the similar effect on frontal slumping speed as varying the frontal width L_f. The faster slumping speed for thick fronts is consistent with active frontogenesis which effectively strengthens the local geostrophic currents and produces stronger dipoles. The reduction in slumping speed with increased Bu is consistent with the experiment set shown in Fig. 4.10b, indicating a shift to higher ϵ (and therefore strongly curved dipole trajectories) with higher Bu. The link between decreased slumping efficiency for increased Bu and more curved dipole trajectories, however, is complicated by the effects of dipole interactions with other eddies and frontal meanders. The relation between the strength of the frontal slumping to dipole ϵ and U_d/U_s distributions remains an open question.

4.7 Discussions

We have simulated instabilities at a surface ocean front that grow to form eddies – in particular dipoles that can self-propagate away from the widening front. As the front spins down, the numerical model runs show a clear inverse energy cascade through which eddies of the same vorticity sign merge as they become sufficiently close to each other. In general, this eddy field constitutes the slumping front, although some dipoles become separated from the front and evolve without frontal influences. In order to remain separated, dipoles must propagate away from the front faster than the frontal slumping speed to avoid interactions and mergers that lead to their re-incorporation into the front.

A closed analytical solution has been derived for the ratio ϵ of the translation velocities of a dipole based on the PV anomalies of its cyclone and anticyclone. We have further related ϵ to the radius of a self-propagating dipole trajectory, where a large propagation radius is found when $\epsilon \to 1$. Our theoretical results provide guidance in interpreting numerical model results. Analysis of dipoles from an ensemble of numerical simulations allows us to obtain statistical properties of dipoles and identify how they change for different frontal configurations. The ϵ distribution has a long high ϵ tail implying strongly curved trajectories due to the dominance of the cyclone in a dipole. The ϵ distribution has only weak dependence on the frontal Ro number and a stronger dependence on the Bu number such that shallow fronts with large Ro/Bu ratio are more favorable to the production of balanced dipoles, although this probability is consistently small (about 20%).

We observe only balanced dipoles to escape the influence of the front, although not all balanced dipoles escape as they are subject to interaction with frontal meanders and other dipoles. Understanding frontal slumping and property transports in the vicinity of fronts is complicated by curved dipole trajectories that lead to recirculation of buoyancy.

The result that the probability of balanced dipole generation is small may be inconsistent with persistent observations of many upper-ocean eddies in the Arctic, if indeed they do translate far from the front as self-propagating dipoles. This suggests that in nature there might exist a mechanism acting to increase the probability of dipole escape. For example, non uniform or time-dependent frontal characteristics may increase the probability of dipole escape. Such fronts could be intermittently unstable, or unstable only in localized areas, which allows for the production of dipole patches separated in time or spatially, thus reducing eddy-eddy interactions. Intermittent or localized dipole production could be related to transient frontal instabilities triggered by wind bursts or localized buoyancy forcing. Note that in a case where PV is not conserved, Thomas et al. [2008] examines the formation of intrathermocline eddies at upper-ocean fronts that are forced by winds. He shows the importance of down-front winds in driving a three-dimensional circulation that subducts surface water of low PV into the stratified interior. Such processes that influence the strengths of cyclone and anticyclone could shift the ϵ distribution towards more balanced values.

While we have put forward dipole self-propagation as a mechanism for eddy propagation from a front, there remains the possibility that background flow could advect eddies away from their originating front, and self-propagation is not required. In the case of Arctic eddies, for example, one could argue that they are advected in the large-scale Beaufort Gyre circulation [see e.g. Proshutinsky et al., 2009; Spall et al., 2008], although for the class of Arctic eddies discussed here the flow field to the south of the originating front is likely to be predominantly in the direction of the front.

Moreover, for background advection to have a significant influence on the eddy pathway, it is necessary to first generate an eddy that is separated from the influence of the front and other eddies. A similar logic applies to the idea of vortex drift due to β-effects.

Finally, we note that only sub-mixed layer anticyclones are persistently detected (i.e. no cyclones) in the observations of shallow eddies in the Arctic Ocean, with a few observations of dipoles under sea ice [e.g. Fedorov and Ginsburg, 1989]. If dipole self-propagation is important, cyclones are also required. It is a reasonable assumption, however, that dipoles are formed, and after some time, the surface intensified cyclonic eddy is dissipated due to Ekman layers associated with under sea ice friction. The sub mixed layer anticyclone remains largely unaffected by surface processes due to a stratification cap at the base of the mixed layer. A similar dissipation process has been investigated for dipoles generated by convection under sea ice [e.g. Chao and Shaw, 1999], where it has been shown that the surface cyclone dissipates while the underlying anticyclone is preserved. Of course, the dissipation of a surface cyclone would affect the trajectory of a dipole and its propagation speed [e.g. Sansón et al., 2001]. As the cyclone dissipates, the dipole loses the ability to self-propagate; the distance traveled by a dipole then depends strongly on surface frictional processes (e.g. sea-ice cover state), and this is the subject of a future study.

Chapter 5

Large-Scale Oceanic Circulation due to Tropical Cyclones

5.1 Introduction

Tropical cyclones (TC) are small-scale phenomena that act locally on short time scales of several hours, however they provide major changes in ocean stratification [Price, 1981]. Their strong surface winds produce turbulent mixing in the ocean. As a result of the mixing of a thermally stratified ocean, warmer waters from the upper ocean penetrate deeper, whereas colder ones entrain from below and thus lead to surface cooling. Satellite observations of sea surface temperatures (SST) also show dramatic cooling under the TC [Monaldo et al., 1997]. Estimates show that $\sim 85\%$ of surface cooling is due to entrainment of cold waters with the rest being caused by atmospheric fluxes [Price, 1981]. The cold anomaly in the upper ocean is then removed by atmospheric heat fluxes within a few weeks resulting in the overall warming of the ocean. The region of the maximum cooling typically has a slight rightward basis. This is caused by the partial resonance of the transient wind motion with inertial oscillations of the ocean currents at the rightward side of a cyclone [Greatbatch, 1984]. Another prominent feature of the local oceanic response is the upwelling of waters beneath the hurricane eye [Ginis, 2002; Ginis and Sutyrin, 1995]. Vertical motion results from divergence of the transport in the mixed layer and penetrates to the bottom monotonically decreasing its intensity with depth [Price et al., 1994]. Adiabatic upwelling of waters creates a cold anomaly, which later becomes geostrophically balanced with the circulating flow around it. The process resembles a large-scale oceanic circulation driven by Ekman pumping caused by the vorticity of the wind stress. From the observational point of view, this is seen from satellite altimeter data, with the depression of SSH reaching a few tens of centimeters [Ginis, 2002]. Described changes introduced in the ocean are substantial and not only important in forecasting the life cycle of a tropical cyclone but could play a role in defining global climate system.

To understand possible impacts of TC on the oceanic circulation lets consider the driving mechanisms. From the energy prospective, the maintenance of wind-driven as well as the thermohaline circulation requires external sources of mechanical energy [Munk and Wunsch, 1998]. Even though the ocean gains a lot of thermal energy it cannot efficiently transform it into the kinetic energy of the circulation because the heating and the cooling occurs at the same geopotential level [Kuhlbrodt, 2008]. Recent studies show that the ocean general circulation is driven by the mechanical energy input from the winds and tides [Wunsch and Ferrari, 2004]. As a result the distribution and the strength of the mechanical energy sources shape the oceanic circulation and control its variability. Ferrari and Wunsch [2008] give a concise review of ocean-circulation energy sources and sinks. Nonetheless, such strongly nonlinear and intense event as TC are typically smoothed out from the global wind-field data and their mechanical energy input is not accounted for.

During the passage of a TC the ocean mixed-layer could deepen dramatically leading to cross-thermocline exchange of waters. Cold waters that reach the surface layer will eventually be restored to near climatological conditions by the net enthalpy fluxes from the atmosphere. Mixing associated with tropical cyclones have had a lot of attention from the scientific community.

Emanuel [2001] argues that the net heat-flux into the ocean on the long-term mean will be balanced by the lateral heat transport away from the mixing zone. This mechanism induces the overturning circulation. Heat fluxes necessary to restore cold wakes induced by tropical cyclones are estimated to be 1.4TW. This is a substantial part of the peak heat transport driven by the meridional overturning circulation [Macdonald and Wunsch, 1996]. Sriver and Huber [2007] calculated the time averaged global diffusivity field attributable to TC by analyzing sea surface temperature anomalies. The peak zonally averaged value they've obtained is $\sim 0.4cm^2/s$, which is comparable to the values used in global ocean-models and with global tracer-release experiments [Ledwell et al., 1993]. They also calculated that about 15% of peak ocean heat transport is associated with the vertical mixing induced by tropical cyclones.

Korty et al. [2008] investigated the feedback of TC mixing and poleward heat transport by the ocean. They identified that two states could exist: one with strong meridional temperature-gradients and weak TC activity and one with weak temperature gradients and strong TC activity. Pasquero and Emanuel [2008] found that mixing leads to the advection by the oceanic circulation of anomalously warm waters toward low latitudes, modifying the mean state of the equatorial basins. Studies of Fedorov et al. [2010] showed that the TC-ocean interaction could provide possible explanation of the permanent El Nino-like conditions in the Pliocene [Fedorov et al., 2006]. Strong and efficient activity of tropical cyclones are able to reduce mean equatorial temperature gradients by warming water along the pathways towards the equator.

Nonetheless, including present day hurricane mixing in simulations of climate did not show a strong impact, despite hypotheses and idealized-model results. One possible explanation could be that a major part of the heat pumped into the ocean is released to the atmosphere in winter when mixed layers and thermocline are substantially deeper than during the summer [Jansen et al., 2010]. Another aspect of hurricane forcing that could

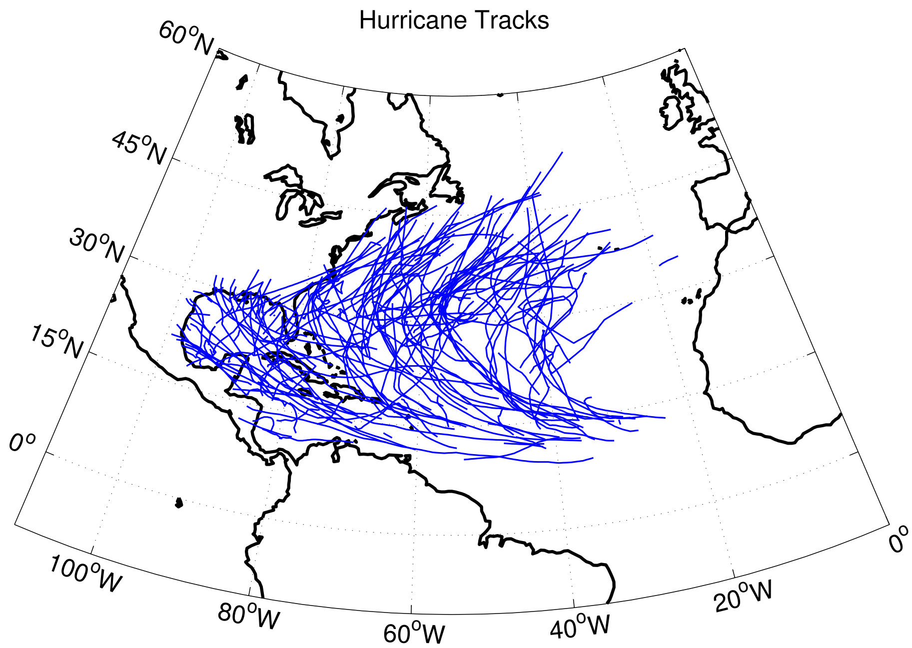

Figure 5.1: Atlantic Ocean hurricane tracks, plotted from the truncated dataset.

affect the global circulation is the cyclonic vorticity input into the ocean. The areas over the ocean where tropical cyclones have their strongest activity are the oceanic subtropical gyres extending from about 10 to $40^o Lat$. The gyres consist of a strong western boundary current and a weak return flow in the interior of the ocean. The transport of mass and heat provided by these gyres is an essential feature of the climate system. These gyres are driven by the large-scale anticyclonic winds composed of westerlies in the mid-latitudes and easterlies at low latitudes. However, the small-scale cyclonic winds from continuously occurring tropical cyclones have a potential to modify the strength of the subtropical gyres. This aspect of hurricane forcing could be much more significant compared to impacts from additional mixing. However, to my knowledge, there are no studies devoted to this issue.

The present study is focused on the basin-scale oceanic circulation established by hurricanes due to their strong but highly transient vorticity forcing. At first, I will present the data involving hurricane observations and construct global estimates of hurricane vorticity input into the ocean. Then I will proceed to idealized ocean modeling in order to explore the establishment of the mean circulation and its sensitivity to details of hurricane forcing.

5.2 Observations of hurricanes

5.2.1 Hurricane tracks and defining parameters

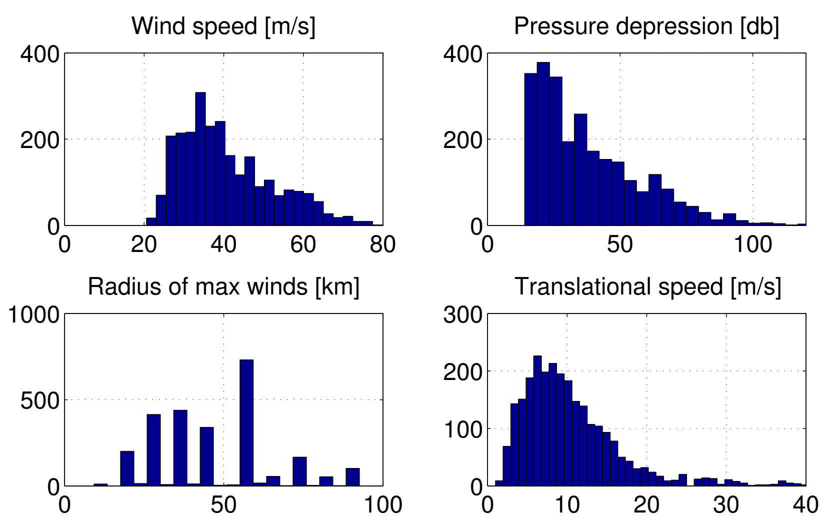

Figure 5.2: Histograms of essential parameters used in the analysis: maximum wind speed, pressure depression, translational speed, and radius of maximum winds.

This section is devoted to the observations of hurricanes in the Atlantic Ocean with the emphasis on parameters relevant for the oceanic response. The data used for the analysis is the Extended Best Track Dataset [Demuth et al., 2006]. The data includes hurricanes observed from the years 1988-2009. The parameters used for this analysis are the pressure depression, maximum wind speed, radius of maximum wind speed, and the position of hurricanes at a temporal resolution of 6 hours. The overall number of observations is about 9000; however, many of those describe weak storms (tropical depression, tropical storms) and some have missing data. Thus, I masked out the observations based on the following criteria: minimum pressure $P < 1000dbars$, maximum winds $V_m > 20m/s$, radius of maximum winds $R_m < 100km$. The remaining tracks consist of about 3000 observations and provide substantial area coverage of the northern part of Atlantic Ocean (Fig. 5.1).

5.2.2 Non-dimensional hurricane parameters

From the oceanic perspective, hurricanes are translating vortices, that transfer momentum from the atmospheric winds into ocean currents. The way the ocean responds to such forcing depends on the spatial scale of a hurricane and on its translation speed. The magnitude of the response is linked to the strength of the winds.

The data shows that hurricanes have a range of wind speeds of $20-80m/s$, pressure depression up to $100hPa$, radii of $10-100km$ and translational speeds of $2-20m/s$ (Fig. 5.2). A more physical view on the problem of oceanic response to a hurricane could be achieved by considering the following non-dimensional parameters of the vortex-ocean system: length scale of the forcing, Froude number, translational speed Greatbatch [1984].

The length scale of a hurricane,L, is non-dimensionalized by the first baroclinic deformation radius R_d (Fig. 5.3b). Typical values of 2-3 signify the importance of the Coriolis effects in the oceanic response to hurricanes. The

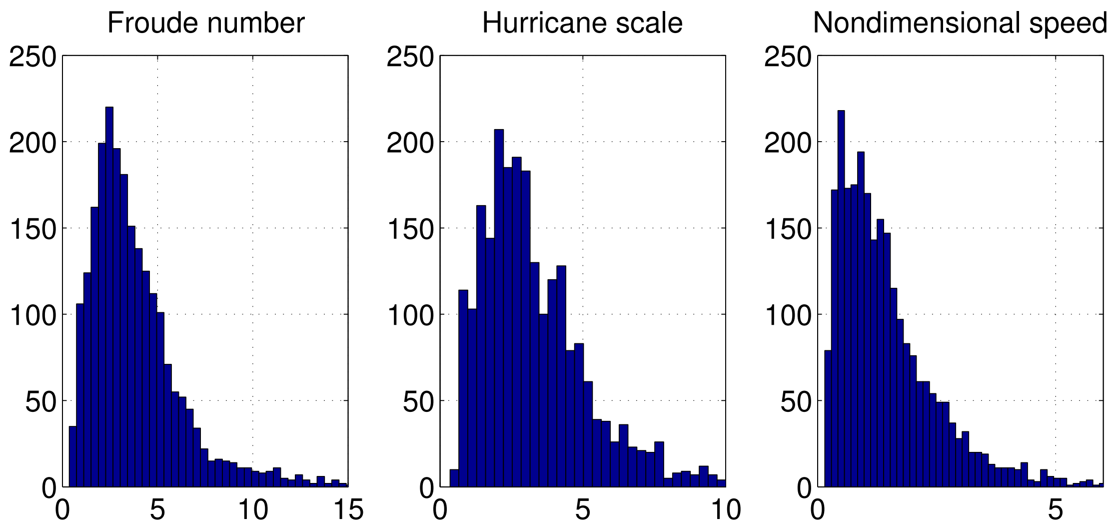

Figure 5.3: Relevant non-dimensional parameters that define the oceanic response to hurricane winds: Froude number, hurricane size, and translational speed, plotted as histograms based on the Atlantic hurricane dataset. Levitus dataset of ocean stratification was used to calculate the first Rossby deformation radii and internal gravity wave speed for the ocean.

Froude number, $Fr = U/c$, is the ratio of the translational speed to the phase speed of the first baroclinic mode. It represents how fast the forcing changes compared to how fast the waves could transport the information about the forcing downstream. Ratios greater than one for present observations (Fig. 5.3a) mean that storms move faster than waves could propagate information downstream. Thus, hurricane forcing for the ocean should be viewed as a fast moving, large scale perturbation.

In this regime the dynamics is determined by a non-dimensional speed ($\hat{U} = U/fL$). Observed values close to unity (Fig. 5.3c) imply that hurricane induced ocean surface currents on the right side of the storm will be in inertial resonance with the hurricane winds. Current on the left side of the storm would be out of phase with the atmospheric winds. This creates an asymmetry in the oceanic response, having a rightward bias. An oceanic response to a hurricane with typical parameters will be discussed in section 5.3.

5.2.3 Occurrence probability and mean upwelling

Hurricanes represent highly transient and extreme forcing, with probability of occurrence over a particular point in the ocean being less than 1 day per year (Fig. 5.4). Nonetheless, their strong cyclonic winds input vast amounts of vorticity into the ocean (Fig. 5.5), inducing mean upwelling of $5 - 10m/yr$. This is a noticeable correction to the large scale atmospheric downwelling of $50m/yr$ that drives the subtropical gyre circulation. Thus, cumulative hurricane forcing has a potential to affect the global circulation in the ocean. The mechanisms through which the small scale hurricane forcing affects the basin wide circulation would be discussed in detail in section 5.4.

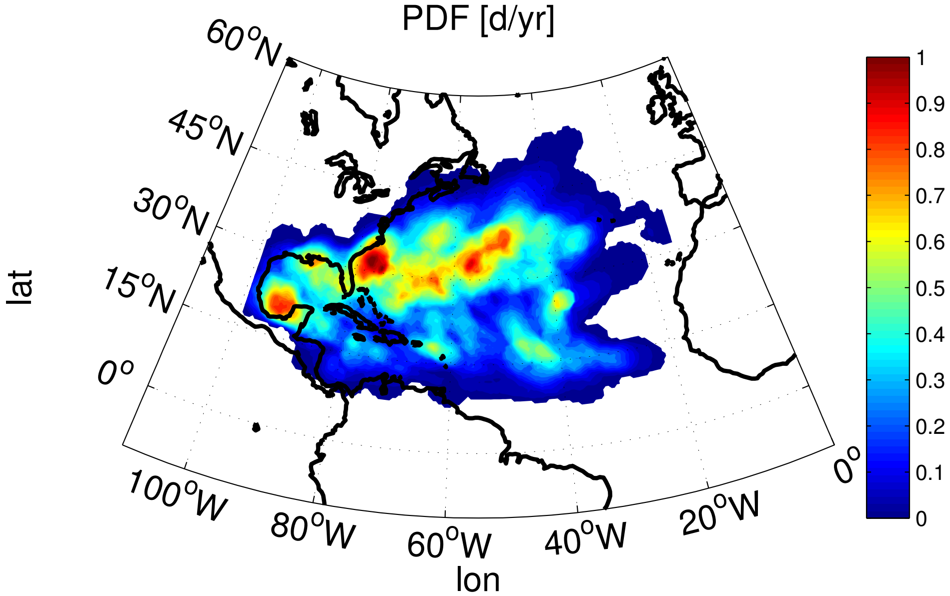

Figure 5.4: Geographic distribution of the probability of hurricane occurrence (in days/year) in the Atlantic Ocean.

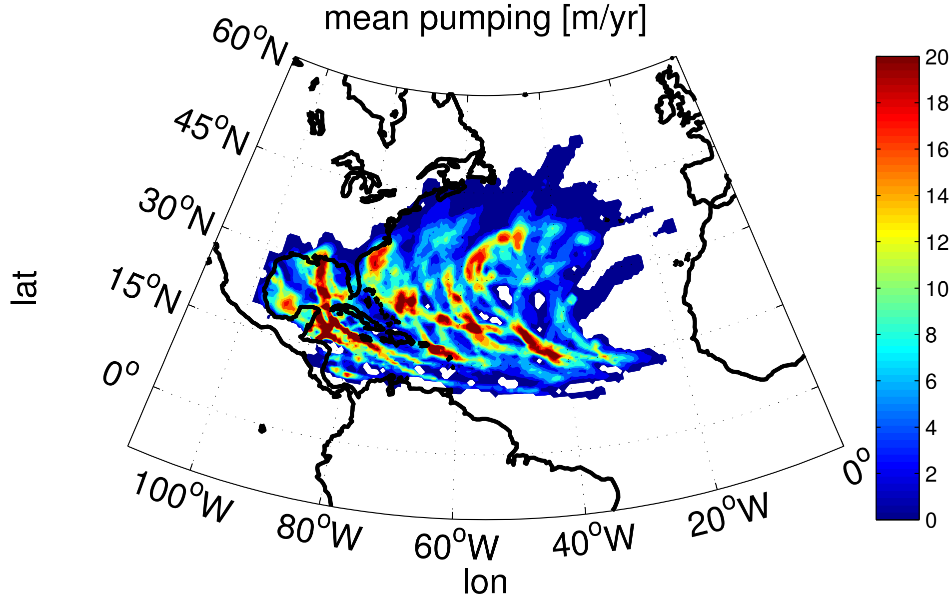

Figure 5.5: Average Ekman upwelling due to cyclonic winds inside the hurricane's core (in m/year).

5.3 Modeling the oceanic response to a translating hurricane

An oceanic general circulation model (GCM) is used to simulate oceanic state subjected to a translating storm. A category four hurricane Frances (2004) is chosen for simulations, because the oceanic response has been observed with the floats deployed before its passage [D'Asaro et al., 2007]. The available observational data provides a good reference test for the model capabilities as it includes essential features of the oceanic response: surface currents, mixed layer deepening, and lifting of the thermocline.

5.3.1 Model description

The model used is M.I.T General Circulation Model [Adcroft et al., 2008]. It is a primitive equation ocean model with an implementation of KPP parametrization of vertical diffusivity Large et al. [1994]. The model consists of 30 levels in the vertical direction, with grid size varying from $5m$ to $50m$; it has a horizontal resolution of $7km$. Periodic boundary conditions are used to conserve energy in the domain. The model is initialized with a zero mean flow and an observed thermal stratification. The system is forced with a translating vortex with a theoretical wind stress Jakobsen and Madsen [2004], calculated using observed hurricane parameters: $Pc = 80db, V_m = 50m/s, Rm = 40km, U = 5.5m/s$. To avoid unnecessary complications, no thermodynamic fluxes were applied at the surface. The model is forced by a translating hurricane for about 2 days, then atmospheric winds are turned off and the model is integrated for several months to see the relaxation response after the strong perturbation.

5.3.2 Forced stage response

As the hurricane passes over the ocean, strong surface currents emerge with magnitudes reaching $1.5m/s$. These currents are stronger on the right side of the hurricane, which is expected as the hurricane's non-dimensional speed $\hat{U} = U/fL$ is close to unity. A strong thermal stratification prevents currents from penetrating to the bottom of the ocean. This creates vertical gradients in velocity, leading to shear instabilities. In turn, these instabilities drive the deepening of the mixed layer and entrain colder waters to the surface. The mixed layer increases to a depth of over $100m$ as well, having a substantial rightward bias (Fig. 5.6). The results of the increased vertical mixing are evident from the sea-surface cooling, reaching magnitudes of about 3^oC (Fig. 5.6). In reality the negative surface temperature anomalies are restored back to original conditions due to increased heat fluxes into the ocean. In present simulations the atmospheric heat fluxes are ignored.

The transport in the mixed layer is divergent, resulting in the upwelling of waters at the center of a storm. The divergence of the currents is due to cyclonic vorticity of hurricane wind stress, which lifts the thermocline by about $25m$ (Fig. 5.6). Away from the hurricane eye, there is a broad and weak downwelling to ensure conservation of mass.

The magnitudes of mixed layer deepening, lifting of the thermocline and surface cooling correspond well to observations (within 20% error). In fact, such an agreement is unexpectedly good, as there are errors made of at least $10-20\%$ in all of the observed parameters defining the hurricane wind-stress field: wind speed, drag coefficient and radius of maximum winds. The emphasis on errors should be put on the drag coefficient as its dependence on wind speed remains poorly understood, especially for severe hurricane winds Powell et al. [2003].

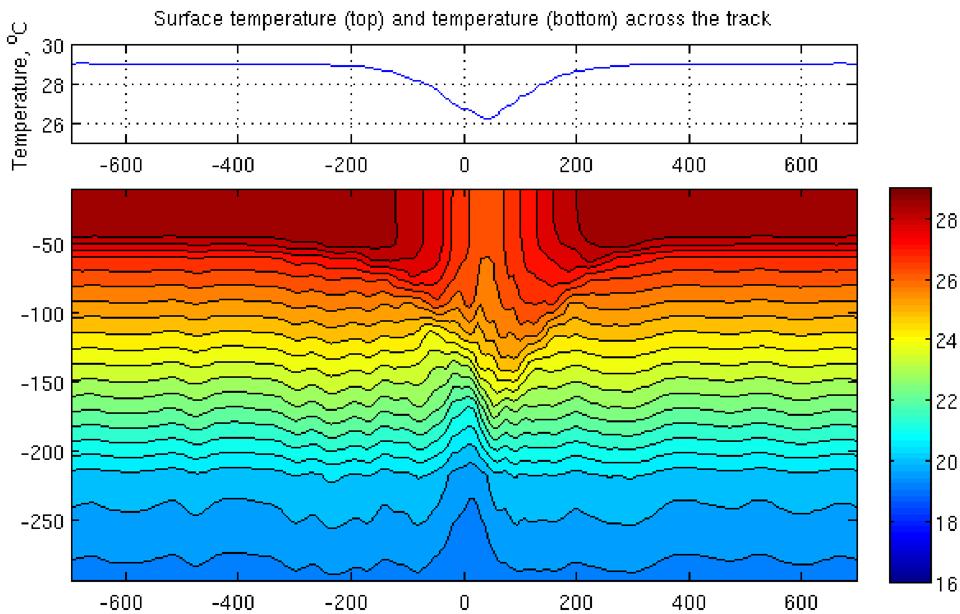

Figure 5.6: Temperature profile of the ocean 2 days after the passage of hurricane Frances, as simulated by the model.(top) Sea surface temperature showing the anomalously cold waters at the surface associated with enhanced mixing due to hurricane winds. (bottom) Oceanic temperature profile (x-axis [km] in the direction perpendicular to hurricane track and y-axis is depth [m]). Note, the presence of the lifted isotherms below the mixed layer associated with Ekman pumping due to cyclonic hurricane winds.

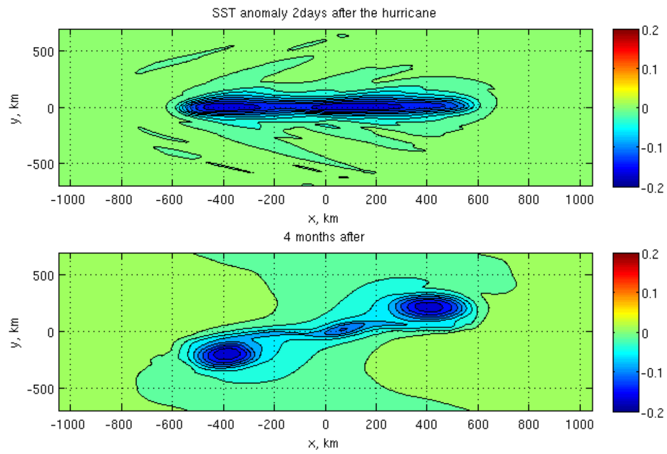

Figure 5.7: The breakup of the geostrophic circulation established after the passage of a hurricane into a series of mesoscale eddies (as simulated by the general circulation model). Plotted: sea surface height anomaly 2 days after the passage of a hurricane (top) and 4 months later (bottom).

5.3.3 Relaxation after the hurricane

The entire domain is filled with internal inertia-gravity waves that tend to disperse energy away from the source. Strong inertial currents in the ocean are adjusted by these waves to balance geostrophically with the pressure gradients created by nonuniform lifting of the thermocline and deepening of the mixed layer. Several days after the passage of a hurricane, a balanced circulation is established along the track.

Ones the geostrophic circulation is formed, it is subject to baroclinic instabilities. In some cases such a circulation breaks up into a series of cyclonic eddies of the size of the first Rossby deformation radius (Fig. 5.7). A typical time scale for this instability is of the order of several months. Thus, the overall effect of hurricanes could be considered as a source of cyclonic anomalies in the ocean. Considering that an average life span of such eddies could reach several years and given a continuous supply by hurricanes one could expect a mean circulation to be established. Such a circulation is discussed in section 5.4. Global impacts of hurricane induced mixing are discussed in Chapter 6.

5.4 Contribution of hurricanes to the oceanic gyre circulation

Hurricanes inject a considerable amount of cyclonic vorticity into the ocean, which manifests itself as the lifting of the thermocline (Fig. 5.5). In this section I investigate a global oceanic response to a continuous supply of these small scale thermocline displacements produced by hurricanes. The simplest model of the oceanic circulation that is capable of reproducing this dynamics is a reduced-gravity shallow-water model. This model is chosen as a good balance between complexity and computational cost. In the following subswillection I will describe the model, the numerical scheme used for integration, and the implementation of hurricanes forcing. Then, I will present the results of the model, with the emphasis on the established time-mean circulation, and its dependence on essential characteristics of the hurricane forcing.

5.4.1 Shallow water model

As an ocean model, I implement forced shallow water equations on a rotating reference frame, with a linear and Laplacian friction. The equations are as follows:

$$\frac{\partial u}{\partial t} - hvq = -\frac{\partial}{\partial x}(K + \Phi) + \tau_x - \alpha u + \nu \nabla^2 u \tag{5.1}$$
$$\frac{\partial v}{\partial t} + huq = -\frac{\partial}{\partial y}(K + \Phi) + \tau_y - \alpha v + \nu \nabla^2 v \tag{5.2}$$
$$\frac{\partial h}{\partial t} + \frac{\partial}{\partial x}(hu) + \frac{\partial}{\partial y}(hv) = 0 \tag{5.3}$$
$$\tag{5.4}$$

where u is zonal and v is meridional velocity, h is the thermocline depth, $q = (f + \xi)/h$ is potential vorticity, $K = 1/2(u^2 + v^2)$ is kinetic energy, and $\Phi = gh$ is geopotential. The beta-plane approximation is used for the Coriolis parameter $f = f_0 + \beta y$. No-slip boundary conditions are applied at all boundaries.

The numerical discretization used for these equations is the one developed by Arakawa and Lamb [1981]. The spatial discretization of the nonlinear terms conserves energy, vorticity, and potential enstrophy in the limit of continuous time. When time is also discretized as well, these quantities are conserved to a good degree. This scheme is computationally expensive compared to other numerical schemes used for shallow water models. However, the benefits of having conservation of energy and vorticity are obvious for the type of simulations discussed here. The scheme allows the model to run under small values of momentum diffusivity, making it possible to control the lifespan of eddies in a wide range. The choice of linear damping is necessary to provide dissipation at large scales.

The model has a rectangular domain with dimensions of 1000km by 1000km and a spatial resolution of 10km. Time-stepping is 30min and the integrations are typically carried out for about 100 years (although a few very long runs were performed to ensure the robustness of the response). The model parameters are as follows: mean thermocline depth is 500m, Coriolis parameter $f_0 = 2 \cdot 10^{-4} 1/s$, $\beta = 2 \cdot 10^{-11} 1/ms$, and a reduced gravity

$g = 0.003 m/s^2$. This gives typical values of the Rossby deformation radius of about 20km.

Hurricanes are prescribed as translating vortexes, with wind profiles being constant along their tracks. The wind profile is a theoretical one, calculated using fixed radius and maximum wind speed [Jakobsen and Madsen, 2004]. The tracks are determined as straight lines connecting two randomly chosen points in the interior of the domain. All hurricanes are moving with a constant translating speed. There is a fixed time delay between the hurricanes. This procedure determines hurricane forcing in a stochastic sense. Thus, the output would be presented in terms of quantities averaged over long periods of time. Now that the model and the forcing field are set, I proceed to numerical simulations.

5.4.2 Modeled oceanic response to hurricanes

The oceanic response to a particular hurricane track is represented by strong currents (u, v), and upwelling of the thermocline (negative anomaly of h). The oceanic response is dominated by inertial motions as the Froude number for hurricanes is larger than one. Nonetheless, a balanced circulation is established along the track several days after the passage of a hurricane. This circulation is subject to instabilities, and in certain cases it breaks up into eddies. Most of the variability in the model is dominated by mesoscale eddies (Fig. 5.8a). Such eddies propagate westward with a speed of the baroclinic Rossby wave and a strong dissipation due to no-slip boundary conditions occurs when they hit the western boundary current. During their westward propagation, they grow in size due to an inverse energy cascade that is shown to take place in geostrophic turbulence [Rhines, 1979].

The cumulative hurricane forcing leads to an increase in the global vorticity, even though it is being forced at small scales. A time mean circulation is established on a basin-wide scale in the ocean (Fig. 5.8b). The circulation has a very distinct pattern: it is a cyclonic gyre, with a strong western

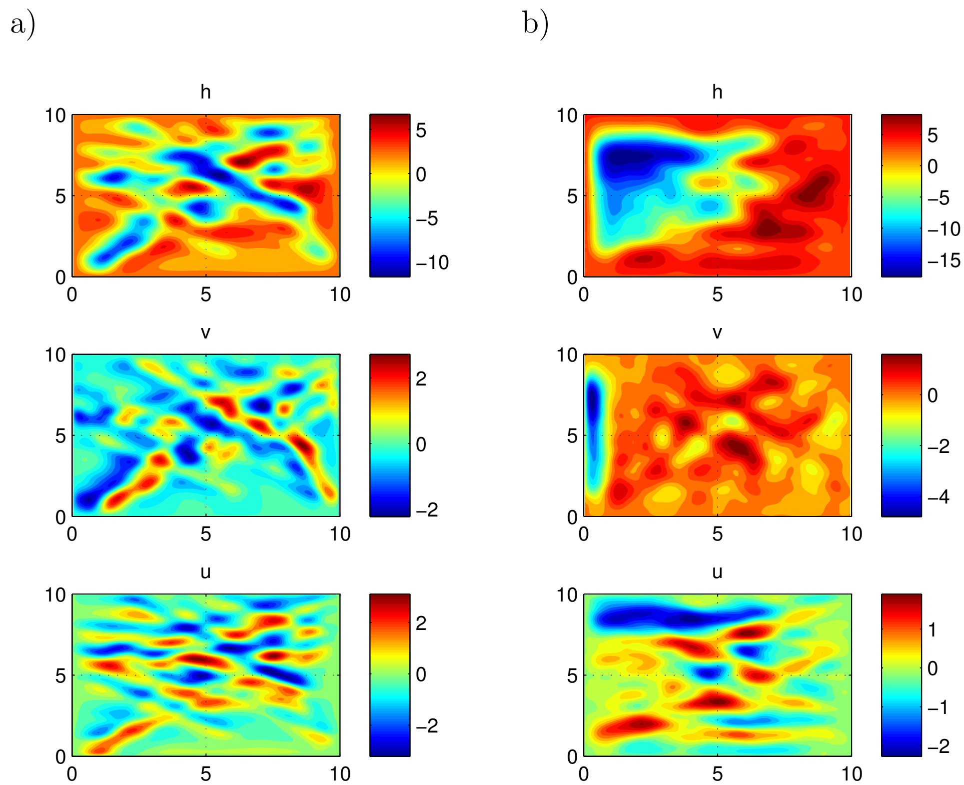

Figure 5.8: Time averaged circulation established in a shallow-water model forced by idealized hurricane tracks. a) Set of panels representing 6 month mean values of thermocline depth anomaly h, zonal velocity u, and meridional velocity v. b) Panels represent 5 year mean anomalies, showing how a basin wide circulation is established.

boundary current flowing southward, and a weak northward flow in the interior. This gyre is an exact opposite of the anticyclonic subtropical gyre in the Atlantic Ocean, that is bounded by the northward flowing boundary current - the Gulf Stream. This experiment was conducted with only hurricane winds included - no large scale atmospheric winds and oceanic circulation were included.

Next, a series of experiments is performed with a background gyre circulation in the ocean. To create this circulation the large scale anticyclonic winds (westerlies and easterlies) are added in the form of cosine function of latitude. These winds create an anticyclonic gyre circulation, having a strong western boundary current flowing northward. The speed of this current is $\sim 6cm/s$, a seemingly small value. However, once it is scaled with the size of the real ocean gyre (about a factor of 4 larger) it is equivalent to a current greater than $\sim 0.2m/s$ (although it is likely that dissipation would considerably dampen the response).

Hurricanes are added to this ocean configuration in a same way as described earlier. An expected qualitative result of these simulations is the weakening of the western boundary current and hence of the overall mass transport. The sensitivity this effect to details of the hurricane forcing is analyzed in terms of the time mean velocity of the western boundary current.

5.4.3 Sensitivity analysis

A lot of emphasis has been put lately on the question of how hurricane properties such as intensity, frequency, and positions of the tracks would change under the global warming scenarios [Pielke et al., 2005; Trenberth, 2005]. Even though at this stage there are no definite answers about the change in hurricane activity, it is important for the understanding of the problem to test the sensitivity of the mean hurricane-driven circulation to hurricane activity.

A set of experiments was performed, with the control parameter being the strength of individual storms. The results on Fig. 5.9 show that the speed of the boundary current decreases with the increasing intensity of the hurricane. The result is expected, as the increase in the magnitude of the cyclonic forcing should decrease the strength of the anticyclonic gyre. For hurricanes (wind stress $\tau \gtrsim 1N/m^2$), the response becomes close to linear, with a slope steeper compared to weaker storms ($\tau < 1N/m^2$). This implies

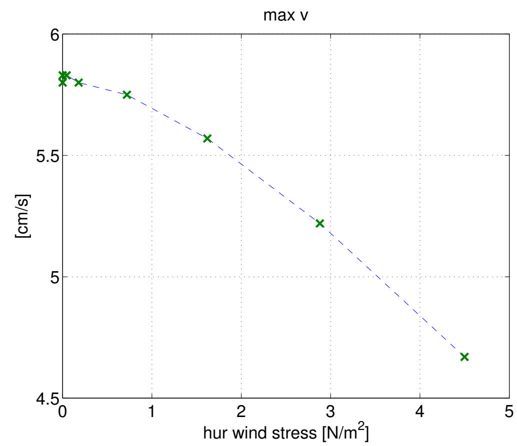

Figure 5.9: Sensitivity of the mean strength of boundary current to the intensity of individual hurricanes. Note, all experiments here have the same average upwelling, but it is caused by hurricanes of different strength.

that, for a fixed mean forcing, stronger hurricanes produce stronger anomalies in circulation compared to weak storms. This potentially occurs because for strong winds surface velocities are highly correlated with the hurricane winds, giving the most energy input. Whereas, for weaker storms there could be destructive influence from past hurricanes. Thus, it could be concluded that as long as the circulation is driven by hurricanes, which are severe storms, the resultant currents should depend only on the mean forcing - independent of the strength of individual hurricanes.

Another important aspect of hurricane forcing is the frequency of their occurrence. On average, there are about 6 hurricanes a year in the Atlantic Ocean, which gives a mean delay time between the hurricanes of about a month and a half (seasonal cycles are ignored here). In the following set of experiments the delay time between the hurricanes is varied in the rage of 0-360 days. Varying the delay time and hence occurrence probability, would lead to changes in the mean hurricane induced upwelling (Fig.5.10, top). The linear dependency is a property of the way hurricanes prescribed in a model.

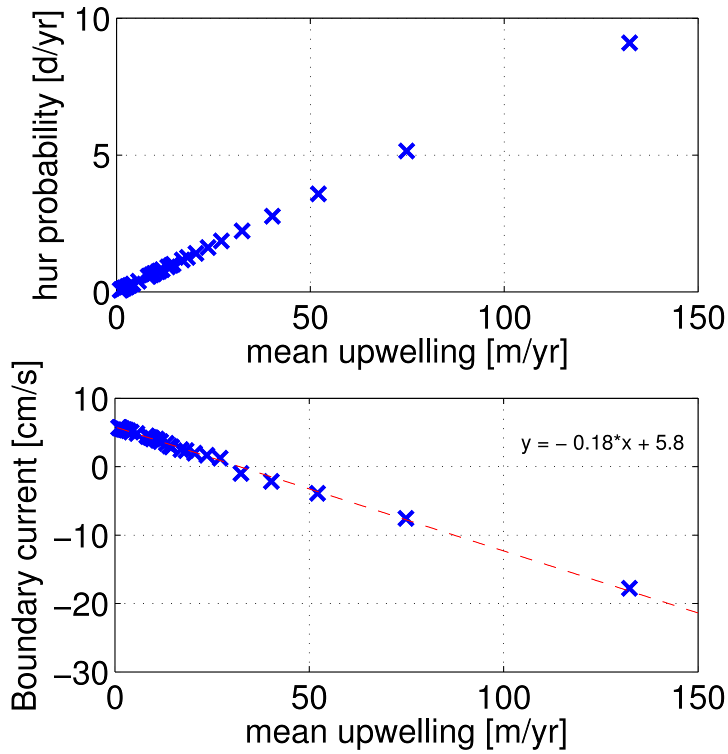

Figure 5.10: Sensitivity of the mean boundary current speed to the occurrence probability of hurricanes. Top panel: the dependence of the mean hurricane induced upwelling on the mean frequency of hurricanes (controlled by time delay between the hurricanes). Bottom: the strength of the boundary current plotted as a function of the mean upwelling.

Simulations show that for more frequent hurricanes the mean boundary current decreases its magnitude. However, this dependence is linear for the entire range of considered frequencies (Fig. 5.10). Since mean upwelling was controlled only by changing hurricane frequency, it could be concluded that the intensity of the hurricane circulation is independent of frequency and depends only on the mean upwelling.

Because the intensity of the hurricane-driven circulation is independent of the strength of individual hurricanes as well as on their occurrence frequency, the time mean forcing plays a crucial role in determining the magnitude of such a circulation. Assuming these statements would hold for larger scale basins as well, we could calculate the intensity of the circulation for the present-day climate. Recall an estimate for the present day hurricane upwelling is about $10m/yr$. For the model basin of size $10^o Lat \times 10^o Lon$, we get that the boundary current should be $1.8cm/s$. However, the boundary current should be proportional to the area of the basin as it conserves mass that is being forced southward in the entire ocean domain. In reality the area of the subtropical gyre affected by hurricanes is about a factor of 10 larger than the area of the model basin used for simulations. Thus, an estimate for the present day hurricane-driven boundary current would be about $20cm/s$, which constitutes about 10% of the magnitude of the Gulf Stream.

Even though hurricanes cover a substantial part of the subtropical gyre, most of the energy they inject into the ocean is concentrated in the western part of the ocean basin. Thus, the current sensitivity test is aimed to explore the effects of spatially varying forcing. The experiment is performed with hurricanes being active only on the western half of the basin. A larger domain ($30^o Lat \times 30^o Lon$) is used for this experiment to demonstrate the robustness of the response in larger-scale basins.

Fig. 5.11 shows the mean circulation that is established after about 100 years. Small scale zonal jets are particularly evident in this simulation, however, there is an overall large scale circulation. It consists of a cyclonic gyre,

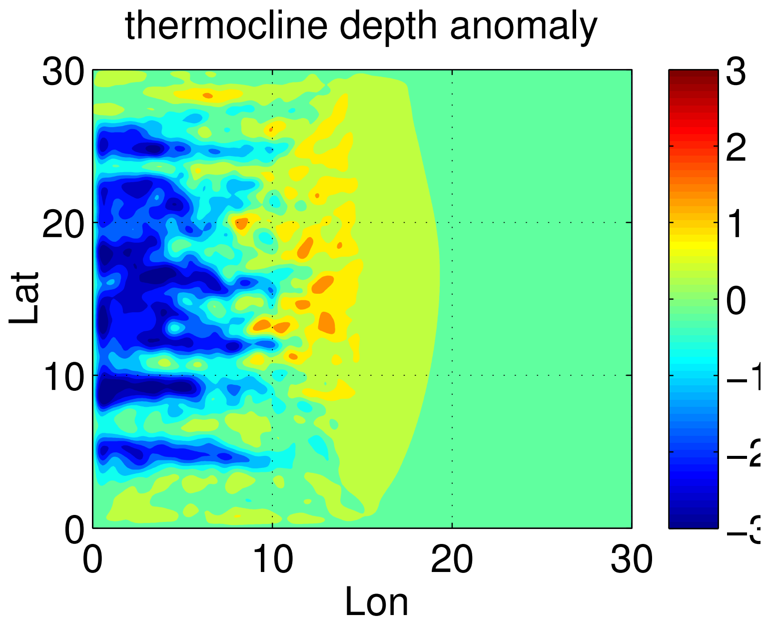

Figure 5.11: The thermocline depth anomaly (m), showing the large scale circulation achieved in the ocean forced by hurricane winds only in the western half of the domain. Note the presence of the zonally aligned structures (jets) and the western boundary intensified gradients implying a strong flow there.

with an intensified western boundary current. However, this gyre is extended only to the western part of the basin (where hurricanes are active), having substantially weaker currents on the eastern side. Thus, the experiments show that it is not required for the hurricanes to have a global basin coverage to form a circulation. For the boundary current to form, it is sufficient for hurricanes to be concentrated on the western side of the basin, which is the case for the present day climate.

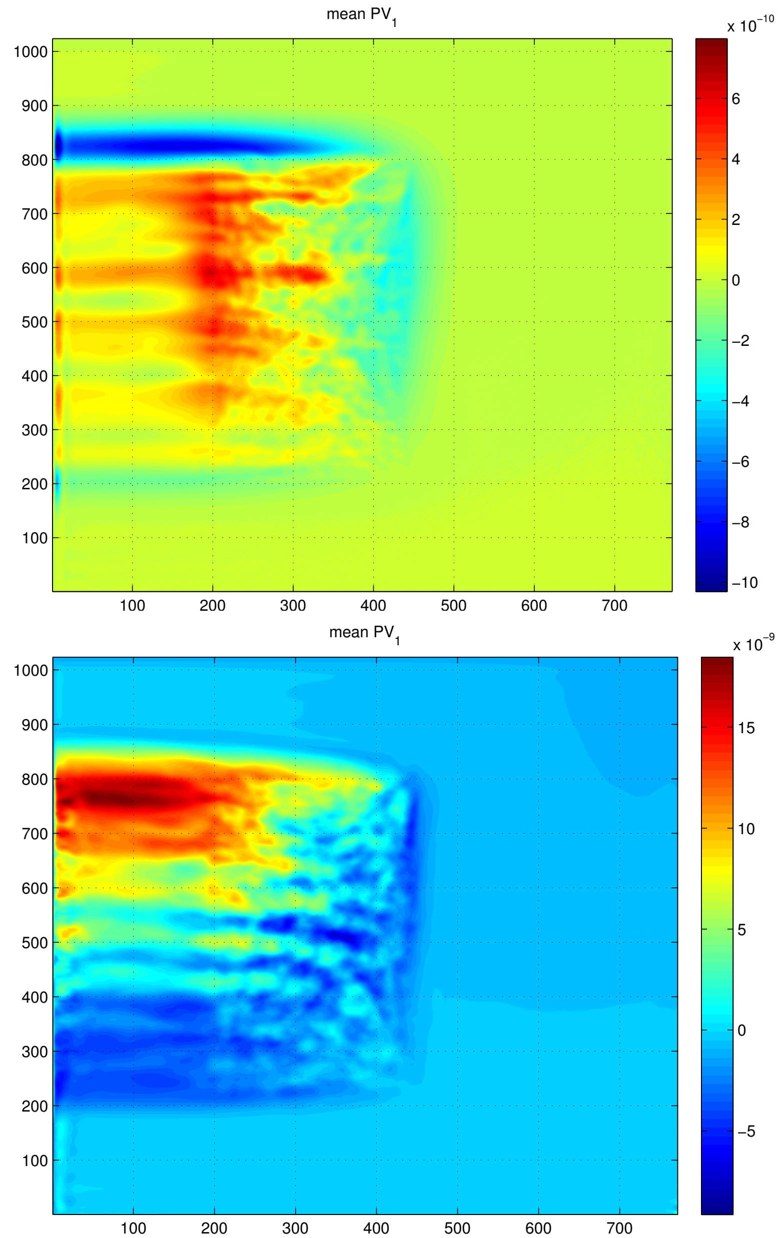

Figure 5.12: Long-term average of the potential vorticity in the top ocean layer of the shallow water model forced by translating shielded vortices. Representative simulations are shown for the cases of (top) weak and (bottom) strong vortices. Note the formation of zonally oriented jets and large scale gyres.

5.4.4 Shielded vortices

The observations of hurricane wind profiles show that the winds decay with the distance away from the core r according to square root law ($u \sim \sqrt{r}$).This giving a decay in wind stress as $1/r$ in the regions outside of the core, and hence a zero vorticity forcing there. Hence the entire forcing is concentrated inside the hurricane's cyclonic core. However it is reasonable to consider hurricanes as finite sized vortices, i.e. at some distance far from the core one could claim that there is no longer a signature of the hurricane ($u = 0$ for $r > R$). But in this case the area integral of vorticity over the whole domain would be zero, meaning that the cyclonic vorticity at the core of a hurricane is exactly compensated by an anticyclonic vorticity away from it. Thus, a better model of hurricane wind profile would be a shielded vortex.

In this case the large-scale oceanic response to hurricanes changes dramatically, since there is no more-time averaged vorticity forcing. In case of weak vortices, the oceanic response is linear and consists of a basic Sverdrup balance between the zonally averaged wind stress curl and the meridional advection. Figure 5.12 (top) shows the time mean potential vorticity anomaly distribution is weak and although it does have large scale features they are explained by the linear dynamics. The negative potential vorticity anomalies are located at the edges of the hurricane activity zone, which is expected as these regions only get the anticyclonic forcing from the tails of wind profiles. The positive gyre in the middle is required to compensate for the negative outside regions.

A distinctly different long term circulation appears for strong shielded vortices; it consists of a double gyre (Fig. 5.12, bottom). The double gyre arises due to an inverse energy cascade from small to large scales. The analysis of this large scale flow pattern is an ongoing research problem.

5.5 Discussion

From the oceanic point of view, hurricanes represent an extremely strong and localized surface wind forcing that produces a significant impact on the oceanic circulation and stratification. Hurricane winds transport momentum into the ocean, producing upper-ocean currents reaching magnitudes of up to $\sim 2m/s$. The mechanical energy is being transfered vertically, as the turbulent mixed layer in the ocean deepens due to shear instabilities. The interior of the ocean is dominated by internal near-inertial gravity waves, that disperse energy away from the source. However, not all of the energy is dispersed after the passage of a hurricane. Some remains in the geostrophic circulation established along the hurricane track. Thus, the ocean receives an overall cyclonic vorticity input from the hurricane. The large scale implications of hurricane activity on the oceanic circulation and thermal structure are split into two contributions.

Increased mixing leads to cold waters being entrained to the surface, causing negative sea surface temperature anomalies. The surface anomaly is restored by atmospheric fluxes within few weeks. The net result is the pumping of heat into the ocean. Global fields of mixing attributable to hurricane activity leads to peak estimates of $\sim 1m^2/s$. The global impact of the increased mixing leads to heat convergence towards the equator. This causes the warming of the cold tongue and reduction of the equatorial temperature gradients - an important parameter of the climate system.

There is a the mean cyclonic vorticity input from hurricane winds into the ocean, which is estimated to have a mean of about 10 meters per year in terms of upwelling of the thermocline. Hurricane occurrence probability is less than a day per year, implying that this is a highly intermittent forcing for the ocean. Nonetheless, modeling studies presented here showed that this type of forcing leads to a mean large-scale circulation in the ocean. This circulation represents a cyclonic gyre, having a boundary current flowing southward and a weaker northward flow in the interior. This mean circulation weakens the anticyclonic subtropical gyre in the Atlantic Ocean. The decrease of the northward boundary current due to present day hurricanes is estimated to be $\sim 20cm/s$ (about 10% of the strength of the Gulf Stream).

A series of sensitivity experiments showed that the magnitude of the hurricane driven circulation depends only on the mean value of the upwelling, not on the details of the forcing such as frequency or strength of individual storms. The model used to obtain these results is a reduced-gravity shallow-water model. It is a highly idealized model but it provides a good conceptual representation of the problem. Bringing the model toward a more realistic regime as well as finding evidence in the ocean observations are essential for further progress.

A majority of global climate models are not capable of running at high enough resolution to resolve the oceanic response to individual hurricanes. There are some ocean models that run under high resolutions; however, their high computational cost allows them to run only for several decades. But even though the ocean-models are capable of resolving hurricane-type forcing, ocean-atmosphere modeling could not reproduce modern climate hurricanes. Thus, there is a need for parametric representation of hurricanes in general circulation models.

For low resolution models, one way of parameterizing hurricanes would be to provide the additional large scale mean wind stress to correct for the input of cyclonic vorticity by hurricanes. This would give a negative correction to the mean anticyclonic circulation, decreasing its transport. The mean stress should be scaled appropriately to represent a strong damping of the energy stored by eddies. Furthermore, this correction should depend on the climatological properties of hurricane activity, which in turn are coupled to the global climate state (the output of the models). This would allow to investigate climate feedbacks related to hurricane-ocean interaction.

For high resolution ocean models hurricanes could be represented in a statistical way. Since ocean's mean response is not sensitive to individual tracks, one could treat hurricanes as randomly appearing vortices with a given probability of occurrence over a particular point in the ocean and a given distribution of their parameters. Observations of hurricanes would be used to construct probability maps of parameters related to hurricane forcing, such as occurrence frequency, wind speed, spatial scales. This approach also avoids the problem of simulating proper tracks from the atmospheric models, and would use instead hurricane climatology from observations.

Chapter 6

Climate Impacts of Oceanic Mixing by Tropical Cyclones

The material contained in this chapter has been published in the *Journal of Geophysical Research* under the title "Climate impacts of intermittent upper ocean mixing induced by tropical cyclones" [Manucharyan et al., 2011].

6.1 Introduction

The intense winds of tropical cyclones cause vigorous ocean vertical mixing [D'Asaro et al., 2007] that brings colder water to the surface while pumping warm surface waters downwards. Experiments with ocean models [Sriver et al., 2010] show that strong storms can induce vertical mixing to depths of 250 m and result in a cooling of 6℃ or more in the storm's wake. It has been argued that this vertical mixing may have global climate impacts by contributing to oceanic poleward heat transport [Emanuel, 2001; Sriver and Huber, 2007] and by modifying ocean circulation and thermal structure [Fedorov et al., 2010]. The overarching goal of the present study is to investigate further the climate impacts of this mixing in a comprehensive coupled general circulation model (GCM). Attempts to quantify the amount of TC mixing from observations have found that tropical cyclones induce an annual mean diffusivity in the range of $1\,cm^2/s$ [Sriver and Huber, 2007; Sriver et al., 2008] to $6\,cm^2/s$ [Liu et al., 2008]. What effects could this additional mixing have on climate?

Using observed tracks of tropical cyclones and a simplified ocean model, Emanuel [2001] estimated that TC-induced mixing contributes $1.4 \pm 0.7\,PW$ in ocean poleward heat transport ($1PW = 10^{15}\,W$), which represents a substantial fraction of the observed heat transport by the oceans. He concluded that tropical cyclones might play an important role in driving the ocean thermohaline circulation and thereby regulating climate. Sriver and Huber [2007] and Sriver et al. [2008] generally supported this conclusion but downgraded heat transport estimates to about $0.3 - 0.5\,PW$.

Using an ocean GCM, Jansen and Ferrari [2009] demonstrated that an equatorial gap in the TC mixing region altered the structure of the TC-generated heat transports, allowing for a heat convergence towards the equator. On the other hand, Jansen et al. [2010] suggested that the climate effects of mixing by TC could be strongly reduced by seasonal factors, namely by the heat release to the atmosphere in winter (this argument was based on the assumption that the mixing did not penetrate significantly below the seasonal thermocline).

Hu and Meehl [2009] investigated the effect of hurricanes on the Atlantic meridional overturning circulation (AMOC) using a relatively coarse global coupled GCM in which tropical cyclones in the Atlantic were included via prescribed winds and precipitation. Their conclusion was that the strength of the AMOC in the model would increase if hurricane winds were taken into account; however, changes in precipitation due to hurricanes would have an opposite effect. More recently, Scoccimarro et al. [2011] used a TC-permitting coupled GCM and estimated the contribution of TC to the annually averaged ocean heat transport an order of magnitude smaller than suggested by Sriver and Huber [2007] and Sriver et al. [2008]. Their model, however, was too coarse to fully resolve tropical storms, leading to the simulated TC activity about 50% weaker with fewer strong storms than the observed.

Korty et al. [2008] developed an intermediate-complexity coupled model with a TC parameterization in the form of interactive mixing in the upper ocean that depended on the state of the coupled system. The main aim of the study was to investigate the potential role of tropical cyclones in sustaining equable climates, such as the warm climate of the Eocene epoch. These authors noted a significant increase in TC-induced oceanic mixing in a warmer climate, an increase in poleward heat transport, and a corresponding warming of high latitudes.

Fedorov et al. [2010] implemented a constant additional mixing within two zonal subtropical bands that they added to the upper-ocean vertical diffusivity in a comprehensive climate GCM. They describe a mechanism in which TC warm-water parcels are advected by the wind-driven circulation and resurface in the eastern equatorial Pacific, warming the equatorial cold tongue by 2-3℃, deepening the tropical thermocline, and reducing the zonal SST gradient along the equator. This leads to El Niño-like climate conditions in the Pacific and changes in the atmospheric circulation (the Walker and the Hadley cells). While the goal of this study was to simulate the climate state of the early Pliocene [Fedorov et al., 2006], these results have much broader implications for the role of tropical cyclones in modern climate.

The conclusions of Fedorov et al. [2010] generally agree with those of Sriver and Huber [2010], who added high-resolution winds from observations to a climate model, and those of Pasquero and Emanuel [2008], who modeled the propagation of oceanic temperature anomalies created by a single instantaneous mixing event. The latter authors found that at least one third of the warm subsurface temperature anomaly was advected by wind-driven circulation towards the equator, which should lead to an increase in ocean heat content in the tropics. In parallel, the impact of small latitudinal variations in background vertical mixing (unrelated to TC) was investigated in a coupled climate model by Jochum [2009], who concluded that the equatorial ocean is one of the regions most sensitive to spatial variations in diffusivity.

Several of the aforementioned modeling studies parametrize the effect of tropical storms by adding annual mean values of the TC-induced diffusivity inferred from observations to the background vertical diffusivity already used in an ocean model. However, a single tropical cyclone induces mixing of a few orders of magnitudes greater than the annual mean value. Thus, a question naturally arises - how reliable are results obtained by representing a time-varying mixing with its annual mean value? To that end, the goal of this study is to explore the role of intermittency (*i.e.* temporal dependence) of the upper-ocean mixing in a coupled climate model.

In our study, to mimic the effects of tropical cyclones, we use several representative cases of time-dependent mixing that yield the same annual mean values of vertical diffusivity. The approach remains relatively idealized, in line with the studies of Jansen and Ferrari [2009] and Fedorov et al. [2010]. A spatially uniform (but time varying) mixing is imposed in zonal bands in the upper ocean. We analyze changes in sea surface temperatures (SST), oceanic thermal structure, the meridional overturning circulation in the ocean and the atmosphere, and poleward heat transports.

In addition, we formulate a simple one-dimensional model of heat transfer to understand the sensitivity of the sea surface temperature (SST) and heat transport to the duration of mixing. It accounts for the gross thermal structure of the upper ocean and incorporates time-dependent coefficients of vertical diffusivity. Using this simple model, we vary the fraction of the year with TC-induced mixing and look at the oceanic response. Both the comprehensive and simple models suggest that highly intermittent mixing should generate a response 30 to 40% weaker than from a permanent mixing of the same average value.

6.2 Climate model and experiments

We explore the global climate impacts of upper-ocean mixing induced by tropical cyclones using the Community Climate System Model, version 3 (CCSM3) [Collins et al., 2006]. The ocean component of CCM3 has 40 vertical levels, a 1.25° zonal resolution, and a varying meridional resolution with a maximum grid size of 1° that reduces to 0.25° in the equatorial region. The atmosphere has 26 vertical levels and a horizontal spectral resolution of T42 (roughly 2.8°x 2.8°). The atmosphere and other components of the model, such as sea ice and land surface, are coupled to the ocean every 24 hours.

The conventional vertical mixing of tracers in the ocean model is given by (1) a background diffusivity ($0.1\, cm^2/s$ in the upper ocean) attributable to the breaking of internal waves which is constant in time [Danabasoglu et al., 2006] and (2) a diffusivity due to shear instabilities, convection and double-diffusion processes parameterized by the KPP scheme [Large et al., 1994], which varies in time and space. The annual mean SST and thermal structure of the upper Pacific for this climate model are shown in Fig. 6.1.

To incorporate the effects of tropical cyclones into the model, we add extra vertical diffusivity in the upper ocean within the subtropical bands, defined here as 8°-40° N/S (Fig. 6.1). This additional diffusivity can vary with time throughout the year but maintains an annual mean value of $1\, cm^2/s$ (ten times larger than the model's background diffusivity). This mean value, when applied everywhere in the subtropical bands, is probably an overestimation for the present climate; however, TC-induced diffusivity may have been even greater in past warm climates [Korty et al., 2008].

The imposed diffusivity is spatially uniform, following the studies of Jansen and Ferrari [2009] and Fedorov et al. [2010] who looked at the gross effects of TC mixing in the subtropical bands and neglected zonal variations in the mixing. We ignore buoyancy effects associated with increased precipitation and heat fluxes generated by TC at the ocean surface [Hu and Meehl, a)

b)

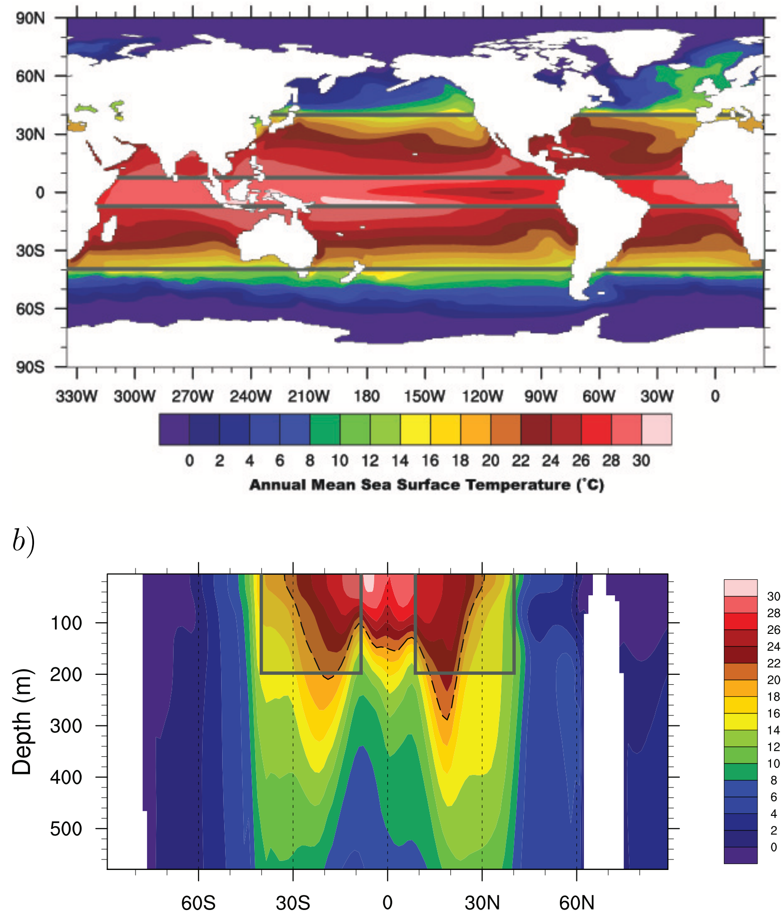

Figure 6.1: The annual mean sea surface temperature (a) and ocean temperature along 180° W (b) as functions of depth; both panels are for the control simulation. In the perturbation experiments additional mixing will be imposed in the zonal bands 8°-40° N and S in the upper 200 m of the ocean as indicated by the shading.

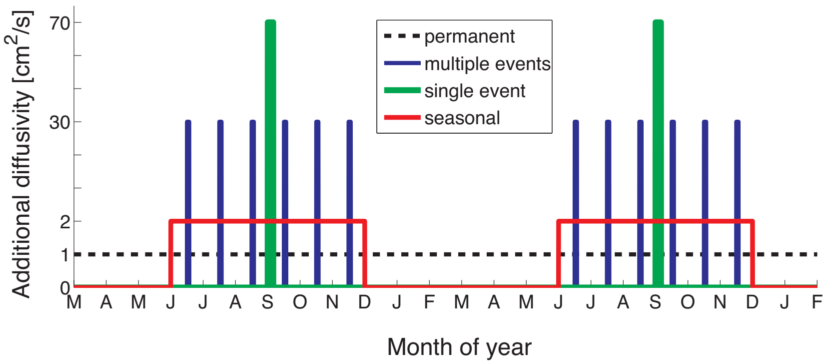

Figure 6.2: Relative duration and magnitude of the added vertical diffusivity that replicates TC-induced mixing in different experiments with the climate model (Permanent, Seasonal, Multiple-event and Single-event). The regions where additional mixing is imposed in perturbation experiments are shown in Fig. 6.1. For further details, see Table 6.1.

2009; Scoccimarro et al., 2011] and focus solely on the mixing effects.

Our choice for the average depth to which TC-mixing penetrates is 200 m. In nature, this depth varies significantly depending on the local ocean stratification and the characteristics of a particular storm. Nonetheless, 200 m appears to be a reasonable value for a number of applications. For example, mixing induced by hurricane Frances in the Atlantic penetrated to about 130 m depth, as measured in the hurricane wake by a deployed array of sea floats [D'Asaro et al., 2007]. However, mixing generated by typhoon Kirogi in the Western Pacific may have penetrated to depths of about 500 m with the strongest effects concentrated in the upper 250 m, as estimated from calculations with an ocean GCM forced by observed winds [Sriver, 2010]. Using a simple model for TC-induced mixing, Korty et al. [2008] estimated the penetration depth at about 200 m for their experiment with moderate concentration of CO_2 in the atmosphere and at 300 m for their warm climate.

We perform four perturbed model experiments with different temporal dependence of TC-induced mixing, and a control run with no additional mixing.

Mixing Cases	T_{on}	T_{off}	D_{max} cm^2/s	OHT PW	SST_b ℃	SST_{ct} ℃	T_m ℃	α
Permanent	12 months	0 months	1	0.12	-0.19	2.3	0.11	1.00
Seasonal	6 months	6 months	2	0.21	-0.30	2.2	0.09	0.99
Multiple Events	2 days	28 day	30	0.16	-0.14	1.7	0.19	0.72
Single Event	5 days	360 days	73	0.13	-0.03	1.7	0.09	0.62

Table 6.1: The main characteristics and results of different perturbation experiments: duration of the imposed mixing (T_{on}, T_{off}), maximum imposed vertical diffusivity (D_{max}), peak anomalies in ocean heat transport (OHT), mean SST changes within the mixing bands (SST_b), the maximum warming of the cold tongue (SST_{ct}), anomalies in global mean surface-air temperature (T_{gm}), and the regression coefficient (α) between SST anomalies in the transient mixing experiments and those in the Permanent mixing run. All properties are the average of the last 25 years of simulation, except the coefficient α which is the average of the last 100 years.

In the experiment referred to as 'Permanent', we specify a diffusivity that remains constant throughout the year. In the other three perturbation experiments the temporal dependence of the mixing is given by step functions alternating between ON and OFF stages. In the 'Seasonal' experiment a constant mixing is applied for only half a year. In the 'Single-event' experiment mixing occurs once a year and lasts only 5 days. The 'Multiple-event' experiment represents 6 major TC a year that last two days each (Fig. 6.2 and Table 6.1). To take into account the seasonality of tropical cyclone activity, TC mixing in these three experiments is imposed only during the warm part of the year in each hemisphere (summer and fall) with a half-a-year lag between different hemispheres.

We emphasize that in all perturbed cases the annual-mean value of TC-induced diffusivity remains the same (1 cm^2/s, similar to that estimated by Sriver and Huber [2007]). Consequently, peak values of the imposed vertical diffusivity for highly intermittent mixing exceed diffusivity for permanent mixing by two orders of magnitude (Table 6.1).

For each perturbed experiment the model is initialized from a 1000 year simulation with preindustrial conditions and spun up for 200 years after introducing the time-varying vertical diffusivity. Similarly, our control experiment is a 200 year continuation of the preindustrial simulation. The results of the experiments will be presented in terms of anomalies from the control run, averaged over the last 25 years of calculations.

6.3 Results from the climate model

6.3.1 The time scales of climate response

We start the discussion of the model results with the time series of several essential climate indices that show the transient response of the climate system to introduced mixing. The time evolution of global-mean surface temperature and the mean top-of-the-atmosphere (TOA) radiation flux indicates that the climate system is adjusting to changes in the ocean diffusivity with an e-folding time scale of nearly 30 years (Fig. 6.3a,b)[1]. After 100 years these variables do not change, except for weak decadal variations. Initially, we see a drop in global-mean temperatures and a counteracting increase in the TOA radiation flux. However, as the TOA radiation imbalance diminishes, the global mean temperature increases and settles at a value slightly greater than in the control run (by $0.1 - 0.2$℃). This increase seems to be robust between different experiments, even though its magnitude is comparable with the internal variability of the control run.

Furthermore, the time series of Niño 3.4 index (indicative of the tropical ocean response) show that a warm temperature anomaly of substantial magnitude emerges along the equator also within the first 30 years of simulations (Fig. 6.3c). This indicates that the initial timescales of the climate response are set by the adjustment of the wind-driven circulation and thermal structure of the upper ocean. That occurs on time scales of 20-40 years [Barreiro

[1]Note that the atmospheric data were saved only for the last 150 years of the Control simulation.

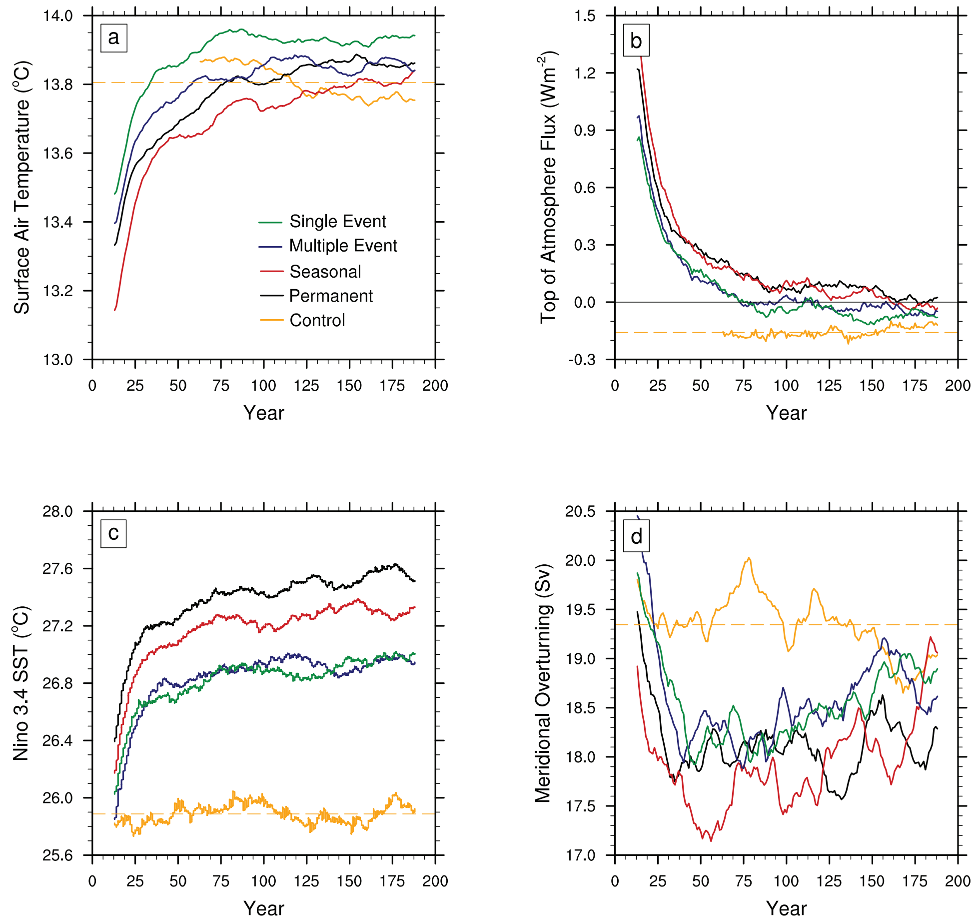

Figure 6.3: The time evolution of global mean temperature, top-of-the-atmosphere radiation imbalance, the Niño 3.4 SST, and the AMOC intensity in different experiments, including the control run (orange line), as simulated by the climate model. A 25-year running mean has been applied.

et al., 2008; Harper, 2000] controlled by a combination of advective, wave and diabatic processes [Boccaletti et al., 2004; Fedorov et al., 2004].

In contrast to the first three indices, the index of the AMOC intensity, related to the deep-ocean circulation, shows a sharp decrease after the additional mixing was imposed, but then follows a very slow recovery (Fig. 6.3d). The deep ocean continues its adjustment on longer time scales (centennial to millennial) that should involve diapycnal diffusion throughout the global ocean [Wunsch and Heimbach, 2008] and processes in the Southern Ocean [Allison et al., 2011; Haertel and Fedorov, 2011].

Nevertheless, after roughly 100 years of simulation, the atmosphere and the upper ocean have gone through their initial adjustment stages and are now experiencing a slow residual climate drift (due to the deep-ocean adjustment) as well as decadal variability. We, thus, focus our discussions on the dynamics of the upper ocean and the atmosphere, but avoid making final conclusions on the state of the AMOC (also see the concluding section).

6.3.2 Climate response

All four perturbation experiments produce similar patterns of SST anomalies generated by TC-induced mixing (Fig. 6.4) independent of the exact temporal dependence of the mixing: a weak surface cooling at the location of mixing and a warming in other regions (mid- and high-latitudes and the equatorial region). The cooling is caused by a greater local entrainment of colder waters from below and pumping of warm surface waters into the interior of the ocean by the additional mixing [Jansen and Ferrari, 2009; Sriver and Huber, 2010; Sriver et al., 2008]. In turn, the warming is caused by the advection of these relatively warm waters, pumped down by mixing, and their subsequent upwelling to the surface away from the source regions. The warming is amplified by atmospheric feedbacks (see below). The overall pattern of the SST response to anomalous mixing is similar to that noted in previous works [Fedorov et al., 2010; Sriver and Huber, 2010].

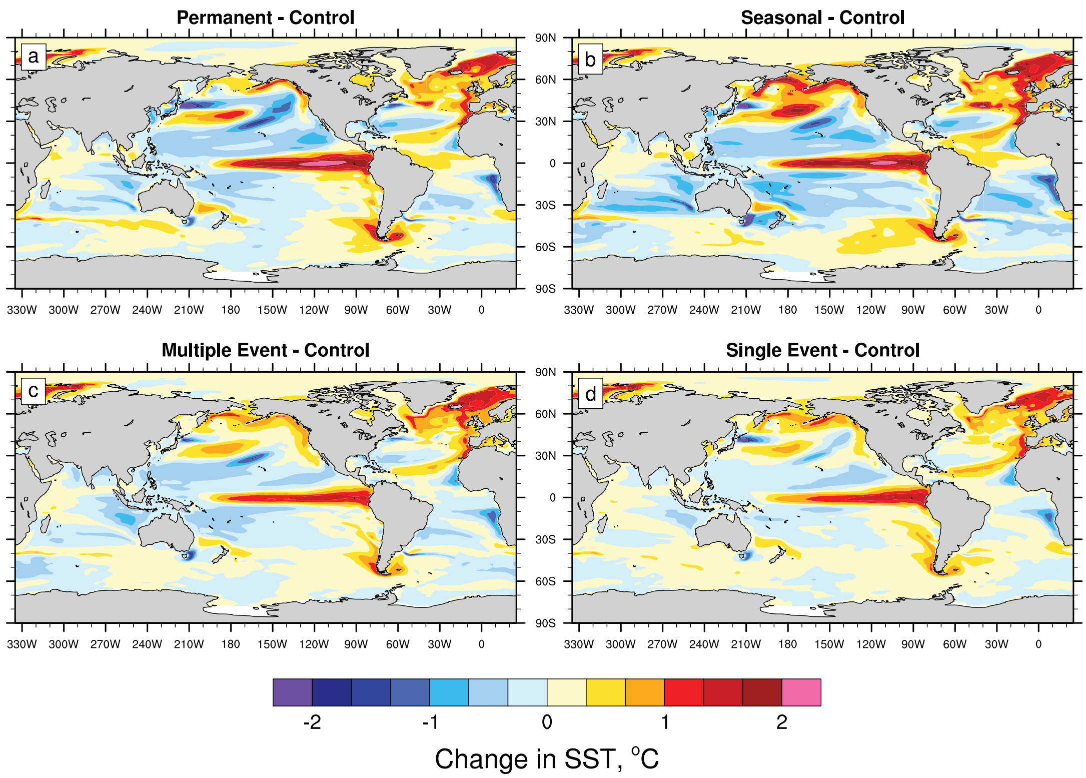

Figure 6.4: Sea surface temperature anomalies in the four different perturbation experiments with added vertical diffusivity. From top to bottom: Permanent, Seasonal, Multiple-event and Single-event experiments. Anomalies are calculated with respect to the Control run and averaged over the last 25 years of calculations.

The largest SST cooling in the mixing bands is achieved for the Seasonal experiment with an average reduction of 0.3℃ and local values reaching 1℃ (Fig. 6.4). Seasonal mixing causes a stronger SST change than the Permanent mixing, because vertical mixing is more efficient in modifying the SSTs during summer, when the thermal stratification is stronger and surface waters are warmer. In contrast, during winter mixed layers are deep and surface waters are relatively cold, which makes it more difficult to modify SSTs by additional mixing. The magnitude of cooling for the Permanent mixing experiment is 0.2℃ on average and decreases slightly as the mixing becomes highly intermittent (Table 6.1).

Perhaps, the most pronounced feature of these experiments is the warming of the cold tongue in the eastern equatorial Pacific that can reach magnitudes over 2℃. In the Permanent and Seasonal experiments the warming has similar strengths with a slightly weaker warming in the Single and Multiple-event experiments. The east-west extent of cold tongue warming is amplified by the weakening of the Walker cell (not shown) via the Bjerknes feedback [Bjerknes, 1969] and a corresponding reduction in the thermocline slope along the equator (Fig. 6.5).

The additional mixing is restricted to a depth of 200 meters, yet, temperature anomalies are seen as deep as 500 meters (Fig. 6.5). The warm surface waters, pumped down by TC mixing, are advected by the wind-driven ocean circulation as well as diffusing downwards by the unaltered deep background mixing. The subsurface temperature signal is again strongest for the Seasonal and the Permanent mixing experiments with temperature anomalies reaching magnitudes of 5-10℃. The spatial structure of the anomalies is similar for all the mixing cases and is characterized by a deepening of the tropical thermocline (Fig. 6.5).

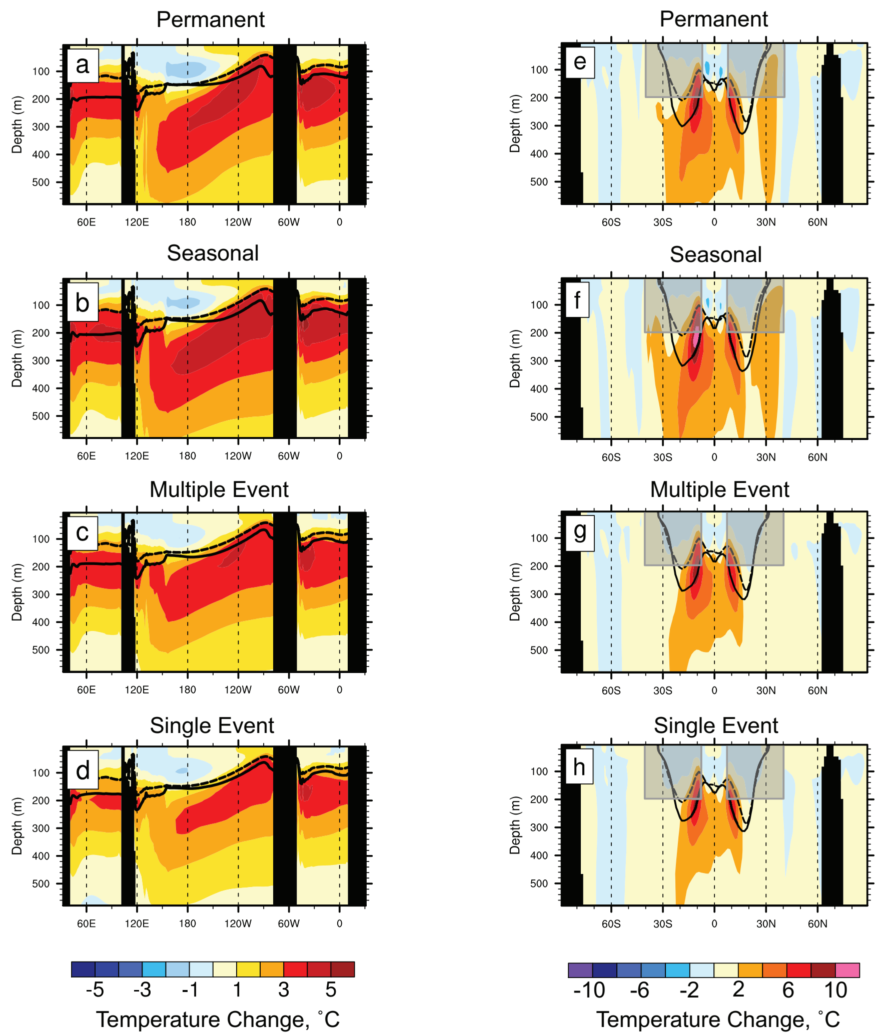

Figure 6.5: Temperature anomalies in the ocean as a function of depth along the equator (left panels) and along 180°W (right panels) for different perturbation experiments. From top to bottom: Permanent, Seasonal, Multiple-event and Single-event experiments. The solid and dashed black lines denote the position of the 20℃ isotherm (a proxy for the tropical thermocline depth) in the perturbation experiments and control run, respectively. Note the deepening of the tropical thermocline, the reduction of the thermocline slope along the equator, and the strong subsurface temperature anomalies that extend to depths of about 500 m. Ocean diffusivity is modified in the upper 200 m in the subtropical bands 8°-40° N/S (gray regions). Anomalies are calculated with respect to the Control run and averaged over the last 25 years of calculations.

6.3.3 Correlation between different experiments

We observe that spatial patterns of the climatological anomalies are strongly similar between different model runs. This brings us back to the question of how good is the approximation of intermittent mixing with its annual mean. To address this question, we choose the Permanent mixing run as the reference case, and compare it to the runs with intermittent mixing with the aim of quantifying the differences and similarities between the cases.

As a representative field for our analysis we use the global spatial pattern of SST anomalies. We choose this particular field as it couples the ocean and the atmosphere and reflects changes occurring in both fluids. At any particular instant in time, the magnitudes of vertical mixing are different in each run, and so are the SSTs. Therefore, we compare time-averaged anomalies, defined here through 25-year running means.

We find that SST anomalies for the intermittent mixing runs are well correlated with anomalies for the Permanent mixing run, with correlation coefficients remaining higher than 0.8 throughout the whole integration (Fig. 6.6a). Although all the runs experience a climate drift as well as low frequency variability, these variations occur in a correlated way. Furthermore, the correlation coefficients have no negative trends, implying that decorrelation time scale between different runs (if decorrelation does occur) is much longer than the 200 year integration time.

The fact that the spatial fields are well correlated, allows us to calculate the relative magnitudes of SST anomalies in the intermittent mixing experiments with respect to SST anomalies for permanent mixing. We assume the following relation between SST anomalies for each run:

$$\Delta SST = \alpha \Delta SST_{perm} + err \tag{6.1}$$

where ΔSST and ΔSST_{perm} are SST anomalies for different intermittent mixing runs and for the Permanent mixing run, respectively, α is the relative

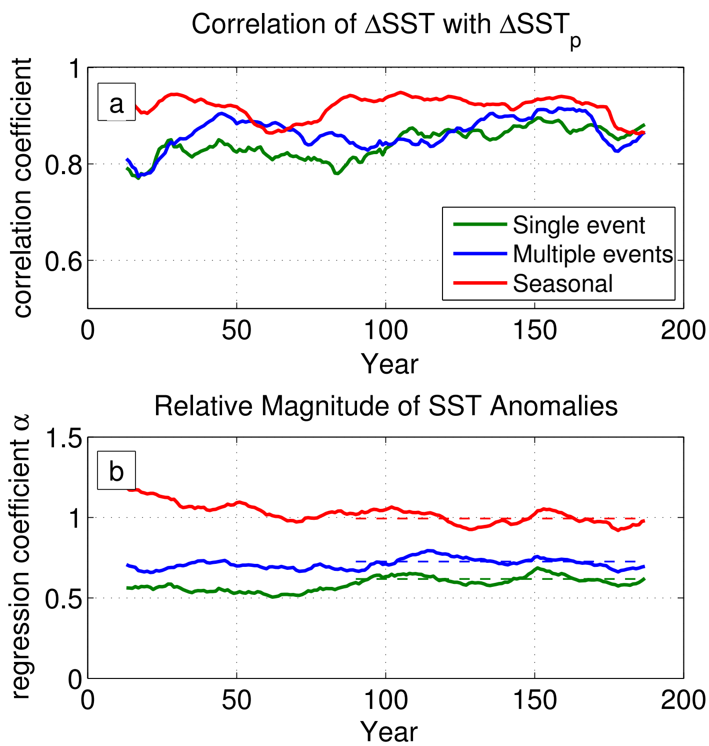

Figure 6.6: (a) Temporal changes of the correlation coefficients evaluated between annual mean SST anomalies in the transient mixing experiments and those in the Permanent mixing run. (b) The same but for the regression coefficient α. These coefficients indicate how close to each other the SST anomalies in different experiments are.

magnitude of the anomaly, and *err* is the error of such an approximation. The regression coefficient α is computed as

$$\alpha = \frac{\langle \Delta SST \cdot \Delta SST_{perm} \rangle}{\langle \Delta SST_{perm} \cdot \Delta SST_{perm} \rangle} \tag{6.2}$$

where the operator $\langle \cdot \rangle$ denotes a dot product between the two fields (weighted by the surface area). When computing these coefficients we actually subtract the means (relatively small) from the SST anomalies. Obviously, for the Permanent mixing experiment, $\alpha = 1$ and $err \equiv 0$. For the intermittent mixing experiments, α shows the relative magnitude of SST anomalies with respect to the Permanent mixing run.

These coefficients stay relatively constant in time after the initial adjustment period (Fig. 6.6b), which allows us to evaluate the relative magnitude of SST anomalies in different experiments. Accordingly, anomalies in the Seasonal experiment have almost the same magnitude as the Permanent case ($\alpha \approx 1$). The Multiple-event and Single-event experiments show relative magnitudes of 72% and 62%, respectively over the last 100 years (Table 6.1). The root-mean-squared error of such a representation lies between 0.2-0.3℃ for the whole duration of the experiments, which implies that approximating the gross effects of intermittent mixing with appropriately scaled permanent mixing will produce a relatively small error (a factor of 2 or 3 smaller than the natural decadal variability of SST anomalies).

6.3.4 Oceanic and Atmospheric overturning circulations and heat transports

Changes in oceanic temperatures are paralleled by anomalies in surface heat fluxes and hence in ocean poleward heat transport (Fig. 6.7). The oceanic heat uptake increases in the regions of additional mixing, which results in two major effects – a stronger ocean heat transport to mid and high latitudes (as suggested by Emanuel [2001]) and anomalous heat convergence towards the

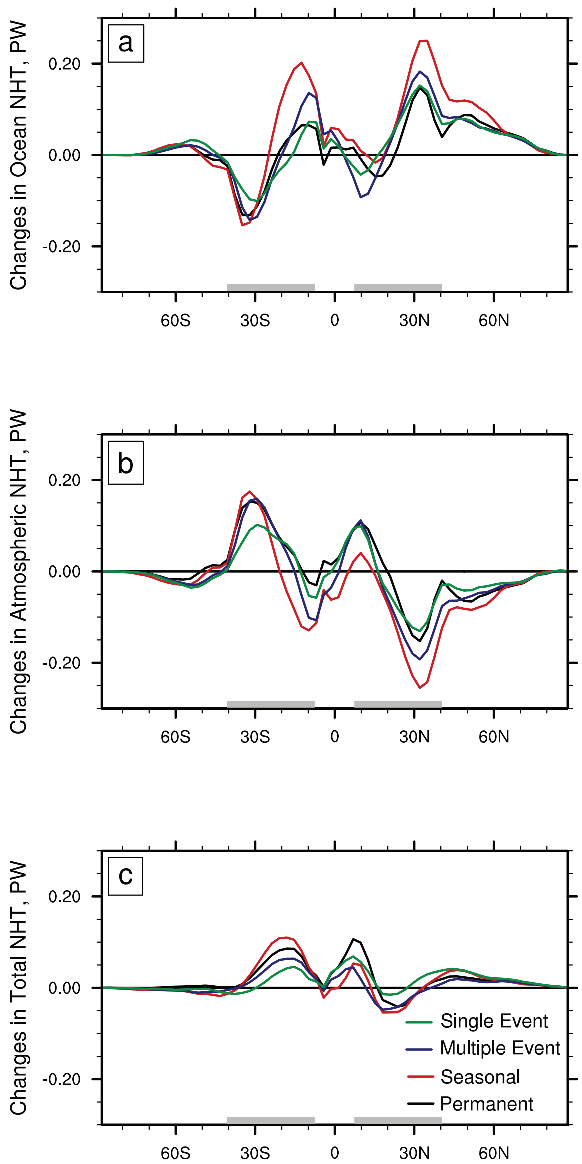

Figure 6.7: Anomalous northward heat transport (OHT) by the ocean (top), the atmosphere (middle), and the entire ocean-atmosphere system (bottom) for different perturbation experiments. Thick gray lines on the horizontal axis indicate the latitudinal extent of the regions with enhanced mixing; the magnitude of decadal changes in the heat transport does not exceed 0.05 PW.

equator (as noted by Jansen and Ferrari [2009] and Fedorov et al. [2010]). The strongest ocean heat transport anomalies are produced by seasonal mixing; it is harder to distinguish between the other cases because of decadal variability. The peak anomalous heat transport by the ocean reaches $0.15 - 0.25\ PW$, which roughly matches the estimates by Sriver and Huber [2007].

The observed increase in ocean heat transport is largely due to changes in the amount of heat transported by the shallow wind-driven circulation, rather than the deep overturning circulation. In fact, we observe an initial weakening of the AMOC (Fig. 6.3d) possibly caused by the surface warming of the Norwegian Sea (Fig. 6.4) which has a stabilizing effect on convection. However, the integration time of our experiments is not sufficient to reach an equilibrium, and at the end of a 200 year simulation the AMOC still exhibits a trend towards higher values. Whether the AMOC eventually returns to its undisturbed strength, or perhaps intensifies in agreement with the hypothesis of Emanuel [2001], is unclear. A definite answer to this question will require several thousand years of calculations.

It is important that SST changes, specifically an increase in the meridional temperature gradient between the subtropics and the equatorial region, cause the intensification of the atmospheric Hadley circulation (Fig. 6.8). As a result, anomalies in oceanic heat transport are partially compensated by the atmosphere (Fig. 6.7) in a manner reminiscent of Bjerknes compensation [Bjerknes, 1964; Shaffrey and Sutton, 2006]. For example, whereas the ocean carries more heat towards the equator, the stronger Hadley circulation transports more heat away from the equator. Consequently, changes in oceanic heat transport of nearly 0.3 PW do not necessarily represent changes in the total heat transport by the system (Fig. 6.7c), which stays below 0.1 PW.

Nevertheless, a substantial fraction of oceanic heat transport remains uncompensated as a stronger poleward heat transport by the ocean induces the atmospheric water vapor feedback in mid to high latitudes and a decrease in global albedo related to changes in low clouds and/or sea ice [Herweijer et al.,

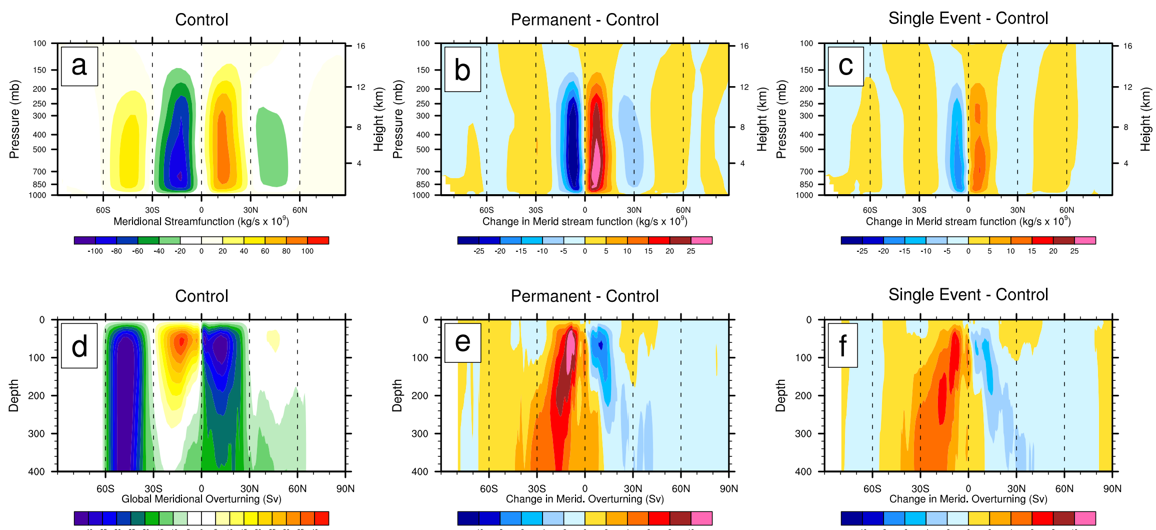

Figure 6.8: (a,d) The zonally averaged atmospheric and oceanic circulations in the control run (the Hadley cells and the STC, respectively) and their anomalies in the Permanent mixing (b,e) and Single-event (c,f) experiments. Note the strengthening of both the atmospheric and shallow oceanic meridional overturning cells. Anomalies are averaged over the last 25 years of calculations.

2005]. Such changes result in a slight increase of global mean temperature (0.1 - 0.2 ℃) in all the experiments with enhanced mixing (Table 6.1).

Finally, one of the consequences of the stronger winds associated with the more intense Hadley circulation is the strengthening of the oceanic shallow overturning circulation – the subtropical cells (STC) in Fig. 6.8. This strengthening of the STC appears to moderate the warming of the equatorial cold tongue but is not able to reverse oceanic heat convergence towards the equator.

6.4 A model of the oceanic stratification subjected to TC mixing

6.4.1 Formulation of the model

To investigate further the ocean sensitivity to intermittent mixing, here we formulate a simple one-dimensional model in the vertical describing the gross thermal structure of the upper ocean when subjected to anomalous mixing events. The model equations for the vertical temperature profile in the subtropical ocean $T = T(z,t)$ are as follows

$$T_t = (\kappa T_z)_z - \gamma(T - T^*) \tag{6.3a}$$

$$\kappa T_z = -\alpha_s(T - T_s),\ z = 0 \tag{6.3b}$$

$$\kappa T_z = \alpha_b(T - T_b),\ z = -H \tag{6.3c}$$

This is a heat transfer equation with horizontal advection parameterized as a restoring term, $-\gamma(T - T^*)$. The restoring time scale, $\gamma^{-1} = 10yr$, is chosen to represent advection by the wind-driven subtropical cell (STC) in the Pacific. The upstream temperature profile T^* is obtained as a steady state solution of equation **??** with a constant background diffusivity, κ_0, and no advective restoring. Thus, the restoring profile T^* is also a steady-state solution of the full system, which will be used as the background profile to compare solutions corresponding to different forms of intermittent mixing. In the coupled climate model both the strength of the circulation and the upstream profile change a little in response to the additional mixing, but we will neglect such effects here.

Atmospheric heat fluxes at the ocean surface are parameterized by restoring the surface temperature to a prescribed atmospheric temperature, T_s (30°C). At the bottom of the integration domain ($H = 300\, m$), the temperature is restored to a deep ocean temperature, T_d (10°C), which is set by the deep ocean circulation. The restoring time scales (or piston velocities, e.g. Griffies et al. [2005]) are $\alpha_s^{-1} = 0.3\, m/day$ at the surface and $\alpha_d^{-1} = 0.08\, m/day$ at the bottom of the domain. These values are chosen in such a way that a surface temperature anomaly caused by a mixing event would be restored roughly within two weeks and temperature anomalies at the bottom of the domain within two months (in terms of e-folding time scales).

The time-dependent vertical diffusivity consists of two components: a background diffusivity, κ_0 ($0.1\, cm^2/s$) and an intermittent diffusivity, $\kappa'(t)$, replicating the effect of TC (with the annual mean value of $1\, cm^2/s$ above $200\, m$, zero below). For simplicity, we neglect the seasonal cycle and restrict the form of $\kappa'(t)$ to a periodic step function with an ON/OFF behavior:

$$\kappa'(t+\tau) = \kappa'(t) = \begin{cases} \kappa_{on}, & 0 < t \leq r\tau \\ 0, & r\tau < t \leq \tau \end{cases} \tag{6.4}$$

The period, τ, of the TC-induced diffusivity is chosen to be one year, yielding one event per year. The parameter, r, is a measure of the mixing intermittency - it indicates the fraction of the year that the TC-mixing is ON [1].

The parameter r provides a link to the coupled model simulations, in which $r = 1$ for the Permanent case, $r = 0.5$ for the Seasonal, and $r = 0.01$ for the Single-event (the Multiple-event case does not have a direct analogue in this framework). The model is integrated numerically for a broad range of parameter r (between $0.003 - 1$) using a finite-difference scheme with a vertical resolution of 5 meters and an adaptive time step. Each experiment lasts for 200 years to match the coupled model experiments and to insure that statistical properties of this system are equilibrated.

6.4.2 Idealized model results

The steady state-solution of equation (6.3) without additional diffusion describes an ocean with a linearly decreasing temperature with depth (Fig. 6.9a, dashed line). Adding permanent diffusivity ($r = 1$) in the upper $200m$ leads to a substantial cooling at the surface and a warming at depth (Fig. 6.9a, solid black line). Note, that warm anomalies penetrate to depths below 200 m where no additional mixing is applied. This is a result of slow diffusion due to the model original background diffusivity. The penetration depth (L_p) is dictated by the balance between vertical diffusion and advective restoring with the following scaling: $L_p \sim \sqrt{\kappa_0/\gamma}$. This gives a penetration depth of 170 m below the additional mixing, which is in rough agreement with the climate model, where strong temperature anomalies are observed at depths of 400-500 m.

When the additional diffusivity varies with time ($r < 1$), so does the temperature profile. During the interval when the transient mixing is ON, the temperature profile becomes more uniform with depth (Fig. 6.9a, dark blue line). However, during the OFF stage this profile gradually relaxes towards the undisturbed temperature distribution (Fig. 6.9a, light blue line).

[1] Note that additional vertical diffusivity during the ON stage (κ_{on}) is normalized by r, so that the annual mean diffusivity stays constant for all experiments

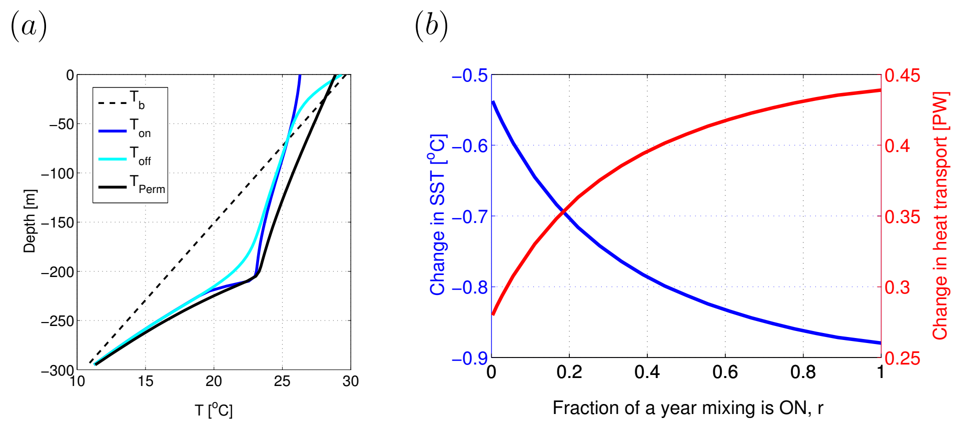

Figure 6.9: (a) Temperature profiles as a function of depth obtained as solutions of the simple one-dimensional model with no additional mixing (dashed line) and with the addition of permanent mixing (solid black line). For comparison, also shown are temperature profiles for an experiment with $r = 0.05$ directly after the mixing event (dark blue line) and after the restoring period (light blue line). (b) Anomalies in surface temperature and ocean heat transport estimated from the simple model for different values of the parameter r. The mean value of the imposed diffusivity ($1\,cm^2/s$) remains the same for all r.

Thus, the intermittent mixing causes large oscillations in ocean temperature. When averaged, these oscillations produce persistent cold anomalies at the ocean surface and warm anomalies at depth. The horizontal advection of these warm subsurface temperature anomalies generates anomalous heat transport (ΔHF), which eventually leads to the warming in the equatorial cold tongue and of mid and high latitudes.

The largest SST cooling (ΔSST) is achieved for constant TC mixing ($r = 1$). As the mixing becomes more intermittent ($r < 1$), the magnitude of the SST change decreases (Fig. 6.9b, blue line). In the limit of very small r (highly intermittent mixing), the average SST anomaly is reduced roughly by $30 - 40\%$, but nevertheless remains significant; that is, short but strong mixing events are indeed important. The magnitude of the anomalous heat transport follows roughly the same dependence on r (Fig. 6.9b, red line).

Overall, such behavior is consistent with the coupled model, implying that TC-induced climate changes are directly related to thermal anomalies generated locally by TC mixing. The magnitude of the changes depends on how intermittent the mixing is, but only to a moderate extent. Both the simple and coupled climate models suggest that parameterizations of TC as a source of permanent mixing may lead to an overestimation of climate impacts of tropical cyclones, but will have the correct spatial pattern.

6.5 Discussion of TC climate impacts

This study investigates the global climate impacts of temporally variable upper-ocean mixing induced by tropical cyclones using a global ocean-atmosphere coupled model and a simple heat-transfer model of the upper ocean. The time-averaged temperature anomalies in the coupled model show robust spatial patterns in response to additional vertical mixing. Specifically, we observe a weak surface cooling at the location of the mixing (~ 0.3℃), a strong warming of the equatorial cold tongue (~ 2℃), and a moderate warming in mid- to high- latitudes ($0.5 - 1$℃). We also observe a deepening of the tropical thermocline with subsurface temperature anomalies extending to $500\,m$. These and other changes, summarized in Table 6.1, are consistent among the different experiments.

Additional mixing leads to an enhanced oceanic heat transport (on the order of $0.2\,PW$) from the regions of increased mixing towards high latitudes and the equatorial region. This effect is partially compensated by the atmosphere, resulting in smaller changes in the total heat transport. An increase of the ocean poleward heat transport agrees with the original idea of Emanuel [2001]. However, it is largely due to the transport by the wind-driven, rather than the thermohaline circulation. There is also a small increase in global mean temperature (~ 0.2℃), associated with the greater ocean heat transport (for a discussion see Herweijer et al. [2005]).

The magnitude of the climate response to enhanced mixing depends not only on the time-averaged value of the added diffusivity, but also on its temporal dependence. In our coupled climate model, a Single-event mixing produces a roughly 40% weaker response than Permanent mixing (with the same annual mean diffusivity). This result is reproduced by our simple one-dimensional heat transfer model for the upper ocean with a time-dependent vertical diffusivity. The simple model shows a similar reduction of the local SST anomaly and the anomalous heat transport from the mixing region when we decrease the fraction of the year with mixing.

The presence of the seasonal cycle in the coupled model amplifies the impact of tropical cyclones as they occur during summer, when warm surface temperatures are favorable for pumping heat into the interior of the ocean. In our coupled model this effect apparently overcomes the effect of seasonality described by Jansen et al. [2010], who emphasized heat release from the ocean back to the atmosphere during winter that could weaken ocean thermal anomalies. Their mechanism appears to be more important for relatively weak cyclones generating shallow mixing, and not for stronger cyclones that contribute most to the mixing.

To address the issue of the model dependency of our conclusions we performed several additional experiments with the Community Earth System Model (CESM), which is a newer version of the model that we used initially (CCSM3). Important differences between the models include the implementation of the near surface eddy-flux parameterization [Danabasoglu et al., 2008; Ferrari et al., 2008] and a new sea-ice component in CESM. Also, we used a lower-resolution version of the new model as compared to CCSM3. The results of the new experiments are very similar to the prior experiments, showing the equatorial warming and the deepening of the thermocline, the cooling of the subtropical bands, and the strengthening of the shallow overturning circulation in the ocean and the Hadley cells in the atmosphere. The patterns of generated climatological SST anomalies remain well-correlated between different mixing runs, with highly intermittent mixing having a somewhat weaker response. The only major difference concerns the AMOC behavior and SST changes in the high-latitude northern Atlantic; in the new model the AMOC intensity does not change in response to additional mixing. The persistent warming of the Norwegian Sea, observed in CCSM, is replaced by a surface cooling balanced by a density-compensating freshwater anomaly. These effects are probably due to the new sea-ice model or the lower model-resolution – the question of their robustness goes beyond the scope of the present paper.

The consistent spatial patterns of the climate response to transient mixing suggest that in coupled climate simulations a highly-intermittent upper-ocean mixing can be represented by adding permanent or constant seasonal mixing, perhaps rescaled appropriately.

Several other relevant questions remain beyond the scope of this study, including the role of spatial variations of the TC-induced mixing and the adiabatic effects of their cyclonic winds on oceanic circulation through Ekman upwelling. It is also feasible that for present-day climate our results actually give the upper bound on the climate response to tropical cyclones. A critical issue is the average depth of mixing penetration – choosing a depth significantly shallower than 200m for the experiments would dampen the overall signal. Restricting the zonal extent of the mixing bands in each ocean basin, more in line with observations, would also reduce the signal.

Ultimately, simulations with TC-resolving climate models will be necessary to fully understand the role of tropical cyclones in climate. However, the current generation of GCMs are only slowly approaching this limit and are still unable to reproduce many characteristics of the observed hurricanes, especially of the strongest storms critical for the oceanic mixing [*e.g.* Gualdi et al. [2008], Scoccimarro et al. [2011], and P.L. Vidale, personal communication].

Chapter 7

Persistent ENSO in a Wide Range of Climates

The material contained in this chapter is currently under review at the *Journal of Climate* under the title "Persistent ENSO in climates with different east-west equatorial SST gradients" [Manucharyan and Fedorov, 2014].

7.1 Introduction

A salient feature of the present-day climate is the zonal asymmetry of sea surface temperatures (SST) in the tropical Pacific, characterized by a vast warm pool in the west and a strong cold tongue in the east. This east-west SST difference and the entire ocean thermal structure along the equator are tightly coupled to the easterly Trade winds of the atmospheric zonal circulation (the Walker cell); interactions between these components of the tropical climate allow for a quasi-periodic oscillation, known as ENSO, in which the winds and the SST gradient relax (El Niño) and strengthen (La Niña) interannually [Clarke, 2008; Philander, 1990; Sarachik and Cane, 2010].

How this oscillation changes when tropical climate changes is an important question for both present and paleo climates [Cobb et al., 2013; Collins

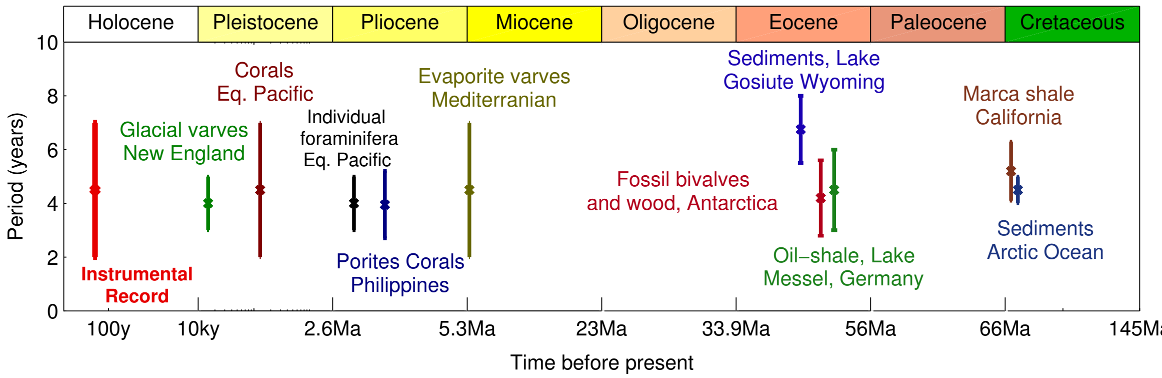

Figure 7.1: Geological evidence suggesting ENSO-like variability in past climates. Vertical bars indicate the dominant frequency bands identified in geological samples from different epochs spanning from the Late Cretaceous to the Pleistocene [data compiled from Cane, 2005; Davies et al., 2011, 2012; Galeotti et al., 2010; Huber and Caballero, 2003; Ivany et al., 2011; Rittenour et al., 2000; Scroxton et al., 2011; Watanabe et al., 2011]. The bands are given as reported in the original studies. For a review of the Holocene data see Cane [2005].

et al., 2010; Fedorov and Philander, 2000, 2001; Koutavas et al., 2006; Yeh et al., 2009]. Although climate models currently predict relatively modest future changes in the mean SST gradient and ENSO, mainly because of compensation between different mechanisms controlling both the mean climate and its variability [DiNezio et al., 2009, 2012], the reliability of these projections is uncertain in view of large differences between the models [Brown et al., 2011; Collins et al., 2010; Guilyardi et al., 2009; Watanabe et al., 2012], which often disagree even on the sign of changes. Consequently, potential shifts in El Niño characteristics with rising atmospheric CO_2 concentration remain a matter of concern.To build confidence in climate projections, understanding past changes in the mean state of the tropics and ENSO is crucial.

Available observational evidence suggests that ENSO was active as far back as the Late Cretaceous [Davies et al., 2011, 2012], Eocene [Huber and

Caballero, 2003; Ivany et al., 2011], Miocene [Galeotti et al., 2010], Pliocene [Scroxton et al., 2011; Watanabe et al., 2011] and Pleistocene [Cane, 2005; Rittenour et al., 2000] epochs (Fig. 7.1) and persisted with some changes through the Holocene [Brown et al., 2006; Cobb et al., 2003, 2013; Koutavas et al., 2006]. While there is a large variety of coral observations from the Holocene the geological evidence is much more limited for earlier time epochs. For example, the varved records from Mediterranean, England, and Antarctica that were found to bare signature of inter-annual variability provide only a hypothetical link to ENSO related climate variability through assumed teleconnections.

The early Pliocene climate, having atmospheric CO_2 concentration between $350 - 400ppm$, draws particular attention as a potential analogue for modern greenhouse conditions [Fedorov et al., 2013]. Proxy records [Dekens et al., 2008; Fedorov et al., 2006, 2013; Wara et al., 2005] indicate that during that time the mean east-west SST gradient was small, perhaps on the order of or below 1-2℃, which is sometimes refereed to as permanent El Niño-like conditions. Apparently, the warm pool temperature stayed fairly constant, whereas the cold tongue was significantly warmer. Nevertheless, recent studies have discovered evidence of a persistent El Niño during the Pliocene [Scroxton et al., 2011; Watanabe et al., 2011]. These findings raise the important questions of how changes in the mean SST gradient affect ENSO and whether the permanent El Niño-like conditions can still sustain interannual variability. While some geological evidence should be treated with caution, their suggestions pose a challenge for the climate community: can we deny or confirm the hypothesis of ENSO existence these vastly different climates based on our theoretical understanding of the phenomenon?

So far, the connection between ENSO and the mean tropical climate has been explored in a broad parameter range within simple, intermediate and hybrid models [An and Jin, 2000; Fedorov and Philander, 2001; Wittenberg, 2002], but not comprehensive coupled models, where the zonal temperature

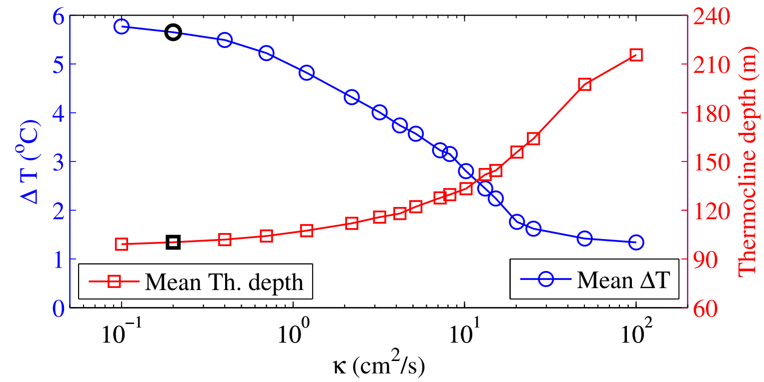

Figure 7.2: The east-west SST gradient dT (blue) and zonally averaged thermocline depth (red) as a function of background diffusivity κ_b in the extra-tropical bands. The mean east-west temperature gradient is estimated as the difference between the maximum and minimum SST along the equator in the Pacific, averaged for the last 100 years of the computations. The thermocline depth is defined as the depth of the appropriate isotherm in each experiment.

gradient is difficult to control. In the present work we have devised an efficient way to alter the mean temperature in the eastern equatorial Pacific (between 6 to 1℃), while keeping temperature in the west nearly constant (Figs. 7.2 and 7.3a), within a state-of-the-art climate model (Methods). Our approach invokes the fact that the equatorial cold tongue is maintained by the upwelling of waters that travel towards the equator from the extra-tropics within the ocean shallow subtropical cells (STC) [Gu and Philander, 1997; McCreary Jr and Lu, 1994]. Changing the temperature of those waters changes the cold tongue temperature.

To make use of this effect, we conduct numerical experiments in which we systematically modify upper-ocean vertical mixing in the extra-tropics (Sec. 7.2). Increasing the mixing warms the waters subducted in the STC and eventually raises the temperature of the cold tongue. In turn, tropical ocean-atmosphere interactions act to establish a new mean state in which weaker east-west SST gradient (ΔT) and zonal winds balance each other in the equatorial band (Figs. 7.2,7.3). Since perturbations are imposed far away from the equator, in the extra-tropics, they do not affect ENSO dynamics directly, but only through changes in this mean state in the tropics.

Recent modeling studies show that ocean mixing in the subtropics, induced for example by tropical cyclones, can indeed warm the equatorial cold tongue [Fedorov et al., 2010; Manucharyan et al., 2011]. However, in the present study, we are not concerned with particular mechanisms that could alter ocean mixing. Rather, we simply use the extra-tropical mixing as an efficient tool to control tropical background conditions.

7.2 Coupled climate model and numerical experiments

The climate model used here is a version of NCARs Community Earth System Model (CESM) that incorporates atmospheric and a land surface models with a spectral truncation of T31 (CAM4 and CLM) coupled to ocean and sea ice components (POP2 and CICE) with a nominally 3° resolution increasing to 1° near the Equator [Shields et al., 2012]. This version of CESM with a relatively low resolution greatly facilitates sensitivity and paleoclimate simulations; the model source code and boundary conditions, are accessible at `http://www.cesm.ucar.edu/models/cesm1.0/`. The integrations start from a pre-existing preindustrial simulation and last for 300-600 years, depending on the experiment. This time is sufficient for the upper ocean to reach equilibrium (with the deep ocean experiencing a weak residual drift [Fedorov et al., 2013; Manucharyan et al., 2011]. In addition, we perform two high resolution simulations (1° ocean grid size increasing to 1/4 ° towards the equator) a preindustrial control and a simulation with strong strong mixing ($\kappa_v = 50cm^2/s$). The analysis of the model output including SST and winds stress is performed on fields averaged between 2.5°S-2.5°N, with Niño3 region defined between 90°W-150°W and 2.5°S-2.5°N.

Throughout the numerical experiments, we vary background vertical diffusivity in the extra-tropical bands (15°-40°, $0-400m$) within the range from -0.1 to 100 cm^2/s. The other, spatially and time varying components of vertical diffusivity, computed by the model itself, are not explicitly modified in these experiments. In one experiment, to reduce the mixing, we multiplied the model original background diffusivity by 0.1, also in the extra-tropical bands. In general, the effect of mixing increases with higher diffusion and with the greater depth of the mixing bands. For our study, these bands are chosen sufficiently far away from the equator, much farther than the typical baroclinic Rossby radius of deformation for the equatorial ocean ($\sim 4°$). Therefore, the imposed perturbations in ocean vertical mixing do not affect ENSO dynamics directly, but only through changes in the background state of the tropics.

7.3 Simulated climates and ENSO

7.3.1 Mean state of equatorial Pacific

Throughout the experiments, as we alter the extra-tropical mixing, we are able to simulate a broad range of equatorial Pacific climates which are dramatically different from its present-day conditions. First, we achieve the mean zonal SST gradients along the equator ranging from 6 to 1.3℃ (5.6℃ in the Control run), while keeping the warm pool temperature nearly constant (Fig. 7.3a). The mechanism of the warming of the cold tongue due to enhanced ocean mixing can be understood from a heat budget perspective a stronger mixing in the extra-tropics induces anomalous ocean heat gain over this region, weakening oceanic heat transport from the equatorial region and increasing the cold tongue temperature [Fedorov et al., 2010; Manucharyan et al., 2011]. Reducing the mixing has an opposite effect. Associated with a reduced SST gradient and the eastward spreading of the warm pool are the changes in atmospheric Walker circulation manifested in reduced trade winds and the eastward spread of the convection region. Furthermore, consistently

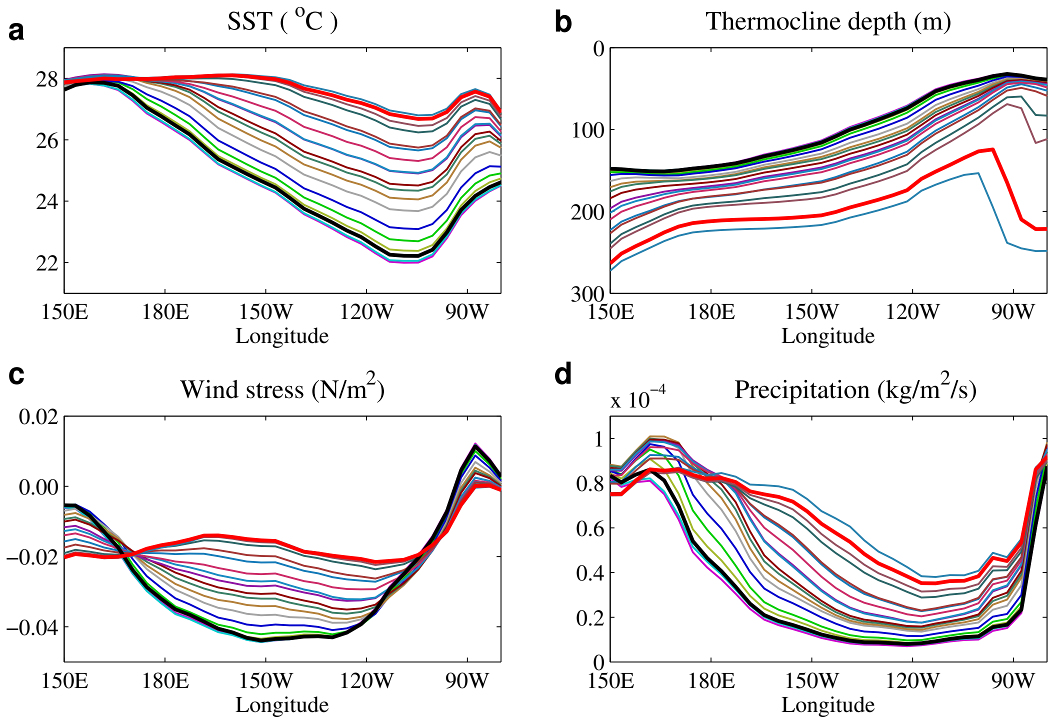

Figure 7.3: Mean tropical climate in different experiments. (a)-(d) The panels show profiles of mean SST, thermocline depth, wind stress, and precipitation in the equatorial Pacific for numerical experiments with different values of ocean diffusivity in the extra-tropics. Note the large changes in the cold tongue temperature (in the east) but little change in the warm pool (in the west). The east-west temperature gradient ΔT is estimated as the difference between the maximum and minimum SST along the equator. Black and red lines, respectively, indicate present-day and a reduced-gradient climates (ΔT=5.6℃and 1.4℃). For smaller values of ΔT note the shift of the maximum wind stress from the central to eastern Pacific and an increase in precipitation over the central and eastern Pacific, which reflect the corresponding shift in atmospheric convection.

with the reduced trade winds we observe the the reduction in the upwelling and deepening of the thermocline (Fig. 7.3b).

It would be of great asset to be able to construct sensitivity experiments that would alter different climate components independently from each other so that the influence of each of them could be assessed. In practice, however, such studies could not be achieved in coupled climate models as all climate components are connected to each other through a complicated sequence of nonlinear interactions. For example, it would be hard (if possible at all) to achieve reduced ΔT with a very strong Walker circulation, or a steep thermocline slope with weak trade winds. Thus, our studies provide a specific set of experiments which have consistent changes in the different climate components. Nonetheless, our sensitivity experiments provides a unique opportunity to investigate ENSO dynamics in climates with weak zonal SST gradients, which was previously impossible to simulate in coupled climate models without directly affecting properties at the equator.

7.3.2 ENSO variability

Throughout all of the simulated climates ENSO remains the most prominent part of the climate signal with the conventional Niño3 index capturing the zone of the highest SST variance in the eastern equatorial Pacific (Fig. 7.4). For convenience purposes we denote different equatorial climates by their value of ΔT which has a one-to-one correspondence to the external parameter (vertical mixing) that we vary (Fig. 7.2). It is important to note here that ENSO dynamics depends on the changes in whole three dimensional background climate state - not only on ΔT (further on we asses the role of each component). The standard deviation of this index in the model reaches 0.9℃for the present-day climate but reduces to 0.6-0.7℃for smaller ΔT (Fig. 7.5a), although the magnitude of strong events decreases more noticeably. The power spectra of the Niño3 index display statistically significant peaks in the interannual frequency range in all experiments (see discussions in Sec.

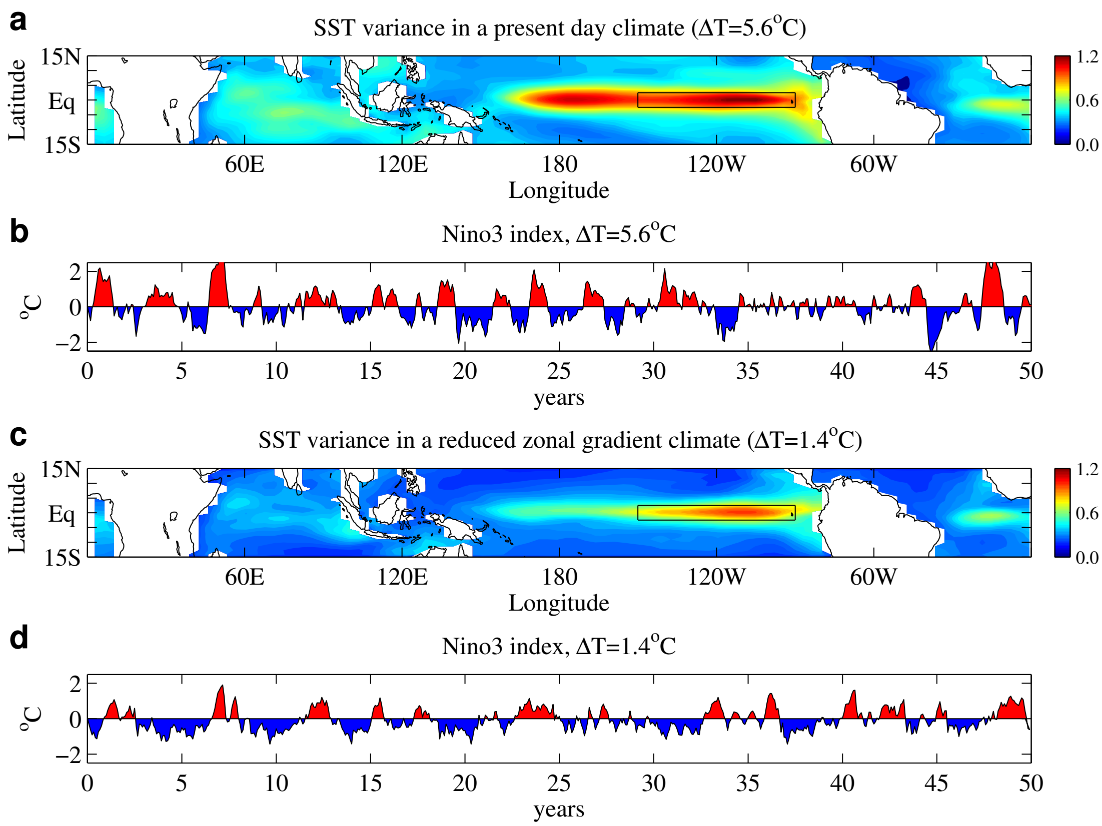

Figure 7.4: (a)-(c) SST variance for a present-day climate (ΔT=5.6°C) and a climate with a reduced SST gradient (ΔT=1.4°C). (b)-(d) The corresponding time series of Niño3 index indicating active ENSO in these two very different climate states. Black box shows geographical location of Niño3 region.

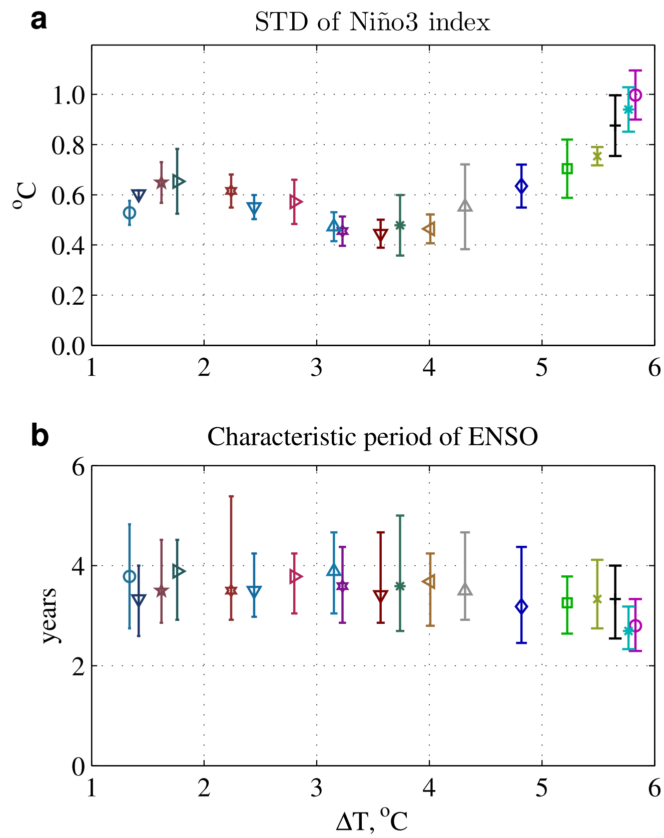

Figure 7.5: The simulated amplitude and period of ENSO. (a) ENSO amplitude, defined as the standard deviation of the Nio3 index. The errorbars show its variability based on 25-year intervals. (b) ENSO characteristic period, defined as the period corresponding to the maximum of the power spectrum in each experiment. The errorbars give uncertainty based on the partial width of these peaks. Both the amplitude and period are plotted as a function of the mean east-west SST gradient ΔT. The simulated present-day climate (Control) corresponds to ΔT=5.6℃.

7.4.4). The dominant period increases slightly for smaller ΔT (Fig. 7.5b); however, this increase should be considered in the context of the broad width of the spectral peaks.

The main features of ENSO, such as the eastward propagation of thermocline depth anomalies or the coupling of wind anomalies to SSTs, are all present in our experiments The dynamics are governed by the recharge-discharge mechanism [Cherchi et al., 2008] in which positive anomalies in ocean heat content (OHC) along the equator precede El Niño events by about a quarter of a period, ranging from 6 months in our control run to 10 months in a reduced ΔT climate (Fig. 7.6). These OHC anomalies, usually referred to as ocean heat recharge, occur as a result of meridional heat redistribution prior to an El Niño and provide an essential mechanism to transition between warm and cold phases of ENSO The recharge-oscillator mechanism is closely related to the delayed oscillator and other simple models of ENSO [Fedorov, 2010].

What explains this robustness of ENSO and relatively small changes in its properties across such large changes in the mean ΔT? To answer this question, here we view ENSO as a noise driven oscillator and evaluate the stability of the internal climate mode governing ENSO dynamics using a linearized heat budget equation for the Niño3 region together with the recharge-oscillator approximations for ocean adjustment.

7.4 ENSO as a damped-driven oscillator

7.4.1 Stability index

The stability of the mode governing ENSO dynamics in the experiments is assessed by estimating the strengths of the relevant positive and negative feedbacks within the recharge-oscillator framework. Here we extend the analysis by Jin et al. [2006] to include an expression for the natural frequency of

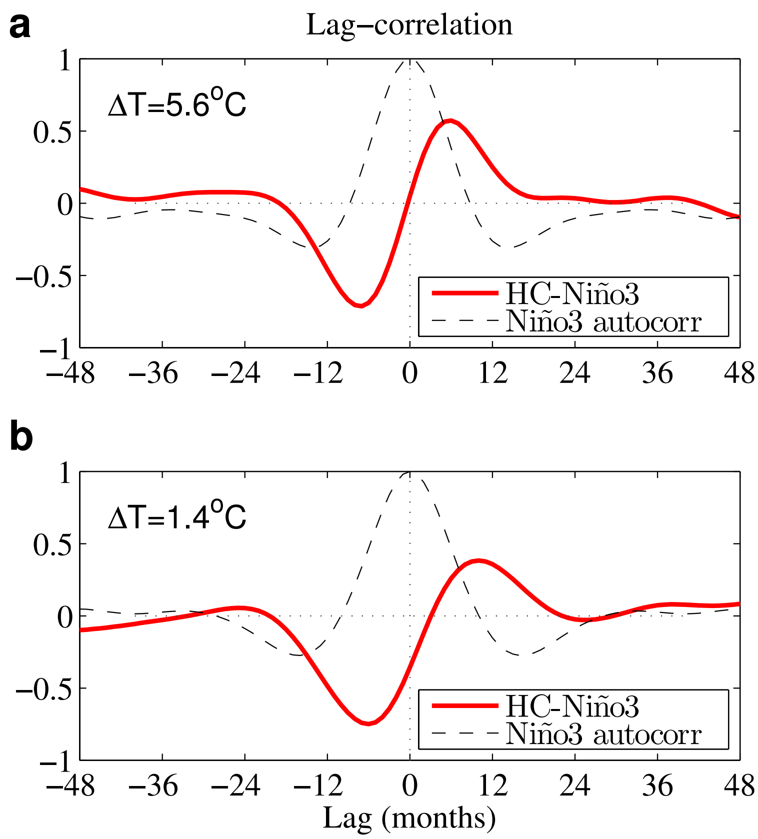

Figure 7.6: Lag-correlations between average OHC anomalies and the Niño3 index (red lines), and the Niño3 auto-correlation (dashed black lines), are shown for (a) ΔT=5.6℃and (b) 1.4℃. Positive lags indicate that OHC anomalies lead the Niño3 index. Ocean heat content (OHC) is defined as temperature in the Pacific ocean averaged between 20 and 300m, 2.5°S-2.5°N, and east of 210E (excluding the Niño3 region which is highly correlated at zero lag). Note that the maximum correlation occurs at a 7 to 10 month lag as OHC anomalies lead SST anomalies, consistent with the heat recharge mechanism of ENSO dynamics in both experiments.

oscillations and argue about the importance of the external noise in sustaining variability.

The Bjerknes Stability Index (δ) is introduced using a linearized heat budget equation for a box encompassing the Niño3 region in the upper ocean:

$$\frac{d < T >}{dt} = 2\delta < T > + F[h], \tag{7.1}$$

$$\frac{d[h]}{dt} = -c < T >, \tag{7.2}$$

where T is the temperature and the operator $< * >$ denotes the average over the Niño3 box, h is the depth of the equatorial thermocline and $[*]$ denotes the zonal mean; δ is the Bjerknes Stability Index (BJ), while $F[h]$ represents the effects of the delayed ocean adjustment or ocean memory [Jin, 1997; Jin et al., 2006]. Dynamical variables $< T >$ and $[h]$ are the perturbations from the climatological mean, whereas the time-independent coefficients are functions of mean state of the equatorial Pacific. Equation 7.2 describes variations in the mean thermocline depth (or warm water volume) as derived, for example, in a low frequency approximation of the equatorial dynamics by Fedorov [2010]. Combining the equations 7.1 and 7.2 we obtain a damped oscillator equation

$$\frac{d^2 < T >}{dt^2} - 2\delta \frac{d < T >}{dt} + \omega_0^2 < T >= N(t), \tag{7.3}$$

where N is the external forcing, and $\omega_0 = \sqrt{cF}$ is the natural frequency. Note, that F is defined as $F = -\beta_{uh} < dT/dx > + < H(w)w/H_m >$ (see Jin et al. [2006]). The BJ index (δ)acts as a stability index for the oscillations governed by the recharge-oscillator model and gives the net growth (when positive) or decay rates (when negative) for the ENSO mode. In the latter case, the external forcing is necessary to sustain continuous oscillations, whereas in the former case the nonlinearities are necessary to prevent the unbounded growth of perturbations.

The BJ index is composed of several contributions:

$$-2\delta = - < u/Lx > - < H(w)w/H_m > -\alpha + \dots$$
$$+\mu_a\beta_u < dT/dx > +\mu_a\beta_w < dT/dzH(w) > +\mu_a^*\beta_h < H(w)w/H_m > . \tag{7.4}$$

(For a systematic derivation of Equation 7.4 and definition of variables see Jin et al. [2006]). Here, the over-bar denotes the climatological mean quantities, $H(w)$ is the Heaviside step function, x and z are the horizontal and vertical coordinates, and u and w are the zonal and vertical velocities. The horizontal and vertical extents of the averaging box are $L_x = 60°$, $L_y = 10°$, and $H_m = 80m$, respectively. We note that using the BJ analysis to understand for example ENSO changes due to global warming scenarios in different models might be of less relevance since the changes in different feedbacks are relatively small and would depend on the location and depth of the Niño3 box. Here, have explored different definitions of the Niño3 box and found that results have quantitative changes that do not affect the main conclusions, which is mainly due to the fact that we simulate a wide range climates with dramatic changes in different feedbacks.

7.4.2 Climate feedbacks

The first three terms in Eq. 7.4 describe negative feedbacks the mean zonal advection, upwelling, and surface heat flux feedbacks, while the last three terms represent the positive thermocline, Ekman pumping, and zonal advection feedbacks.

Negative advection feedbacks are associated with the mean flow (zonal and vertical) acting to damp Niño3 temperature anomalies. The thermodynamic feedback (proportional to α) is associated with the surface heat fluxes: shortwave, longwave, latent, and sensible, which collectively act as a damping term. Its magnitude is computed as a linear regression of the net anomalous surface heat flux over the Niño3 region onto the Niño3 SST index.

The magnitudes of positive feedbacks depend on several sensitivity parameters (defined in Eqs. (5)-(8) of Jin et al. [2006]) that characterize ocean response to wind stress and atmospheric response to SST. For instance, the atmospheric sensitivity parameters μ_a and μ_a^* assume a linear response of Niño3- and zonally-averaged wind stress anomalies, respectively, to Niño3 temperature anomalies. Analogously, the oceanic sensitivity parameters β_u and β_w assume a linear response of anomalous zonal and vertical velocities in the equatorial band to Niño3 wind stress anomalies. Parameter β_h gives the linear sensitivity of the thermocline tilt to the zonally-averaged wind stress anomalies. Particular values of these parameters are obtained by using linear regressions between the corresponding variables (Fig. 7.7). Before the computations, all the time series are smoothened to filter out short-scale variability.

The BJ index gives the growth or decay rates of the ENSO mode and identifies key feedbacks that contributes to its stability, including the positive thermocline, Ekman and advection feedbacks and various damping processes, all of which change in different climates.

One of the main factors destabilizing tropical climate is the thermocline feedback, in which SST in the eastern equatorial Pacific is modified by the mean upwelling of subsurface temperature anomalies associated with thermocline depth anomalies (induced by wind stress variations). This factor becomes a positive feedback via the coupling of wind stress to SST anomalies. When the cold tongue gets anomalously warm, the equatorial easterly winds relax, deepening the thermocline in the east and leading to further warming. As we move to climates with smaller ΔT, the effect of this feedback on the system stability increases slightly at first but then substantially decreases (Fig. 7.8a).

These changes in the strength of the thermocline feedback result from

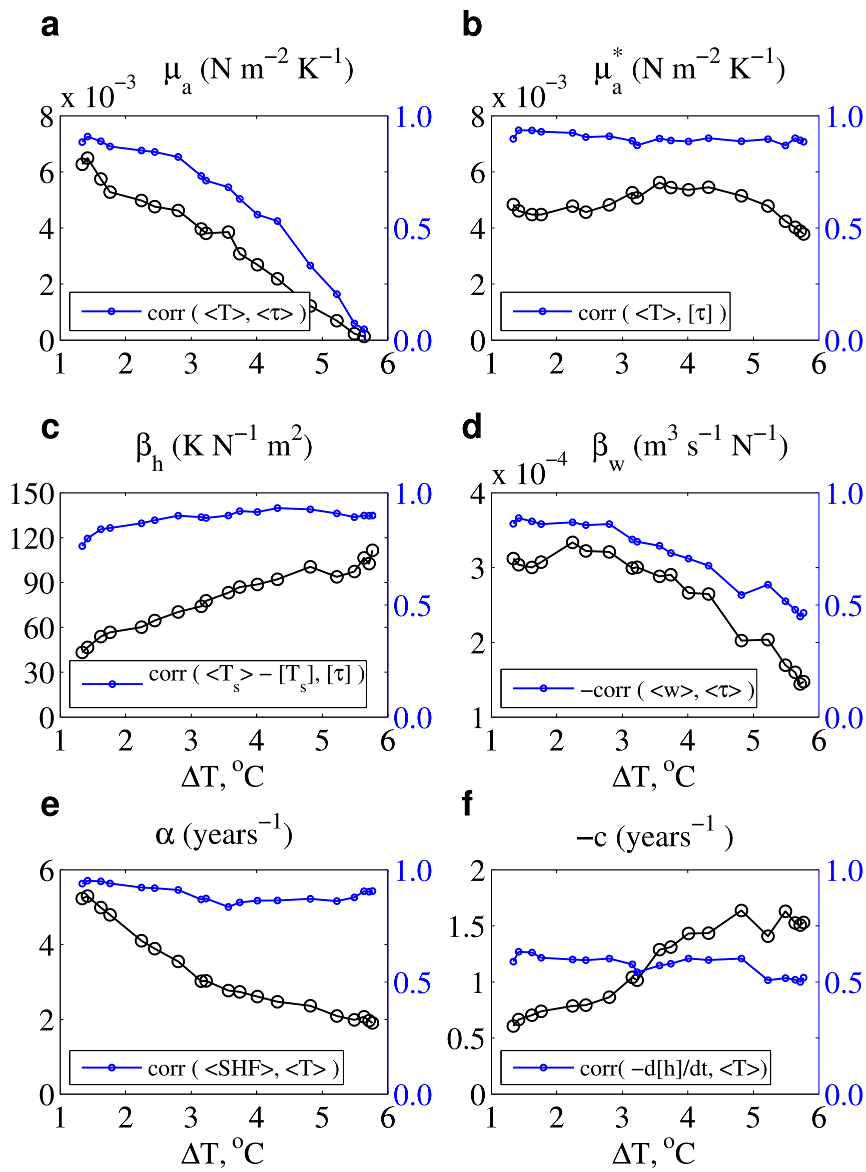

Figure 7.7: Oceanic and atmospheric sensitivity coefficients estimated for different climates (a,b) parameters μ_a and μ_a^* showing the sensitivity of Niño3- and zonally-averaged wind stress anomalies to Niño3 temperature anomalies, as obtained from linear regressions. (c) The sensitivity of the thermocline tilt to zonally-averaged wind stress, β_h, and (d) the sensitivity of vertical velocity to perturbations in wind stress, β_w, over the Nio3 region. (e) The strength of the thermodynamic damping α and (f) coefficient c in Eq. 7.2. Correlations between the appropriate pairs of time series used to calculate regressions are plotted as blue curves on right y-axis.

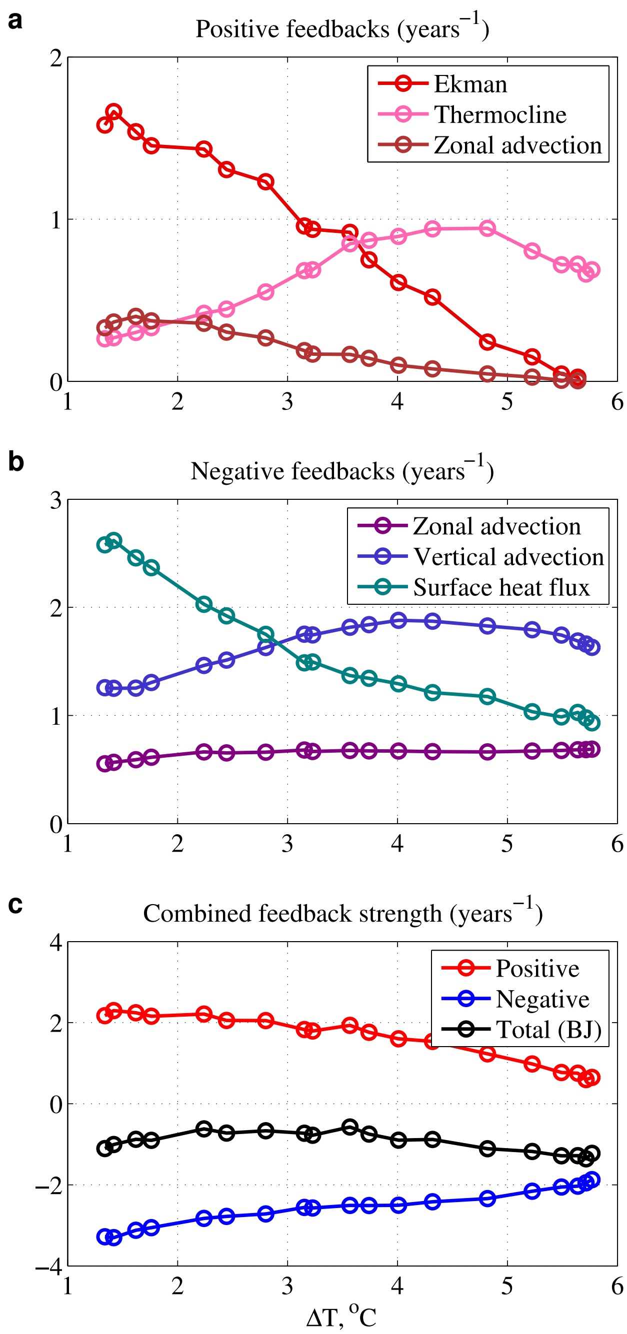

Figure 7.8: The strength of ocean-atmosphere feedbacks .(a) Positive feedbacks including the thermocline, Ekman pumping, and advection feedbacks. (b) Negative feedbacks due to the damping of temperature anomalies by mean advection and upwelling, and by surface heat fluxes. (c) Net positive and negative feedbacks as well as the total Bjerknes Stability Index (black line). The Bjerknes Index stays negative and fairly constant mainly due to the compensating effects of increasing Ekman feedback and thermodynamic damping.

several competing factors: weaker mean equatorial upwelling due to weaker zonal winds (Fig. 7.3b), a deeper ocean thermocline (Fig. 7.3c), and the reduced sensitivity of subsurface temperature (and thermocline tilt) to zonally-averaged wind stress anomalies (Fig. 7.7c). In contrast, the ocean-atmosphere coupling, estimated through a linear regression of wind stress anomalies onto the Niño3 index, increases as the atmospheric Walker circulation becomes more sensitive to SST perturbations in warmer climates (Fig. 7.7a).

While the thermocline feedback weakens a little, it is the Ekman pumping feedback that becomes more destabilizing for smaller ΔT (Fig. 7.8a). In the Ekman feedback, SST is modified by anomalous upwelling acting on the mean thermal stratification. During warm episodes for example, a relaxation of zonal winds reduces upwelling of colder waters, facilitating the growth of initial SST perturbations. In the present-day climate, wind stress anomalies are most pronounced in the western equatorial Pacific (Fig. 7.9a), where the mean stratification is weak, limiting the magnitude of the Ekman feedback. However, for smaller ΔT, the region of atmospheric convection spreads eastward and wind stress anomalies move closer to SST anomalies in the eastern Pacific (Fig. 7.9b), amplifying the Ekman feedback. A similar mechanism works to strengthen the zonal advection feedback, but the latter remains relatively weak. Overall, positive feedbacks intensify for smaller ΔT.

Negative feedbacks describe the damping of surface temperature anomalies by various processes (Fig. 7.8b). The main negative feedback involves the damping of SSTs by the mean upwelling of subsurface waters, which decreases for smaller ΔT. The damping of SST by the mean zonal flow also decreases but to a lesser degree. In contrast, the effective thermodynamic damping by surface heat and radiation fluxes increases several-fold. This increase is dominated by the shortwave flux component associated with clouds. As the region of atmospheric convection shifts eastward, anomalies in cloud cover shield the eastern Pacific from shortwave radiation, damping warm SST anomalies. Largely because of this factor, the combined negative feedbacks

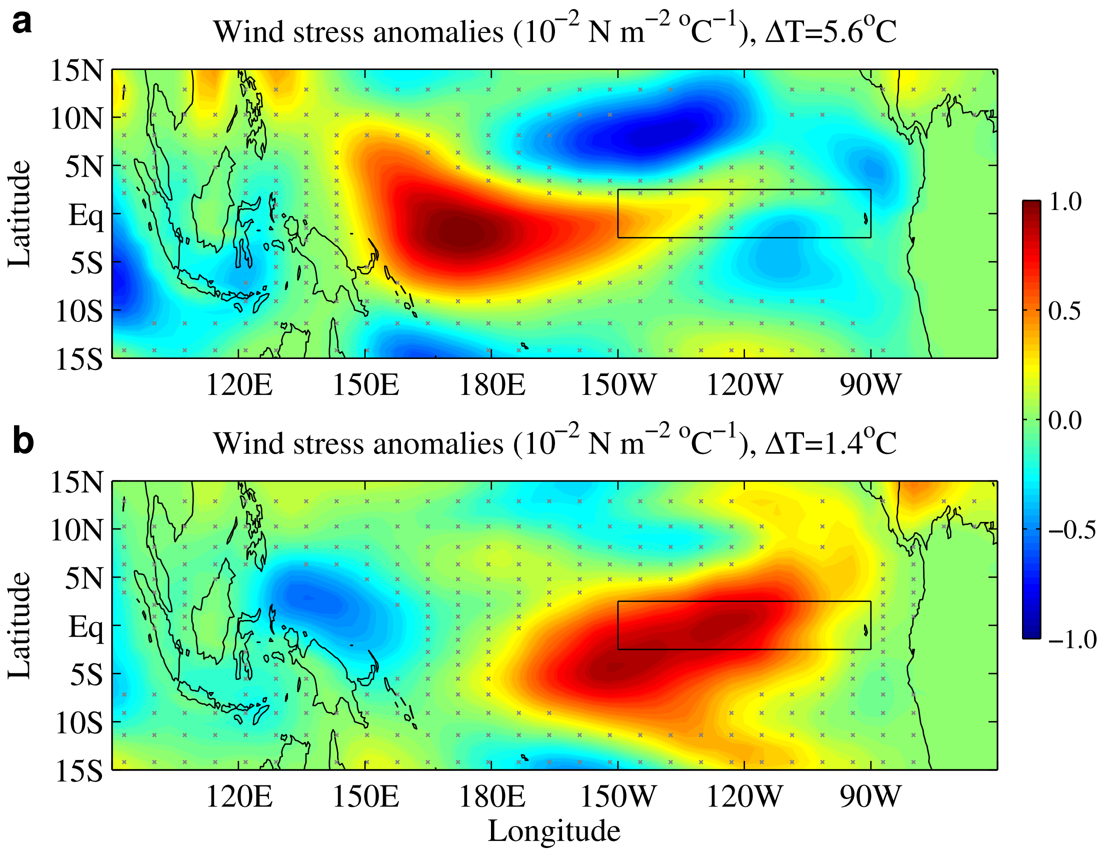

Figure 7.9: The structure of wind stress anomalies associated with interannual variability in the two experiments. (a)-(b) Regressions of the model wind stress onto the Niño3 index, in N/m2/℃, showing the spatial shape and amplitude of wind stress anomalies for a given SST anomaly for two experiments with ΔT=5.6℃and 1.4℃. For larger values of ΔT, equatorial wind stress anomalies are centered west of the Dateline. For smaller ΔT, wind stress anomalies are located closer to the eastern Pacific.

also strengthen for smaller ΔT.

The total BJ index (the sum of negative and positive feedbacks) remains negative (Fig. 7.8c), which implies that the model ENSO is controlled by a damped mode across a broad range of climates. Remarkably, despite large variations in negative and positive feedbacks, the magnitude of the BJ index changes relatively little, and the e-folding decay timescale of the ENSO mode stays close to 1 year. We note here that the BJ stability analysis performed by Kim and Jin [2011] on reanalysis data (a combination of model constantly adjusted by the observational data) shows weaker damping with values of BJ index ($-0.25 years^{-1}$) and a similar amplitude of ENSO events ($\sim$ 0.9℃). The discrepancy is due to our climate model overestimating the magnitude of vertical advection damping and underestimates positive effects of thermocline and zonal advection feedbacks. These are known issues with the climate models consistent with westward overextension of the cold tongue resulting in a more damped ENSO mode with $\delta \sim 1 year^{-}1$. Nonetheless, the magnitudes of ENSO events in our control run are comparable to observations (0.9℃, [Kim and Jin, 2011]). Acknowledging the biases in the model, here we put stress on the relative changes in magnitudes of these feedbacks that occur as we move through different climates.

7.4.3 Frequency of natural oscillations

Across the entire range of simulated climates, the model produces power spectra with a broad interannual peak between 2-7 years clearly distinct from red noise (Fig. 7.10). The dominant period of ENSO shows a slight increase for smaller ΔT (Fig. 7.5b), from roughly 3 to 4 years. Taking a Fourier spectrum of the Eq. 7.3 we obtain the shape of the energy spectra:

$$|\tilde{T}(\omega)|^2 = \frac{|\tilde{N}(\omega)|^2}{(\omega^2 - \omega_0^2)^2 + \delta^2\omega^2}. \quad (7.5)$$

As a first order approximation we assume the forcing is independent of

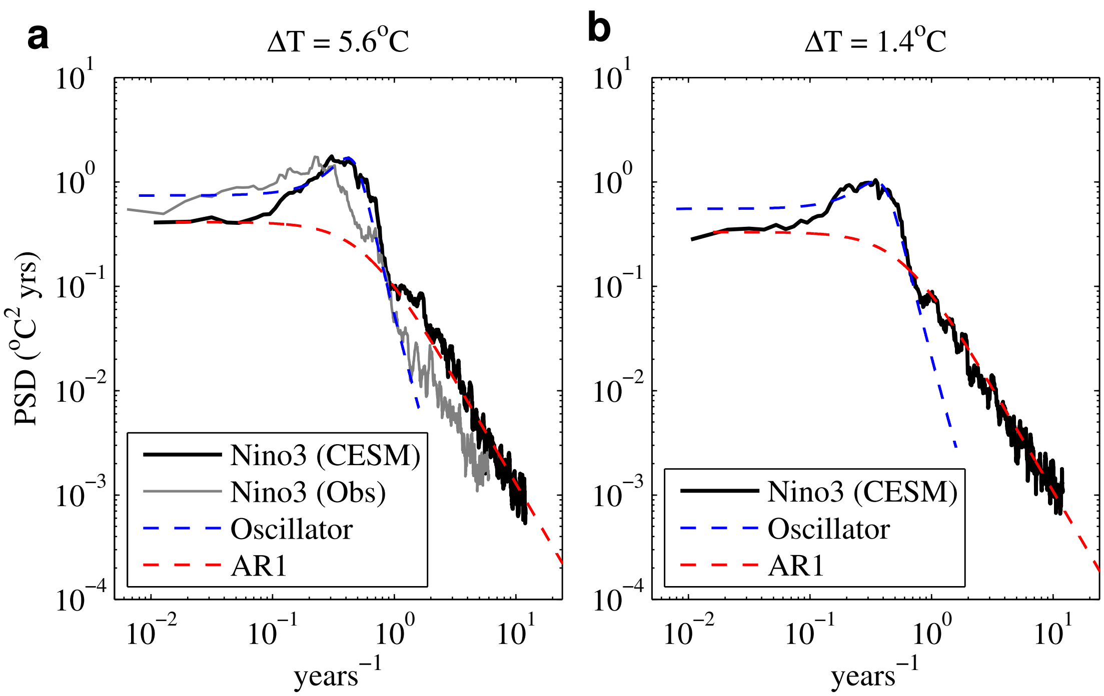

Figure 7.10: Power spectra of the Niño3 index. (a)For present-day and (b) reduced dT climates along with corresponding spectra of AR1 process (dashed green) and damped oscillations (red). Note the change in spectral slope from ω^{-2} at sub-annual time scales (corresponding to $AR1$ process) to ω^{-4} at inter-annual time scales (corresponding to damped oscillator spectrum).

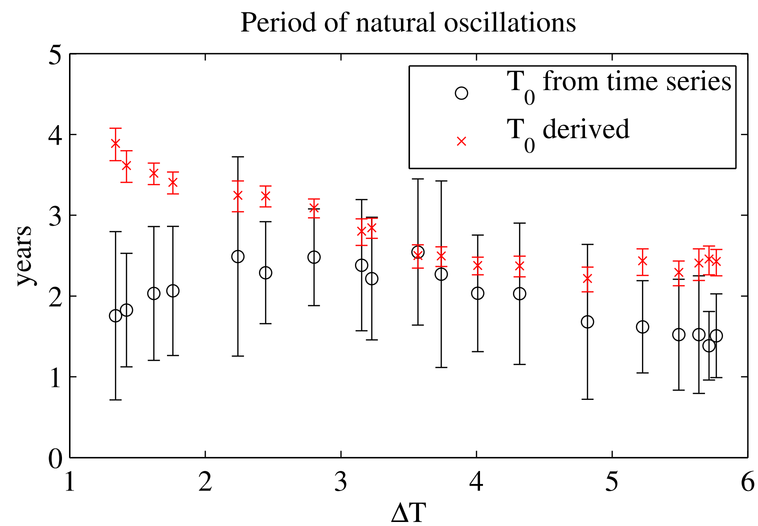

Figure 7.11: Comparison between the period of natural oscillations of ENSO mode calculated from the frequencies corresponding to spectral peaks adjusted by the damping as $\omega_0^2 = \omega_{max}^2 + 2\delta^2$ (black) and as estimated from the BJ analysis $\omega_0 = \sqrt{(cF)}$ (red).

the ENSO dynamics with decorrelation time scales much shorter then the dominant ENSO frequency. The forcing thus could be considered as Gaussian white noise, for example, emerging from atmospheric weather. Since the power spectral density of white noise is a constant, the spectral peak $\omega_{max}^2 = \omega_0^2 - 2\delta^2$ would then be shifted towards lower values compared to the natural frequency ω_0 due to the presence of damping, which also leads to the broadening of the spectral peak. Taking frequencies of the dominant peak from Niño3 spectra (Fig. 7.5b) and adjusting their values due to damping δ calculated from BJ analysis, we obtain an estimate of the natural frequency of oscillations and can compare it to our estimate based on the background state: $\omega_0 = \sqrt{cF}$. Considering the simplicity of proposed idealized model the data shows good agreement of the periods from present-day climates up to $\Delta T = 2°C$ (Fig 7.11); the largest disagreement comes for a small range of weaker ΔT climates where the BJ analysis shows a significant increase in period (up to 4 years) while the estimate from the time series stays closer to 2 years.

The possible reasons for this disagreement include two factors. First, the increased period (from BJ analysis) is mainly due to decrease of the regression constant c (relating tendency in mean subsurface temperatures to Niño3 index, see eq. 2) by a factor of 3, and due to relatively small changes in F. Second, in case the damping strength (δ) is overestimated it would lead to a decreased period estimated from spectral peaks. Both of these factors are affected by the chosen depth of the Niño3 box (H_m), which in order to improve agreement should be chosen depending on the background climate state: in weaker ΔT climates, increasing H_m leads to a reduction of damping and decrease in c. If one wishes to get the best quantitative agreement of the idealized model with the output of the GCM, one would need to use variable locations of the Niño3 box and the advection depth. In this study however, we fix the location of the box for simplicity as we aim to understand the dynamical reasons behind the observed changes in ENSO.

This increase in period is related to several factors, including a slowing-down of equatorial waves responsible for ocean adjustment. We find that in warmer climates the speed of equatorial Kelvin and Rossby waves decreases by about 20-30%, as the weaker ocean stratification overcomes the effect of a deeper thermocline An and Jin [2001]; Fedorov and Philander [2001]; Wittenberg [2002]. Secondly, the shift of wind stress anomalies from the western to central Pacific (Fig. 6) lengthens the distance that wind-generated Rossby waves must travel to reach the basin western boundary. These factors more than compensate the tendency of enhanced Ekman and advection feedbacks to shorten the oscillation period An and Jin [2001]; Wittenberg [2002]; Yeh et al. [2009].

7.4.4 Niño3 spectrum and strength of noise

We argue that the main dynamics of ENSO could be simplified down to a lower dimensional dynamical system - an oscillator. However, since a we showed that this oscillator is damped (BJ¡0), sustaining continuous variability requires the presence of external forcing. In this idealized framework, the forcing comes from all the unresolved physics acting on short time scales, which could be considered as noise so long as the processes are so distinct in time that they have an autocorrelation decay time scales much smaller then the inter-annual ENSO frequencies. The noise comes in from different components such as atmospheric weather affecting ocean in the form of wind stress, surface heat fluxes including radiative fluxes associated with cloud systems, heat advection processes in the ocean associated with waves and other mixed layer processes. The spread in the relations between different parameters which were calculated using linear assumptions also could be considered a source of noise. Given that a myriad of different processes affect the system at the same time, it is not possible to separate contributions from each component. Nonetheless, these processes leave a signature in the time series of Niño3 index, which we use to estimate the effective strength of noise.

On a log-log plot, the Niño3 index spectrum shows nearly linear dependence of energy density on the frequency on times scales between a month and a year, followed by a a sudden increase in the slope at around 1 year and a broad peak at around 2-3 years (Fig. 7.10). The sharp change in slope suggest that Niño3 index is affected by different processes on different time scales. For sub-annual variability the slope on a log-log plot is close to -2, consistent with the red noise spectrum. At these time scales the main dynamics of the surface ocean could be approximated as a restoring to climatology affected by the noise processes, creating variability. A simple representation of this is the AR1 process:

$$dx/dt = -\alpha x + N(t), \text{ and } \; |\tilde{x}(\omega)|^2 = \frac{\sigma^2}{\alpha^2 + \omega^2}, \tag{7.6}$$

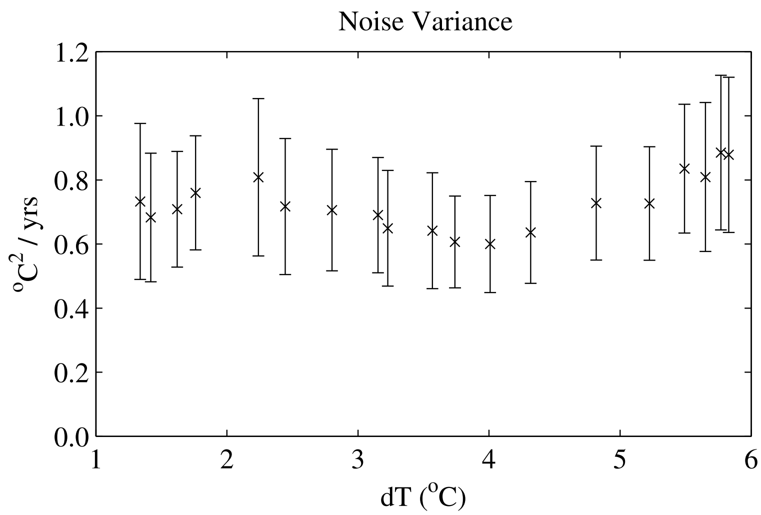

Figure 7.12: Estimate of the magnitude of external noise as estimated from the spectrum of Niño3 time series by fitting AR1 process to sub-annual time scales.

where $1/\alpha$ is the restoring time scale and σ is the variance of external noise (assumed to white). At high frequencies ($\omega >> \alpha$) the power is -2, consistent with the Niño3 spectrum at sub-annual time scales. This allows to find the magnitude of noise at this time scales by fitting the amplitude to a -2 power law to Niño3 spectrum (Fig. 7.10, dashed red). This noise is then transformed into a forcing of the damped oscillations which create a broad peak and as we show the magnitudes of the estimated noise did not significantly change throughout the simulated climates (Fig. 7.12).

On interannual time scales, the slope of the spectrum sharply changes from -2 to -4 right before the peak, which is consistent with the dynamics and the power spectrum of the noise driven damped oscillator (Eq. 7.5, Fig. 7.10).Here, σ^2 is the variance of white noise forcing, $\omega 0$ is the natural frequency of oscillator and delta is the damping coefficient. The peak is located at $\sqrt{\omega_0^2 + 2\delta^2}$ (shifted towards lower values from ω_0), its width depends on the amount of damping, and high omega asymptote has a power of -4.

We use the obtained values of the damping δ and ω_0 from the BJ analysis and only estimate the amplitude to obtain a relatively good fit to the Niño3 spectrum (Fig. 7.10). Thus, AR1 process at sub-annual time scales (Fig. 7.10, dashed red) and the model of noise driven damped oscillator on inter-annual time scales (Fig. 7.10, dashed blue) provide a good approximation to describe tropical variability.

7.5 Discussions

We presented a sensitivity analysis of ENSO dependence on the background state of the Pacific ocean within a state of the art climate model. We used a very specific set of climates featuring reduced climatological zonal SST gradients that were achieved by varying extra-tropical vertical diffusivity which indirectly altered tropical Pacific climatology. Along with a reduced SST gradient the climates featured a consistent reduction in the Walker circulation, eastward spread of the convection region, as well as deeper and a more diffuse thermocline.

Here, we take the recharge-discharge framework to represent ENSO dynamics. Using the BJ stability analysis we showed how the three dimensional changes in atmospheric and oceanic currents and stratification alter the strengths of the key coupled feedbacks associated with ENSO. In experiments with reduced ΔT the thermocline feedback is substantially weakened whereas the Ekman feedback dominates amongst the different positive feedbacks a situation opposite to the present-day climate. The increase in Ekman feedback is associated with the dramatic eastward shift of wind stress anomalies. The strong positive feedback is largely compensated by the negative thermodynamic damping which is greatly amplified in reduced ΔT climates due to increased cloud cover sensitivity to Niño3 anomalies. As a result ENSO mode remains damped throughout the experiments with damping time scale staying close to about a year. In this damped system the variability could be sustained by external forcing which, as suggested from the spectral analysis of Niño3 time series, could be represented by the additive white noise with relatively constant amplitude throughout the experiments. The frequency of the natural oscillations estimated based on background state increase from 2 to 4 years as we move to smaller ΔT climates, which is in rough agreement with the frequency estimates from the Niño3 time series spectrum.

We emphasize here that ΔT was used only to label equatorial background climate states in order to avoid using extra-tropical vertical mixing coefficient that was used as a tool to obtain a set of climates (technically speaking any other model state index that depends monotonically on the value of vertical mixing could have been used). ENSO properties depend on the 3D ocean-atmosphere background state, and the performed BJ stability analysis shows how its different components affect the damping rates and dominant frequency of inter-annual variability. Nonetheless, the analysis revealed that in small ΔT climates most dominant factors are the Ekman feedback and thermodynamic damping both of which amplify as manifestation of the transient dynamics of the Walker circulation which depends crucially on the climatological SST and do not directly depend on the ocean stratification. Thus, we expect that despite the fact that there might exist a variety of climates with reduced ΔT each having different oceanic stratification, the ENSO mode in all of these climates would be subject to enhanced destabilizing effects of Ekman feedback.

Proxies for Pliocene climate so far has been related to only SST providing no reliable information about the oceanic stratification (i.e. thermocline depth/sharpness). Furthermore, the direct modeling approach to simulate the Pliocene climate by adjusting the continental boundaries, removing the continental ice and introducing etc , have failed so far to explain the key features of this climate such as the reduced zonal and meridional temperature gradients and thus suggesting a search for missing mechanisms or alternative parameterizations of unresolved physical processes [Fedorov et al., 2013]. Thus, there is an uncertainty in the state of the ocean in such a climate even though there exist knowledge about SST. For example, by varying cloud properties within a climate model achieve a similar magnitude reduction of ΔT with virtually no changes in the equatorial thermocline depth and sharpness. The oceanic stratification would affect the strength of thermocline feedbacks, which is virtually absent in our weak ΔT experiments, but could still be prominent in other reduced ΔT climates. Nonetheless, the robustness of ENSO through a variety of simulated climate agrees with the available observational evidence of ENSO in reduced ΔT geological epochs (Fig. 7.1). Contrary to suggestions in Davies et al. [2011, 2012]; Watanabe et al. [2011] a weak mean zonal SST gradient (permanent El Niño-like conditions) and ENSO do not preclude one another. For small ΔT, one could expect a reduction of ENSO magnitude by 30-40%, but not its full disappearance.

The climate models assessing impact of global warming predict mean climates with a slight reduction in ΔT, shallowing and sharpening of the thermocline but no reliably evidence for changes in ENSO variance. It is assumed to be due to compensation between different feedbacks: the increased thermocline and Ekman feedbacks would amplify ENSO but increased cloud feedback would dampen it. The uncertainty comes from the fact that the climate changes are relatively small and the exact magnitudes of feedbacks could not be detected with reliable error bounds due to noise and natural climate variability at all time scales. Thus, the characteristics of ENSO stay essentially the same contrary to the set of climates presented here where the variability moved from being driven purely due to remote thermocline feedback to the locally driven Ekman-type ENSO.

At last, we would like to mention that there are several apparent limitations in the present study. For example, we do not address the ultimate causes of changes in the zonal SST gradient we simply induce those changes from the extra-tropics. Consequently, we do not explicitly consider changes in tropical climate caused by variations in Earths precession or obliquity [Clement et al., 1999, 2000; Timmermann et al., 2007], volcanic or solar forcing [Mann et al., 2005], or very high CO_2 levels [Cherchi et al., 2008]. Nor does our method simulate ΔT below 1℃. Nevertheless, although some of our results might be model or approach dependent, the major physical inferences should hold (e.g., the eastward shift of wind anomalies or weaker ocean stratification for smaller ΔT).

Chapter 8

Summary

The ocean response to hurricane winds. Hurricanes are relatively rare localized atmospheric vortices with winds of extreme strength that actively interact with the ocean. The turbulent ocean currents associated with a passage of a hurricane entrain colder waters from depth of a thermally stratified ocean to its surface. In turn, hurricanes, that feed on latent heat fluxes from warm ocean waters, substantially weaken. Thus, ocean dynamics plays an important role in prediction of hurricane intensity. I characterized the evolution of the mixed layer in a set of laboratory experiments aimed to simulate hurricane forcing. I explained the observed dependencies with scaling laws derived from energy budget model and provided estimates of a turbulent entrainment coefficient (Manucharyan & Caulfield). Experiments further revealed the formation of a series of small scale mixed layers (staircases) located below the thick surface boundary layer. Despite their small spatial scales their presence increases the buoyancy flux by about 50%. To explain their dynamics, I devised an idealized phenomenological model of the turbulent buoyancy transport and identified the regimes under which these fine structures can form as an instability (Manucharyan, 2010). Guided by insights from experiments, I analyzed the observational data of hurricanes tracks, and estimated that their vorticity input into the ocean constitutes about 20% of the input from climatological winds (Manucharyan & Fedorov). The long term effects of hurricane forcing on climate are investigated further.

Eddy generation at surface ocean fronts. This study is aimed to explain the persistent observations of sub-mixed layer eddies (ocean vortices) in the Arctic Ocean at great distances away from ocean fronts where they form. Such eddies affect the melting of sea ice due to increased heat fluxes associated with their turbulent currents. Here, I investigate the instabilities of fronts that separate mixed layers of different depths (also analogous to ocean conditions after the hurricane) with the aim to characterize their ability to generate isolated eddies. High resolution fluid dynamics simulations revealed that for such fronts the fastest growing mode of instability is in the form of a self-propagating dipole that could transport heat and salt across the front. However, most of them are formed unbalanced, with strongly curved trajectories that lead to their recirculation back to the front. I derived an idealized quasi-geostrophic model of such a dipole and found parameters that control their maximum separation distance from the front. I further constructed a method to detect and track these dipoles, characterized their key properties in relation to frontal configurations, and classified the fronts in terms of generation probability of far propagating dipoles; shallow fronts, separating mixed layers of similar depths are more favorable (Manucharyan & Timmermans, 2013). The results provide useful guidance for employment of observational instruments in ocean frontal regions.

Long term impacts of hurricane forcing on climate. I have investigated the ocean response to hurricanes on time and spatial scales of the order of the forcing scale, but can such localized events cumulatively affect the long term climate? Here, I separate the two different effects of hurricanes on ocean: the increased upper ocean mixing and the vorticity input into the currents. The vorticity forcing deposits energy into quasi-geostrophic ocean currents in the form of a series of cyclonic eddies along the hurricane track.

These eddies drift westward, interact with currents and other eddies and are subjected to dispersion and dissipation. I investigated this convoluted dynamics in a shallow water ocean model where I prescribed hurricanes as vortices moving in random directions. As a long time average, such forcing generated multiple zonal jets as well as a basin-wide gyre type circulation with a strong western boundary current. The formation of stationary large scale structures from localized forcing of fluids remains an open question for my future work.

Qualitatively different effects arise from intermittent upper ocean mixing. Since cold waters entrained to the surface are warmed by the atmosphere there is a net input of heat into the upper ocean. I investigated these effects in the framework of an advection-diffusion equation with a time dependent diffusivity and established a relation between the frequency of the mixing events and the amount of heat being fluxed through the surface boundary: the higher the frequency the less efficient this heat pump is (Manucharyan & Fedorov, 2011). In a steady state view the influx of heat needs to be balanced by its transport away from the regions of hurricane activity. An important result is that part of this heat is advected by the mean circulation towards equatorial Pacific Ocean and decreases its zonal temperature gradient – a key element of tropical dynamics. Such a climate resembles conditions of the Pliocene epoch which is so different from present that climate models are completely unable to reproduce it. This gave me an opportunity to investigate the dynamics of such unexplored climates.

El Niño dynamics from past to present climates. The El Nio - Southern Oscillation (ENSO) is a pronounced mode of climate variability that originates in the tropical Pacific and affects weather patterns worldwide. Growing evidence suggests that ENSO was active over vast geological epochs including the Pliocene epoch ($\sim$3 million years ago) despite its profound changes in tropical climate. The mechanisms for sustained ENSO in such climates are poorly understood. Here, I use a comprehensive climate model to explore the sensitivity of ENSO on the mean equatorial temperature gradient in the Pacific (Manucharyan & Fedorov). For the whole range of climates ENSO remained surprisingly robust. To explain it, I assessed the magnitude of ocean-atmosphere feedbacks that control the stability of the natural mode of ENSO by systematically reducing the underlying fluid dynamics equations down to a model of damped noise driven oscillator. The spectral analysis of the ENSO time series showed a good agreement with the derived model. I further estimated that throughout different climates the damping rates stay nearly constant with the strength of noise only slightly reduced, rationalizing the persistent climate variability. This study gives insight into the dynamics of ENSO in a wide range of climates and, in particular, reconciles the seemingly contradictory findings of strong variability and the small east-west temperature gradient during the Pliocene.

Rotating density currents on a slope. Density currents, so ubiquitous to geophysical flows, are fluid masses submerged into relatively stationary ambient fluids of different density, with their motion driven by the buoyancy force. The dynamics of such currents is significantly affected by the turbulent entrainment processes which lead to exchange of density and momentum with the environment. Together with my colleagues, I investigated the role of rotation on the efficiency of the turbulent entrainment (Manucharyan *et al*). We systematically derived a mathematical model for these currents and obtained its analytical solutions. We further performed a set of laboratory experiments to confirm key prediction of the analytical model the existence of the critical depth at which the dense current (initially released at the tip of the cone) does not move downwards but instead rotates around the cone. Experimentally established dependence of this critical depth on rotation rate, combined with derived analytical solutions, allowed us to quantify the suppression of effecting entrainment rate due to rotation. The results are an important step towards understanding the nature of turbulence in the presence of rotation.

Appendix A

Quasi-Geostrophic Model of a Dipole

A.1 Point vortices

We first consider point vortices and later include more realistic Gaussian vortices. The leading-order approximation to dipole dynamics can be recovered from the linear 2.5-layer quasi-geostrophic equations [Pedlosky, 1982], assuming that PV anomalies for each of the vortices as well as their separation distance Δ are known:

$$\nabla^2\psi_1 + F_1(\psi_2 - \psi_1) = S_1\delta(\mathbf{r}) \tag{A.1}$$

$$\nabla^2\psi_2 + F_2(\psi_1 - \psi_2) - F_3\psi_2 = S_2\delta(\mathbf{r} - \boldsymbol{\Delta}). \tag{A.2}$$

Here $\psi_{1,2}$ are the stream functions in layers 1 and 2, $F_{1,2,3}$ are the stratification parameters (Eq. 4.15) and $S_{1,2}$ are the dipole PV anomalies multiplied by mean layer thickness in corresponding layers. Layer 2 has a PV anomaly that is offset by a distance Δ with respect to the center of the PV anomaly in layer 1. This introduces an asymmetry in an otherwise axisymmetric set-up. However, the solution to the linear equations can be split into a sum of two: one having a PV anomaly in layer 1 only, and another having PV anomaly in layer 2 only. The two solutions obey the same equation set, with the difference in the source terms:

$$\nabla^2\psi_1 + F_1(\psi_2 - \psi_1) = S_1\delta(r) \tag{A.3}$$

$$\nabla^2\psi_2 + F_2(\psi_1 - \psi_2) - F_3\psi_2 = S_2\delta(r), \tag{A.4}$$

now in terms of polar coordinate r, where in one solution we set $S_1 = 0$ and in another $S_2 = 0$. This linear system of coupled equations can be decoupled into two independent vertical mode equations

$$\nabla^2\Psi_{1,2} - c_{1,2}\ \Psi_{1,2} = Q_{1,2} \tag{A.5}$$

using a linear substitution $\Psi_{1,2} = (F_2 + F_3 - c_{1,2})\psi_1 + F_1\psi_2$ where $Q_{1,2}$ is the source term (linear combination of S_1 and S_2) and $c_{1,2}$ are two positive constants defined as

$$c_{1,2} = \frac{F_1 + F_2 + F_3}{2} \pm \sqrt{\frac{(F_1 + F_2 + F_3)^2}{4} - F_1F_3}. \tag{A.6}$$

The equations for Ψ are identical to a 1.5-layer quasi-geostrophic system with $c = 1/\lambda^2$ being a stratification parameter corresponding to the internal deformation radius λ for this mode. We thus split the equations into two modes (first and second baroclinic modes) to obtain

$$\nabla^2\Psi_1 - 1/\lambda_1^2\Psi_1 = ((F_2 + F_3 - c_1)S_1 + F_1 S_2)\delta(r) \tag{A.7}$$
$$\nabla^2\Psi_2 - 1/\lambda_2^2\Psi_2 = ((F_2 + F_3 - c_2)S_1 + F_1 S_2)\delta(r). \tag{A.8}$$

These are the modified Bessel equations for which fundamental solutions bounded at infinity are the modified Bessel functions K_0:

$$\Psi_1 = ((F_2 + F_3 - c_1)S_1 + F_1 S_2)K_0(r/\lambda_1) \tag{A.9}$$
$$\Psi_2 = ((F_2 + F_3 - c_2)S_1 + F_1 S_2)K_0(r/\lambda_2). \tag{A.10}$$

The original variables are recovered by the inverse transformation:

$$\psi_1 = -\frac{\Psi_1 - \Psi_2}{c_1 - c_2} \tag{A.11}$$
$$\psi_2 = -\frac{\Psi_1(F_2 + F_3 - c_2) - \Psi_2(F_2 + F_3 - c_1)}{F_1(c_1 - c_2)}. \tag{A.12}$$

Next we consider the two cases, each with a PV anomaly in only one of the layers. In the first case with $S_2 = 0, S_1 \neq 0$,

$$\Psi_1 = S_1(F_2 + F_3 - c_1)K_0(r/\lambda_1) \tag{A.13}$$
$$\Psi_2 = S_1(F_2 + F_3 - c_2)K_0(r/\lambda_2). \tag{A.14}$$

In this case, the layer 1 vortex induces a circulation in layer 2, which advects the vortex in layer 2 and

$$\psi_2 = S_1 F_2 \frac{K_0(r/\lambda_1) - K_0(r/\lambda_2)}{c_2 - c_1}, \tag{A.15}$$

since $(F_2 + F_3 - c_1)(F_2 + F_3 - c_2) = -F_1 F_2$.

In the second case with $S_2 \neq 0, S_1 = 0$,

$$\Psi_1 = S_2 F_1 K_0(r/\lambda_1) \tag{A.16}$$

$$\Psi_2 = S_2 F_1 K_0(r/\lambda_2). \tag{A.17}$$

In this case, the layer 2 vortex induces a circulation in layer 1, which advects the vortex in layer 1 and

$$\psi_1 = S_2 F_1 \frac{K_0(r/\lambda_1) - K_0(r/\lambda_2)}{c_1 - c_2}. \tag{A.18}$$

Given the velocity fields induced by each of the vortices, the propagation speeds of the vortex centers can be deduced

$$U_i = u_i|_{r=\Delta} = \frac{\partial \psi_i}{\partial r}|_{r=\Delta},\ i = 1, 2. \tag{A.19}$$

Since ψ_1 and ψ_2 have the same functional form, we can easily obtain the important ratio $\epsilon = U_2/U_1$ which determines the radius of the dipole trajectory:

$$\epsilon = \frac{S_1}{S_2}\frac{F_2}{F_1} = \frac{S_1}{S_2}\frac{H_1}{H_2}. \tag{A.20}$$

A.2 Gaussian vortices

The derivations in Appendix A.1 provide a Green's function for the vortex stream function, which can be used to recover the circulation of a vortex with an arbitrary shape of PV anomaly. One could obtain it by taking a convolution of the Green's function with a source term, which requires evaluating a two-dimensional integral. In the case of axisymmetric vortices with a Gaussian PV distribution (a good approximation to the eddies observed in the simulations), the problem can be simplified through the use of the Hankel transformation:

$$\hat{\Psi}(k) = \int_0^\infty \Psi(r) J_0(kr) r dr \tag{A.21}$$

$$\Psi(r) = \int_0^\infty \hat{\Psi}(k) J_0(kr) k dk, \tag{A.22}$$

where J_0 is a zeroth-order Bessel function of the first kind [Abramowitz and Stegun, 1972]. We use a Gaussian profile for the source term $Q = Q_0 exp(-\frac{r^2}{2\sigma^2})$, where parameters Q_0 and σ are obtained by the best fit to PV anomalies in corresponding layers (Fig. 4.8a). Note that after splitting equations into contributions from individual eddies the source term Q is proportional to either S_1 or S_2 (not their linear combination), thus preserving the Gaussian form. Applying the Hankel transform to Eq. A.5 (and dropping subscripts 1 and 2) we obtain a solution in k space:

$$\hat{\Psi} = -\frac{\hat{Q}}{k^2 + c}, \tag{A.23}$$

where $\hat{Q}(k) = Q_0 \sigma^2 exp(-\frac{k^2}{2\sigma^2})$. The solution in r space is expressed in the form of a one dimensional integral

$$\Psi(r) = -Q_0 \sigma^2 \int_0^\infty \frac{exp(-\frac{k^2\sigma^2}{2})}{k^2 + c} J_0(kr) k dk, \tag{A.24}$$

which is evaluated numerically. A linear inverse transformation (Eq. A.11, A.12) to original variables is then applied and the azimuthal velocity fields are calculated as derivatives of the stream functions (as in the case of point vortices).

The procedure allows us to separate the velocity field in a dipole into contributions from individual eddies and thus obtain the self-advecting velocities $U_{1,2}$. The propagating velocity of the surface cyclonic vortex U_1 is calculated as the velocity generated by the anticyclonic vortex (u_1) at the location of the core of the cyclonic vortex and *vice versa*. We calculate U_1 as $u_1(r)$ averaged over the interval $[\Delta - \sigma, \Delta + \sigma]$.

Appendix B

Entraining Plume Model

B.1 Derivation of plume equations

The plume model is derived from first principles by considering buoyancy-driven boundary-layer flow on a cone as illustrated in figure 3.1. We present a derivation below for an isolated current of angular extent $\Delta\theta$, with the axisymmetric plume equations recovered as the special case of $\Delta\theta = 2\pi$. Starting from the Reynolds-Averaged Navier-Stokes equations for rotating, buoyancy-driven flow in cylindrical coordinates (r, θ, z), we transform to a coordinate system (s, η, θ) where s is parallel and η is perpendicular to the conical surface. If the cone apex is at $\eta = s = 0$ and $r = z = 0$, then $r = s\cos\alpha + \eta\sin\alpha$, $z = -s\sin\alpha + \eta\cos\alpha$ and we denote the velocity as $\mathbf{u} = (u_s, u_\eta, u_\theta)$ in the (s, η, θ) coordinate system. The transformed Navier-

Stokes equations yield

$$\frac{1}{r}\frac{\partial}{\partial s}(ru_s^2)+\frac{1}{r}\frac{\partial}{\partial \eta}(ru_su_\eta)+\frac{1}{r}\frac{\partial}{\partial \theta}(u_\theta u_s)=-\frac{1}{\rho_0}\frac{\partial \tilde{P}}{\partial s}+\frac{u_\theta^2\mathrm{cos}\alpha}{r}+2\Omega\mathrm{cos}\alpha u_\theta+\ldots$$
$$+\frac{\rho}{\rho_0}g\mathrm{sin}\alpha+F_s, \tag{B.1}$$

$$\frac{1}{r}\frac{\partial}{\partial s}(ru_\theta u_s)+\frac{1}{r}\frac{\partial}{\partial \eta}(ru_\theta u_\eta)+\frac{1}{r}\frac{\partial}{\partial \theta}\left(u_\theta^2\right)=-\frac{1}{\rho_0 r}\frac{\partial \tilde{P}}{\partial \theta}-\frac{u_\theta(u_s\mathrm{cos}\alpha+u_\eta\mathrm{sin}\alpha)}{r}+\ldots$$
$$-2\Omega(u_s\mathrm{cos}\alpha+u_\eta\mathrm{sin}\alpha)+F_\theta, \tag{B.2}$$

$$\frac{1}{r}\frac{\partial}{\partial s}(ru_su_\eta)+\frac{1}{r}\frac{\partial}{\partial \eta}(ru_\eta^2)+\frac{1}{r}\frac{\partial}{\partial \theta}(u_\theta u_\eta)=-\frac{1}{\rho_0}\frac{\partial \tilde{P}}{\partial \eta}+\frac{u_\theta^2\mathrm{sin}\alpha}{r}+\ldots$$
$$+2\Omega\mathrm{sin}\alpha u_\theta-\frac{\rho}{\rho_0}g\mathrm{cos}\alpha+F_\eta, \tag{B.3}$$

$$\frac{1}{r}\frac{\partial}{\partial s}(ru_s)+\frac{1}{r}\frac{\partial}{\partial \eta}(ru_\eta)+\frac{1}{r}\frac{\partial u_\theta}{\partial \theta}=0, \qquad \text{and} \tag{B.4}$$

$$\frac{1}{r}\frac{\partial}{\partial s}(r\rho u_s)+\frac{1}{r}\frac{\partial}{\partial \eta}(r\rho u_\eta)+\frac{1}{r}\frac{\partial}{\partial \theta}(\rho u_\theta)=0, \tag{B.5}$$

where $\tilde{P}=P-\Omega^2r^2/2$ is an effective pressure including the fluid pressure P and centrifugal contribution from the rotating reference frame. The frictional force $\mathbf{F}=(F_s,F_\eta,F_\theta)$ includes both viscous shear stresses and eddy-momentum fluxes due to the time average of turbulent fluctuations in velocity as

$$\mathbf{F}=\nabla\cdot\tau=\nu\nabla^2\mathbf{u}-\nabla\cdot\left(\overline{\mathbf{u}'\mathbf{u}'}\right).$$

The density current has a shallow characteristic thickness H compared to the distance L flowed along slope, and so we apply a boundary layer approximation under the condition $L \gg H$ [Schlichting et al., 1968]. This yields

$$
\begin{aligned}
\frac{1}{r}\frac{\partial}{\partial s}(ru_s^2) + \frac{1}{r}\frac{\partial}{\partial \eta}(ru_s u_\eta) + \frac{1}{r}\frac{\partial}{\partial \theta}(u_\theta u_s) =& \frac{u_\theta^2 \text{cos}\alpha}{r} + 2\Omega\text{cos}\alpha u_\theta + \dots \\
&+ \frac{\rho - \rho_0}{\rho_0} g\text{sin}\alpha + \frac{1}{r}\frac{\partial}{\partial \eta}\left(r\tau_{\eta s}\right),
\end{aligned}
\tag{B.6}
$$

$$
\frac{1}{r}\frac{\partial}{\partial s}(ru_\theta u_s) + \frac{1}{r}\frac{\partial}{\partial \eta}(ru_\theta u_\eta) + \frac{1}{r}\frac{\partial}{\partial \theta}u_\theta^2 = - \frac{u_\theta u_s \text{cos}\alpha}{r} - 2\Omega\text{cos}\alpha u_s + \frac{1}{r}\frac{\partial}{\partial \eta}\left(r\tau_{\eta\theta}\right),
\tag{B.7}
$$

$$
\frac{1}{r}\frac{\partial}{\partial s}(ru_s) + \frac{1}{r}\frac{\partial}{\partial \eta}(ru_\eta) + \frac{1}{r}\frac{\partial u_\theta}{\partial \theta} = 0, \qquad \text{and}
\tag{B.8}
$$

$$
\frac{1}{r}\frac{\partial}{\partial s}(r\rho u_s) + \frac{1}{r}\frac{\partial}{\partial \eta}(r\rho u_\eta) + \frac{1}{r}\frac{\partial}{\partial \theta}(\rho u_\theta) = 0,
\tag{B.9}
$$

where ρ_0 is the environmental density far away from the current and $\tau_{\eta s}$, $\tau_{\eta\theta}$ are components of τ.

Plume equations can be derived by averaging (B.6)–(B.9) azimuthally and normal to the slope. We define the effective plume width b, downslope velocity w, azimuthal velocity v, and density ρ according to (3.5)–(3.8), where the current has angular extent $\Delta\theta$ and the cone has local radius r_s. One could interpret these definitions in terms of piecewise-constant "top-hat" profiles over a rectangle in (η, θ) space, although such an assumption is not required. Under the assumption of self-similarity, the other integral terms arising are approximated by

$$
\int_0^{2\pi}\int_0^{\infty} u_\theta^2 d\eta d\theta = \beta_1 b v^2 \Delta\theta, \qquad \int_0^{2\pi}\int_0^{\infty} r u_\theta d\eta d\theta = \beta_2 b v r_s \Delta\theta, \qquad \text{and}
$$

$$
\int_0^{2\pi}\int_0^{\infty} u_\theta u_s d\eta d\theta = \beta_3 b w v \Delta\theta,
\tag{B.10}
$$

where the shape factors β_1, β_2, and β_3 are constants, with $\beta_1 = \beta_2 = \beta_3 = 1$

for "top-hat" profiles [Linden, 2000]. Finally, we denote the effective entrainment velocity v_e as

$$\int_0^{2\pi} r u_\eta \,|_{\eta=\infty}\, d\theta \cong -\Delta\theta r_s v_e, \tag{B.11}$$

and effective drag components as

$$\int_0^{2\pi} r\tau_{\eta s} d\theta \cong \Delta\theta r_s \tau_s, \qquad \text{and} \qquad \int_0^{2\pi} r\tau_{\eta\theta} d\theta \cong \Delta\theta r_s \tau_\theta. \tag{B.12}$$

Using the above definitions and assuming $\beta_1 = \beta_2 = \beta_3 = 1$, a domain integration $\int_0^{2\pi}\int_0^{\infty}(\cdot) r d\eta d\theta$ of (B.6)–(B.9) yields

$$\frac{d}{ds}(bw^2 r_s) - bv^2 \mathrm{cos}\alpha = 2\Omega\mathrm{cos}\alpha bvr_s + \frac{\tilde{\rho}-\rho_0}{\rho_0} br_s g\mathrm{sin}\alpha - r_s\tau_s - \frac{d\mathrm{ln}\Delta\theta}{ds} bw^2 r_s, \tag{B.13}$$

$$\frac{d}{ds}(bwvr_s) + bwv\mathrm{cos}\alpha = -2\Omega\mathrm{cos}\alpha bwr_s - r_s\tau_\theta - \frac{d\mathrm{ln}\Delta\theta}{ds} bvwr_s, \tag{B.14}$$

$$\frac{d}{ds}(bwr_s) = r_s v_e - \frac{d\mathrm{ln}\Delta\theta}{ds} bwr_s, \qquad \text{and} \tag{B.15}$$

$$\frac{d}{ds}\left(\frac{\rho-\rho_0}{\rho_0} br_s w\right) g\mathrm{sin}\alpha = -\frac{d\mathrm{ln}\Delta\theta}{ds}\frac{\tilde{\rho}-\rho_e}{\rho_0} bwr_s g\mathrm{sin}\alpha, \tag{B.16}$$

which after some algebraic manipulation are equivalent to (3.1)–(3.4) . In the axially-symmetric case the flow is 2π-periodic with $\Delta\theta = 2\pi$ so that $d\ln\Delta\theta/ds = 0$ and the system is closed. For an isolated plume of angular extent $\Delta\theta < 2\pi$ a separate closure assumption is required to determine $\Delta\theta$ and describe the physical processes responsible for azimuthal widening of the current. However, whenever the terms involving $d\ln\Delta\theta/ds$ are small, then the isolated plume evolves according to the same leading-order dynamics as the axisymmetric case. Formally this condition can be estimated from

$$\frac{d\,(\ln\Delta\theta)}{ds} \ll \frac{d\,[\ln(bwr_s)]}{ds},\ \frac{d\,[\ln(bw^2r_s)]}{ds},\ \frac{d\,[\ln(bwvr_s)]}{ds},\ \frac{d\,(\ln[bwr_s\,(\tilde{\rho}-\rho_0)])}{ds}. \tag{B.17}$$

Whenever (B.17) is satisfied, the single-stream flow of an isolated plume forms an angular subsection of the corresponding axisymmetric flow.

B.2 Fixed point analysis

In order to determine the fixed points and attractors for the system (3.16)–(3.18), we make the substitutions

$$x = FE^{-2/3}\xi^{-8/3}, \quad y = P^2E^{-4/3}\xi^{-10/3}, \quad \text{and} \quad z = VE^{-2/3}\xi^{-8/3}, \tag{B.18}$$

and define $\zeta = \ln\xi$, yielding

$$\frac{dx}{d\zeta} = -\frac{8}{3}x + 2\sqrt{y} - \frac{2K}{E}\frac{x^{3/2}}{y}, \tag{B.19}$$

$$\frac{dy}{d\zeta} = 2\sqrt{x} - \frac{10}{3}y, \qquad \text{and} \tag{B.20}$$

$$\frac{dz}{d\zeta} = -\frac{11}{3}z + \sqrt{y} - \frac{K}{E}\frac{z\sqrt{x}}{y}. \tag{B.21}$$

Note that this system can be treated as closed in the following manner. Consider z as determined from (B.21) to be slaved to x and y as determined from (B.19) and (B.20). Setting $dx/d\zeta = dy/d\zeta = dz/d\zeta = 0$ yields the

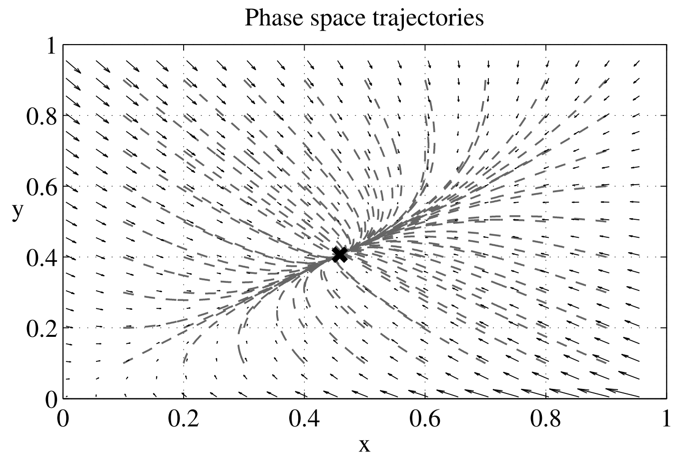

Figure B.1: Convergence of all trajectories (x, y) to the fixed point (cross symbol) corresponding to (3.22)–(3.20), for the special case $K = 0$. Short arrows show the local flow direction $(dx/d\zeta, dy/d\zeta)$, with example trajectories indicated by dashed curves.

unique fixed point

$$
\begin{aligned}
x = \bar{x} &\equiv \frac{9}{2^{8/3}5^{2/3}\left(1+\frac{5}{4}\frac{K}{E}\right)^{4/3}}, \\
y = \bar{y} &\equiv \frac{9}{2^{4/3}5^{4/3}\left(1+\frac{5}{4}\frac{K}{E}\right)^{2/3}}, \qquad \text{and} \\
z = \bar{z} &\equiv \frac{9}{2^{2/3}5^{2/3}11\left(1+\frac{5}{4}\frac{K}{E}\right)^{1/3}\left(1+\frac{5}{11}\frac{K}{E}\right)},
\end{aligned} \tag{B.22}
$$

corresponding to the special solution (3.20)–(3.22).

To determine the stability, we linearize about the fixed point by letting $x = \bar{x}+\chi_x$, $y = \bar{y}+\chi_y$ and $z = \bar{z}+\chi_z$. Writing $\chi = (\chi_x, \chi_y, \chi_z)$ with $|\chi| \ll 1$, this yields the linearised system

$$\frac{\partial \chi}{\partial \zeta} = D\chi, \tag{B.23}$$

where

$$D = \begin{pmatrix} -\frac{8}{3} - \frac{3\sqrt{\bar{x}}}{\bar{y}}\frac{K}{E} & \frac{1}{\sqrt{\bar{y}}} + \frac{2\bar{x}^{3/2}}{\bar{y}^2}\frac{K}{E} & 0 \\ \frac{1}{\sqrt{\bar{x}}} & -\frac{10}{3} & 0 \\ -\frac{\bar{z}}{2\bar{y}\sqrt{\bar{x}}}\frac{K}{E} & \frac{1}{2\sqrt{\bar{y}}} + \frac{\bar{z}\sqrt{\bar{x}}}{\bar{y}^2}\frac{K}{E} & -\frac{11}{3} - \frac{\sqrt{\bar{x}}}{\bar{y}}\frac{K}{E} \end{pmatrix}. \tag{B.24}$$

Substituting for $\bar{x}$, $\bar{y}$, and $\bar{z}$ we find that the eigenvalue of the matrix D corresponding to the evolution of the slaved coordinate z is $\lambda = -11/3 - 5K/3E$, which is always negative. The remaining two eigenvalues of D are given by $\lambda = -b/2 \pm \sqrt{b^2 - 4c}/2$ where

$$b = 6 + 5\frac{K}{E}, \qquad c = \frac{20}{3} + \frac{25}{3}\frac{K}{E}. \tag{B.25}$$

Since $0 < c < b^2/4$, these eigenvalues are negative and the fixed point is asymptotically stable. Because the closed system (x, y) is two dimensional, the unique fixed point serves as an attractor for all solution trajectories with different initial conditions. An example of the evolution of the (x, y) trajectories corresponding to the closed sub-system (B.19) and (B.20) is illustrated in figure B.1.

B.3 Rotating density currents on a planar slope

The plume model can also be generalised for rotating density currents on a planar slope inclined at an angle α to the horizontal. The planar slope limit can either be derived from first principles using the method of appendix B.1 (not detailed here), or else recovered from the axisymmetric model (3.1)–(3.4) by considering the conceptual limit of a large radius of curvature $r_s \to \infty$, but with the equivalent plume width $a = r_s \Delta\theta$ remaining finite. In this planar slope limit the downslope fluxes of mass, downslope momentum, across-slope momentum and buoyancy are now described by

$$\frac{d}{ds}\left(abw\right) = aE\sqrt{v^2+w^2}, \tag{B.26}$$

$$\frac{d}{ds}\left(abw^2\right) = abg\sin\alpha\frac{\rho-\rho_0}{\rho_0} - abfv - aKw\sqrt{v^2+w^2}, \tag{B.27}$$

$$\frac{d}{ds}\left(abwv\right) = abfw - aKv\sqrt{v^2+w^2}, \qquad \text{and} \tag{B.28}$$

$$\frac{d}{ds}\left(abw\frac{\rho-\rho_0}{\rho_0}\right) = 0, \tag{B.29}$$

where s is the downslope distance, and we define the across-slope distance x along isobaths. In this planar slope limit, the effective plume width b, downslope plume velocity w, across-slope velocity v and mean density ρ are defined in terms of the fluxes

$$\int_{-\infty}^{\infty}\int_{0}^{\infty} u_s \, d\eta \, dx \equiv abw, \tag{B.30}$$

$$\int_{-\infty}^{\infty}\int_{0}^{\infty} u_s^2 \, d\eta \, dx \equiv abw^2, \tag{B.31}$$

$$\int_{-\infty}^{\infty}\int_{0}^{\infty} u_x u_s \, d\eta \, dx \equiv abvw, \qquad \text{and} \tag{B.32}$$

$$\int_{-\infty}^{\infty}\int_{0}^{\infty} u_s \frac{\tilde{\rho}-\rho_0}{\rho_0} \, d\eta \, dx \equiv abw\frac{\rho-\rho_0}{\rho_0}, \tag{B.33}$$

where $u_x(x, s, \eta)$ is the across slope velocity field in planar coordinates. Similarly to the axisymmetric case we neglect lateral spreading driven by across-slope variations in hydrostatic pressure and mixing at the current sides, so that the planar current width a is assumed constant. After dividing (B.26)-(B.29) through by the constant a, the resulting differential equations can describe either flows from an infinite line source at $s = s_I$, or else the path lines of a single stream flow of constant width from a localised line-source at $s = s_I$ with effective width $0 < x < a$.

A leading-order similarity solution, and asymptotic corrections to account for initial conditions can be derived in a fashion similar to the axisymmetric case, which we summarise with brevity below. The downslope buoyancy flux per unit width Q_B is conserved, with (B.29) integrating to yield

$$bwg\sin\alpha\,\frac{\rho-\rho_0}{\rho_0} = Q_B = \text{constant}. \tag{B.34}$$

We define

$$\xi = \frac{sf}{Q_B^{1/3}}, \quad P = \frac{bwf}{Q_B^{2/3}}, \quad W = \frac{bw^2 f}{Q_B}, \quad V = \frac{bwvf}{Q_B}, \tag{B.35}$$

which represent dimensionless downslope distance, and dimensionless downslope fluxes of mass, downslope momentum, and across-slope momentum, respectively. Defining the variable $F = V^2 + W^2$ for convenience, the governing equations (B.26)-(B.28) combine to give

$$\begin{aligned}
\dot{P} &= E\frac{\sqrt{F}}{P}, && \text{(B.36)}\\
\dot{F} &= 2P - 2K\frac{F^{3/2}}{P^2}, \qquad \text{and} && \text{(B.37)}\\
\dot{V} &= P - KV\frac{\sqrt{F}}{P^2}, && \text{(B.38)}
\end{aligned}$$

where $\dot{[\,]} \equiv d/d\xi$. The leading-order dynamics are characterised by a special solution for a line source of buoyancy with negligible initial fluxes of mass and momentum, with initial conditions $P = V = W = F = 0$ imposed at a particular downslope position $\xi = \xi_0$. We obtain power-law similarity solutions

$$\begin{aligned}
P &= \frac{E^{2/3}}{\left(1+\frac{K}{E}\right)^{1/3}}\left(\xi-\xi_0\right), && \text{(B.39)}\\
F &= \frac{E^{2/3}}{\left(1+\frac{K}{E}\right)^{4/3}}\left(\xi-\xi_0\right)^2, \qquad \text{and} && \text{(B.40)}\\
V &= \frac{E^{2/3}}{2\left(1+\frac{K}{E}\right)^{1/3}\left(1+\frac{K}{2E}\right)}\left(\xi-\xi_0\right)^2. && \text{(B.41)}
\end{aligned}$$

Comparing the power-law exponents in the solutions (B.39)–(B.41) with those in (3.20)–(3.22), we see that the downslope fluxes of mass and across-slope momentum grow more slowly in planar geometry than their axisymmetric counterparts. However, the flow in planar geometry develops in a fashion qualitatively similar to the axisymmetric case, and in particular exhibits a critical level $s = s_{cr}$ where the downslope flow ceases ($w = 0$). The critical level is determined by solving $W^2 = F - V^2 = 0$ for $\xi = \xi_{cr}$, which yields

$$s_{cr} - s_0 = 2\frac{\left(1+\frac{K}{2E}\right)^{1/2}}{\left(1+\frac{K}{E}\right)^{1/3}}\left(\frac{Q_B}{Ef^3}\right)^{1/3}, \tag{B.42}$$

in dimensional units.

The similarity solution (B.39)–(B.41) is exact for initial conditions with $P = V = F = 0$ at $\xi = \xi_0$, but similarly to the axisymmetric case we also expect this solution to capture the leading-order asymptotic behaviour for large ξ when more general initial conditions are used. However, the similarity solution does not satisfy all possible initial conditions with fluxes $P = P_0$, $F = F_0$ and $V = V_0$ imposed at $\xi = \xi_I$. In a fashion similar to the axisymmetric case, we therefore derive linearised corrections to the similarity solution for planar geometry. The resulting combination of similarity solution plus leading-order corrections can be used to approximate solutions with non-zero initial fluxes of mass and momentum imposed at some $\xi = \xi_I$, with the similarity solution describing the asymptotic leading-order behaviour for larger ξ. Following the method of §3.3.3, we perturb the similarity solution

$$P = P_a + \hat{P}, \qquad F = F_a + \hat{F}, \qquad V = V_a + \hat{V}, \tag{B.43}$$

where $P = P_a$, $F = F_a$ and $V = V_a$ are given by (B.39)–(B.41) with ξ_0 an as-yet-undetermined virtual origin [see Hunt and Kaye, 2001, for example], and $\hat{P} \ll P_a$, $\hat{F} \ll F_a$, $\hat{V} \ll V_a$. Setting $K = 0$ again for mathematical simplicity, and linearizing (B.36)–(B.38) we find

$$\frac{d\hat{P}}{d\xi} = \frac{\hat{F}}{2\left(\xi - \xi_0\right)^2} - \frac{\hat{P}}{\left(\xi - \xi_0\right)}, \tag{B.44}$$

$$\frac{d\hat{F}}{d\xi} = 2\hat{P}, \qquad \text{and} \tag{B.45}$$

$$\frac{d\hat{V}}{d\xi} = \hat{P}. \tag{B.46}$$

Combining (B.44) and (B.45) results in the second order differential equation

$$(\xi - \xi_0)^2 \frac{d^2 \hat{F}}{d\xi^2} + (\xi - \xi_0) \frac{d\hat{F}}{d\xi} - \hat{F} = 0, \tag{B.47}$$

which has a regular singular point at $\xi = \xi_0$. The resulting solution is

$$\hat{F} = B_1 (\xi - \xi_0) + \frac{B_2}{(\xi - \xi_0)}, \tag{B.48}$$

$$\hat{P} = \frac{B_1}{2} - \frac{B_2}{2 (\xi - \xi_0)^2}, \qquad \text{and} \tag{B.49}$$

$$\hat{V} = \frac{B_1 (\xi - \xi_0)}{2} - \frac{B_2}{2 (\xi - \xi_0)} + B_3, \tag{B.50}$$

where the constants $B_{1,2,3}$ are chosen so that the total solution (B.43) satisfies the initial conditions for F, P, and V at $\xi = \xi_I > \xi_0$. For this approximate solution, there is still the freedom to choose the virtual origin correction ξ_0. One could potentially choose ξ_0 so that the initial conditions $P = P_0$, $F = F_0$ and $V = V_0$ imposed at $\xi = \xi_I$ lie close to the similarity solution, thus improving the accuracy of the linearisation. For example, choosing ξ_0 so that $P_a(\xi_I) = P_0$ would be a convenient and simple choice. Alternatively, one might try to determine a virtual origin correction explicitly using analytical methods [Hunt and Kaye, 2001], although such an analysis has not been attempted here. The sum of the similarity solution (B.39)–(B.41) and correction (B.48)–(B.50) then constitutes an approximate solution that satisfies the initial conditions and captures the leading-order asymptotic behaviour for large ξ.

References

Milton Abramowitz and Irene A Stegun. Handbook of mathematical functions with formulas, graphs, and mathematical tables. national bureau of standards applied mathematics series 55. tenth printing. 1972. 213

A Adcroft, JM Campin, S Dutkiewicz, C Evangelinos, D Ferreira, G Forget, B Fox-Kemper, P Heimbach, C Hill, E Hill, et al. Mitgcm user manual, 2008. 85, 127

Kristina Ahlnäs, Thomas C Royer, and Thomas H George. Multiple dipole eddies in the alaska coastal current detected with landsat thematic mapper data. *Journal of Geophysical Research: Oceans (1978–2012)*, 92(C12): 13041–13047, 1987. 82

L.C. Allison, H.L. Johnson, and D.P. Marshall. Spin-up and adjustment of the antarctic circumpolar current and global pycnocline. *Journal of Physical Oceanography*, 2011. 155

Soon-Il An and Fei-Fei Jin. An eigen analysis of the interdecadal changes in the structure and frequency of enso mode. *Geophysical research letters*, 27 (16):2573–2576, 2000. 175

Soon-Il An and Fei-Fei Jin. Collective role of thermocline and zonal advective feedbacks in the enso mode*. *Journal of climate*, 14(16):3421–3432, 2001. 195

A. Arakawa and V.R. Lamb. A potential enstrophy and energy conserving scheme for the shallow water equations. *Monthly Weather Review*, 109(1): 18–36, 1981. 132

WD Baines and JS Turner. Turbulent buoyant convection from a source in a confined region. *Journal of Fluid Mechanics*, 37(01):51–80, 1969. 49

NJ Balmforth, S.G.L. Smith, and WR Young. Dynamics of interfaces and layers in a stratified turbulent fluid. *Journal of Fluid Mechanics*, 355: 329–358, 1998. 3, 12, 31

GI Barenblatt, M. Bertsch, R.D. Passo, VM Prostokishin, and M. Ughi. A mathematical model of turbulent heat and mass transfer in stably stratified shear flow. *Journal of Fluid Mechanics*, 253:341–358, 1993. 31

M. Barreiro, A. Fedorov, R. Pacanowski, and S.G. Philander. Abrupt climate changes: how freshening of the northern atlantic affects the thermohaline and wind-driven oceanic circulations. *Annu. Rev. Earth Planet. Sci.*, 36: 33–58, 2008. 153

Morris A Bender, Isaac Ginis, and Yoshio Kurihara. Numerical simulations of tropical cyclone-ocean interaction with a high-resolution coupled model. *Journal of Geophysical Research: Atmospheres (1984–2012)*, 98 (D12):23245–23263, 1993. 2

J. Bjerknes. Atlantic air-sea interaction. *Advances in Geophysics*, 10(1):82, 1964. 163

J. Bjerknes. Atmospheric teleconnections from the Equatorial Pacific. *Monthly Weather Review*, 97(3):163–172, 1969. ISSN 1520-0493. 157

G. Boccaletti, R.C. Pacanowski, S.G.H. Philander, and A.V. Fedorov. The thermal structure of the upper ocean. *Journal of physical oceanography*, 34(4):888–902, 2004. 155

Giulio Boccaletti, Raffaele Ferrari, and Baylor Fox-Kemper. Mixed layer instabilities and restratification. *Journal of Physical Oceanography*, 37(9): 2228–2250, 2007. 81, 90

Jaclyn N Brown, Alexey V Fedorov, and Eric Guilyardi. How well do coupled models replicate ocean energetics relevant to enso? *Climate dynamics*, 36 (11-12):2147–2158, 2011. 174

Josephine Brown, M Collins, Alexander Tudhope, et al. Coupled model simulations of mid-holocene enso and comparisons with coral oxygen isotope records. *Advances in Geosciences*, 6:29–33, 2006. 175

Mark A Cane. The evolution of el niño, past and future. *Earth and Planetary Science Letters*, 230(3):227–240, 2005. xxviii, 174, 175

Eddy C Carmack. The arctic oceans freshwater budget: Sources, storage and export. In *The freshwater budget of the Arctic Ocean*, pages 91–126. Springer, 2000. 49

X Carton. Oceanic vortices. In *Fronts, Waves and Vortices in Geophysical Flows*, pages 61–108. Springer, 2010. 82

Xavier Carton. Hydrodynamical modeling of oceanic vortices. *Surveys in Geophysics*, 22(3):179–263, 2001. 82, 93, 97, 99

Claudia Cenedese and Claudia Adduce. Mixing in a density-driven current flowing down a slope in a rotating fluid. *Journal of Fluid Mechanics*, 604: 369–388, 2008. 51, 80

Claudia Cenedese and Claudia Adduce. A new parameterization for entrainment in overflows. *Journal of Physical Oceanography*, 40(8):1835–1850, 2010. 50, 51

Claudia Cenedese, Jack A Whitehead, TA Ascarelli, and M Ohiwa. A dense current flowing down a sloping bottom in a rotating fluid. *Journal of Physical Oceanography*, 34(1):188–203, 2004. 51, 80

Shenn-Yu Chao and Ping-Tung Shaw. Close interactions between two pairs of heton-like vortices under sea ice. *Journal of Geophysical Research: Oceans (1978–2012)*, 104(C10):23591–23605, 1999. 116

Dudley B Chelton, Michael G Schlax, and Roger M Samelson. Global observations of nonlinear mesoscale eddies. *Progress in Oceanography*, 91(2): 167–216, 2011. 108

Annalisa Cherchi, Simona Masina, and Antonio Navarra. Impact of extreme co2 levels on tropical climate: a cgcm study. *Climate dynamics*, 31(7-8): 743–758, 2008. 183, 201

L Chérubin, X Carton, and DG Dritschel. Vortex dipole formation by baroclinic instability of boundary currents. *Journal of physical oceanography*, 37(6):1661–1677, 2007. 82

Allan J Clarke. *An introduction to the dynamics of El Nino & the Southern Oscillation*. Access Online via Elsevier, 2008. 173

AC Clement, R Seager, and MA Cane. Orbital controls on the el nino/southern oscillation and the tropical climate. *Paleoceanography*, 14 (4):441–456, 1999. 201

Amy C Clement, Richard Seager, and Mark A Cane. Suppression of el niño during the mid-holocene by changes in the earth's orbit. *Paleoceanography*, 15(6):731–737, 2000. 201

William S Cleveland. Lowess: A program for smoothing scatterplots by robust locally weighted regression. *The American Statistician*, 35(1):54–54, 1981. 71

Kim M Cobb, Christopher D Charles, Hai Cheng, and R Lawrence Edwards. El niño/southern oscillation and tropical pacific climate during the last millennium. *Nature*, 424(6946):271–276, 2003. 175

Kim M Cobb, Niko Westphal, Hussein R Sayani, Jordan T Watson, Emanuele Di Lorenzo, H Cheng, RL Edwards, and Christopher D Charles. Highly variable el niño–southern oscillation throughout the holocene. *Science*, 339 (6115):67–70, 2013. 173, 175

Mat Collins, Soon-Il An, Wenju Cai, Alexandre Ganachaud, Eric Guilyardi, Fei-Fei Jin, Markus Jochum, Matthieu Lengaigne, Scott Power, Axel Timmermann, et al. The impact of global warming on the tropical pacific ocean and el niño. *Nature Geoscience*, 3(6):391–397, 2010. 173, 174

W.D. Collins, M.L. Blackmon, G.B. Bonan, J.J. Hack, T.B. Henderson, J.T. Kiehl, W.G. Large, D.S. McKenna, C.M. Bitz, C.S. Bretherton, et al. The community climate system model version 3 (CCSM3). *Journal of Climate*, 19(11):2122–2143, 2006. ISSN 1520-0442. 149

Y Couder and C Basdevant. Experimental and numerical study of vortex couples in two-dimensional flows. *J. Fluid Mech*, 173(1986):225–251, 1986. 82

G. Danabasoglu, R. Ferrari, and J.C. McWilliams. Sensitivity of an ocean general circulation model to a parameterization of near-surface eddy fluxes. *Journal of Climate*, 21(6):1192–1208, 2008. 171

Gokhan Danabasoglu, William G. Large, Joseph J. Tribbia, Peter R. Gent, Bruce P. Briegleb, and James C. McWilliams. Diurnal coupling in the tropical oceans of ccsm3. *Journal of Climate*, 19(11):2347–2365, June 2006. doi: 10.1175/JCLI3739.1. 149

E.A. D'Asaro, T.B. Sanford, P.P. Niiler, and E.J. Terrill. Cold wake of

Hurricane Frances. *Geophysical Research Letters*, 34(15):L15609, 2007. ISSN 0094-8276. 2, 127, 145, 151

Andrew Davies, Alan ES Kemp, and Heiko Pälike. Tropical ocean-atmosphere controls on inter-annual climate variability in the cretaceous arctic. *Geophysical Research Letters*, 38(3), 2011. xxviii, 174, 200

Andrew Davies, Alan ES Kemp, Graham P Weedon, and John A Barron. El niño–southern oscillation variability from the late cretaceous marca shale of california. *Geology*, 40(1):15–18, 2012. xxviii, 174, 200

P.A. Davies, Y. Guo, D.L. Boyer, and A.M. Folkard. The flow generated by the rotation of a horizontal disk in a stratified fluid. *Fluid Dynamics Research*, 17(1):27–47, 1995. 13

Wilhelmus PM de Ruijter, Hendrik M van Aken, Emilio J Beier, Johann RE Lutjeharms, Ricardo P Matano, and Mathijs W Schouten. Eddies and dipoles around south madagascar: formation, pathways and large-scale impact. *Deep Sea Research Part I: Oceanographic Research Papers*, 51(3): 383–400, 2004. 82

Petra S Dekens, Ana Christina Ravelo, Matthew D McCarthy, and Christopher A Edwards. A 5 million year comparison of mg/ca and alkenone paleothermometers. *Geochemistry, Geophysics, Geosystems*, 9(10), 2008. 175

J.L. Demuth, M. DeMaria, and J.A. Knaff. Improvement of advanced microwave sounding unit tropical cyclone intensity and size estimation algorithms. *Journal of applied meteorology and climatology*, 45(11):1573–1581, 2006. 122

Pedro N DiNezio, Amy C Clement, Gabriel A Vecchi, Brian J Soden, Benjamin P Kirtman, and Sang-Ki Lee. Climate response of the equatorial pacific to global warming. *Journal of Climate*, 22(18):4873–4892, 2009. 174

Pedro N DiNezio, Ben P Kirtman, Amy C Clement, Sang-Ki Lee, Gabriel A Vecchi, and Andrew Wittenberg. Mean climate controls on the simulated response of enso to increasing greenhouse gases. *Journal of Climate*, 25 (21):7399–7420, 2012. 174

ET Eady. Long waves and cyclone waves. *Tellus*, 1(3):33–52, 1949. 93

TH Ellison and JS Turner. Turbulent entrainment in stratified flows. *J. Fluid Mech*, 6(3):423–448, 1959. 2, 51, 52, 53

K. Emanuel. Contribution of tropical cyclones to meridional heat transport by the oceans. *Journal of Geophysical Research*, 106:14, 2001. ISSN 0148-0227. 119, 145, 146, 161, 170

Alexey V Fedorov. Ocean response to wind variations, warm water volume, and simple models of enso in the low-frequency approximation. *Journal of Climate*, 23(14):3855–3873, 2010. 183, 185

Alexey V Fedorov and S George Philander. Is el niño changing? *Science*, 288(5473):1997–2002, 2000. 174

Alexey V Fedorov and S George Philander. A stability analysis of tropical ocean-atmosphere interactions: Bridging measurements and theory for el niño. *Journal of Climate*, 14(14):3086–3101, 2001. 174, 175, 195

AV Fedorov, RC Pacanowski, SG Philander, and G. Boccaletti. The effect of salinity on the wind-driven circulation and the thermal structure of the upper ocean. *Journal of physical oceanography*, 34(9):1949–1966, 2004. 155

AV Fedorov, PS Dekens, M. McCarthy, AC Ravelo, PB DeMenocal, M. Barreiro, RC Pacanowski, and SG Philander. The Pliocene paradox (mechanisms for a permanent El Nino). *Science*, 312(5779):1485, 2006. 6, 119, 147, 175

A.V. Fedorov, C.M. Brierley, and K. Emanuel. Tropical cyclones and permanent El Niño in the early Pliocene epoch. *Nature*, 463(7284):1066–1070, 2010. ISSN 0028-0836. 6, 119, 145, 147, 148, 149, 155, 163, 177, 178

AV Fedorov, CM Brierley, KT Lawrence, Z Liu, PS Dekens, and AC Ravelo. Patterns and mechanisms of early pliocene warmth. *Nature*, 496(7443): 43–49, 2013. 175, 177, 199

KN Fedorov and AI Ginsburg. Mushroom-like currents (vortex dipoles): one of the most widespread forms of non-stationary coherent motions in the ocean. *Mesoscale/Synoptic Coherent Structures in Geophysical Turbulence*, 50:1–14, 1989. 116

H.J.S. Fernando. Turbulent mixing in stratified fluids. *Annual review of fluid mechanics*, 23(1):455–493, 1991. 12

R. Ferrari and C. Wunsch. Ocean circulation kinetic energy: Reservoirs, sources, and sinks. *Annual Review of Fluid Mechanics*, 41(1):253, 2008. 118

R. Ferrari, J.C. McWilliams, V.M. Canuto, and M. Dubovikov. Parameterization of eddy fluxes near oceanic boundaries. *Journal of Climate*, 21(12): 2770–2789, 2008. 171

M Fleury, M Mory, EJ Hopfinger, and D Auchere. Effects of rotation on turbulent mixing across a density interface. *Journal of Fluid Mechanics*, 223:165–191, 1991. 3

Glenn R Flierl, Melvin E Stern, and John A Whitehead. The physical significance of modons: Laboratory experiments and general integral constraints. *Dynamics of atmospheres and oceans*, 7(4):233–263, 1983. 82

GR Flierl. Isolated eddy models in geophysics. *Annual review of fluid mechanics*, 19(1):493–530, 1987. 99

GR Flierl, VD Larichev, JC McWilliams, and GM Reznik. The dynamics of baroclinic and barotropic solitary eddies. *Dynamics of Atmospheres and Oceans*, 5(1):1–41, 1980. 99

Baylor Fox-Kemper, Raffaele Ferrari, and Robert Hallberg. Parameterization of mixed layer eddies. part i: Theory and diagnosis. *Journal of Physical Oceanography*, 38(6):1145–1165, 2008. 90

Simone Galeotti, Anna von der Heydt, Matthew Huber, David Bice, Henk Dijkstra, Tom Jilbert, Luca Lanci, and Gert-Jan Reichart. Evidence for active el niño southern oscillation variability in the late miocene greenhouse climate. *Geology*, 38(5):419–422, 2010. xxviii, 174, 175

JR Garratt, PAC Howells, and E Kowalczyk. The behavior of dry cold fronts traveling along a coastline. *Monthly weather review*, 117(6):1208–1220, 1989. 48

I. Ginis. Tropical cyclone-ocean interactions. *Atmosphere-ocean interactions*, 1:83, 2002. 118

I. Ginis and G. Sutyrin. Hurricane-generated depth-averaged currents and sea surface elevation. *Journal of physical oceanography*, 25(6):1218–1242, 1995. 118

R.J. Greatbatch. On the response of the ocean to a moving storm: Parameters and scales. *Journal of physical oceanography*, 14(1):59–78, 1984. 117, 122

SM Griffies, A. Gnanadesikan, KW Dixon, JP Dunne, R. Gerdes, MJ Harrison, A. Rosati, JL Russell, BL Samuels, MJ Spelman, et al. Formulation of an ocean model for global climate simulations. *Ocean Science*, 1(1):45–79, 2005. ISSN 1812-0784. 166

RW Griffiths. Gravity currents in rotating systems. *Annual Review of Fluid Mechanics*, 18(1):59–89, 1986. 3, 48, 78

Vladimir M Gryanik. Dynamics of singular geostrophic vortices in a two-layer model of the atmosphere (ocean). *Izvestiya atmospheric and oceanic physics*, 19:171–179, 1983. 95

Vladimir M Gryanik, MA Sokolovskiy, and J Verron. Dynamics of heton-like vortices. *Regular and Chaotic Dynamics*, 11(3):383–434, 2006. 95

Daifang Gu and S GH Philander. Interdecadal climate fluctuations that depend on exchanges between the tropics and extratropics. *Science*, 275 (5301):805–807, 1997. 6, 176

S. Gualdi, E. Scoccimarro, A. Navarra, et al. Changes in tropical cyclone activity due to global warming: Results from a high-resolution coupled general circulation model. *Journal of climate*, 21(20):5204–5228, 2008. 172

Eric Guilyardi, Andrew Wittenberg, Alexey Fedorov, Mat Collins, Chunzai Wang, Antonietta Capotondi, Geert Jan Van Oldenborgh, and Tim Stockdale. Understanding el niño in ocean-atmosphere general circulation models: Progress and challenges. *Bulletin of the American Meteorological Society*, 90(3):325–340, 2009. 174

J Gula, R Plougonven, and V Zeitlin. Ageostrophic instabilities of fronts in a channel in a stratified rotating fluid. *Journal of Fluid Mechanics*, 627: 485, 2009. 113

P Haertel and A.V. Fedorov. The ventilated ocean: overturning circulation and stratification in an ocean with adiabatic interior. *J. Phys. Oceanography, accepted*, 2011. 155

S. Harper. Thermocline ventilation and pathways of tropical–subtropical water mass exchange. *Tellus A*, 52(3):330–345, 2000. 155

Steven Herbette, Yves Morel, and Michel Arhan. Subduction of a surface vortex under an outcropping front. *Journal of physical oceanography*, 34 (7):1610–1627, 2004. 81

C. Herweijer, R. Seager, M. Winton, and A. Clement. Why ocean heat transport warms the global mean climate. *Tellus A*, 57(4):662–675, 2005. ISSN 1600-0870. 163, 170

NG Hogg and HM Stommel. The heton, an elementary interaction between discrete baroclinic geostrophic vortices, and its implications concerning eddy heat-flow. *Proceedings of the Royal Society of London. A. Mathematical and Physical Sciences*, 397(1812):1–20, 1985. 4, 82, 95

A. Hu and G.A. Meehl. Effect of the atlantic hurricanes on the oceanic meridional overturning circulation and heat transport. *Geophysical Research Letters*, 36(3):L03702, 2009. 146, 149

Matthew Huber and Rodrigo Caballero. Eocene el niño: evidence for robust tropical dynamics in the" hothouse". *Science*, 299(5608):877–881, 2003. xxviii, 174

GO Hughes and RW Griffiths. A simple convective model of the global overturning circulation, including effects of entrainment into sinking regions. *Ocean Modelling*, 12(1):46–79, 2006. 49

GR Hunt and NG Kaye. Virtual origin correction for lazy turbulent plumes. *Journal of Fluid Mechanics*, 435:377–396, 2001. 225, 226

Herbert E Huppert et al. Gravity currents: a personal perspective. *Journal of Fluid Mechanics*, 554:299–322, 2006. 47

VV Ivanov, GI Shapiro, JM Huthnance, DL Aleynik, and PN Golovin. Cascades of dense water around the world ocean. *Progress in Oceanography*, 60(1):47–98, 2004. 48

Linda C Ivany, Thomas Brey, Matthew Huber, Devin P Buick, and Bernd R Schöne. El niño in the eocene greenhouse recorded by fossil bivalves and wood from antarctica. *Geophysical Research Letters*, 38(16):L16709, 2011. xxviii, 174, 175

F. Jakobsen and H. Madsen. Comparison and further development of parametric tropical cyclone models for storm surge modelling. *Journal of wind engineering and industrial aerodynamics*, 92(5):375–391, 2004. 127, 133

M. Jansen and R. Ferrari. Impact of the latitudinal distribution of tropical cyclones on ocean heat transport. *Geophys. Res. Lett*, 36:L06604, 2009. 146, 148, 149, 155, 163

M.F. Jansen, R. Ferrari, and T.A. Mooring. Seasonal versus permanent thermocline warming by tropical cyclones. *Geophysical Research Letters*, 37(3):L03602, 2010. ISSN 0094-8276. 120, 146, 170

Fei-Fei Jin. An equatorial ocean recharge paradigm for enso. part i: Conceptual model. *Journal of the Atmospheric Sciences*, 54(7):811–829, 1997. 185

Fei-Fei Jin, Seon Tae Kim, and Luis Bejarano. A coupled-stability index for enso. *Geophysical research letters*, 33(23), 2006. 183, 185, 186, 187

M. Jochum. Impact of latitudinal variations in vertical diffusivity on climate simulations. *Journal of Geophysical Research (Oceans)*, 114(C13):01010, 2009. 148

Peter D Killworth. On the motion of isolated lenses on a beta-plane. *Journal of Physical Oceanography*, 13(3):368–376, 1983. 108

Seon Tae Kim and Fei-Fei Jin. An enso stability analysis. part ii: results from the twentieth and twenty-first century simulations of the cmip3 models. *Climate Dynamics*, 36(7-8):1609–1627, 2011. 192

R.L. Korty, K.A. Emanuel, and J.R. Scott. Tropical cyclone-induced upper-ocean mixing and climate: Application to equable climates. *Journal of Climate*, 21(4):638–654, 2008. 119, 147, 149, 151

Athanasios Koutavas, George C Olive, Jean Lynch-Stieglitz, et al. Mid-holocene el niño–southern oscillation (enso) attenuation revealed by individual foraminifera in eastern tropical pacific sediments. *Geology*, 34(12): 993–996, 2006. 174, 175

R Krishfield, J Toole, Andrey Proshutinsky, and Mary-Louise Timmermans. Automated ice-tethered profilers for seawater observations under pack ice in all seasons. *Journal of Atmospheric and Oceanic Technology*, 25(11): 2091–2105, 2008. xx, 83

T. Kuhlbrodt. On sandström's inferences from his tank experiments: a hundred years later. *Tellus A*, 60(5):819–836, 2008. 118

Guillaume Lapeyre, Patrice Klein, and Bach Lien Hua. Oceanic restratification forced by surface frontogenesis. *Journal of physical oceanography*, 36 (8):1577–1590, 2006. 90, 113

W.G. Large, J.C. McWilliams, and S.C. Doney. Oceanic vertical mixing: A review and a model with a nonlocal boundary layer parameterization. *Reviews of Geophysics*, 32(4):363–403, 1994. ISSN 8755-1209. 127, 149

J.R. Ledwell, A.J. Watson, and C.S. Law. Evidence for slow mixing across the pycnocline from an open-ocean tracer-release experiment. *Nature*, 364 (6439):701–703, 1993. 119

Craig M Lee, Leif N Thomas, and Yutaka Yoshikawa. Intermediate water formation at the japan/east sea subpolar front. *Oceanography*, 19(3):110, 2006. 81

Sonya Legg and John Marshall. A heton model of the spreading phase of open-ocean deep convection. *Journal of physical oceanography*, 23(6):1040–1056, 1993. 82

Sonya Legg, Helen Jones, and Martin Visbeck. A heton perspective of baroclinic eddy transfer in localized open ocean convection. *Journal of physical oceanography*, 26(10):2251–2266, 1996. 82

F Lignieres, C Catala, and A Mangeney. Angular momentum transfer in pre-main-sequence stars of intermediate mass. *Astronomy and Astrophysics*, 314:465–476, 1996. 48

PF Linden. Convection in the environment. *Perspectives in fluid dynamics: A collective introduction to current research*, pages 289–345, 2000. 218

L.L. Liu, W. Wang, and R.X. Huang. The mechanical energy input to the ocean induced by tropical cyclones. *Journal of Physical Oceanography*, 38 (6):1253–1266, 2008. ISSN 1520-0485. 146

A.M. Macdonald and C. Wunsch. An estimate of global ocean circulation and heat fluxes. *Nature*, 382(6590):436–439, 1996. 119

Michael E Mann, Mark A Cane, Stephen E Zebiak, and Amy Clement. Volcanic and solar forcing of the tropical pacific over the past 1000 years. *Journal of Climate*, 18(3):447–456, 2005. 201

GE Manucharyan. Dynamics of the mixed layers in stratified sheared flows. *Annual Proceedings Volume of the WHOI GFD Summer School*, pages 240–259, 2010. 11

GE Manucharyan and AV Fedorov. Persistent enso in climates with dierent east-west equatorial sst gradients. *Journal of Climate*, under review, 2014. 173

GE Manucharyan and M.-L. Timmermans. Generation and separation of mesoscale eddies from surface ocean fronts. *Journal of Physical Oceanography*, 43(12), 2013. 81

GE Manucharyan, CM Brierley, and AV Fedorov. Climate impacts of intermittent upper ocean mixing induced by tropical cyclones. *Journal of Geophysical Research: Oceans (1978–2012)*, 116(C11), 2011. 145, 177, 178

GE Manucharyan, W Moon, F Sevellec, AJ Wells, J.-Q. Zhong, and JS Wettlaufer. Steady turbulent density currents on a slope in a rotating fluid. *Journal of Fluid Mechanics*, in press, 2014. 47

Julian P McCreary Jr and Peng Lu. Interaction between the subtropical and equatorial ocean circulations: The subtropical cell. *Journal of Physical Oceanography*, 24(2):466–497, 1994. 176

Christopher F McKee and Eve C Ostriker. Theory of star formation. *arXiv preprint arXiv:0707.3514*, 2007. 47

JJ Monaghan. Gravity current interaction with interfaces. *Annu. Rev. Fluid Mech.*, 39:245–261, 2007. 47

F.M. Monaldo, T.D. Sikora, S.M. Babin, and R.E. Sterner. Satellite imagery of sea surface temperature cooling in the wake of hurricane edouard (1996). *Monthly weather review*, 125(10):2716–2727, 1997. 117

Yves Morel and James McWilliams. Effects of isopycnal and diapycnal mixing on the stability of oceanic currents. *Journal of physical oceanography*, 31 (8):2280–2296, 2001. 82

Yves G Morel, David S Darr, and Claude Talandier. Possible sources driving the potential vorticity structure and long-wave instability of coastal upwelling and downwelling currents. *Journal of physical oceanography*, 36 (5):875–896, 2006. 113

BR Morton, Geoffrey Taylor, and JS Turner. Turbulent gravitational convection from maintained and instantaneous sources. *Proceedings of the Royal Society of London. Series A. Mathematical and Physical Sciences*, 234(1196):1–23, 1956. 49, 52, 53, 54, 58

W. Munk and C. Wunsch. Abyssal recipes ii: energetics of tidal and wind mixing. *Deep-Sea Research Part I*, 45(12):1977–2010, 1998. 118

Doron Nof. On the β-induced movement of isolated baroclinic eddies. *Journal of Physical Oceanography*, 11(12):1662–1672, 1981. 108

Doron Nof. The translation of isolated cold eddies on a sloping bottom. *Deep Sea Research Part A. Oceanographic Research Papers*, 30(2):171–182, 1983. 50

G. Oster and M. Yamamoto. Density Gradient Techniques. *Chemical Reviews*, 63(3):257–268, 1963. 14

Y.G. Park, JA Whitehead, and A. Gnanadeskian. Turbulent mixing in stratified fluids: layer formation and energetics. *Journal of Fluid Mechanics*, 279:279–311, 1994. 12

C. Pasquero and K. Emanuel. Tropical Cyclones and Transient Upper-Ocean Warming. *Journal of Climate*, 21(1):149–162, 2008. ISSN 0894-8755. 119, 147

Joseph Pedlosky. Geophysical fluid dynamics. *New York and Berlin, Springer-Verlag, 1982. 636 p.*, 1, 1982. 99, 209

Joseph Pedlosky. The instability of continuous heton clouds. *Journal of the atmospheric sciences*, 42(14):1477–1486, 1985. 82

S George Philander. *El Niño, La Niña, and the southern oscillation*, volume 46. Academic press San Diego, 1990. 6, 173

OM Phillips. Turbulence in a strongly stratified fluid -is it unstable? In *Deep Sea Research and Oceanographic Abstracts*, volume 19, pages 79–81. Elsevier, 1972. 3, 12, 27

RA Pielke, C. Landsea, M. Mayfield, J. Laver, and R. Pasch. Hurricanes and global warming. *Bulletin of the American Meteorological Society*, 86(11): 1571–1575, 2005. 135

RT Pollard and LA Regier. Vorticity and vertical circulation at an ocean front. *Journal of Physical Oceanography*, 22(6):609–625, 1992. 113

LM Polvani. Two-layer geostrophic vortex dynamics. part 2. alignment and two-layer v-states. *Journal of Fluid Mechanics*, 225:241–270, 1991. 99

E.S. Posmentier. The generation of salinity finestructure by vertical diffusion. *Journal of Physical Oceanography*, 7(2):298–300, 1977. 12, 29

M.D. Powell, P.J. Vickery, and T.A. Reinhold. Reduced drag coefficient for high wind speeds in tropical cyclones. *Nature*, 422(6929):279–283, 2003. 128

Larry J Pratt, Ulrike Riemenschneider, and Karl R Helfrich. A transverse hydraulic jump in a model of the faroe bank channel outflow. *Ocean Modelling*, 19(1):1–9, 2007. 55

James F Price and Molly O'Neil Baringer. Outflows and deep water production by marginal seas. *Progress in Oceanography*, 33(3):161–200, 1994. 47, 48

J.F. Price. Upper ocean response to a hurricane. *Journal of Physical Oceanography*, 11:153–175, 1981. 2, 117

J.F. Price, T.B. Sanford, and G.Z. Forristall. Forced stage response to a moving hurricane. *Journal of physical oceanography*, 24(2):233–260, 1994. 118

M Princevac, HJS Fernando, and Charles D Whiteman. Turbulent entrainment into natural gravity-driven flows. *Journal of Fluid Mechanics*, 533: 259–268, 2005. 50, 51

Andrey Proshutinsky, Richard Krishfield, Mary-Louise Timmermans, John Toole, Eddy Carmack, Fiona McLaughlin, William J Williams, Sarah Zimmermann, Motoyo Itoh, and Koji Shimada. Beaufort gyre freshwater reservoir: State and variability from observations. *Journal of Geophysical Research: Oceans (1978–2012)*, 114(C1), 2009. 115

T. Radko. Mechanics of merging events for a series of layers in a stratified turbulent fluid. *Journal of Fluid Mechanics*, 577:251–273, 2007. 41

Jean N Reinaud, Xavier Carton, et al. The stability and the nonlinear evolution of quasi-geostrophic hetons. *Journal of Fluid Mechanics*, 636:109, 2009. 93

Peter B Rhines. Geostrophic turbulence. *Annual Review of Fluid Mechanics*, 11(1):401–441, 1979. 90, 133

Michel Rieutord and J-P Zahn. Turbulent plumes in stellar convective envelopes. *Astronomy and Astrophysics*, 296:127, 1995. 48

Tammy M Rittenour, Julie Brigham-Grette, and Michael E Mann. El nino-like climate teleconnections in new england during the late pleistocene. *Science*, 288(5468):1039–1042, 2000. xxviii, 174, 175

Philip G Saffman. *Vortex dynamics*. Cambridge university press, 1992. 97

Satoshi Sakai. Rossby-kelvin instability: a new type of ageostrophic instability caused by a resonance between rossby waves and gravity waves. *J. Fluid Mech*, 202:149–176, 1989. 90, 113

L Zavala Sansón, GJF van Heijst, and NA Backx. Ekman decay of a dipolar vortex in a rotating fluid. *Physics of Fluids*, 13:440, 2001. 116

Edward S Sarachik and Mark A Cane. *The El Niño-southern oscillation phenomenon*. Cambridge University Press, 2010. 173

Lars R Schade and Kerry A Emanuel. The ocean's effect on the intensity of tropical cyclones: Results from a simple coupled atmosphere-ocean model. *Journal of the atmospheric sciences*, 56(4):642–651, 1999. 2

Hermann Schlichting, Joseph Kestin, Hermann Schlichting, and Hermann Schlichting. *Boundary-layer theory*, volume 539. McGraw-Hill New York, 1968. 217

Enrico Scoccimarro, Silvio Gualdi, Alessio Bellucci, Antonella Sanna, Pier Giuseppe Fogli, Elisa Manzini, Marcello Vichi, Paolo Oddo, and Antonio Navarra. Effects of tropical cyclones on ocean heat transport in a high resolution coupled general circulation model. *J. Climate*, 2011. doi: 10.1175/2011JCLI4104.1. URL `http://journals.ametsoc.org/doi/abs/10.1175/2011JCLI4104.1`. 146, 151, 172

N Scroxton, SG Bonham, REM Rickaby, SHF Lawrence, M Hermoso, and AM Haywood. Persistent el niño–southern oscillation variation during the pliocene epoch. *Paleoceanography*, 26(2), 2011. xxviii, 6, 174, 175

L. Shaffrey and R. Sutton. Bjerknes Compensation and the Decadal Variability of the Energy Transports in a Coupled Climate Model. *Journal of Climate*, 19:1167, 2006. ISSN 0894-8755. 163

GI Shapiro and AE Hill. Dynamics of dense water cascades at the shelf edge. *Journal of Physical Oceanography*, 27(11):2381–2394, 1997. 48, 78

GI Shapiro and AG Zatsepin. Gravity current down a steeply inclined slope in a rotating fluid. In *Annales Geophysicae*, volume 15, pages 366–374. Springer, 1997. 48

Christine A Shields, David A Bailey, Gokhan Danabasoglu, Markus Jochum, Jeffrey T Kiehl, Samuel Levis, and Sungsu Park. The low-resolution ccsm4. *Journal of Climate*, 25(12):3993–4014, 2012. 177

JH Simpson and JD Woods. Temperature microstructure in a fresh water thermocline. *Nature*, 226(5248):832, 1970. 11

John E Simpson. *Gravity currents: In the environment and the laboratory.* Cambridge University Press, 1999. 47

K Shafer Smith and Geoffrey K Vallis. The scales and equilibration of midocean eddies: Freely evolving flow. *Journal of Physical Oceanography*, 31 (2):554–571, 2001. 90

Peter C Smith. A streamtube model for bottom boundary currents in the ocean. In *Deep Sea Research and Oceanographic Abstracts*, volume 22, pages 853–873. Elsevier, 1975. 48

MA Sokolovskiy and J Verron. Finite-core hetons: Stability and interactions. *Journal of Fluid Mechanics*, 423:127–154, 2000. 93

Michael A Spall. Frontogenesis, subduction, and cross-front exchange at upper ocean fronts. *Journal of Geophysical Research: Oceans (1978–2012)*, 100(C2):2543–2557, 1995. 81, 82, 84, 90

Michael A Spall and David C Chapman. On the efficiency of baroclinic eddy heat transport across narrow fronts*. *Journal of physical oceanography*, 28 (11):2275–2287, 1998. 81, 82, 110

Michael A Spall, Robert S Pickart, Paula S Fratantoni, and Albert J Plueddemann. Western arctic shelfbreak eddies: Formation and transport. *Journal of Physical Oceanography*, 38(8):1644–1668, 2008. 115

R.L. Sriver. Tropical cyclones in the mix. *Nature*, 463:25, 2010. 151

R.L. Sriver and M. Huber. Observational evidence for an ocean heat pump induced by tropical cyclones. *Nature*, 447(7144):577–580, 2007. ISSN 0028-0836. 5, 119, 145, 146, 152, 163

R.L. Sriver and M. Huber. Modeled sensitivity of upper thermocline properties to tropical cyclone winds and possible feedbacks on the Hadley circulation. *Geophysical Research Letters*, 37(8):L08704, 2010. ISSN 0094-8276. 147, 155

R.L. Sriver, M. Huber, and J. Nusbaumer. Investigating tropical cyclone-climate feedbacks using the trmm microwave imager and the quick scatterometer. *Geochemistry Geophysics Geosystems*, 9(9):Q09V11, 2008. 146, 155

R.L. Sriver, M. Goes, M.E. Mann, and K. Keller. Climate response to tropical cyclone-induced ocean mixing in an Earth system model of intermediate complexity. *Journal of Geophysical Research*, 115(C10):C10042, 2010. ISSN 0148-0227. 145

Melvin E Stern and JA Whitehead. Separation of a boundary jet in a rotating fluid. *Journal of Fluid Mechanics*, 217(1):41–69, 1990. 82

Peter H Stone. On non-geostrophic baroclinic stability. *Journal of the Atmospheric Sciences*, 23(4):390–400, 1966. 90

Bruce R Sutherland, Joshua Nault, Kerianne Yewchuk, and Gordon E Swaters. Rotating dense currents on a slope. part 1. stability. *Journal of Fluid Mechanics*, 508:241–264, 2004. 66

GE Swaters. Mathematical modelling of solitary oceanographic vortices. In *Fluid Vortices*, pages 575–615. Springer, 1995. 99

GI Taylor. Tidal friction in the irish sea. *Philosophical Transactions of the Royal Society of London. Series A, Containing Papers of a Mathematical or Physical Character*, 220:1–33, 1920. xvii, 55, 57, 64

Leif N Thomas. Formation of intrathermocline eddies at ocean fronts by wind-driven destruction of potential vorticity. *Dynamics of Atmospheres and Oceans*, 45(3):252–273, 2008. 81, 87

Leif N Thomas, Amit Tandon, and Amala Mahadevan. Submesoscale processes and dynamics. *Ocean modeling in an eddying regime*, pages 17–38, 2008. 81, 115

A Timmermann, SJ Lorenz, SI An, A Clement, and SP Xie. The effect of orbital forcing on the mean climate and variability of the tropical pacific. *Journal of Climate*, 20(16):4147–4159, 2007. 201

Mary-Louise Timmermans, J Toole, Andrey Proshutinsky, R Krishfield, and A Plueddemann. Eddies in the canada basin, arctic ocean, observed from ice-tethered profilers. *Journal of Physical Oceanography*, 38(1):133–145, 2008. xx, 82, 83, 84

Mary-Louise Timmermans, Andrey Proshutinsky, Jennifer Francis, and Lawrence Hamilton. Taking stock of arctic sea ice and climate. *Bulletin of the American Meteorological Society*, 90(9):1351–1353, 2009. 49

John M Toole, Richard A Krishfield, Mary-Louise Timmermans, and Andrey Proshutinsky. The ice-tethered profiler: Argo of the arctic. 2011. xx, 83

K. Trenberth. Uncertainty in hurricanes and global warming. *Science*, 308 (5729):1753, 2005. 135

JS Turner. Turbulent entrainment: the development of the entrainment assumption, and its application to geophysical flows. *J. Fluid Mech*, 173 (431):71, 1986. 49, 50

Geoffrey K Vallis. *Atmospheric and oceanic fluid dynamics: fundamentals and large-scale circulation.* Cambridge University Press, 2006. 99

GJF Van Heijst and HJH Clercx. Laboratory modeling of geophysical vortices. *Annual Review of Fluid Mechanics*, 41:143–164, 2009. 82

GJF Van Heijst and JB Flor. Dipole formation and collisions in a stratified fluid. 1989. 82

SI Voropayev, Ya D Afanasyev, and IA Filippov. Horizontal jets and vortex dipoles in a stratified fluid. *Journal of Fluid Mechanics*, 227(1):543–566, 1991. 82, 93

AK Wåhlin and Claudia Cenedese. How entraining density currents influence the stratification in a one-dimensional ocean basin. *Deep Sea Research Part II: Topical Studies in Oceanography*, 53(1):172–193, 2006. 49

Michael W Wara, Ana Christina Ravelo, and Margaret L Delaney. Permanent el niño-like conditions during the pliocene warm period. *Science*, 309 (5735):758–761, 2005. 175

Masahiro Watanabe, Jong-Seong Kug, Fei-Fei Jin, Mat Collins, Masamichi Ohba, and Andrew T Wittenberg. Uncertainty in the enso amplitude change from the past to the future. *Geophysical Research Letters*, 39(20), 2012. 174

Tsuyoshi Watanabe, Atsushi Suzuki, Shoshiro Minobe, Tatsunori Kawashima, Koji Kameo, Kayo Minoshima, Yolanda M Aguilar, Ryoji Wani, Hodaka Kawahata, Kohki Sowa, et al. Permanent el niño during the pliocene warm period not supported by coral evidence. *Nature*, 471 (7337):209–211, 2011. xxviii, 174, 175, 200

Mathew Wells, Claudia Cenedese, and CP Caulfield. The relationship between flux coefficient and entrainment ratio in density currents. *Journal of Physical Oceanography*, 40(12):2713–2727, 2010. 50, 51

MG Wells. Influence of coriolis forces on turbidity currents and sediment deposition. In *Particle-Laden Flow*, pages 331–343. Springer, 2007. 50, 51, 76, 80

MG Wells and JS Wettlaufer. Two-dimensional density currents in a confined basin. *Geophysical & Astrophysical Fluid Dynamics*, 99(3):199–218, 2005. xvii, 51, 57

MG Wells and JS Wettlaufer. The long-term circulation driven by density currents in a two-layer stratified basin. *Journal of Fluid Mechanics*, 572: 37–58, 2007. 49

Alexander V Wilchinsky, Daniel L Feltham, and Paul R Holland. The effect of a new drag-law parameterization on ice shelf water plume dynamics. *Journal of physical oceanography*, 37(7):1778–1792, 2007. 78

Achim Wirth. On the basic structure of oceanic gravity currents. *Ocean Dynamics*, 59(4):551–563, 2009. 48, 78

Achim Wirth. Estimation of friction parameters in gravity currents by data assimilation in a model hierarchy. *Ocean Science Discussions*, 8(1):159–187, 2011. 49

Andrew Thorne Wittenberg. *ENSO response to altered climates*. PhD thesis, Princeton University, 2002. 175, 195

Fred Wobus, Georgy I Shapiro, Miguel AM Maqueda, and John M Huthnance. Numerical simulations of dense water cascading on a steep slope. *Journal of Marine Research*, 69(2-3):2–3, 2011. 48, 78

C. Wunsch and R. Ferrari. Vertical mixing, energy, and the general circulation of the oceans. *Annu. Rev. Fluid Mech.*, 36:281–314, 2004. 118

C. Wunsch and P. Heimbach. How long to oceanic tracer and proxy equilibrium? *Quaternary Science Reviews*, 27(7-8):637–651, 2008. 155

Sang-Wook Yeh, Jong-Seong Kug, Boris Dewitte, Min-Ho Kwon, Ben P Kirtman, and Fei-Fei Jin. El niño in a changing climate. *Nature*, 461(7263): 511–514, 2009. 174, 195

Andrew N Youdin and Frank H Shu. Planetesimal formation by gravitational instability. *The Astrophysical Journal*, 580(1):494, 2002. 48